The University Of Sheffield.

Department
of
Mechanical
Engineering

# Experimental Study of Turbulence in Transient Channel Flows

by

## Benjamin Segun Oluwadare

Supervised by Professor Shuisheng He

A DISSERTATION

Submitted in partial fulfilment of the requirements
for the degree of Doctor of Philosophy

Department of Mechanical Engineering

The University of Sheffield

October 2019

# Abstract

Experimental studies have been carried out to improve our understanding of the behaviour of turbulence under transient conditions by expanding the new perspective recently established numerically by He and Seddighi (J. Fluid Mech., 715: 60-102, 2013), Seddighi et al. (Flow Turbulence Combustion., 92: 473-502, 2014) and He and Seddighi (J. Fluid Mech., 764: 395-427, 2015). The present work significantly extends the flow conditions investigated in a previous study by Mathur et.al. (J. Fluid Mech., 835: 471-490, 2018) using the same experimental facility. Particle Image Velocimetry (PIV) has been used to measure instantaneous velocities during the transient conditions and Constant Temperature Anemometry (CTA) with hot-film sensors is used to measure the wall shear stress. The length, width, and height of the test rig measured 8000 $mm$, 350 $mm$ and 50 $mm$, respectively, and water is used as the working fluid. Flow is accelerated from an initial statistically steady turbulent flow to final statistically steady turbulent flow. This is achieved using a pneumatic control valve. The ramp rate, start and end Reynolds numbers and the period of acceleration are varied to study their effects.

The response of all the accelerating flows investigated is shown to be characterised by laminar-turbulent transition, which follows a three-stage development that is similar to the three-stage response reported by He and Seddighi (J. Fluid Mech., 715: 60-102, 2013) resembling the three stages of boundary layer bypass transition induced by free-stream turbulence. These are buffeted laminar boundary layer, intermittent turbulence spot formation, and a fully developed turbulent boundary layer. The first stage consists of an enhancement and elongation of the pre-existing streaky structures in the flow. In the second stage, the secondary instabilities of the streaky structures increase, and the formation of isolated turbulence spots can be seen. The turbulence spots grow with time and merge with each other. These turbulence spots fill the entire wall-bounded surface when the flow has become fully developed turbulent flow in the third stage. In accordance with this three-stage response, the skin friction coefficient ($C_f$) increases sharply initially and reaches its maximum value due to the creation of a thin boundary layer near the wall that results in an increase of velocity gradient, strain rate and viscous force. As the boundary layer thickness increases by diffusion, the viscous force and skin friction coefficient decrease. The minimum point of the skin friction coefficient marks the beginning of transition. It increases again during the transitional period due to the generation of ‘‘new’’ turbulence near the wall. The first peak that the $C_f$ attains after its recovery marks the completion of transition.

It has been shown that as the initial Reynolds number increases while the final Reynolds number remains fixed, the time of onset of transition reduces. The process of transition to turbulence becomes very subtle and the transition features are not clearly seen from the visualisation and $C_f$ responses when the initial Reynolds number is high. The characteristic of transition is however unambiguously seen in the response of turbulence especially in the wall normal fluctuating velocity, which remains unchanged during the pre-transition period. On the other hand, the process of transition to turbulence is strong when the initial Reynolds number is small and the transition features are visible in the responses of $C_f$ as well as turbulence. The effect of varying the acceleration period is investigated while the initial Reynolds number and final Reynolds numbers remain fixed. The time at which transition to turbulence occurs increases as the acceleration period increases and vice versa. The response of the wall shear stress follows rather closely the quasi-steady variations when the acceleration is very slow. However, again, the response of turbulence clearly demonstrates the distinct nature of transition even in such slow accelerations.

It has previously been shown that the time-developing boundary layer in a step increase of flow rate forms rapidly near the wall and grows into the flow. In the present study, it has been demonstrated that a temporally developing boundary layer is also resulted in the gradually accelerating flows which is formed as a result of a continuous change in velocity gradient near the wall and then expands into the flow. The pre-transitional stage of the temporally developing boundary layer of the present gradual acceleration coincides with the temporally developing boundary layer illustrated by an extended solution to Stokes' first problem based on the integration of many small step increases in flow rate.

Modifications have been made to the equivalent Reynolds number ($Re_t$) and the initial turbulence intensity ($Tu_0$) proposed by He and Seddighi (J. Fluid Mech., 764: 395-427, 2015) in order to account for the slow accelerating flows and the continuous change of the bulk velocities of the cases investigated. It has been shown that the critical equivalent Reynolds number ($Re_{t,cr}$) based on these modifications and the initial turbulence intensity ($Tu_0$) are well correlated for all cases studied and a power-law relation is established.

# Acknowledgements

Firstly, I give all glory, honour and adoration to the Almighty God, who framed the universe by His word, and for His good health, grace and providence upon me throughout the period of my PhD research at the University of Sheffield.

I will ever be grateful to my financial sponsor – Petroleum Technology Trust Fund (PTDF) for providing the financial support for my PhD programme at the University of Sheffield in the United Kingdom, without which this research would not have been achieved. Special thanks also to the government of Federal Republic of Nigeria for the establishment of PTDF. Indeed, PTDF has affected the lives of many youths academically through both local and overseas scholarships and I am proud to count myself amongst their number. I am also indebted to the management of Ekiti State University, Ado-Ekiti (EKSU) for the approval of my study leave in order to pursue this programme.

Special thanks go to my supervisor, Professor Shuisheng He, for introducing me to the field of turbulence and for being a source of valuable consultation and inspirational guidance. His broad knowledge of the subject of turbulence and experimental experience has contributed to making this research a success. His answers to every question presented to him during meetings have given me a strong foundation in the study of turbulence and helped me to produce a publishable thesis deserving of the research that has been undertaken thus far. I am grateful to him for the helpful feedback he has provided in proof-reading my dissertation. Based on the knowledge that I have gained from my supervisor and my PhD research degree programme, I can confidently say that I feel better prepared for my future career.

Special thanks go to Dr Robert J. Howell, my DDP supervisor, for his valuable suggestions regarding my Training Need Analysis (TNA).

I would also like to acknowledge the assistance of the Technical Staff of Mechanical Engineering workshop of the University of Sheffield, especially the senior technician attached to my laboratory (Mr Oliver Cooper) who helped me during the repair and maintenance of the experimental rig. Their assistance during the relocation of my experimental rig to the new location is highly appreciated.

Special thanks also to staff members of Dantec Dynamics Inc., Dr Ivan Zadrazil (International Sales Manager), Dr Philippe Galtier and Dr Robert Jaryczewski for their helpful assistance during my experimental investigations in the laboratory. When my Particle Image Velocimetry (PIV) work station crashed, the assistance of Dr Ivan Zadrazil in obtaining a newer version of DynamicStudio software is highly appreciated.

Sincere appreciation goes to the members of Heat, Flow and Turbulence Research Group of the University of Sheffield who have contributed substantially towards the success of my research – Dr Mehdi Seddighi, Dr Sam Gorji, Dr Akshat Mathur, Dr Kui He, Dr Muhsin Mohd Amin, Dr Cosimo Trinca, Dr Bo Liu, Dr Xiaoxue Huang, Mr Kenneth Chinembiri, Mr Jundi He, Mr Yanfein Gao and Miss Xu Wang. It is absolutely amazing to know you all.

My sincere appreciation goes to my lovely parents for the inspiration and support given to me throughout my life. They encouraged me to always aim higher and supported my education.

Finally, I will ever be grateful to my dear wife and soulmate, Feyisetan, and my amazing children, Abiola and Oluwabukunmi, for their sacrifices and endless love. I am always proud of you; you are so precious to me.

# Table of Contents

# List of Figures

# List of Tables

# Nomenclature

| | |
|---|---|
| $C_f(t)$ | Skin friction coefficient |
| $M$ | Magnification factor |
| $Re$ | Reynolds number |
| $Re_b$ | Reynolds number based on channel half-height and bulk velocity |
| $Re_{t,cr}$ | Critical equivalent Reynolds number |
| $\Delta Re_{t,cr}$ | Transitional period Reynolds number |
| $Re_t$ | Equivalent Reynolds number |
| $Re_{turb}$ | Fully-turbulent Reynolds number |
| $Re_\tau$ | Friction velocity Reynolds number |
| $Re_\theta$ | Momentum thickness Reynolds number based on centreline velocity |
| $H$ | Shape factor |
| $t$ | Time in second |
| $Tu_0$ | Initial turbulence intensity |
| $u$ | Streamwise velocity |
| $v$ | Wall-normal velocity |
| $w$ | Spanwise velocity |
| $U_{conv}$ | Convective velocity |
| $U_b$ | Bulk velocity |
| $U_c$ | Centreline velocity |
| $U_\infty$ | Free-stream velocity |
| $u_\tau$ | Friction velocity |
| $u'$ | Fluctuating streamwise velocity |
| $v'$ | Fluctuating wall-normal velocity |
| $w'$ | Fluctuating spanwise velocity |
| $u'_{rms}$ | Fluctuating streamwise root-mean-square velocity |
| $v'_{rms}$ | Fluctuating wall-normal root-mean-square velocity |
| $w'_{rms}$ | Fluctuating spanwise root-mean-square velocity |
| $\overline{u'v'}$ | Reynolds shear stress |
| $W$ | Channel width |
| $x$ | Streamwise direction |
| $y$ | Wall-normal direction |
| $z$ | Spanwise direction |

| | |
|---|---|
| $\Delta t$ | Acceleration period |
| $\mathrm{d}t$ | Time between the two light pulses |
| $\Delta t_{ac}$ | Acceleration rate |
| $h$ | Channel half-height |
| $d_{PIV}$ | Length of the interrogation |
| $d$ | Probe diameter |
| $\tau_w$ | Wall shear stress |
| $\Delta x$ | Displacement |

***Greek symbols***

| | |
|---|---|
| $\mu$ | Dynamics viscosity |
| $\nu$ | Kinematics viscosity |
| $\kappa$ | von Kármán constant |
| $\delta$ | Channel half-height |
| $\gamma$ | Intermittency |
| $\rho$ | Density |
| $\eta$ | Stokes' dimensionless similarity variable |
| $\sigma$ | Repeatability |
| $\tau$ | Small time step |
| $\theta$ | Momentum thickness |

***Subscripts***

| | |
|---|---|
| $\wedge$ | Perturbation velocity component |
| $*$ | Outer scalling |
| $+$ | Inner scalling |

***Subscripts***

| | |
|---|---|
| $rms$ | Root mean square |
| $turb$ | Fully developed turbulent state |
| $max$ | Maximum value |
| $0,1$ | Initial and final states |
| $b$ | Bulk value |
| $c$ | Centreline |
| $cr$ | Critical state |
| $Stokes$ | Relating to the solution of extended Stokes' solution |
| $du$ | Relating to perturbation flow |

***Abbreviations***

| | |
|---|---|
| $CCD$ | Charged-Coupled Device |

| | |
|---|---|
| $CTA$ | Constant-Temperature Anemometer |
| $DAQ$ | Data Acquisition |
| $LES$ | Large-Eddy Simulation |
| $DNS$ | Direct Numerical Simulation |
| $FOV$ | Field of View |
| $FST$ | Free-Stream Turbulence |
| $IA$ | Interrogation Area |
| $PIV$ | Particle Image Velocimetry |
| $TS$ | Tollmien-Schlichting |
| $PVC$ | Polyvinyl Chloride |
| $RANS$ | Reynolds-Avergaed Navier-Stokes |
| $LDV$ | Laser Droppler Velocimetry |
| $LRN$ | Low-Reynolds Number |

# Chapter 1

# Introduction

## 1.1 Research background

In fluid mechanics, turbulence has received significant attention since the seminar work of the second professor of engineering in England on transition from laminar to turbulence (Reynolds, 1883). In most engineering applications, flows are turbulent in nature. Unsteady flows occur in a channel when the discharge varies with time due to ramping up or ramping down the rate of the flow. Thus, the study of unsteady flows experimentally and numerically in pipes/channels has been ongoing for over a century. Unsteady turbulent flows are encountered in many engineering applications. Examples include the movement of oil and gas in pipelines, the flow used by chemical engineers for proper mixing of mixtures in order to accelerate rates of chemical reactions in liquids, boundary layer growth on the wings of an aircraft, flow of fluid inside nuclear power plants, and flow of fluid inside internal combustion engines. Unfortunately, the turbulence in unsteady flows which is frequently encountered in the above engineering applications is highly complex and not well known. Accurate determination of wall shear stress near the walls of pipes/channels is vital for the design and construction of efficient pipeline systems in the oil and gas industries. Indeed, a complete understanding of unsteady turbulent flows is expedient in designing and controlling flow systems such as starting and tripping of pumps, biological circulatory systems, railway tunnels, nuclear power plant, internal combustion engines, the flow of blood in the human body, flow in the pipe of an oil refinery and the shut down of valves in a pipeline system; (He and Seddighi, 2013; Tennekes, Hendrik & Tennekes, 1972).

This current study is concerned with the transition of transient turbulent flow in a channel. The transition of transient turbulent flow has been studied numerically using direct numerical simulations (DNS) by He and Seddighi (2013), Seddighi et al. (2014), and He and Seddighi (2015). The authors have established that the transition of transient turbulent flow resembles that of laminar-turbulent bypass transition on a flat plate boundary layer flow even though the initial flow is turbulent. This new concept has been confirmed experimentally by Mathur (2018). This current study aims to extend the knowledge further by increasing the flow conditions. The initial Reynolds numbers of this current study have been increased higher than that of Mathur (2018). The transition procedure is investigated as the initial and final Reynolds numbers are varied. Moreover, the flow conditions of the slow acceleration of this current study have been increased higher than that of Seddighi et al. (2014), and the periods of acceleration are varied and the turbulence features in the transient turbulent flow are studied.

## 1.2 Aims and objectives of the study

This current study is aimed at consolidating and expanding the new perspective of the behaviour of transient turbulent flow established by He and Seddighi (2013; 2015) and Seddighi et al. (2014). In brief, they have established that transient turbulent flow is characterised by a laminar to turbulent transition despite the initial flow condition being turbulent. The procedure resembles that of bypass transition induced by free-stream turbulence. The main focus of this present investigation is to study the response of turbulence in the near-wall of a temporal accelerating flow due to sudden and controlled opening of a pneumatic control valve. The flow acceleration is obtained from the initial statistically steady turbulent flow to the final statistically turbulent flow following the opening of a pneumatic control valve. This current research specifically aims to achieve the following objectives: 1) the effect of the variation of the initial Reynolds number on the transition to turbulence with a fixed final Reynolds number, 2) the effect of varying the final Reynolds number with a fixed initial Reynolds number during transient flow conditions, 3) the effect of varying the acceleration periods of the transient with a fixed initial and fixed final flow condition, 4) the effect of varying the acceleration periods on fixed initial Reynolds number and varied final Reynolds number. The Reynolds number of the initial statistically steady turbulent flow is denoted as $Re_0$ and that of the final flow is denoted as $Re_1$. The initial Reynolds number ($Re_0$) is obtained from the flow of known velocity that is allowed for 120 $secs$ before accelerating linearly to a final Reynolds number ($Re_1$) within a short time. The temporally developing boundary layer generated near the walls is then compared with the extended laminar boundary layer to study the representation of mean flow and skin friction coefficient with the laminar flow at the initial stage of the transient flow. The transient procedure is studied using standard methods: Particle Image Velocimetry (PIV) and Constant Temperature Anemometry (CTA) with hot-film sensors. For comparison purposes, the steady experimental data is compared with the DNS data of Lee and Moser (2015). The unsteady experimental results are compared with the numerical results of the rapid increase of flow rate of He and Seddighi (2013; 2015) and the slower accelerating flow of Seddighi et al. (2014).

In order to achieve the above objectives, the current study has carried out the following tasks:

- To re-design the current channel flow facility at the new location-George Porter Building for better flow visualisation;
- To greatly improve the flow visualisation and increase the experimental measurement area from $3\delta \times 3\delta$ to $4\delta \times 4\delta$;
- To carry out experiments to determine mean and turbulence statistics on smooth surface channel bed with different Reynolds' number ratios based on different intial and final Reynolds numbers;
- To analyse the response of mean flow and turbulence statistics on the same initial and final flow conditions with different acceleration periods.

## 1.3 Thesis framework

This thesis comprises six chapters. Chapter one consists of a brief description of the research background, the aims and specific objectives of the current study, and the thesis outline that provides a guide to its readers. Chapter two presents a review of related journal articles on bypass transition on flat plate boundary layer flow, transient turbulent flow over smooth walls, accelerating flows from rest or laminar ramping up to turbulent flow, and the new interpretation to transition to turbulence of transient turbulent flows. Following this, Chapter three presents a detailed discussion of the experimental channel flow rig, the measurement devices utilised and the methods of data acquisition adopted. Chapter four contains a presentation of the data obtained from the study of the variation of Reynolds number ratios in transient turbulent flow in a smooth-surface channel. In Chapter five, a full discussion of the data of accelerating flows with different acceleration ratess is presented. The last chapter provides concluding remarks concerning the findings of the investigations described in the thesis and presents recommendations for future work to be done on the basis of this research.

## Chapter 2

# Research Background and Literature Review

## 2.1 Introduction

Due to its pervasiveness in many engineering problems, it is important to gain knowledge of turbulent flow as possible. This chapter presents a detailed description of the investigations that have been carried out numerically and experimentally by dedicated researchers in the areas of transient turbulent flows in channel and bypass transition associated with flat plate boundary layer flows. Indeed, the study of turbulence to find solutions to engineering problems has been on-going for over a century by many researchers. Although considerable progress has been recorded in this time, there are many aspects of turbulence that remain unexplored and unknown. For instance, despite extensive investigations having been conducted on turbulence, there is no absolute consensus on its definition. Experiments show that at any fixed point in the turbulent field, the velocity varies irregularly with time about a mean value. For the purpose of contributing substantially to the study of turbulence research, it is expedient that the related journal articles in the field are reviewed. In this chapter, the background of laminar and turbulent flows is explained followed by a thorough review of the literature related to these topics of study. This literature review chapter is organised as follows. Firstly, the transition from laminar to turbulence is explained, followed by the characteristics of turbulent flows. The concept of the boundary layer is elucidated and followed by a thorough literature review on bypass transition. The knowledge of bypass transition on flat plate boundary layer flows is expedient in this current study and many relevant papers are reviewed. Following this, transient turbulent flows over smooth surfaces are presented with their subdivisions: periodic unsteady flow and non-periodic unsteady flow. Related papers of non-periodic unsteady flow, which is the main focus of the current study, are presented. Finally, relevant studies of the new interpretation of transient turbulent flow transition in channel, which this current study is built on, are discussed.

## 2.2 Laminar and turbulent flow

In laminar flow, the movement of the particles is parallel to streamlines and the layers of the fluid are not mixed (see Figure 2-1). Turbulent flow is characterised by a chaotic movement of fluid particles. The fluid velocity varies irregularly and randomly and there is a mixing of fluid at different heights from the wall. The flow properties in turbulent flow depend on time, and the flow becomes difficult to predict because of eddies.

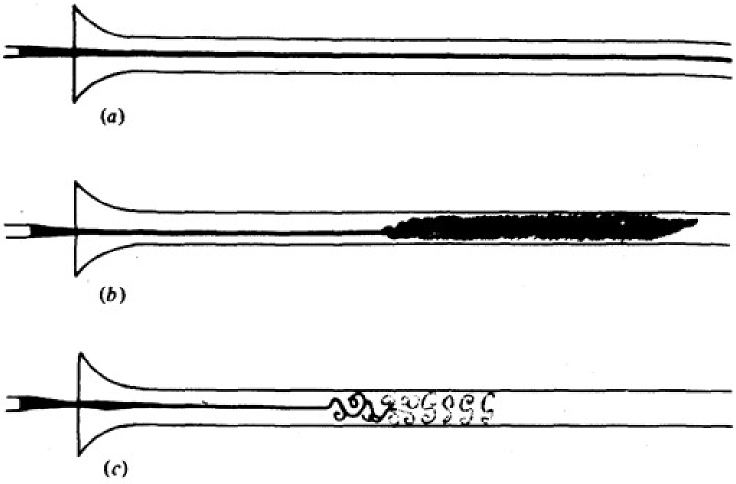

***Figure 2-1 Reynolds' experimental observations showing the nature of fluid flow (Reynolds, 1883).***

Reynolds' (1883) experimental investigation, as shown in Figure 2-1a, 2-1b and 2-1c, demonstrated laminar and turbulent flow by adding dye into the flow field at the centre of a large pipe made of glass and observing the direction of the dye in the flow under different flow rates. The flow rate was adjusted using a flow control valve attached to the end of the pipe. The experiments showed that at low velocity, the layer of the dye flowed parallel to the streamlines of the flow and the layers of the dye did not cross each other. Furthermore, the adjacent flow layers did not mix. As the velocity of flow was increased by small increments, layers of the dye mixed with the surrounding water and filled the flow region with coloured water, as shown in Figure 2-1b. The flow at this point referred to as transitional flow. Finally, as the velocity of the flow further increased, the flow became turbulent at which point the vortex in the flow broke up and occupied the cross-section of the pipe. The layers of the fluid flow mixed with the adjacent layers and there was disorderliness in the direction of flow, as shown in Figure 2-1c. The nature of fluid flow was described by Haywood (1996) and is presented in Figure 2-2. When the flow is laminar, the layer of fluid is in parallel to the mean flow but when the flow has become turbulent, eddies of different sizes are moved across the mean flow. The current study is based on these procedures.

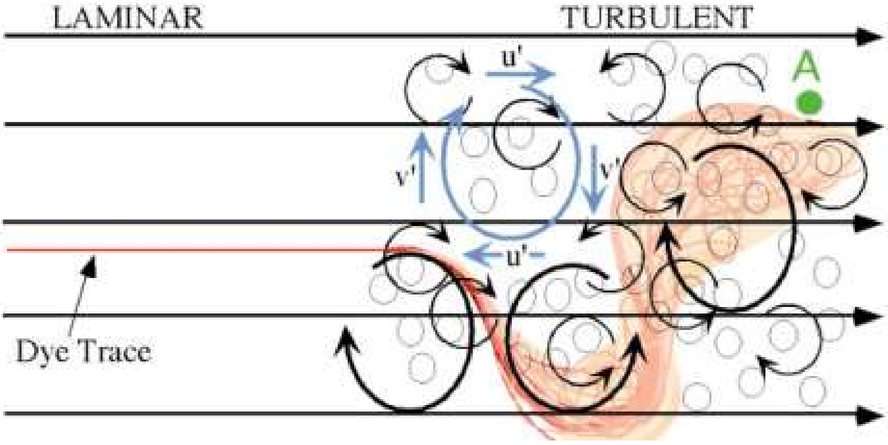

***Figure 2-2: Nature of laminar and turbulent flow (Haywood, 1996).***

The nature of turbulent flow can be understood by considering taps of water with different flow rates. As the flow rate increases, the flow has a greater tendency to become turbulent. However, if the flow through the taps of water is replaced by oil, which is more viscous in nature, a much higher flow rate is required for the flow to be turbulent. The tendency of the flow to become turbulent decreases with an increase in viscosity, whereas it increases with an increase in flow velocity. Reynolds number is a parameter that can be used to determine if the flow is laminar or turbulent and can be calculated by the following equation: $Re = \frac{inertial\, force}{viscous\, force} = \frac{\rho UD}{\mu}$. This dimensionless Reynolds number is a useful parameter that can be used to characterise the fluid flow's nature and is defined as the ratio of inertial force to the viscous force. At low velocity, the viscous effect will dampen out any flow perturbation that is generated in the flow. This causes the flow to be maintained in a laminar state. However, as the viscous effect in the flow does not become sufficient enough to dampen any perturbation generated in the flow, it becomes turbulent when the inertial force is higher than the viscous force.

### 2.2.1 Characteristics of turbulent flow

Turbulent flow can be considered as a highly chaotic motion which results from the growth of instabilities in a flow that is initially laminar. It is a characteristic feature that is revealed when a flow deviates from being laminar. The fluctuations of velocity and pressure at a given point in time in the fluid flow form the most important characteristic of turbulent flow, a flow which can be generated either by shear stress at the wall or a free shear layer of fluid flow in wake etc., at different velocities. In terms of differentiating turbulent flow from laminar, the following characteristics can be used (Tennekes, Hendrik & Tennekes, 1972):

**Irregularity -** The deterministic model to turbulence problems has been made impossible with irregularity or randomness characteristics. Due to the high level of fluctuations in turbulent flow, statistical methods are used to describe the flow properties.

**Dissipation –** Dissipation is always associated with the turbulent flow. The internal energy of the fluid increases as the kinetic energy is changed into heat as a result of viscous shear stresses. When no energy is supplied, turbulent flow dies out rapidly and the flow becomes laminar.

**Diffusivity –** Turbulent flow is characterised by chaos and diffusivities. However, when a flow is chaotic and not diffusive, then it is not turbulent flow. Diffusivity of the turbulent flow leads to an increase in momentum, heat, and mass transfer when there is rapid mixing of the fluid particles.

**Three-dimensional vorticity fluctuations –** The vorticity-maintenance mechanisms, such as stretching of three-dimensional vortices, play a prominent role in the study of turbulence. However, turbulence is three dimensional and it consists of a high level of fluctuating vorticity.

**High Reynolds number –** The flow becomes turbulent at higher Reynolds numbers. When the Reynolds number is high, the laminar flow becomes unstable due to instability in the flow causing a transition to turbulence. The interaction between the viscous terms and the inertial terms in the dimensionless Reynolds equation determines the nature of the flow. At low Reynolds number, viscous terms are relevant and any instability in the flow is dampened.

Conversely, inertial terms dominate the viscous effect and the flow becomes turbulent when the Reynolds number is high.

In fluid mechanics, there are three types of averages: ensemble, spatial and time average. Averaging is the process of obtaining mean value of random variables, such as velocity and wall shear stress, which are captured in a given experiment over space and time. In other words, averages can be performed in space, time and over certain realisations. An average over different experimental runs is known as the ensemble average. In further detail, time average is performed over a specified period of time while the spatial average is performed over a homogeneous direction in space. In the second paper presented to the Royal Society by Osborne Reynolds, the instantaneous velocity was described as the addition of mean and fluctuating velocities. The basis of the RANS equation that is famous among the computational fluid dynamic software packages today is formulated when the decomposition is substituted to the Navier-Stokes equations Reynolds (1895), followed by performing an average on the equation.

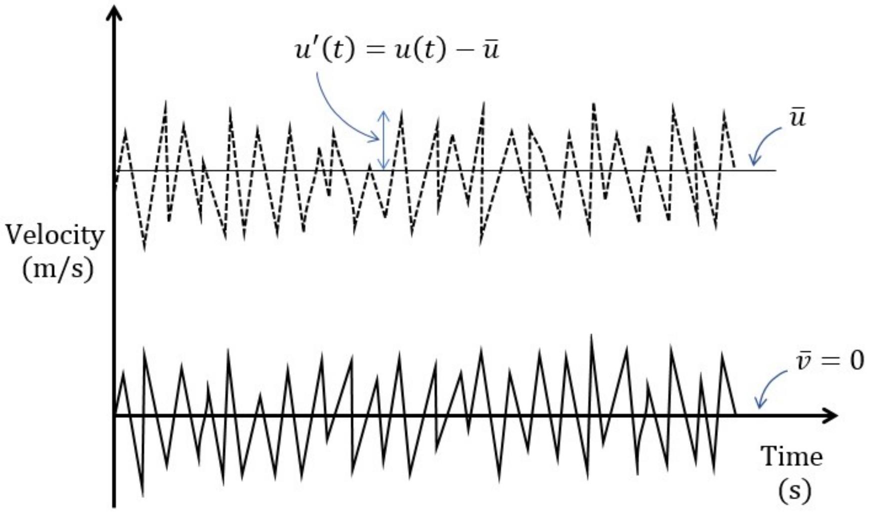

***Figure 2-3: Variation of velocities u and v with time.***

Flow fluctuation and rotation cause eddies and make the velocity fluctuate in turbulent flows. As an example, Figure 2-3 shows how the turbulent fluctuations cause the velocities to vary on both the $x$ and $y$-axes. Reynolds decomposition is a mathematical method that shows how instantaneous quantities are decomposed into a mean value and fluctuating value.

$$u(t) = \bar{u} + u'(t) \tag{2.1}$$

$$v(t) = \bar{v} + v'(t) \tag{2.2}$$

where $\bar{u}$ and $\bar{v}$ are the mean velocities and the $u'$ and $v'$ are fluctuation velocities.

For laminar and steady flows, the instantaneous velocity is equivalent to the mean velocity, $u(t) = \bar{u}$ throughout the period of observation. Eq. (2.3)**Error! Reference source not found.** can be used to obtain root-mean-square velocity fluctuations, $u_{rms}$ for a continuous recording. If the level of turbulence in the flow is higher, the value of velocity fluctuation, $u_{rms}$ will be larger.

$$u_{rms} = \sqrt{\overline{u'(t)^2}} \tag{2.3}$$

### 2.2.2 Wall-bounded flows

The wall or surface is expedient in the generation of turbulence although turbulent flow can be generated as a result of mean velocity differences in a free shear flow, for instance the flow of jets, wakes and mixing layers. Further, turbulent flow is produced on walls or surfaces due to the vorticity that is generated by the oncoming flow, and then the velocity is brought to rest in order to satisfy the no-slip condition. Flows in wall-bounded surfaces are either referred to as internal flows such as flow through pipes and channels or external flows such as flow around the ships' and aircraft's hulls. More specifically, fluid flow can either be laminar or turbulent based on the following factors: Reynolds number, the level of roughness of the wall surface and turbulence intensity (Pope, 2000).

### 2.2.3 Shear stress at the wall

In a location close to the wall, wall shear stress and viscosity are very important quantities in the study of turbulence behaviour in a channel flow. Total shear stress equals the sum of the viscous stress, $\mu d\langle u\rangle/dy$ and the Reynolds stress, $-\rho\langle u'v'\rangle$. At the wall, the Reynolds stress becomes zero and the viscous stress becomes wall shear stress. Further, the wall shear stress, $\tau_w$ exerted by the fluid on the wall, is $\mu(d\langle u\rangle/dy)_{y_w}$, where $\mu$ fluid dynamic viscosity and $d\langle u\rangle/dy$ is the velocity gradient near the wall. Viscosity is significant in the near-wall region, but has negligible effect on the mean velocity in the outer region of the flow.

## 2.3 Boundary layer

In Ludwig Prandtl's 1904 paper, the concept of the boundary layer was first introduced. He suggested that the flow over a solid wall consists of two parts. The first part comprises the region where fluid flow moves near the wall. At this region, there is high level of shear stress between the fluid layers and high-velocity gradient due to the significant influence of viscosity. The second part is the region outside the boundary layer. In this region, the flow may be considered as inviscid. As the boundary layer increases in thickness, a reduction in both velocity gradient and shear stress is caused. The distance from the wall to the location where viscous flow attains 99% of the free-stream velocity is referred as the thickness of the boundary layer.

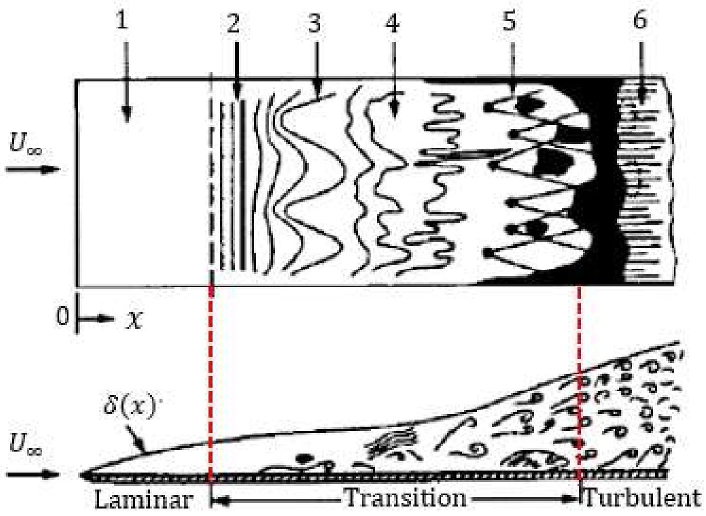

***Figure 2-4: Boundary layer development on a flat plate and the procedure of transition to turbulence on a smooth flat plate (White, 1974).***

When a fluid passes over a solid wall, an adhesion occurs between the layer of fluid and the surface of the solid wall. The layer of the fluid adheres to the wall surface of the solid and the no-slip condition occurs. When the fluid's layer is still flowing above the solid surface, retardation through the action of viscosity occurs from the fluid's layer that cannot slip away. Moreover, the fluid's layer that cannot slip away causes the formation of retardation to the adjacent layers of the fluid and a small layer near the wall surface is grown. At that small region, there is a rapid increase in flow velocity from zero which approaches the free-stream velocity. This small region adjacent to the wall is known as the boundary layer. Shear stress is exerted by the fluid at the wall and is calculated as $\tau_w = \mu(\partial u/\partial y)_{y_w}$. This shear stress produces instability that generates turbulence in the flow: the turbulence level in the flow is stronger if the variation of velocity spatially (shear stress) is stronger.

Figure 2-4 shows the division of a flat plate boundary layer flow into a laminar boundary layer, transition region and a turbulent boundary. The viscous effects in the laminar boundary layer are very high and damped down fluctuations which causes the flow to remain laminar. Transitional flow still behaves as some laminar flow features with an appearance of intermittent burst of turbulence spots. When the fluid velocity increases, the inertial force in the flow becomes dominant over the viscous force. This causes the boundary layer to become unstable and the flow becomes turbulent. It is important to note that the critical Reynolds number that marks the onset of transition is inversely proportional to perturbations in the flow. A flow with high level of perturbation has a low critical Reynolds number while that of low perturbation has a high critical Reynolds number (Schlichting, 2000).

Furthermore, apart from the Reynolds number, transition in the laminar boundary layer flow can be triggered by many other factors such as the roughness of the wall, streamwise pressure in the outer flow and level of free-stream turbulence (perturbation) of the outer flow. As flow passes the edge of a flat plate, different stages occur before the transition to turbulence. The different stages are designated by numbers for better identification. 1) In this stage, the flow is laminar and stable; 2) Unsteady streamwise waves (2-D Tollmein Schlichting waves) develop and replace the region of laminar flow; 3) The waves referred to as Tollmien-Schlichting (*T*-*S*) waves are amplified further downstream of the plate and lead to the formation of three-dimensional and vortex structures; 4) The vortex is seen to deteriorate; 5) Turbulence spots are seen to form; 6) Turbulence spots merge together and fill the entire flow region (White, 1974; Schlichting, 2000). When the level of the initial perturbation exceeds a certain threshold, the amplification of the weak perturbations in the flow is bypassed. In this situation, the amplification of three-dimensional disturbances takes place instead of Tollmien-Schlichting (*T*-*S*) waves. The procedure involved is well described in § 2.4.

## 2.4 Bypass transition

The new knowledge of the transient turbulent flow of  is based on laminar-turbulent bypass transition. As the present study focuses on the expansion of the above study, research on bypass transition is reviewed in this section. The study of the procedure of laminar-turbulent transition has been ongoing by numerous researchers using numerical and experimental techniques since the inception of the research carried out on the flow by Reynolds (1883) The knowledge of the procedures involved in the transition to turbulence has a significant impact in proffering solutions to many design problems such as the management of wall shear stress, mixing processes, flow prediction and heat transfer in engineering. In terms of specific examples, flow instabilities that result in turbulence in a pipe/channel under applied pressure gradient have been investigated using linear theory (Orr, 1907; Schmid, 2001). For very small perturbations in the flow, Meseguer and Trefethen (2003) have predicted stability for Reynolds number in a pipe flow. In the investigation on plane Poiseuille channel flow carried out by Orszag (1971) using the Chebyshev method, it was reported that the flow remained steady up to $Re_c(=\frac{U_c\delta}{v}=5772.22)$ where $U_c$ is the velocity at the centre of the channel, $v$ is known as the kinematic viscosity of the working fluid and $\delta$ is the half-height of the channel. The transition to turbulence can occur earlier in boundary layer, pipe and channel flows with a high level of disturbances in the flow. Schmid (2001) defined the critical Reynolds number in the flow as the Reynolds number when the flow becomes unstable linearly.

The investigation of the transition from laminar boundary layer to turbulent was first carried out by Burgers (1924) and later comprehensive studies on transition to turbulence on flat plate boundary layer flows were reported by Dryden (1938; 1939). In boundary-layer flows, there are mainly two classes of transition to turbulence. The first class is a natural transition and the second class is bypass transition. In a natural transition, the flow is associated with weak disturbances and the flow undergoes very slow changes due to viscous effects. As the perturbations in the flow grow in amplitude, two-dimensional Tollmien-Schlichting ($T$-$S$) waves are produced and also grow in magnitude, which leads to a three-dimensional secondary instability and consequently, a break down of the turbulent flows. In this class of transition procedure, turbulence spots that lead to the onset of turbulence are generated as a result of these waves. It should be noted that the free-stream t turbulence ($FST$) in natural transition is far less than 0.01 ($Tu \ll 1\%$). In addition, the flow is characterised by a slow process and occurs at high transitional Reynolds number, $Re_x (= \frac{xU_\infty}{v} = 10^6)$ where $U_\infty$ is the free-stream velocity, $x$ is the distance from the leading edge and $v$ is the kinematic viscosity of the fluid (Kleiser & Zang, 1991).

The second class of transition is referred to as bypass transition where the level of free-stream turbulence ($FST$) is greater than 0.01 ($Tu > 1\%$). The breakdown to turbulence may take place at a Reynolds number which is significantly less than $10^6$. When free-stream turbulence ($Tu$) is greater than 0.01, the instabilities in the flow rapidly develop, and the transition to turbulence occurs promptly. In this case, Tollmien-Schlichting waves are bypassed (Morkovin, 1969; Klebanoff, 1971; Kleiser & Zang, 1991; Kenneth & Takeo, 1993; Kachanov, 1994; Boiko et al., 1994; Saric et al., 2002). Morkovin (1969) formulated the phrase term ''bypass transition'' when he observed that strong amplification of perturbation in the flow can cause the Tollmein-Schlitching waves to be bypassed.

The solutions for unsteady two-dimensional streamwise waves were first reported by Tollmien (1929) and Schlichting (1933). The existence of the waves was verified in the experimental investigation of zero-pressure gradient boundary layer carried out by Schubauer and Skramstad (1948), thereby explaining the naming of Tollmien-Schlichting ($T$-$S$) waves. During the experiments, the authors placed a rope grid in the settling chamber of their wind tunnel, and the results obtained were compared with the case of undisturbed free stream. An increase in the activity of waves led to the formation of turbulence spots in the flow. Further formation of turbulence spots downstream of the flow boundary layer covers the whole wall surface when the flow became fully developed turbulent flow. Following these experiments, experimental investigations of Klebanoff, Tidstrom, and Sargent (1962) revealed that the amplification high speed streaky structures and low speed streaky structures in streamwise direction does not depend on Tollmein-Schlichting ($T$-$S$) when the free-stream turbulence

($FST$) is moderate. Finally,Arnal Juillen and Michel (1978) and Morkovin (1984) have shown that the presence of TS waves has no significant contribution to the process of transition when free-stream turbulence ($FST$) is greater than 0.01 ($Tu > 1\%$). The data obtained from the experimental investigations on boundary layer transition conducted by Roach and Brierley (1992) revealed that transition to turbulence occurred through the amplification of Tollmein-Schlicting ($T$-$S$) waves when the free-stream turbulence ($FST$) was low $Tu < 1\%$). However, the Tollmein-Schlicting ($T$-$S$) waves seemed to disappear when the free-stream turbulence was higher than one ($Tu > 1\%$). Thus, the ($T$-$S$) waves were bypassed as free-stream turbulence greater one ($Tu > 1\%$), and the second class of transition to turbulence, known as bypass transition, occurred.

Boiko et al. (1994) investigated the effects of Tollmien-Schlichting ($T$-$S$) waves on the process of transition at free-stream turbulence equal to 0.015 ($Tu = 1.5\%$). They reported that at small-amplitude, TS-waves were involved in nonlinear flow/wave interactions, resulting in a regeneration of TS-waves in the unsteady frequency band. Additionally, ($T$-$S$) waves were easily observed in the boundary layer that was subjected to moderate free-stream turbulence ($FST$) of less than 0.01 ($Tu < 1\%$) though they reported difficulty in detecting Tollmein-Schlichting ($T$-$S$) waves in a flow that consisted of a free-stream turbulence greater than 0.01 ($Tu > 1\%$). During the experiments the authors introduced controlled oscillations produced by vibrating ribbon for detecting small-amplitude waves when the boundary layer was subjected to high free-stream turbulence greater than 0.01 ( $Tu > 1\%$). They confirmed the possibility of detecting small-amplitude waves in a boundary layer subjected to high free-stream turbulence ($FST$) of at least 0.015. It was also reported that the number of turbulence spots formed that triggered onset transition was increased by the presence of ($T$-$S$) waves.

In a bypass transition process, the flow development occurs in three stages: the buffeted laminar boundary layer; intermittent turbulence spot formation region and the fully developed turbulent flow boundary layer. The buffeted laminar boundary layer region is typified by a reduction of the skin friction coefficient and a growth of velocity fluctuations in streamwise direction while the boundary layer remains stable to disturbances. As the amplitude of the disturbances increases, this leads to an increase of streamwise fluctuating velocity. Low-frequency perturbations then penetrate through the boundary layer resulting in elongated streaks, the formation of which is known as Klebanoff modes; high-frequency perturbations are filtrated out by the boundary layer (Jacobs & Durbin, 2001; Zaki & Saha, 2009). Kendall (1985) studied elongated structures in streamwise direction with small spanwise scales in a laminar boundary layer induced by free-stream turbulence. It should be noted that Klebanoff modes are believed to be a partial cause of the transition from laminar to turbulence at moderate free-stream turbulence ( $FST$ ) levels. The author observed low-frequency fluctuations that grew linearly with the thickness of the boundary layer in the flow. For a very small free-stream turbulence less than 0.05% ($Tu < 0.05\%$), the flow remained a laminar boundary layer flow throughout the investigation (Watmuff, 2004). In similar studies, Goldstein and Wundrow (1998) and Leib, Wundrow and Goldstein (1999) reported that the formation of low-speed streaky structures and high-speed streaky structures was a result of the amplification of low-frequency structures in the flow. It is now accepted that in the region of intermittent turbulence spot formation, localised disturbances trigger the instabilities that finally change into turbulence spots. In addition, the size of the spots increase and combine together in the downstream of the flat plate boundary layer flow. In the fully developed turbulent boundary layer region, disturbances in the flow are amplified downstream and the flow structures break down completely. At this point, the whole span of the boundary layer is covered by turbulence structures.

Furthermore, in a flat plate boundary layer flow subjected to free-stream turbulence, the streaky structures of high and low streamwise velocities develop to secondary instability and eventually breakdown to turbulence. The streaky structures in the flow grow according to transient growth theory. This procedure was demonstrated experimentally by Matsubara and

Alfredsson (2001) using the flow visualisation technique and hot-wire anemometry to acquire data for the determination of the streaky structures in streamwise and spanwise directions. It was explained by the authors that the spanwise scale of the instabilities approached the thickness of the boundary layer in downstream of the flow but increased beyond the boundary layer thickness when near the leading edge. They concluded that an increase in the distance from the leading edge is proportional to the growth of the energy of the streamwise velocity fluctuation. The above experimental observations are consistent with the previous experimental investigation carried out by Westin et al. (1994) using hot-wire anemometry for data acquisition. In a similar vein, Jacobs and Durbin (2001) have revealed that in the $x$-direction of the leading edge of the boundary layer, streaks of low speed can become unstable when they are exposed to free-stream forcing of high-frequency instabilities. The point of the procedure at which the disturbances in the free stream, such as vorticity, enter the boundary layer as steady or unstable fluctuations is referred to as receptivity (Morkovin, 1969). In a receptivity study conducted by Kendall (1985), the presence of the elongation of streamwise structure at the leading edge of the boundary layer and these streaky structures led to low-frequency fluctuation and large amplitude in the boundary layer.

Vaughan and Zaki (2011) and Zaki (2013) studied instability in the boundary layer numerically and introduced two classifications of the secondary instability of streaks inside the boundary layer as inner and outer instabilities. They found that a series of frequencies and amplitudes influence the growth rates of instabilities. They presented findings indicating that the outer instability occurs in the presence of finite amplitude streaks near the leading edge of the boundary layer. The inner instability thus has a relationship with Tollmien-Schlichting ($T$-$S$) waves and it occurs in the presence of infinitesimal amplitude. The rate of its growth depends directly on the increment of the amplitude and the frequency of the pre-streaky structures. Moreover, the outer classification of the secondary instability has been revealed in both numerical and experimental investigations of Jacobs and Durbin (2001) and Matsubara and Alfredsson (2001).

Arnal, Juillen and Michel (1978) reported that minimum value of about 5-7% of streak amplitude is enough to trigger transition. Further, numerical investigation by Vaughan and Zaki (2011) showed that the streak breakdown to turbulence occurs at critical streak amplitude of about 10% of the free-stream magnitude. The experimental investigation of Mandal et al. (2010) on bypass transition in a boundary layer at different levels of free-stream turbulence revealed a similar value. In a related study, Andersson et al. (2001) investigated the effects of streak instability on the breakdown to turbulence inside the boundary layer using direct numerical simulation. The critical streak instability modes for the transition to turbulence were presented as sinuous and varicose instability modes. Moreover, the critical streak amplitude for breakdown to turbulence was reported as 26% of the free-stream magnitude for sinuous instability mode and 37% of the free-stream magnitude for varicose instability mode.. In a slightly more recent study on boundary layer based on zero-pressure gradient by Brandt and Henningson (2002), the values of the critical streak amplitudes were confirmed. Brandt et al. (2003) then studied secondary instability of streaks in the boundary layer and reported the dominance of sinuous instability over varicose instability but that at very a high amplitude, the streak of varicose became unstable. Most recently, in the investigations carried out numerically by Brandt, Schlatter and Henningson (2004), the presence of these two types of instability was observed.

Westin et al. (1994) showed that in a flat plate boundary layer flow that is induced by free-stream turbulence, the shape of the leading edge has a great influence on the transition location. The experimental studies of Fransson et al. (2005) then confirmed the relationship between *FST* and the critical Reynolds number that was proposed by Andersson, Berggren and Henningson (1999). In context, in a flat plate boundary layer flow where the boundary layer develops spatially, the Reynolds number at which transition occurs is known as the critical Reynolds number. The value of this critical Reynolds number depends on free-stream turbulence (Andersson et al.,1999; Brandt, Schlatter, & Henningson, 2004; Fransson et al., 2005; Ovchinnikov, Choudhari, & Piomelli, 2008). In other related research, Andersson et al. (2001) studied growth of energy of the primary disturbance in boundary layers using optimal disturbance theory. It was reported that the maximum energy is proportional linearly to the distance from the leading edge. They have shown that at the optimal disturbance, streamwise vortices develop into streamwise streaks. Indeed, the optimal perturbation on a flat-plate boundary layer obtained by the authors is similar to the one presented by Luchini (2000). Interestingly, Westin et al.'s (1994) experimental data showed the proportionality of the square root of the distance from the leading edge and the growth of the root mean square (r.m.s) velocity fluctuation in the streamwise direction. This is in conformity with the findings of Luchini (2000).

The experimental investigations of Fransson et al. (2005) used a wide range of $FST$ (1.4% and 6.7%) to study transition procedure in the flat plate boundary layer flow. They utilised four turbulence-generating grids: one active grid and three passive grids. The variation of different free-stream turbulence intensities was achieved using the active grid. They made an effort to create correlations for the modelling of the transitional zone and reported that the amplitude of boundary-layer fluctuation developed slowly near the leading edge, closer than farther downstream in the boundary layer. It was concluded that the initial disturbance energy generated in the boundary layer is proportional to the square of the turbulence intensity ($Tu^2$) and that the transitional Reynolds number is proportional inversely to the square of the turbulence intensity ($Tu^2$) and increases with the length of the transitional zone.

Matsubara and Alfredsson (2001) studied perturbation growth in the flat plate boundary layer flow that was subjected to free-stream turbulence. The range of free-stream turbulence intensities studied was $Tu = 1 - 6\%$ as well as the impact of free-stream turbulence on the growth of instabilities in the flat plate boundary layer flow before the streaky structures breakdown to turbulence. They reported that the spanwise length of the streaks decreased as free-stream turbulence intensity increased. They also reported that the spanwise length increased slightly with the downstream distance as boundary-layer thickness increased. The spanwise length of the perturbations approached the boundary-layer thickness farther downstream of the boundary layer and was larger than boundary-layer thickness near the leading edge of the boundary layer.

The direct numerical simulations of Ovchinnikov et al. (2008) were designed to investigate the transition to turbulence of a boundary layer that was subjected to high-amplitude of free-stream turbulence intensity of $Tu = 6\%$. The study revealed the significance of the length scale of free-stream turbulence in the process of transition to turbulence. It was observed that free-stream velocity with a larger length scale led to the formation of wave packets at the upstream regions where the streaks were detected. However, the flat plate boundary layer flow with a smaller length scale led to the formation of outer instability. Further illumination was provided by Nagarajan, Lele and Ferziger (2007) who observed that the elongation of free-stream vortices at the leading edge was due to elongation of vortex lines within the boundary layer using large-eddy simulation. The authors noted that wave packets occurred in the lower portion of the boundary layer, and these wave packets were in the spanwise velocity component (z-direction). Formation of spanwise wave packets that led to breakdown to turbulence was observed at the blunt leading edge when free-stream turbulence intensity was high. They also observed a flat plate boundary layer flow with small free-stream turbulence and sharp leading edge and reported the development of low-speed streaks leading to transition as confirmed by Brandt et al. (2004). Having explored the subject of bypass transition in details, the following section reviews the previous investigations carried out by dedicated researchers in accelerating flow staring from zero (rest) or laminar.

## 2.5 Transition to turbulence in an accelerating flow from rest or a laminar flow

The motion of viscous fluid that flows along a smooth surface at a low Reynolds number $Re$, tends to be regular. This is known as laminar flow as the viscous force (μu/L) in the flow is higher than the inertial force ($\rho u^2$). Furthermore, the movement of the fluid changes and becomes irregular and chaotic as the Reynolds number increases. At this stage, the flow is unstable, and the motion of the fluid becomes complex. A further increase in the value of velocity causes the motion of the fluid to become more complex. For flow to become turbulent, there must be a percentage of perturbation that is initiated from the instability in the flow ( Taylor, 1923; Davidson, 2015).

The experimental investigations on transition to turbulence in accelerating flows have been carried out by numerous dedicated researchers such as Rotta (1956), Carstens (1956), Maruyama, Kuribayashi and Mizushina (1976), Leutheusser and Lam (1977), Koppel' and Liiv (1977), Maruyama Kato and Mizushina (1978), Lefebvre and White (1989; 1991), Darbyshire and Mullin (1995) and Annus and Koppel (2011), all of whom have made substantial contributions in the study of transition to turbulence for flow starting from rest and laminar. These contributions are summarised in the following section.

Leutheusser and Lam (1977) carried out an experimental investigation on accelerated flow starting from rest and showed that laminar-turbulent transition is time delayed. It was observed during the experiments carried out by Van der Sande (1980) that acceleration was delayed during the flow acceleration from rest. The author recorded transition to turbulence at a critical time of 4. 2 s and 95% of final mean bulk velocity which is equivalent to mean velocity of 1.15 $m/s$ and critical Reynolds number of $Re_D = 57500$. In the experimental investigation of Koppel' & Liiv (1977) of an accelerated flow starting from rest, the authors reported delay during the transition from laminar to turbulence. During the experiments, the transitional Reynolds number occurred from 78,000 to 234500 and acceleration from 0.68 to 11.78 $m/s^2$.

Numerous experimental investigations on the transition of laminar to turbulent have shown that the critical Reynolds number ranges between $Re = 1800$ and $Re = 2300$. (Wygnanski & Champagne , 1973; Wygnanski et al., 1975 and Han et al., 2000). From their results, the value of the minimum Reynolds number at transition at which transition from laminar to turbulence will occur is at $Re = 1800$. This is very close to the value obtained in Reynolds' experiment. In subsequent experiments, the value of the upper critical Reynolds number was increased to $10^5$(Pfenniger, 1961).

Furthermore, the critical Reynolds number was reported to be significantly higher in a flow acceleration from rest carried out by Lefebvre and White (1989). The experimental investigations were conducted on the test section with 0.05 $m$ diameter and 30 $m$ length. Flow acceleration during the experiments varied between 1.8 to 11.8 $m/s^2$ and the global transition was observed to occur as transition occurred almost at the same time on all the instruments. As the flow acceleration increased, transitional Reynolds number ranged between $2x10^5$ and $5x10^5$ and the transition to turbulence was delayed by acceleration. Lefebvre and White (1991) then studied flow acceleration from rest to further extend the knowledge of transition to turbulence. The authors changed the diameter of the test section from 0.05 $m$ to 0.09 $m$. The flow acceleration ranged from 0.2 to 11.2 $m/s^2$ and the highest critical Reynolds number that got during the experiments was $1.1x10^5$. Their test results were correlated with different parameters (convective acceleration, $K_a$ and pipe Reynolds number, $Re_D$) and it was revealed that transition time was dependent on both acceleration and pipe diameter. Following this study, the transition to turbulence of an accelerated flow starting from rest was experimentally investigated by Annus & Koppel (2015) using Particle Image Velocimetry (PIV). At the point of transition, the authors studied the development of the velocity component radially. It was concluded, in conformity with the previous authors, that pipe diameter has a significant impact on the Reynolds number at transition. Prior to this, Nakahata et al. (2007) conducted tests for the determination of the critical Reynolds number in an accelerated pipe flow. The experiments were similar to the tests conducted by Lefebvre and White (1991), and the transition to turbulence was determined using the output signal of Hot-Wire Anemometer. The authors studied the correlation that occurred between the two tests and the equation for the critical Reynolds number was thus proposed. The authors also confirmed that in an accelerated flow, transition time and critical Reynolds number are dependent on acceleration and diameter of the pipe. Measurements were made using Laser Dropper Velocimeter (LDV) and the surface shear stress sensor was used to determine the time of transition.

In a related study, Greenblatt and Moss (2003) experimentally investigated quick transition on accelerated flows starting from rest. The authors also studied the effects of transition during the flow deceleration and the time taken to achieve transition in the two types of flow was observed. It was reported that time taken to attain transition was reduced during flow deceleration and the time of transition was increased during the accelerating flow.

An accelerated flow starting from rest was also investigated experimentally by Kataoka, Kawabata and Miki (1975) to study the effect of acceleration on the transition from laminar to turbulent flow. During the experiments, a centrifugal pump and a solenoid valve were used to generate a rapid change in flow rate. The final flow conditions of the cases considered ranged from Reynolds number $Re = 1910 - 11900$. It was reported that the time taken for the transition from laminar to turbulence reduced when there was an increment in the final Reynolds number. The electrochemical method was used to measure the velocity profiles during the investigations and the growth of the velocity profiles was studied, with the authors observing a minimum profile at the axis of the pipe. However, a maximum velocity profile was observed in the region intermediate between the wall and the centreline.

Kurokawa and Morikawa (1986) carried out experimental and theoretical investigations on accelerating and decelerating transient flows in a smooth pipe for the determination of turbulence characteristics. They reported two patterns of transition procedure during the transition from laminar to turbulence for both slow and fast accelerations. For a fast acceleration, velocity increased in the centre of the flow at the transition but decreased at a location near the wall. The procedure was reversed during slow acceleration at the transition where the velocity increased near the wall and decreased in the core of the flow. The authors also reported an increase in Reynolds number at transition as the imposed acceleration increased during the transition from laminar to turbulent. Building on this research, experimental investigations of laminar to turbulent transition in accelerating pipe flow were carried out by (Lefebvre & White, 1989; Lefebvre & White, 1991). The flow started from rest and accelerated to statistically steady turbulent flow using water as a working fluid. It was reported that an increase in acceleration rate increased the critical Reynolds number and a relationship between the acceleration and critical Reynolds number was derived by the authors from the acquired data. More recently, Knisely, Nishihara and Iguchi (2010) experimentally studied Reynolds number at transition in constant-acceleration flow started from the laminar state using air as working fluid. The authors further improved the equation and found that the relationship between the Reynolds number at transition and acceleration rate appears to be similar to that of constant acceleration started from rest.

## 2.6 Transient turbulent flows over smooth surfaces

The frequent occurrence of transient turbulent flow in many engineering applications has motivated numerous dedicated researchers in fluid mechanics to investigate transient flows of various types. In the unsteady turbulent flow, flow properties vary with time. These types of flow are grouped under two categories; namely, periodic unsteady flow and non-periodic unsteady flow. The periodic unsteady flows are divided into oscillatory and pulsating flows with the major difference then being the mean flow values. To further explain, oscillatory flow has a flow around zero mean value while pulsating flow occurs at the non-zero mean value. Accelerating flow and decelerating flow are the two types of non-periodic flows. Sudden acceleration and deceleration are associated with non-periodic flows which form the scope of this current study. Studies of flows through pipes, flat plates and channels have been reported by several researchers, the simplicity of their geometries being helpful in the fundamental investigation of transient turbulent flows – of these three geometries, channel has been chosen for this current study. As the body of literature on the study of transient turbulent flows is vast, only papers that are directly relevant to these current investigations - studies of turbulence in transient turbulent flows are reviewed here.

### 2.6.1 Periodic unsteady flows

Periodic unsteady flow can frequently be observed in many engineering applications, for instance, flow through an automobile’s internal combustion engines, stirling engine, nozzels and turbomachines. Indeed, periodic pulsating flows are observed in many engineering devices and human systems: artery, internal combustion engines, pumps, turbines, and hydropower. With the help of the reciprocating device, water can be pumped through the wall-bounded channel. Due to its proliferation, experimental and numerical investigations have been studied on periodic turbulent flow by various researchers in pipes and channels. For a general background to the study of turbulence, several journal articles on this topic have been reviewed.

Experimental investigations on pulsating turbulent flow in examining the variation of turbulence structures in a pulsating cycle are complicated. In pulsating flow, the periodic flow rate is imposed as the pressure gradient changes with time in the flow. In an earlier study, Mizushina, Maruyama and Shiozaki (1974) carried out experimental investigations on pulsating flow in a tube of 0.02 m diameter and 2 m long to study turbulence generation. The authors characterised the generation of turbulence by using critical pulsation period, $T_c$ which is equivalent to the maximum time at which bursts occur. They observed that in a flow when the time of pulsation was longer than the critical pulsation time $T_c$, bursting of turbulence was independent of the pulsation time. An experimental investigation similar to Mizushina et al.'s (1974) was carried to study the generation of turbulence and its transportation in the core of the flow. It was shown that turbulence transportation did not depend on the frequency of pulsation. The authors reported the dynamic procedure by which bursts take place in pulsating turbulent flow and concluded that the dynamic behaviour of turbulence in pulsating turbulent flow is characterised by resonance and coherency: the resonance controls the generation of turbulence while coherency is related to the spread of the generated turbulence to the core of the flow (Mizushina, Maruyama, & Hirasawa, 1975).

Following this, Ramaprian and Tu (1980) carried out an experimental investigation to study periodic oscillatory flow at a mean Reynolds number of 2100 using oil as the working fluid. Data was acquired using Laser Doppler Anemometry (LDA) in a smooth pipe at oscillation frequencies that varied between 0.05 and 1.75$Hz$. They noted that the periodic structure of fully turbulence of an oscillatory flow appeared as oscillatory laminar flow at the same value of the dimensionless Strouhal number. It was concluded that oscillation frequency and the Strouhal number both affect the oscillatory turbulent flow (Ramaprian & Tu, 1980).

Furthermore, Tu and Ramaprian (1983) and Ramaprian and Tu (1983) performed experimental investigations on periodic turbulent pipe flow at an average Reynolds number of 50,000. Data was acquired between oscillation frequency of 0.5 $Hz$ with oscillation amplitude 64% and oscillation frequency of 3.6 $Hz$ with oscillation amplitude 15%. They observed that pulsating frequency had a significant effect on turbulent flow while the effects of oscillation amplitudes were slight on the turbulent flow. The authors proposed a turbulent Stokes number to describe turbulent periodic flow as a result of an interaction that occurs during the imposed pulsation and the process of turbulence bursting as $\omega D/u_\tau$ (where $\omega$ is the frequency of the imposed oscillations, $u_\tau$ is the wall friction velocity and D is the diameter pipe). Five categories of regimes of forced oscillation were defined which are low-frequency, intermediate-frequency, high-frequency, rapid-oscillation and quasi-steady.

In an experimental study, Mao and Hanratty (1986) investigated wall shear stress in pulsating pipe flow. The authors used an electrochemical technique for the measurement of wall shear stress in a pipe of the diameter of $0.194\,m$. A linear response was obtained during the experiments due to a small value of oscillation amplitude. A dimensionless frequency was proposed as $\omega^+ = {}^{\omega v}/_{u_\tau^2}$ (where $\omega$ is the frequency of the imposed oscillations, $u_\tau$ is the wall friction velocity, and $v$ is the kinematic viscosity). At a very small value of dimensionless frequency, there was a quick change in wall shear stress.

Ohmi, Kyomen, and Usui (1978) experimentally investigated pulsating turbulent flow over a range of Reynolds numbers and frequencies. The authors reported that at very low frequencies the flow tended to be in the quasi-steady state and the instantaneous and time-mean velocities were equal to those in steady flows. In a similar vein, Tardu and Binder (1993) reported the effect of amplitude modulation on wall shear stress in a turbulent channel flow using Laser Doppler Anemometry (LDA) and hot-film sensors for data acquisition. It was found that as the dimensionless frequency $\omega^+$ increased from 0 (pseudo-steady) to about 0.02, and the amplitude of the modulation of unsteady wall shear reduced from 1 to about 0.1. Further increment of the frequency increased the amplitude of the modulation to around 0.6. This was concluded to have occurred due to the interaction between the imposed frequency and turbulence, which then led to enhancement of turbulence.

Tardu, Binder and Blackwelder (1994) performed experimental investigations on pulsating channel flow over a wide range of frequencies ($\omega^+ = 0.0005 - 0.03$) and amplitudes (10-70% of the mean velocity at the centre of the channel) to determine turbulence characteristics using the hot-film method. The authors proposed a dimensionless Stokes-length as $l_s^+ = l_s u_\tau / v$ where $l_s = \sqrt{2v/\omega}$ (length scale), $u_\tau$ is the wall friction velocity, $\omega$ is the frequency of the imposed oscillations, and $v$ is the kinematic viscosity. A reduction in amplitude of oscillation for both turbulent wall shear stress and velocity fluctuation was observed for the dimensionless Stokes-length less than 10 ($l_s^+ < 10$). It was concluded that, apart from a large number of amplitude pulsations, wall shear stress and velocity fluctuation are not affected by forced pulsating frequency but turbulence intensities are affected by periodic oscillation as $l_s^+ > 10$. These findings are in conformity with the earlier research performed by Ohmi et al. (1978), that at a lower frequency, turbulence characteristics are not affected by imposed unsteadiness. Much more recent research by Sundstrom, Mulu and Cervantes (2016) determined wall shear stress in a pulsating turbulent flow using Laser Doppler Velocimetry (LDV) and flush-mounted hot-film sensor. The required flow rate oscillations during the experiments were obtained by controlling a frequency-converter which produced voltage variation in the pump. Investigations were performed on a wide range of frequencies ($\omega^+ = 0.003 - 0.03$). At a low frequency, it was reported that wall shear stress is proportional to dimensionless Stokes length $l_s^+ = \sqrt{2/\omega^+}$. In pulsating turbulent flows, wall shear stress and turbulence measurements in channel and pipe have been reported by numerous authors (Tardu & Vezin, 1995; Finnicum & Hanratty,1998; Lodahl, Sumer & Fredsoe, 1998).

In another key study, Scotti and Piomelli (2001) used both direct numerical simulation (DNS) and large-eddy simulation (LES) to study turbulent pulsating flows in a channel. The results of turbulence statistics and coherent structures were reported. It was reported that imposed unsteadiness has an influence on turbulence coherent structures. In order to study turbulence transportation, the authors proposed turbulent Stokes length as $l_t = \sqrt{2(v + v_t\,)/\omega}$ where $v_t$ is eddy viscosity and $v$ is molecular kinematic viscosity. By taking eddy viscosity as $v_t\ = ku_t l_t$ where $k$ is von $k\acute{a}rm\acute{a}n$ and $u_t$ is wall friction velocity, which is defined as $u_t\ = \sqrt{\tau_w/\rho}$ where $\tau_w$ is wall shear stress and $\rho$ is density, it was shown that the fluctuations generated at the wall are reduced during transportation to the centre of the flow due to the viscous sub-layer region.

Tardu and Vezin (2004) and Tardu (2007) reported the role of inner and outer structures in the near wall turbulence of pulsating turbulent flow, with Tardu and Maestri (2010) concluding that mean turbulence intensity increases due to imposed oscillations. In further illumination on the topic, Manna and Vacca (2008) carried out large-eddy simulation (LES) of the pulsating turbulent flow to study the effect of imposed unsteadiness on the coherent structure near the wall. It was reported that the structure of turbulence near the wall reduced as a result of periodic pulsation. In terms of the effects of acceleration and deceleration on turbulence intensity, a study by Gerrard (1971) based on a mean Reynolds number of 3770 reported that the turbulence intensity increased when decelerating the flow and it diminished when accelerating the flow with concurrent re-laminarisation effects.

In a related study, He and Jackson (2009) experimentally investigated pulsating turbulent pipe flow using Laser Doppler Anemometer (LDA) equipment for the determination of instantaneous velocity over a wide range of imposed frequencies. Turbulence statistics were obtained from the ensemble-average of the instantaneous velocity. The authors varied the inner dimensionless frequency $\omega^+ = ({}^{\omega v}/_{u_\tau^2})$ from 0.004-0.04 and the outer dimensionless frequency $(\omega D/u_\tau)$ was varied from 1.8-18. The results obtained from high and low frequencies were reported: the core region of the flow revealed "frozen" slug-like behaviour at higher pulsating frequencies vanished at a lower frequency while the amplitude of the velocity modulation remained the same throughout the oscillations. At a location near the wall, the maximum amplitude of the velocity modulation occurred, and it moved away from the wall with a reduction in pulsation frequency while a very small pulsation frequency revealed a maximum amplitude at the core of the pipe. As a result of the turbulence kinetic energy redistribution between the axial component and radial component, both axial and radial components of r.m.s fluctuating velocity responded equally at the centre of the flow, but the responses were not the same in the near wall region of the flow as a delay was experienced in the radial component relative to the axial component. It was also reported by the authors that the amplitude of stretching of both axial and radial r.m.s turbulence fluctuations in the centre of the flow decreased as the pulsation frequency increased and finally reduced to zero when the turbulence field became ''frozen'' at the centre of the flow. The procedure for turbulence formation and its transportation was also reported: when there was an imposed pulsation on the flow rate, turbulence first occurred in the near wall region of the pipe before transporting to the centre of the pipe.

On a final note, substantial efforts in the study of turbulence statistics in pulsating turbulent flows around a non-zero mean value and oscillatory flows around zero mean value have been made by Mankbadi and Liu (1992), Fornarelli and Vittori (2009), Van der (2011) and Manna,Vacca and Verzicco (2012),

## 2.6.2 Non-periodic unsteady flows

Non-periodic transient flows frequently occur in many applications of engineering: flow through pipeline networks that contain reciprocating pumps in oil and gas industries, flow through nuclear power plants, flow through opening and closing valve that produces a quick change in the flow rate and flow around wings of aircraft. It also occurs in natural systems such as the flow of blood in arteries. This type of flow occurs when the flow in the channel is subjected to temporal changes due to the variation in flow rate from the pneumatic control valve. Thus, understanding the turbulence characteristics of transient turbulent flows aids greatly in the design of the systems mentioned. Acceleration and deceleration flows are examples of non-periodic transient flow. These flows are associated with non-periodic unsteady flows where turbulence responses can be studied. These responses include formation of turbulence near the wall, redistribution of kinetic energy generated during turbulence formation, and transportation of turbulence generated near the wall to the centre of the channel. By comparing acceleration/deceleration flow in the past with other types of flows, it is clear that less attention has been focused on non-periodic transient flow. The relevant studies on non-periodic transient flows are here reviewed as a basis on which this study is conducted , a study which focuses on flow in a channel being subjected to temporal changes in order to study the effects of mean velocity and turbulence statistics in the flow.

Maruyama, Kuribayashi and Mizushina (1976) performed experimental investigations on the study of turbulence in transient flow following step-increase and step-decrease in flow rate using an aqueous solution as a working fluid in a pipe of an internal diameter of 0.051 $m$ and 12 $m$ long. A step change of flow rate was applied to the flow with a range of Reynolds numbers between 5000 and 10000 (initial Reynolds number $Re_0$ = 5000; final Reynolds number $Re_1$ = 10000). It was reported that turbulence varied with time and space due to the unsteadiness of the flow which resulted from the step change of the flow rate. The values of mean and fluctuating velocities were acquired through the ensemble average of the required runs. The ‘‘new’’ flow rate generated turbulence near the wall and then transported to the core of the pipe. It was proposed by the authors that turbulence generated at $t > 0$ be referred to as ‘‘new’’ turbulence and the turbulence generated at $t < 0$ be referred to ‘‘old’’ turbulence. They also observed that the response of turbulence underwent a longer delay at the core of the pipe. Two dominant procedures were reported from the two cases of step change investigated. It was observed that the formation and growth of the ‘‘new’’ turbulence structures due to a step-increase of the flow rate were the dominant procedures, along with the decay of the ‘‘old’’ turbulence structures in step decrease in the flow rate.

Much more recently, He and Jackson (2000) experimentally investigated transient turbulence behaviour over a wide range of Reynolds numbers between 7000 and 45200 ($Re_0$ = 7000 and $Re_1$ = 45200) using a Laser Doppler Anemometer (LDA) for the measurement of three components of local velocity. Ensemble average was performed on the acquired data for the determination of mean velocity, fluctuating velocity in streamwise direction, fluctuating velocity in wall-normal direction, and turbulence shear stress. The experimental study was based on a linear increase and decrease of flow rate with water used as the working fluid. It was reported that turbulence was generated first near the wall and spread to the core of the pipe due to the action of turbulent flow diffusion. They identified three delays that were characterised by turbulence responses: delay in turbulence formation, delay in kinetic energy distribution between the three components and delay in radial growth of turbulence. By comparing the delays that occurred in both accelerating and decelerating flows, it was reported, the delay that occurred during the decelerating flow was smaller. It was further reported that the velocity in streamwise direction responded earlier in the wall region than the two remaining components, but all the three components responded at roughly the same time in the centre of the pipe. The authors proposed two different forms of non-dimensional parameters. Due to delays in turbulence transportation, the non-dimensional ramp rate parameter $\gamma[= (dU_b/dt)(1/U_{b0})(D/U_{\tau 0})\ ]$ is used to calculate the extent at which the turbulence energy was different from the quasi-steady flow. When the dimensionless ramp rate was far less than one $(\gamma \ll 1)$, the structure of turbulence was the same as that of steady pipe flow which was referred to as "pseudo-steady transient pipe flow". In their study, the structure of the turbulence was different from that of steady pipe flow when the dimensionless ramp rate was greater than one $(\gamma > 1)$. A non-dimensional time delay parameter $\tau^+\left[= \sqrt{2\tau U_{\tau 0}}/D\right]$ is used to determine the delay associated with radial growth of turbulence. Furthermore, turbulence in the flow was reported to generate a two-stage response: a slow response at the initial stage of the flow and quick response after the slow response. The results obtained experimentally by the authors show the response of turbulence statistics during the decelerating and accelerating flows and provide further understanding to the study of turbulence dynamics.

Greenblatt and Moss (2004) also carried out an experimental investigation on an unsteady flow that was accelerated rapidly with higher initial and final Reynolds numbers using a single-component Laser Doppler Velocimeter for the determination of turbulence statistics at higher ramp rates. Though the range of Reynolds numbers ($Re_0$ = 31000 and $Re_1$ = 82000) and acceleration rates were higher than in the study by He and Jackson (2000), their results of turbulence generation in near-wall and transportation to the centre of the pipe were the same. They observed delays during turbulence formation and its transportation. It was reported that at the core of the pipe, turbulence froze and the second peak turbulence intensity occurred in the region away from the wall at $y^+ = 300$. Moreover, an increase in acceleration rate caused the mean velocity profile to be shifted towards the wall. It was concluded that the acceleration rate has no significant influence on turbulence transportation.

The study of wall shear stress in a flow acceleration and deceleration due to its usefulness in engineering applications has received the attention of dedicated researchers in the area of fluid dynamics. For instance, Shuy (1996) experimentally investigated wall shear stress response in both accelerating and decelerating turbulent flows using water as a working fluid over a range of Reynolds numbers ($Re_0$ = 40000 and $Re_1$ = 140000). The response of wall shear stress obtained was similar to that of Kurokawa and Morikawa (1986). The author reported that during the accelerating flows, wall shear stress decreased below the quasi-steady value and increased above pseudo-steady value during the decelerating flows. The results of Kurokawa and Morikawa (1986) and Shuy (1996) actually contradicted the earlier results of Daily et al. (1955). It should be noted though that the authors did not present the assessment of the parameters, such as the rate of acceleration and diameter of the pipe, both of which have been shown to have a strong influence on the wall shear stress.

Investigations on wall shear stress in turbulent flows by Ainola et al. (1983) and Proudovsky and Oreshkin (1985) have shown that wall shear stress increases above quasi-steady value during flow acceleration and decreases below quasi-steady value when the flow is decelerating. These wall shear responses in both accelerating and decelerating conform with the data presented by He and Jackson (2000). Similarly, He, Ariyaratne and Vardy (2008) numerically studied the effects of wall shear stress during the acceleration of turbulent flows and reported the effects of turbulence behaviour near the wall in the pipe. The flow conditions

($Re_0$ = 7000 and $Re_1$ = 45200) of the experimental study by He and Jackson (2000) were simulated. During the initial stage of the accelerating flow from the statistically steady turbulent state, the wall shear stress increased and overshot the quasi-steady value of the wall shear stress due to the effects of inertia. The delays in turbulence response countered the effects of the inertia at the later stage of the flow then the wall shear stress undershot the quasi-steady value. It was reported that it took a longer time for the processes of overshooting and undershooting to be completed for lower Reynolds numbers than higher Reynolds numbers. They also found that wall shear stress increased and approached the value of quasi-steady in the later stage of the flow acceleration as turbulence formation began to occur. They concluded that the two factors that lead to the development of wall shear stress are inertia and delay in turbulence response as the velocity of the flow changes with time.

More recently, Chung (2005) numerically investigated sudden changes of pressure gradients on a fully-developed channel flow that was subjected to deceleration. A step decelerating flow was performed on the fully developed flow in the range of Reynolds number ($Re_\tau = 180\ and\ Re_\tau = 120$) is based on of friction velocity ($u_\tau$) and channel half-height ($\delta$). Two different types of relaxations were discovered: a slow relaxation was found at the statistically steady state of the flow after the occurrence of the fast relaxation at the beginning of the decelerating flow. The ramp-down of flow rate due to a quick change in pressure gradient resulted in the anisotropic responses of turbulence in all directions, and the kinetic energy distribution in x-direction was observed to be higher than the quasi-steady value, but the kinetic energy in wall-normal direction and spanwise direction was less than the pseudo-steady value. The response of velocity in x-direction shows the anisotropic response of turbulence near the wall. Following this study, Jung and Chung (2012) investigated the response of temporal acceleration on fully developed turbulent pipe flow using large-eddy simulation (LES). In the analysis of their fluctuating velocities, they observed three delays: the delay in the radial transportation of turbulence, delay in turbulence formation and delay in the turbulence kinetic energy redistribution in the flow. These delays confirmed the three delays earlier reported in the experimental investigation of He and Jackson (2000).

Seddighi et al. (2011) numerically studied the effect of turbulence statistics in step-accelerating flow and step-decelerating flow. The turbulence response in the flow was compared in the two types of flow. When turbulence intensities of both flows were compared, it was revealed by the authors that the turbulence intensity of the accelerating flow was more sensitive than that of decelerating flow of the samemean flow conditions. At the initial stage of step accelerating flow, wall shear stress first increased beyond the pseudo-steady value and then undershot before it approached the pseudo-steady value. These procedures occurred in the opposite trend during the step decelerating flow; however, wall shear stress first undershot and then overshot before approaching the pseudo-steady value. It was reported by the authors that the development of wall shear during the step accelerating flow conformed with that of linearly accelerating flow cases that were previously reported (He & Jackson, 2000). Related findings were reported in a numerical study by He et al. (2008). There was a long delay at a location near the wall than that of the buffer region ($5 < y^+ < 30$ ). This delay establishes the fact that the response of turbulence first occurs at the region where turbulence formation is high before its transportation to the core of the flow.

He, Ariyaratne and Vardy (2011) experimentally investigated turbulent accelerating flow and used hot-film anemometry for the measurement of wall shear stress from a different number of repeats. Ensemble-average was performed on many repeated runs for the determination of mean wall shear stress and perturbation from it (root-mean-square (r.m.s) of fluctuating turbulent wall shear stress). The authors varied both Reynolds number and acceleration rate during the experiments. Initial and final flow conditions were varied between $Re_0$ = 4500 and $Re_1$ = 210000 and the ramp-up times varied between $6 - 17$ $secs$. It was reported that wall shear stress responded in three stages in the flow. At the commencement of the accelerating flow, change in wall stress was high with an increase in Reynolds number. During this stage, wall shear stress was observed to increase greatly and exceeded the pseudo-steady value. The increment continued slowly and then reduced below the pseudo-steady value. The behaviour of wall shear stress in this stage resembled that of laminar flow and turbulent wall shear stress at this stage was "frozen", denoting that the inertial effect was responsible for the development of wall shear stress. During the second stage, both wall shear stress and turbulent wall shear stress increased and exceeded their quasi-steady counterparts. In stage three, the value of wall shear stress and that of turbulent wall shear stress fluctuated around the quasi-steady values. The experimental results conformed with numerical investigations of He et al. (2008).

The numerical studies of Ariyaratne, He and Vardy (2010) confirmed that during decelerating flows, wall shear stress responded in the same way as accelerating flows, but that "frozen" turbulence at the very early stages in the flow countered the consequence of inertial effect. The range of Reynolds numbers reported for the decelerating turbulent flows was the same as that of He and Jackson (2000), but the diameter of the pipe used for the experiments varied. It was stated that both inertia and turbulence response significantly impacted the wall shear stress of decelerating flows. The authors defined the wall shear stress as the sum of quasi-steady wall shear stress and transient components of wall shear stress, $\tau_w (= \tau_{ws} + \tau_{wu})$ . The decomposition of the wall shear stress was also reported by He and Ariyaratne (2011). They noted that the value of wall shear stress in decelerating flows was smaller than quasi-steady wall shear decelerating flow. In the downstream of the pipe diameter of $0.2032\ m$, a sharp reduction of wall shear stress was observed. The relative importance of the inertia and "frozen" turbulence determined whether negative and positive values of unsteady component wall shear stress occurred. Related results of decelerating flows have been reported by Coleman, Kim and Spalart (2003). The authors carried out numerical studies of spatially decelerating flows using direct numerical simulation (DNS). It was reported that when the turbulence intensities increased at the outer layer, it resulted in a decrease in the turbulence intensities at the near wall. They also noted a flow separation at the end of deceleration. Finally, a turbulent boundary layer flow subjected to adverse pressure gradient has been reported to have a flow separation near the wall and to share a resemblance with linearly decelerating channel flow. Thus, the imposition of an adverse pressure gradient to statistically steady turbulent flow results in instability and flow separation near the wall (Krogstad & Skåre, 1995; Nagano, Tsuji & Houra, 1998).

He and Ariyaratne (2011) carried out numerical studies on wall shear stress in turbulent flows in conformity with the numerical studies of He et al. (2008) on accelerating flows. The authors confirmed that turbulence was ‘‘frozen’’ at the early stage of the flow. They reported that the fluctuation of wall shear stress that occurred during the early stage of the flow can be predicted by ‘‘laminar-flow formulation’’ (He & Ariyaratne, 2011). At a later stage, wall shear stress increased as a result of the newly generated turbulence.

He and Seddighi (2013) reported that there was a noticeable similarity in the procedure of transition to turbulence of flat plate boundary layer flow and the transition of transient turbulent flow. More specifically, its flow rate and bypass transition induced by Free-Stream Turbulence ($FST$) suddenly increased to it’s final flow rate. The authors performed a numerical study of unsteady channel flows in which the flow rate was increased from initial statistically steady turbulent flow to final statistically steady turbulent flow ($Re_0$ = 2825 and $Re_1$ = 7404). They reported that the procedure of transition of a low-Reynolds number turbulent flow behaved as a transition to turbulence of flat plate boundary layer flow. It was confirmed that the three stages of transition (pre-transition , transition and fully turbulence) in unsteady channel flows are equal to the three regions of boundary layer bypass transition (buffeted laminar boundary layer, intermittent turbulence spot formation, and the fully developed turbulent boundary layer). The process of transition in the unsteady channel flow represents an alternative to transition induced by free-stream turbulence ($FST$). In this method of transition to turbulence, the required disturbance in the flow was provided by wall shear flow of the initial flow condition with initial streaky structures.

Accelerating flow in channel starting from an initial statistically steady turbulent flow has been investigated numerically by Seddighi et al. (2014) using direct numerical simulation (DNS). They reported that the procedure for transition to turbulence was the same as that of the step change reported by He and Seddighi (2013). It was also observed that a sharp boundary layer was produced rapidly on the wall during the step change while time-developing boundary layer was generated during linearly accelerating flow as the velocity gradient changed continuously adjacent to the wall. The procedure of transition resembled that of bypass transition induced by free-stream turbulence ($FST$) in a boundary layer.

Having reviewed relevant prior investigations on periodic and non-periodic unsteady flow, the next section provides detailed reviews of the journal papers related to the new perspective of transient turbulent flows.

## 2.7 A new perspective of transient turbulent flow transition

The new interpretation of the transition to turbulence of transient turbulent flow in a rectangular channel is based on laminar-turbulent bypass transition. Previously, it has been reported that transient turbulent channel flow has a laminar-like character when the viscous layer develops rapidly with time from the wall before the occurrence of transition. Fundamental studies which have influenced and inspired this research are presented initially before a full description of the experimental procedure and analysis of the results.

Direct numerical simulation (DNS) investigations conducted by He and Seddighi (2013; 2015) on step increase of flow rate and Seddighi et al. (2014) on a slower increase in flow rate have revealed novel data aiding our understanding of the transition to turbulence of transient turbulent flow in a channel. He and Seddighi (2013) reported that transition to turbulence occurred in a low Reynolds number flow, increasing rapidly in flow rate to a higher Reynolds number which resembled laminar-turbulent transition, albeit the initial flow was already turbulent. It was reported by the authors that the initial turbulent flow did not gradually change to a new one from the early flow structures as a result of a quick increase in flow rate, but it underwent a process that involved three distinct stages before developing into the final turbulent state. The three distinct stages of process for changing flow structures are pre-transition, transition and fully turbulence. These are similar to the buffeted laminar flow, the intermittent flow and fully developed turbulent flow regions that are known as the three zones of boundary layer bypass-transition (Jacobs & Durbin, 2001). It was reported that a sudden change in velocity of the initial flow led to the formation of a thin layer of high-velocity gradient and viscous force close to the wall of the channel in stage one, and that this boundary layer grows with time untill the flow becomes fully developed.

In principal, the initial streaky structures in the flow act as a disturbance to the temporally developing boundary layer. The streaky structures of both high and low streamwise fluctuating velocities are elongated in stage one. Towards the end of the pre-transition stage, the elongated streaky structures break and the initial streaky structures in the flow function as a disturbance to temporal developing boundary. Stage two of the process is transition, whereby the turbulence spots are formed as a result of elongated streaks and these isolated spots spread and join together. During stage three, the whole wall-bounded channel is filled with “new” turbulence. The three stages of flow structures are shown in Figure 2-5. The development of the skin friction coefficient in Figure 2-6 clearly shows the time when the transition starts and when the transition completes, as well as the streamwise fluctuating velocity contours at $y^{+0} = 5.3$ where $y^{+0}(= {}^{u_{\tau0}y}/_{v} = 5.3)$, whereby $y^{+0}$ is dimensionless wall distance based on friction velocity, $u_{\tau0}$ is the friction velocity of the initial transient turbulent flow, $y$ is the wall distance and $v$ is the kinematic viscosity of the working fluid. Frames are presented in dimensionless time $t^{*}(= tU_{b1}/\delta)$ where $U_{b1}$ is the bulk velocity of the final stage of the flow and $\delta$ is the half-height of the channel. Frame $t^{*} = 0$ shows the statistically steady turbulent flow before the step change. In this stage, streamwise fluctuating velocity is low but the existence of small patches of low and high streamwise fluctuating velocities are seen. Before the frame $t^* = 15$, streaks of high and low streamwise fluctuating speeds are elongated and developed with time. At frame $t^* = 20$, the elongated streaky structures break and lead to the formation of turbulence spots. These turbulence spots spread and merge with each other in the wall-bounded surface. At $t^* = 42$, the entire wall-bounded surface is filled with turbulence.

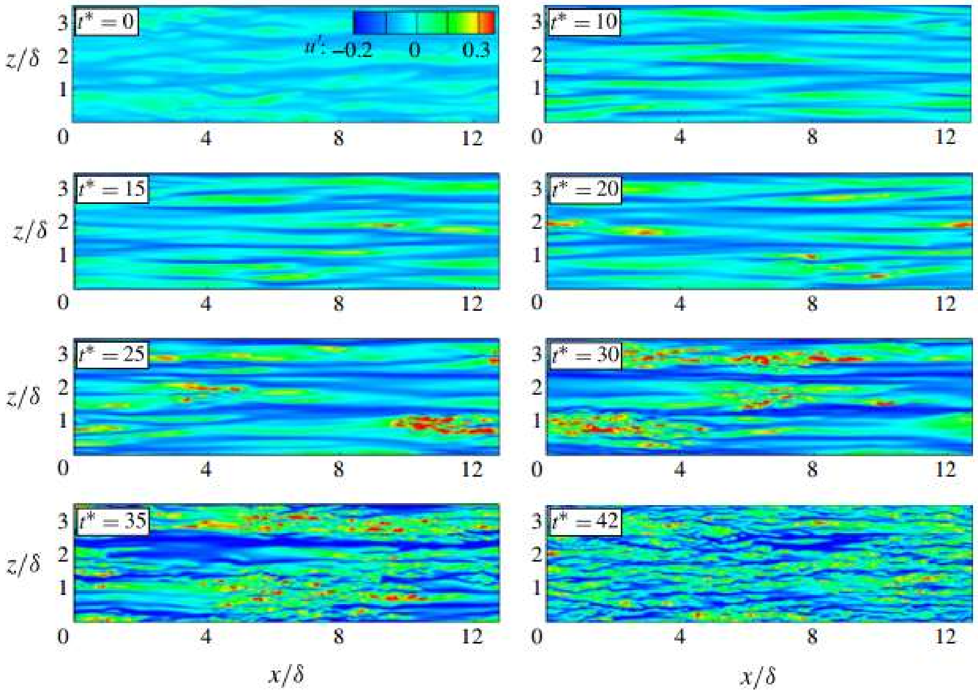

**Figure 2-5: Contour plots of streamwise fluctuations in a horizontal plane (He & Seddighi, 2013).**

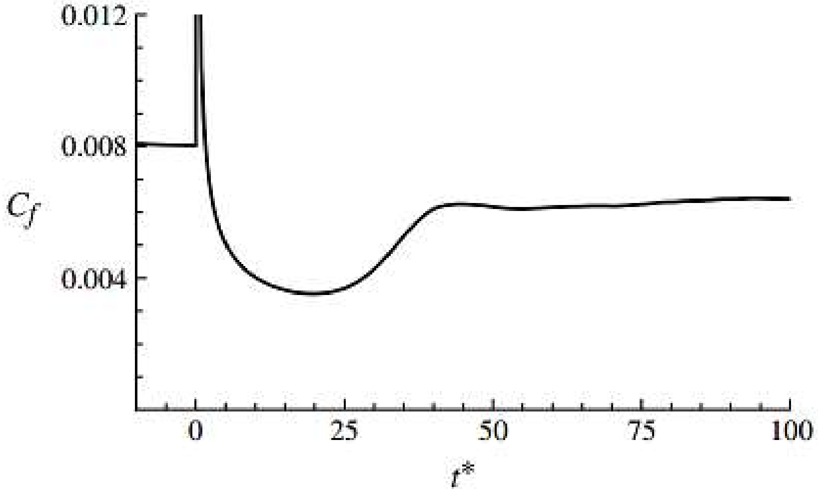

**Figure 2-6: Development of skin friction coefficient with time during unsteady channel flow (He & Seddighi, 2013).  .**

Figure 2-6 shows the development of skin friction coefficient ($C_f$) during the transition to turbulence. At $t^* \leq 0$, the value of the skin friction coefficient is equivalent to the initial flow condition of the transient turbulent flow. During the step increase of flow rate at $\Delta t^* = 0.22$, the value of skin friction increases rapidly in fractions of a second to a higher value before it then reduces rapidly and attains a minimum value at $t^* = 20$. As a result of the newly generated turbulence in the flow, skin friction increases again and attains a maximum peak at $t^* = 42$. At this point, the entire wall-bounded surface has been filled with turbulence.

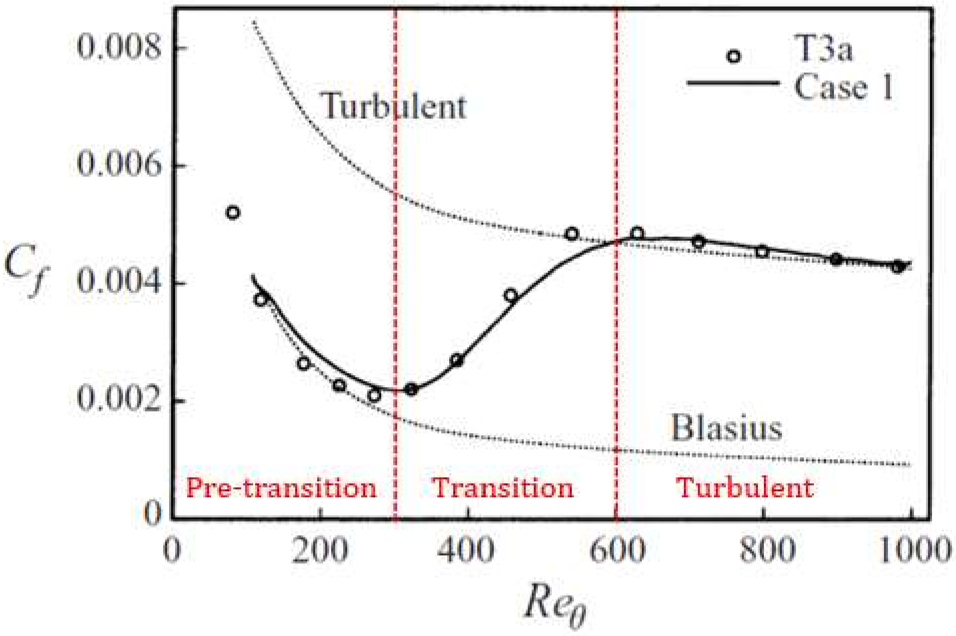

***Figure 2-7: Skin friction development with momentum thickness Reynolds number (Jacobs & Durbin, 2001).***

In the numerical study of Jacobs and Durbin (2001) on the transition to turbulence on flat plate boundary layer flow, the development of skin friction was used to determine when transition starts and ends. The authors plotted the data of skin friction coefficient against the momentum thickness Reynolds number, as shown in Figure 2-7. The onset of transition was determined as the minimum value of skin friction coefficient before increasing again due to the new formation of turbulence in the flow. The start and competition of transition were determined as $Re_\theta = 300$ and $Re_\theta = 600$, respectively.

In other related research, Seddighi et al. (2014) numerically investigated slower accelerating turbulent flow and concluded that the turbulence behaviour of the flow was similar to earlier results reported by He and Seddighi (2013). In comparison with He and Seddighi (2013), both accelerating flow and step-increase of flow rate consisted of three stages of development, but the stretching of the streaks in an accelerating flow during the pre-transition was not strong. It was reported that a new boundary layer was generated instantly near the wall during step-increase of flow rate whereas the constant change of velocity gradient in accelerating flow caused a gradually developing boundary layer. Contour plots in Figure 2-8 show the flow behaviour of the slower accelerating flow. The fluctuating velocity in streamwise direction normalised by initial bulk velocity was used to show the turbulence structures at a different period, although the changes that took place in accelerating flow were very small when it was compared with the step-increase of He and Seddighi (2013). Between $t^* = 0$ and $t^* = 14$, the pre-transitional stage, streaks were formed and stretched/elongated. Between $t^* = 18$ and $t^* = 24$, known as the transitional stage, isolated turbulence spots were formed from the elongated streaks, then spread and merged with each other with time. The fully developed turbulent stage occurred when the whole wall-bounded surface was covered with ‘‘new’’ developed turbulence structures. Building on this body of knowledge, in this current study, ramping-up flows at different acceleration periods are investigated.

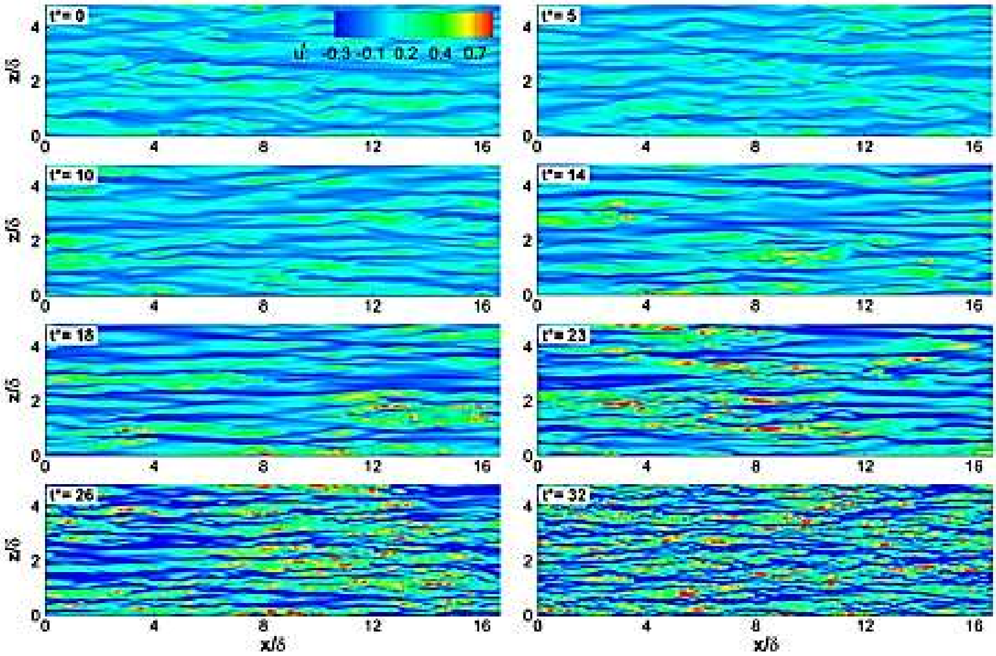

***Figure 2-8: Contour plots of streamwise fluctuations acceleration flow (Seddighi et al., 2014).***

The numerical investigations of He and Seddighi (2015) on step-increase of flow rate focused on different Reynolds number ratios. The range of Reynolds numbers reported by the authors are $Re_0$ = 2800 & $Re_1$ = 3100, $Re_0$ = 2800 & $Re_1$ = 3500, $Re_0$ = 2800 & $Re_1$ = 4200, $Re_0$ = 2800 & $Re_1$ = 5300, $Re_0$ = 2800 & $Re_1$ = 10000 and $Re_0$ = 2800 & $Re_1$ = 12600 which are equal to Reynolds number ratios of 1.1, 1.3, 1.5, 1.9, 3.6 & 4.5, respectively. It was concluded that the variation in the turbulence structures depends on the range of Reynolds numbers. They reported that the stretching of the streaks occurred at the pre-transitional stage during high ratio step-change in flow rate. The generation and transportation of isolated turbulence spots at the transition were clearly observable at higher Reynolds number ratios, while the change in turbulence structures are not clearly seen in lower Reynolds number ratios. In addition, the transitional process was not evident through flow visualisation. It was, however, shown that the fluctuating velocity in the x-direction was similar, and the transient flow was characterised by laminar-turbulent transition for all the Reynolds number ratios investigated.

For transient flow, the authors defined an equivalent Reynolds number, mimicking that used in flat plate boundary layer flow (i.e. the Reynolds number based on the distance from the leading edge of the boundary layer as $Re_x(=\frac{xU_\infty}{v})$, where distance from the edge of the plate is denoted as $x$ and $U_\infty$ is the free-stream velocity). In a fully developed channel flow, the convective velocity can be considered as the bulk velocity $U_{b1}$, then the equivalent distance from the edge of the plate can be represented as $x = tU_{b1}$. Therefore, the equivalent Reynolds number can be written as $Re_t(=\frac{tU_{b1}^2}{v})$ or $Re_t(= t^*Re_1)$ where $t^*(=\frac{tU_{b1}}{\delta})$, $Re_1\left(=\frac{\delta U_{b1}}{v}\right)$. The time and equivalent Reynolds number at which the skin friction coefficient reaches the minimum value are known as critical time $t_{cr}$ and critical equivalent Reynolds number $Re_{t,cr}$, respectively. The variation of skin friction coefficient $C_f(=\frac{2\tau_w}{\rho U_b^2})$ with the equivalent Reynolds number shows that the critical equivalent Reynolds number decreases as the skin friction coefficient increases and the initial Reynolds number ($Re_0$) increases, as shown in Figure 2-9. In the second case, the initial Reynolds number is increased from a fixed value to different final Reynolds numbers. The value of theoretical equivalent Reynolds number increases while the minimal skin friction coefficient decreases. The variations of the skin friction coefficient are shown in Figure 2-9.

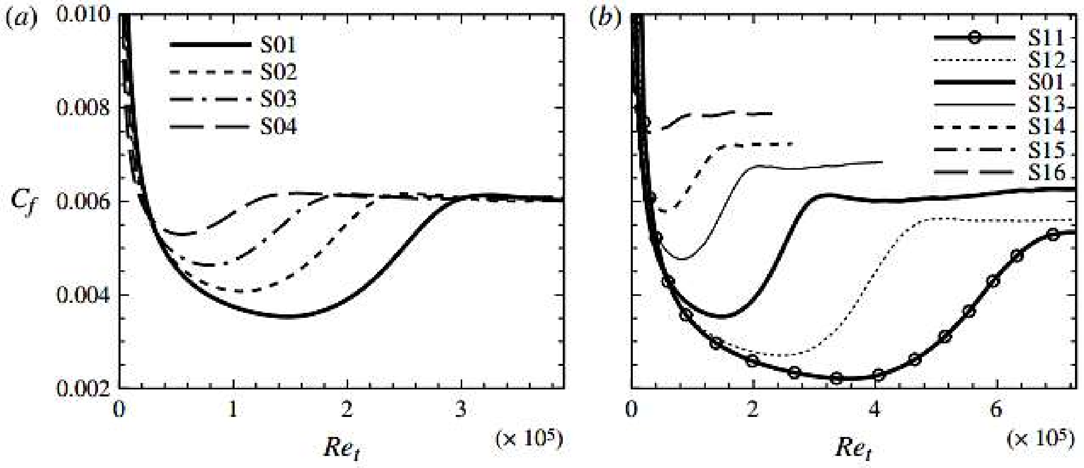

***Figure 2-9: Variation of the skin friction coefficient with equivalent Reynolds number (He and Seddighi (2015).***

In flat plate boundary layer flow research, it has been found that the critical Reynolds number is inversely proportional to the square of free-stream turbulence ( $FST$ ) intensity

($Re_{cr} \sim Tu_0^{-2}$)) (Andersson et al., 1999; Fransson et al., 2005). Andersson et al. (1999) in particular have proposed an empirical relationship, $Re_{x.cr} = 144 Tu_0^{-2}$ to calculate the critical Reynolds number in a spatially developing boundary layer flow. Further, Blumer and Van Driest (1963) established a correlation that relates free-stream turbulence ($FST$) intensity and the critical Reynolds number from their experimental data of flat plate boundary layer flows as $1\big/\sqrt{Re_{x,cr}} = a + b\sqrt{Re_{x,cr}} Tu_0^2$ where $a = 10^{-4}$ and $b = 62.5 \times 10^{-8}$.

He and Seddighi (2015) commented that the following parameters may influence the transition procedure in an unsteady flow:

(i) $Re_0 (= \frac{\delta U_{b0}}{v})$, the value of the initial Reynolds number controls the free-stream turbulence intensity ($FST$). If the initial Reynolds number is increased, the skin friction coefficient increases while the initial free-stream turbulence intensity decreases. $Re_0$ denotes the initial Reynolds number for the unsteady flow.

(ii) $Re_1 (= \frac{\delta U_{b1}}{v})$, the value of the skin friction coefficient decreases as the final Reynolds number of the unsteady flow increases. The value of $U_{b1}$ is equivalent to free-stream velocity in the flat plate boundary layer flow.

(iii) $(U_{b1} - U_{b0})$ or $(Re_1 - Re_0)$. The velocity is used to describe the time-developing boundary layer and produce a variation on the flow rate.

(iv) $\frac{(U_{b1} - U_{b0})}{\Delta t}$ is known as acceleration rate. It calculates how rapidly the flow rate changes in the flow.

(v) $T_{u0}$ is known as the free-stream turbulence intensity of the initial flow. Its value is influenced by $Re_0$ and $Re_1$. $T_{u0} (= \frac{(u'_{rms,0})_{max}}{U_{b1}})$. where $(u'_{rms,0})_{max}$ is the maximum value of the wall-normal profile of the streamwise $rms$ velocity at t=0.

The current study aims to extend the knowledge that the onset of transition depends on the initial turbulence intensity which is determined by Reynolds number ratio.

Recent experimental investigations on accelerating channel flow have been reported by Gorji (2015). The author used state-of-the-art techniques (Laser Doppler Anemometer (LDA) and Particle Image Velocimetry (PIV)) for the measurement of turbulence statistics. The determination of the beginning of transition and the completion of it was obtained from fluctuating velocities in wall-normal and streamwise directions as the author could not utilise hot-film sensors due to installation difficulties. Mathur (2016) numerically and experimentally studied turbulence statistics in accelerating flow and decelerating flow. The numerical study was based on direct numerical simulations (DNS) and large-eddy simulations (LES). Experimental data was obtained through the particle image velocimetry (PIV) and constant temperature anemometry (CTA). The development of skin friction coefficient from the experimental data agreed with the numerical data from DNS & LES. In summary, the early response of the flow was characterised by the quick development of the skin friction coefficient which resulted from the plug-like response of the channel flow. The critical time, which indicates the beginning of transition period for all the flow conditions, was reported. The critical time determines the beginning of the transition, where the skin friction coefficient reduces to a minimum value. At the transition, the formation and transportation of the ''new'' turbulence caused the skin friction coefficient to increase rapidly. The experimental data and the numerical data agreed for the entire range of Reynolds numbers reported by the author. The trend of the wall shear stress reported is in conformity with the previous studies by He et al. (2008; 2011), He and Ariyaratne (2011) and Seddighi et al. (2014) and there were three stages in the flow. At the pre-transition stage, as with the earlier results on wall shear stress, the wall shear stress overshot the psuedo-steady value at the commencement of acceleration, and a thin boundary layer formed near the wall. The boundary layer that formed as a result of rapid acceleration spread into the flow and reduced (undershot) the wall shear stress below the quasi-steady value. In the transition stage, the generation of "new" turbulence caused the wall shear stress to increase, and in stage three the wall shear stress varied within the quasi-steady value.

Direct numerical simulations (DNS) were carried out by Jung and Kim (2016) and Jung and Kim (2017a; 2017b) to study the response of turbulence in a transient channel flow. The simulation started with an initial statistically steady turbulent flow and accelerated to the final turbulent flow. During the sudden increase of the initial flow rate to the higher value, the behaviour of the transient flow was studied. The friction Reynolds number of the simulation was fixed while the final Reynolds numbers varied. The initial friction Reynolds number $Re_{\tau 0}(= {}^{y u_{\tau 0}}/_{v} = 180)$ (where $u_{\tau 0}$ is friction velocity of the initial transient flow, $y$ is the distance from the wall, and $v$ is the kinematic viscosity of the working fluid) and the final Reynolds numbers, $Re_{\tau 1}$ were 250, 300, 350 and 395. A wide range of acceleration rates was used to study the effects of turbulence in the location near the wall of the channel. The numerical findings of the authors revealed that transition to turbulence of high final/initial Reynolds number ratio resembles transition induced by free-stream turbulence ($FST$), as stretching of pre-streaky turbulence structures, streaks elongation and formation of turbulence spots were observed. However, the flow progressively changed and the process of turbulence formation that leads to a transition to turbulence did not occur clearly when the final/initial Reynolds number ratio was small.

Adding to these findings, He, Seddighi and He (2016) studied transient turbulent flow in a pipe numerically using direct numerical simulations. The initial statistically steady turbulent flow was increased rapidly to the final flow condition and the characteristics that occur during transient flow were investigated. The authors have shown that the procedure of transition to turbulence resembles laminar-turbulent transition induced by free-stream turbulence ($FST$) and is similar to the transition to turbulence in a channel reported by He and Seddighi (2013). They have shown that the behaviour of channel and pipe flows in the near wall is similar, but some discrepancies were noted at the centres of pipe flow and channel flow. It was reported that the relationship between critical Reynolds number and turbulence intensity that was earlier introduced for a channel flow also correlated with the pipe flow. In the study, initial Reynolds number $Re_0 = 2650$ was fixed while the final Reynolds number varied ($Re_1 = 3000, 5220\ and\ 7362$). It was discovered that the correlation $Re_{\tau,cr}(= 1340T_{u0}^{-1.71})$ reported by He and Seddighi (2015) on transient channel flow can also be utilised for pipe flow. He et al. (2015) investigated the response of turbulence due to the rapid increase of initial statistically steady turbulent flow to the final turbulent flow using direct numerical simulations (DNS), large-eddy simulations (LES) and experiments. The results of their findings have revealed that the process of transition to turbulence resembles a laminar-turbulent transition induced by free-stream turbulence, despite the initial Reynolds number being turbulent. The investigations were carried out on both smooth and rough surfaces. The correlation that relates the critical Reynolds number and turbulence intensity in transient channel flow had been previously reported as $Re_{\tau,cr}(= 1340T_{u0}^{-1.71})$. The the results presented follow the trend of the correlation except when the initial turbulence intensity was less than 0.02 ($T_{u0} < 0.02$). The authors proposed a correlation between the transitional Reynolds number $\Delta Re_{t,cr}$ and the critical Reynolds number $Re_{t,cr}$ as $\Delta Re_{t,cr}(= 16.43Re_{t,cr}^{0.781})$. It was reported, for a rough wall, that the roughness of the surface triggered transition to turbulence and that it occurred more rapidly than on a smooth wall. Following this, Seddighi et al. (2015) numerically studied the response of turbulence when the flow rate increased from an initial statistically steady turbulent flow to the final statistically steady turbulent flow over a rough wall. It was reported that the procedure of transition to turbulence was similar to the transition of laminar-turbulence roughness-induced even though the initial stationary flow was turbulent.

As with the flat plate boundary layer flow, the viscous layer develops rapidly with time in transient channel flow. During the rapid increase of flow rate, a uniform increment of velocity occurs everywhere in the flow region except in the location near the wall where a thin boundary layer of high-velocity gradient forms as a result of a no-slip boundary condition. This thin boundary layer grows into the flow with time in a similar fashion to the spatial boundary layer development of a flow on a flat plate. He and Seddighi (2013) proposed an equation to describe the boundary layer development as $\bar{U}^{\wedge}\left({}^{y}/_{\delta}, t\right) = \left[\frac{\bar{U}\left({}^{y}/_{\delta},t\right)-\bar{U}\left({}^{y}/_{\delta},0\right)}{\bar{U}_c(t)-\bar{U}_c(0)}\right]$ where $\bar{U}\left({}^{y}/_{\delta}, t\right)$ is the mean velocity at different values of time, $\bar{U}_c(t)$ is the velocity at the centre of the pipe, $y$ is the distance from the wall, $\delta$ is the half-height of the channel, and $t$ is the time after the acceleration commences. This equation has been used by Jung and Kim (2017b), and Sundstrom and Cervantes (2018c) in their studies of accelerating turbulent flows starting from a statistically steady turbulent flow for the determination of perturbation velocities. Sundstrom and Cervantes (2018a) experimentally investigated accelerating and decelerating pipe flow using particle image velocimetry (PIV) and hot-film sensor techniques for the measurement of mean velocity and turbulence statistics. They confirmed that the response of mean and turbulence during transient flow occurs in three stages in channel, as previously reported by Seddighi et al. (2015), He, Seddighi and He (2016) and Jung and Kim (2017a; 2017b). The authors directed attention to the first stage at which wall-normal and spanwise directions did not respond to the initial flow acceleration. The authors investigated the temporal boundary layer development in terms of perturbation during the transient flow. At the initial stage of transient flow, it was reported that temporally developing of mean and turbulence statistics in both accelerating and decelerating flows was similar during the initial stage of the transient flow. However, as the transient flow continued after the initial stage, the similarity of the two types of flow reduced.

More recently, Mathur, Seddighi and He (2018) confirmed three stages response during the time-developing boundary layer using large-eddy simulations (LES). The investigations were carried out on high and low Reynold number ratios. It was reported that when the Reynolds number ratio was high, the turbulence features that occurred during the transition were notable. The stretching of the pre-existing structures and elongation of streaks were visible, but these features were not clearly seen with a low Reynolds number ratio. Mathur et al. (2018) experimentally and numerically investigated an accelerating flow starting from initially turbulent flow. The authors reported that the transition of channel turbulent flow resembled that of laminar-turbulent transition in a flat plate boundary layer flow. It was reported that the recovery of the skin friction coefficient during the transitional stage was a result of transition of the new temporal developing boundary layer near the wall. The numerical investigation of Mathur et al. (2018) on channel flows and experimental study of Bhushan et al. (2018) on flat plate boundary layer flow confirm three-stage response during transient flows. The authors used the minimum value of skin friction to mark the onset of transition. A temporal acceleration was performed on two flow conditions to investigate the turbulence response using large-eddy simulations (LES) by Talha and Chung (2015). An initial flow condition of $Re_0 = 3500$ that consisted of the half-height of the channel and bulk velocity was maintained at statistically steady state before it was linearly increased to the final flow condition $Re_1 = 22600$. During the accelerating flow, the effects of wall shear stress and other turbulence statistics were investigated. The authors identified the three delays previously reported in experiments of He and Jackson (2000) in their LES results.

Sundstrom and Cervantes (2018b) carried out experimental investigations on transient turbulent and pulsating flows in a pipe and used particle image velocimetry (PIV) technique and anemometry with hot-film sensors for data acquisition. They performed ensemble-averaged on the acquired data to determine mean and turbulence statistics of the flow. The response of wall shear stress and turbulence at the location near the wall was reported. The investigation reconfirmed the three stages of transition procedure that were earlier reported on transient turbulent flows (He & Seddighi, 2013; Seddighi et al., 2014; He & Seddighi, 2015). Sundstrom and Cervantes (2017) studied wall shear stress in a uniform and nonuniform transient pipe flow and also confirmed the three stages (pre-transition, transition and fully turbulence) of transition to turbulence in transient turbulent flow and showed that the process of transition to turbulence in a transient flow resembles laminar-turbulent bypass. The authors confirmed that streamwise fluctuating velocity increased during the pre-transitional stage while both wall-normal fluctuating velocity and Reynolds shear stress remained unchanged. It was reported that transition to turbulence initiated when wall-normal fluctuating velocity and Reynolds shear stress started to respond to flow. Table 2-1 below provides previous investigations that are closely relevant to this current study.

***Table 2-1: Numerical and experimental studies of a new perspective of transient turbulent flows.***

| Authors/Date | Method | Remarks |
|---|---|---|
| He and Seddighi (2013) | DNS | Established a novel perspective that the procedure of transition of transient turbulent flow is a laminar-turbulent transition that is similar to the transition to turbulence of a flat plate boundary layer flow. Three stages of transition procedure were established similar to that of the flat plate boundary layer flow of Jacobs and Durbin (2001). |
| Seddighi et al. (2014) | DNS | Reported that the procedure of transition of transient turbulent flow is similar to that of He and Seddighi (2013), but the onset of transition was delayed. |
| He and Seddighi (2015) | DNS | The authors varied both initial and final Reynolds numbers systematically. It |

| | | |
|---|---|---|
| | | was also concluded that the transition procedure is characterised by laminar-turbulent transition. |
| Jacobs and Durbin (2001). | DNS | Reported three stages of transition to turbulence in a flat plate boundary layer flow. |
| Gorji (2015) | PIV/LDA | Studied turbulence statistics in transient turbulent flow experimentally. |
| Mathur (2016) | PIV | Studied mean velocity and turbulence statistics in accelerating and decelerating flows. |
| Jung and Kim (2016) | DNS | The authors investigated the response of turbulence during the accelerating of initial statistically steady turbulent flow to a higher flow rate. |
| Jung and Kim (2017a) | DNS | It was confirmed that the transition of a fully developed turbulent flow in a channel is a laminar-like transition. |
| Jung and Kim (2017b) | DNS | The authors varied the initial Reynolds number that is based on friction velocity. The laminar-like transition was observed at the early stage of the flow acceleration. |
| He, Seddighi and He (2016) | DNS | The authors revealed that the procedure of transition of transient turbulent flow resembles that of the |

| | | |
|---|---|---|
| | | laminar-turbulent transition of a flat plate boundary layer flow. They reported that the characteristics of channel flow near the wall are similar to that of pipe flow. |
| Mathur, Seddighi and He (2018) | LES | Confirmed three stages during the transition of transient turbulent flow. Reported that turbulence features in the flow become visible at higher Reynolds number ratios. |
| Mathur et al. (2018) | PIV | The authors confirmed the three-stage response during the transition procedure of transient turbulent flows. |
| Sundstrom and Cervantes (2018a) | PIV/Hot-film anemometry | The authors confirmed the three stages of transition of transient turbulent channel flows of He and Seddighi (2015). |
| Bhushan et al. (2018) | DNS | Reported three-stage of transition from laminar to turbulence in a flat plate boundary layer flow. |
| He et al. (2008) | CFD Model | The authors studied wall shear stress during flow acceleration. At the early stage of the flow acceleration, wall shear stress increased and overshot that of the quasi-steady value. The result conformed with the |

| | | |
|---|---|---|
| | | previous investigations of He and Jackson (2000). |
| He. Ariyaratne and Vardy (2011) | Hot-film anemometry | The authors reported the response of wall shear stress in three stages. At the initial stage, wall shear increased and overshot the quasi-steady value. The results conform with that of He et al. (2008). |
| Seddighi et al. (2011) | DNS | At the initial stage of the accelerating flow, wall shear stress increased and overshot the quasi-steady value. |
| Talha and Chung (2015) | LES | The authors reported a rapid increment of wall shear stress in the early stage of the turbulent channel flow. |
| Sundstrom and Cervantes (2017) | Hot-film anemometry | Studied wall shear stress in accelerating turbulent pipe flow. The authors reported three stages of wall shear stress development. |
| Sundstrom and Cervantes (2018b) | Hot-film anemometry | The authors reconfirmed the three-stage development of wall shear stress. |

## 2.8 Summary

This chapter has reviewed the previous investigations on the acceleration of statistically steady turbulent flow in a smooth channel by dedicated researchers. Mean and turbulence statistics of accelerating flows (non-periodic flows) and pulsating flows (periodic flows) have been discussed. The two classifications of transition (natural transition and bypass transition) on a flat plate boundary layer flow have been described. In natural transition, the free-stream turbulence intensity is far less than 0.01 ($Tu \ll 1\%$).while the value of free-stream turbulence intensity is greater than 0.01 ($Tu > 1\%$) for the bypass transition. The three stages of flow development in a flat plate boundary layer flow have been reported: the buffeted laminar boundary layer, intermittent turbulent spot formation region, and the fully developed turbulent boundary layer. Relevant papers related to the new interpretation of the transition of transient turbulent flow in a channel have been reviewed. The new perspective has revealed that the transition of transient turbulent flows resembles a laminar-turbulent bypass transition, although the initial flow is turbulent. The three stages of flow development (pre-transition, transition, and fully turbulence) have been reported and the stages resemble that of flat plate boundary layer flow. This new perspective has been confirmed experimentally by Mathur (2018). This current study is to extend the knowledge further by increasing the flow conditions. The initial Reynolds numbers of this current study have been increased higher than that of Mathur (2018) and Seddighi et al. (2014), while the process of transition of transient turbulent flow is studied. The next chapter provides a full description of the experimental setup and data acquisition.

## Chapter 3

# Experimental Setup and Measurement Techniques

---

## 3.1 Introduction

An experimental method has been adopted in this study of streamwise mean velocity and of turbulence statistics in transient flows. This chapter describes the flow facility, experimental setup, flow control, Particle Image Velocimetry (PIV) system, measurement techniques, Constant Temperature Anemometry (CTA) and data processing. A series of measurements were taken using Particle Image Velocimetry (PIV) and constant temperature anemometry techniques in a wall-bounded channel flow. The measurements of instantaneous and mean velocities were obtained through PIV while hot-film sensors that were controlled by Constant

Temperature Anemometer. This technique was used to measure the instantaneous wall shear stress over many repeated runs. The experimental setup was also used to study steady flow conditions, and the results obtained were compared with the numerical data of Lee and Moser (2015). The processes involved in the measurements of the instantaneous velocities and turbulence statistics at different flow conditions are explained in this chapter.

## 3.2 Wall-bounded channel flow facility

In fluid dynamics, the knowledge of the behaviour of wall-bounded flow (internal flow) is of great in important in many engineering applications such as flow through pipeline network in oil and gas and turbomachinery. A large-scale flow loop designed by Gorji (2015) and modified by the present author at the new location (Fluids Laboratory, George Porter Building, the University of Sheffield) was used to study turbulence behaviour in unsteady laminar and turbulent flows over a smooth surface of a wall-bounded channel. A schematic diagram of the wall-bounded channel flow facility with the equivalent coordinate system applied throughout the experiment is depicted in Figure 3-1. To decide on the measurements of the flow facility, existing literature was consulted. It was found that the aspect ratio (W/H) that determines the width and the height of the channel has been investigated by several researchers (Hanjalić & Launder, 1972; Dean, 1978; Monty, 2005 & Hong et al., 2011). To be more specific, Dean (1978) reviewed literature on channel flow facilities published between 1928 and 1976 and suggested that the ratio of the width of the channel to the height of the channel must be 7, so that secondary flow could be avoided at the mid-span of the channel. The results of the investigations by Hanjalić & Launder (1972) and Hong et al. (2011) on channel flow facilities are in conformity with the results reported by Dean (1978). In addition, Monty (2005) performed investigations on the required length and height for a fully-developed flow to be attained in both smooth channels and pipes. The author concluded that for a fully-developed mean and turbulence profiles in the channel to be attained, the ratio of the length to height (L/H) must be 130. In this study, the length, width, and height of the test rig are 8000 *mm*, 350 $mm$ and 50 $mm$, respectively. The width to height $\left({}^{W}/_{H}\right)$ ratio is 7 and the length to height $(L\ /\ H)$ ratio is 160. Thus, the design of the flow facility conforms to these suggestions.

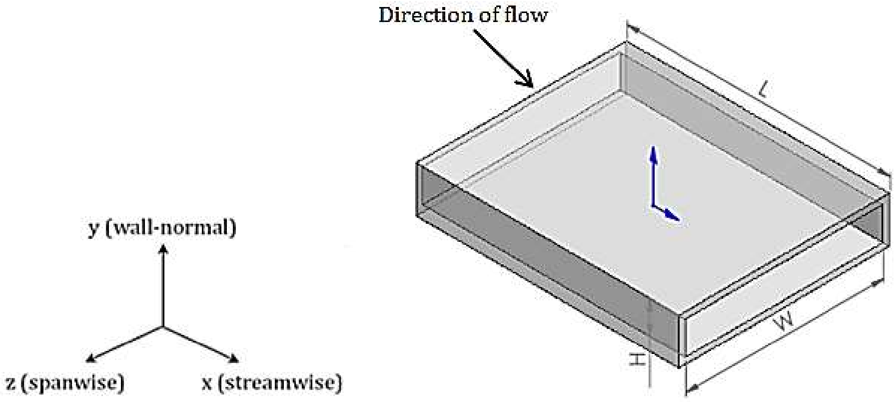

*Figure 3-1: Schematic of the channel flow test section.*

## 3.3 Experimental setup

All experiments were conducted in a rectangular channel flow loop that consists of the following components: bottom tank, overhead water tank, centrifugal pump, magnetic flow meter, pneumatic control valve, manual valve, stainless steel adaptor, CCD camera, laser, test section and a honeycomb flow straightener. The height from the water free surface of the overhead tank to that of the bottom tank is 5.31 $m$. The channel-test section's height to the floor of the laboratory is 1.21 $m$.

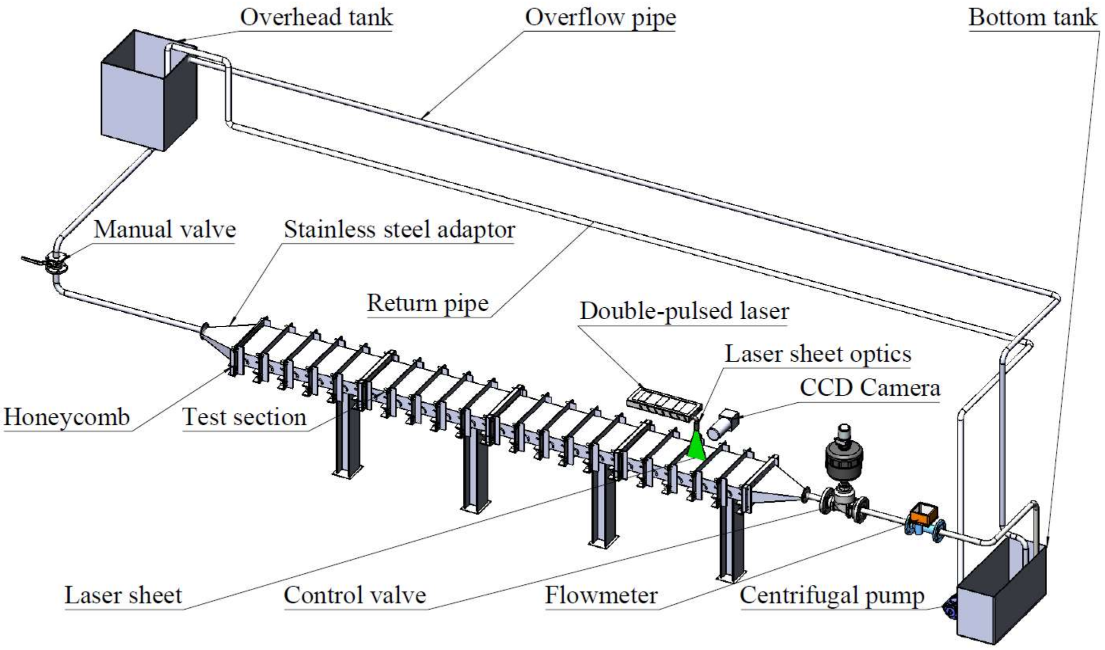

***Figure 3-2: Schematic diagram of the experimental channel flow facility.***

The capacities of the bottom tank and overhead water tank are 3000 litres and 1000 litres, respectively: sufficient to achieve a continuous flow loop. The capacity of the overhead tank was increased at the new laboratory (George Porter Building) to 1000 litres compared to 400 litres at the old laboratory (Mappin Building). The new size of overhead tank greatly reduced bubbles transferred from the bottom tank through the return pipe because of longer settling time. In order to completely remove air bubbles that resulted from the air entrapment and cavitation from the bottom tank of the system, a mesh screen was installed to cover the end of the return pipeline that delivered water to the overhead tank. The end of the overflow pipe that led to the bottom tank was installed far from the suction pipe and the pipe was submerged in the bottom tank. The pipeline of the overflow helped to transfer excess water to the bottom tank from the overhead tank whilst also ensuring that the driving pressure gradient was held constant by maintaining a constant height of the water in the overhead tank throughout the experiments.

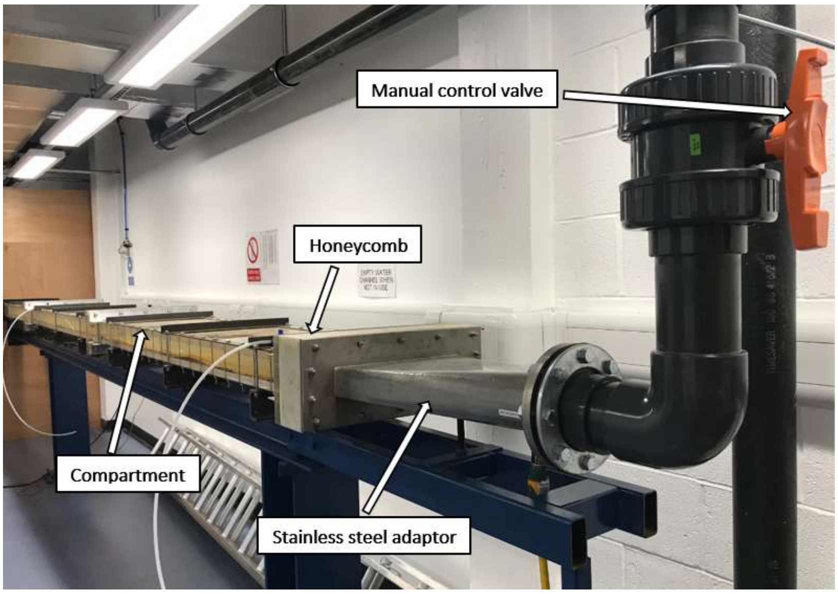

***Figure 3-3: Test rig showing channel compartments, manual control valve, honeycomb and stainless steel adaptor.***

The water from the overhead tank flowed through the manually regulated on/off valve mounted on the PVC pipeline and into the test section through the stainless-steel adaptor and honeycomb flow straightener, as shown in Figure 3-3. It then flowed from the test section to the bottom tank through the stainless-steel adaptor that was installed immediately after the end of the test section and passed through a pneumatic control valve and magnetic flow meter before it was discharged into the bottom tank. The pipeline that extended from the magnetic flow meter was submerged properly into the bottom tank in order to reduce the formation of bubbles in the bottom tank. A four-inch bore $4KW$, three-phase, four-pole centrifugal pump transferred water discharges to the bottom tank from the test section through the four-inch Poly Vinyl Chloride (PVC) return pipeline to the overhead tank.

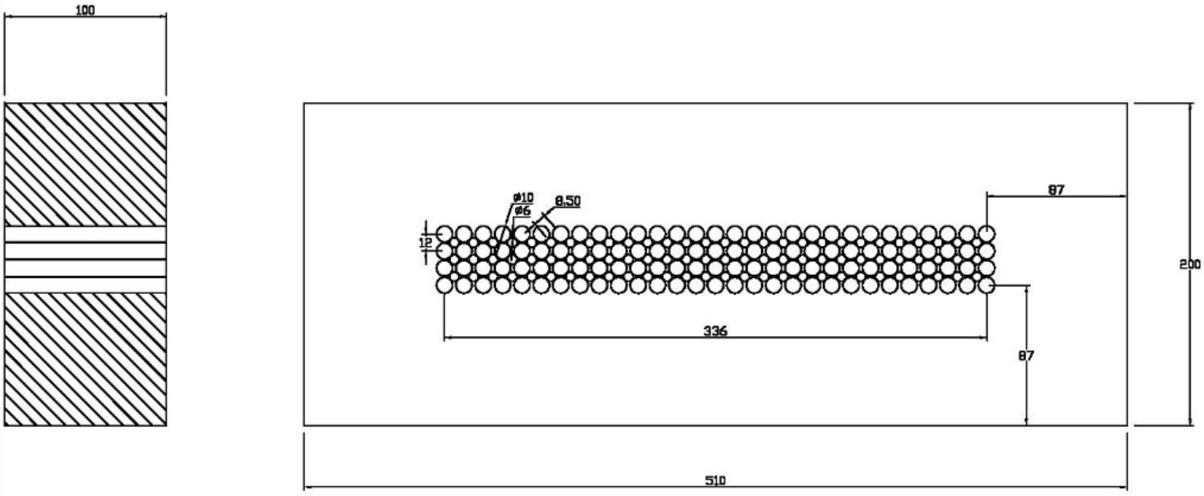

***Figure 3-4: The honeycomb unit made from PVC block (dimensions in mm).***

A PVC honeycomb flow straightener shown in Figure 3-4 was installed between the stainless-steel adaptor and the inlet test section. This helped to achieve flow development in the test section by removing the large-scale swirls generated from the bends between the overhead water tank and inlet stainless-steel adaptor. The fully developed turbulent flow was achieved first in the test section before the flow acceleration using the pneumatic control valve. The flow started to develop from the exit of the honeycomb flow straightener and become fully developed turbulent flow at a distance of 100H (where H is the channel height = 50 $mm$) from the exit of the honeycomb flow straightener.

## 3.4 The channel test section and flow control

As stated earlier, the length, width and height of the flow facility measured 8000 $mm$, 350 $mm$ and 50 $mm$, respectively, with a ratio of length to the height of 160 and width to the height of 7. Transparent Perspex Plate of 20 $mm$ thickness was used for the construction of the test channel section, and the thickness of the smooth wall used for this current study is 10 $mm$. The channel test section consisting of four compartments was used, as shown in Figure 3-3, each with a length of 2000 $mm$. The measuring equipment-laser, camera, and hot-film sensors were mounted on the fourth compartment of the test section, as shown in Figure 3-5. For the purpose of increasing the optical access at the fourth compartment of the test section (measurement section), a glass window 50 $mm$ high and 700 $mm$ long was installed on one side of the measuring section. It should be noted that there was water leakage at the joints of the four compartments in the new location (George Porter Building) after the assembly of all components. Grooves were thus created at the end of each compartment using Makita DTM50Z cordless multi-tool 18V. The grooved joints of each compartment were then joined using Loctite 3090 and the water leakage stopped.

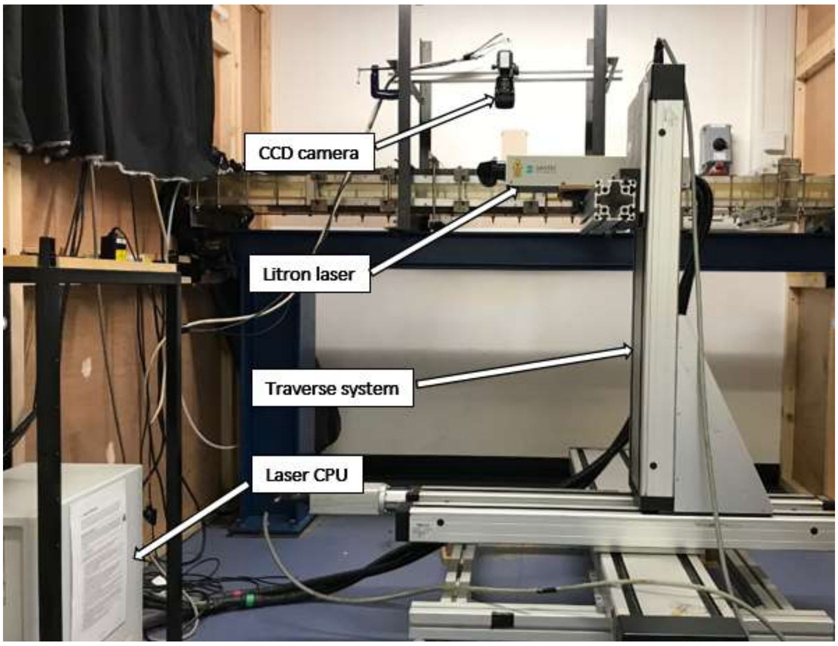

***Figure 3-5: Laser room showing laser system, CCD camera and traverse system.***

Figure 3-6 shows the 4'' pneumatic control valve used to control the flow in the channel flow loop facility. It was installed at a distance of 1000 mm from the outlet of the stainless-steel-adaptor, a distance considered appropriate for optimum performance of the valve. For the regulation of the flow rate through the valve, equal proportions of flow and valve lift characteristics were adopted.

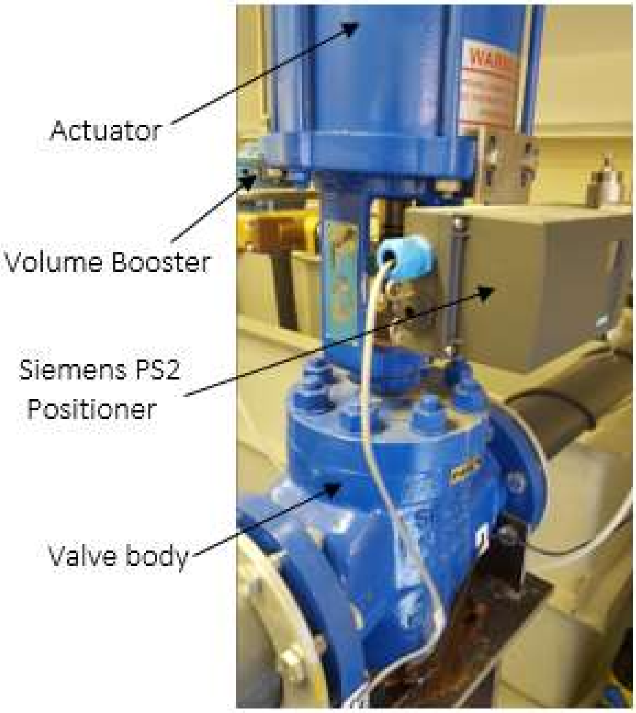

***Figure 3-6: Pneumatic control valve.***

Figure 3-7 shows the comparison of the operational curve with its inherent curve during valve opening. The inherent curve of the valve was obtained when the flow rate was measured at different valve lifts and at a constant pressure drop across the valve; however, the operational curve of the valve is characteristic of the configuration of the flow system. For an accelerating flow, the required acceleration occurs as the pneumatic control valve opens suddenly or in a controlled manner. The time period at which acceleration occurs in the flow depends on the operational curve of the pneumatic valve and the final flow condition. The pneumatic control valve used in this current study consisted of an actuator, valve body, positioner and volume boosters, as shown in Figure 3-6. The actuator, which consisted of a diaphragm, spring, valve stem, plug and seat, used high pressure compressed air to produce a linear motion. The actuator was used to provide a high level of accuracy in stem positioning and the volume booster was used to increase the stroking speed of the actuator in conjunction with the positioner. Finally, a Siemens PS2 positioner controlled the position of the valve trim using a 4-20 mA signal. For the operation of the regulated glove valve, compressed air at a pressure of

4 bars was supplied to the system through the positioner and volume boosters. A Phoenix Contact three-way isolating amplifier that was supplied with 0-10 volts signal from the National Instruments Data Acquisition (DAQ) device was then used to generate the signal for the operation of the system. The device, which consisted of 16 analog input ports and 16 analog output ports, was connected to a computer with programmable software via a universal serial bus (USB) port. A computer with DAQ software, DAQ device and sensors comprised the complete DAQ system. To complete the setup, a 4-inch ISOMAG magnetic flowmeter and hot-film sensors were connected to the analog input of the device. The following procedures show how the valve operating curve was converted to flow conditions: 1) determined the flow rate for every valve lift, 2) obtained bulk velocity ($U_b$) from each flow rate, 3) performed interpolation on the bulk velocity ($U_b$), and the value of each valve lift in order to get the value of valve lift for each flow condition. For a known Reynolds number ($Re_b$), the bulk velocity ($U_b$) was determined as, $U_b = {}^{Re_b v}/_{\delta}$ where $\delta$ is the half-channel height and $v$ is the kinematic viscosity of the working fluid.

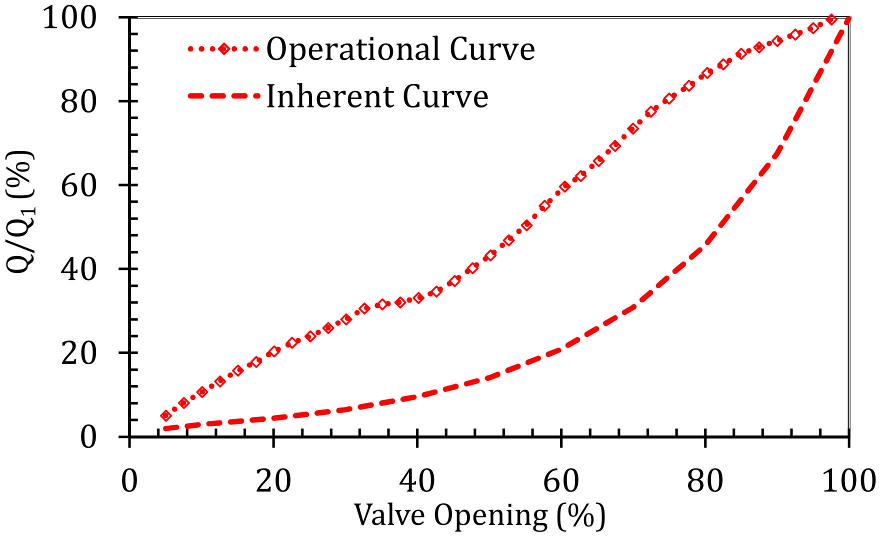

***Figure 3-7: Operational and inherent characteristics of the regulator valve.***

A 4-inch ISOMAG magnetic flowmeter was used in this experimental setup and was located at a distance of 1000 mm from the exit pipe of the pneumatic control valve. The flowmeter was able to measure bulk flow variations up to 62 $m^3/hr$ and was connected to the analog-to-digital converter of the USB-6211 DAQ device supplied by National Instruments. The output signal of the 4-inch ISOMAG magnetic flowmeter was within 4-20 $mA$, equivalent to 0-10 $volts$ by conversion with a 250 Ω resistor.

In this research, the measurements of wall shear stress and instantaneous velocity were obtained from Constant Temperature Anemometry (CTA) using hot-film sensors and Particle Image Velocimetry (PIV), respectively. The hot-film sensor panel was installed at a distance slightly greater than 7,850 $mm$ downstream from the inlet of the test section, and the measuring section of the experimental setup, which consisted of a hot-film sensor panel, camera, traverse and the laser, was well enclosed to prevent the radiation of the laser harming the eyes of the users.

## 3.5 Measurement principles of the Particle Image Velocimetry system

The principle of Particle Image Velocimetry (PIV) can be explained through the analogy of measuring the velocity of a car by taking two photographs of it in motion, with the second taken 1 second later than the first. The velocity of the car can then be determined by measuring the distance travelled between the first photograph and the second photograph and dividing it by time (1 second). In this current study, instead of one car, thousands of micron-diameter seeding particles were visible in the flow. The velocity of these particles can be measured using PIV, which is a non-instructive optical method that is used to measure instantaneous fields of velocity vector of a flow field. The principle involves seeding the fluid with particles of smaller diameter that are assumed to follow the flow accurately. The displacements of those particles in the flow region are captured with CCD camera and a laser sheet provides illumination to the plane to be imaged. PIV is then used to determine instantaneous flow fields of the vector velocity in a measurement plane by measuring the displacement ($\Delta x$) of many seeding particles that follow the motion of the working fluid (water) and divide it by the time taken to travel between the two light pulses. The displacement ($\Delta x$) of the seeding particles is obtained by comparing the positions of the seeding particles in two separate frames over a known time between the two light pulses. This method is commonly used in experimental fluid dynamics to obtain the global velocity in a fluid flow (Adrian & Jerry, 2011). A standard PIV setup from Dantec Dynamics was utilised in this research consisting of the following components: a litron pulsed laser, light sheet optics, CCD camera, camera lens, synchroniser (timer box), DynamicStudio software, camera tripod, seeding particles and traverse system.

### 3.5.1 Charge-Coupled Device (CCD)

In this current study, two velocity components were measured with a single CCD camera. A 12-bit CCD camera (FlowSense 4M MKII) from Dantec Dynamics with an image resolution of 2048×2048 pixels was used throughout the experimental process to capture images of the flow field. The measurement of three velocity components for the whole field can be obtained using Stereoscopic PIV. The camera that was used in this study has zero intensity at a dark pixel and 4096 intensities at a fully bright pixel. The 12-bit CCD camera was used to capture two single exposed laser sheets separated by the time between the two light pulses in the flow region. A Nikon AF Micro-Nikkor 60 $mm$ f/2.8D lens with a focal length of 60 mm, a minimum aperture number of f/32 (when the aperture is fully closed) and maximum aperture number of f/2.8 (when the aperture is fully open) was fitted to the 12-bit CCD camera that was positioned on a tripod mounted on a traverse system. The traverse system allowed the camera to be perpendicular to the laser sheets. Moreover, the traverse system aided the movement of the 12-bit CCD camera 1mm forward and backward in both vertical and horizontal directions during camera calibration. The camera calibration was completed once the seeding particles captured by the 12-bit CCD camera were focussed (when the seeding particles appeared as if stars in the night sky). The traverse system moved the camera or laser that was mounted on it in three dimensions. A higher version of Dantec Dynamic Software (DynamicStudio v3.41), which incorporates advanced cross-correlation algorithms, was used to process the two frames to generate a single instantaneous velocity field. To ensure accurate measurements during all the experiments, the synchronising of the camera and laser pulses is recommended. The linking of the laser, camera and the computer was accomplished using a NI PCI-E 1427 DAQ card from National Instruments in addition to a Dantec Dynamics synchroniser (timer box), which was controlled by a NI PCI 6602 timer board and connected to the camera using a BNC cable. The synchroniser (timer box) which enables the PIV system to be computer controlled.

#### *3.5.1.1 Basic lens operation*

In terms of lens operation, the amount of light that enters a camera is determined by the lens aperture (how widely open it is) expressed in f-numbers. A higher f-number (f/22) denotes a more narrow aperture, and so less light is allowed to enter the camera and vice versa. During the experiments, adjustments were made to the aperture starting with a high f-number in order to protect the light sensitivity of the camera from being saturated and thereby causing damage. Laser energy and the aperture of the camera were carefully adjusted for all the experiments.

#### *3.5.1.2 Camera calibration*

The camera was calibrated by setting up a scale factor to correlate the physical dimension of an object to the corresponding dimensions in the camera. This is necessary to relate the relationship between a pixel in the image and the actual dimension of the field of view (FOV). DynamicStudio software was used to process the images, and this measures images in pixels. The scale factor then translated the measurements in pixels to physical units. To measure the scale factor during the camera calibration, a known distance between two points was used to establish the actual pixel size in millimetres. A known width of the calibration object captured was saved then in the calibration folder of the DynamicStudio software, and the distance between the two points of the calibration image determined the field of view (FOV) of the lens.

Finally, the calibrated data was saved in the project file of the DynamicStudio database to provide reference data for all other experimental data.

### 3.5.2 Laser system

The determination of the instantaneous velocity in both streamwise and wall-normal directions was obtained using the integrated PIV system of Dantec Dynamics. Generally speaking, in order to avoid blurred images being acquired during experiments, laser pulses are required. Laser sheets that emerged from laser sheet optics provided an illumination source to the seeding particles in the target area in the flow similar to the photographic flash of a digital camera. A focal adjuster on the laser sheet optics was rotated in order to adjust the focal point of the laser sheets which were focused when at their thinnest. Laser sheet optics was fitted to a Litron Laser (Nano-S-65-15PIV Nd: YAG) with resonators that generate an infra-red laser sheet at 1064 $nm$ (invisible) and Harmonic Generator Assembly that converts the sheet to a wavelength of 520 $nm$ (green). The litron laser has a maximum output energy of 65 $mJ$/pulse with a pulse rate of 15 $Hz$. In this present PIV system, the maximum trigger rate of the pulsed laser after the synchronisation with the camera was 7 $Hz$. The time between the two light pulses used for steady and unsteady cases in this research is 900 $\mu s$ and 300 $\mu s$, respectively.

#### *3.5.2.1 Time between the two light pulses*

The time between the two light pulses is always determined carefully for steady and unsteady flow experiments for the determination of streamwise mean velocity and turbulence statistics. In addition to the use of a correlation map produced using DynamicStudio software, a test case of the same flow condition was run using different times between the two light pulses in order to determine the best value to use for the experiment.

#### *3.5.2.2 Laser system control box*

The laser's functionality was controlled using a laser system control box connected to the laser central processing unit (CPU). This allowed adjustments to be made to the repetition rate, switching on the laser, switching on the laser cooling system, and the operation of the shutter. During the experiments, the control box helped to regulate energy of each laser in conformity with the aperture of the camera.

### 3.5.3 Seeding particles

In order to capture raw images of the flow field, reflecting particles had to be added to the working fluid. In this current study, silver coated hollow glass spheres (model:10089-SLVR) with a mean diameter of 14 $\mu m$ and density of 1.65 $g/cc$ (1650 $Kg/m^3$) were added to the working fluid inside the bottom tank. The seeding particles in the flow were captured by CCD camera for PIV-processing.

### 3.5.4 Operating procedure of Particle Image Velocimetry system

At the initial stages of the experiment, the Particle Image Velocimetry (PIV) components were prepared. Figure 3-8 shows the different components of the PIV system and illustrates how the velocity field can be obtained using this technique. In brief, seeding particles were added to the working fluid (which flowed in cycles through the test section) for the reflection of the imaged plane. The particles were small enough to follow the flow and large enough to reflect light in

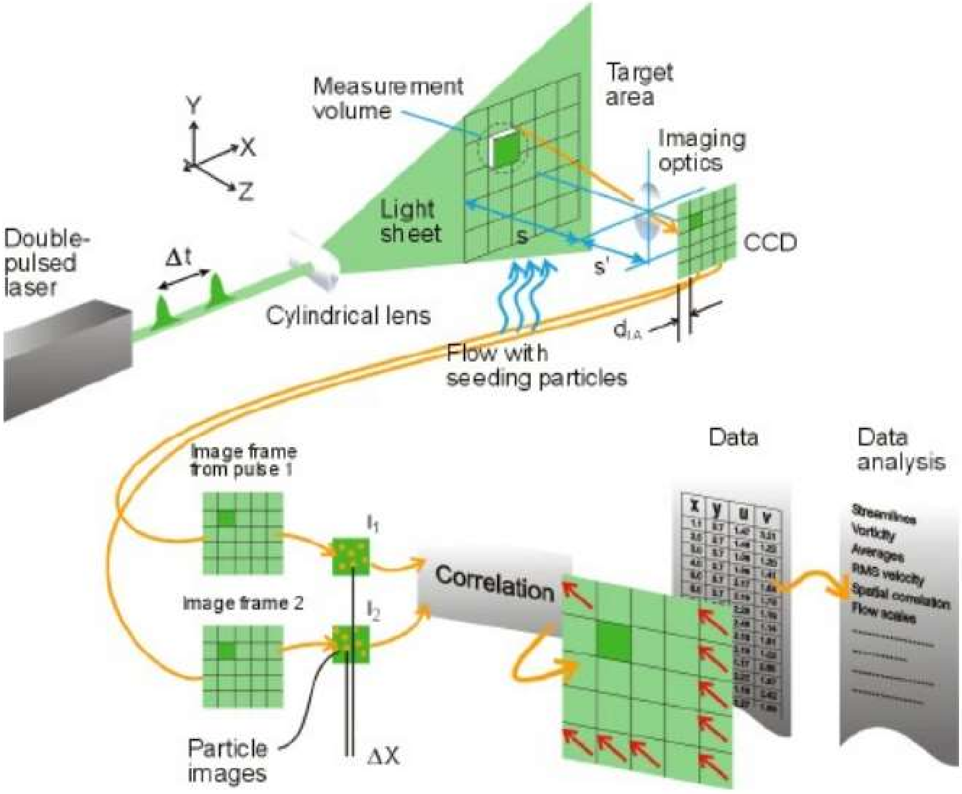

***Figure 3-8: The components of particle image velocimetry system (Dantec Inc.).***

the imaged area. Camera calibration was done when the seeding particles were observed to be distributed uniformly in the flow. The laser system was then switched on and images for calibration captured using the CCD camera. During the calibration, the required field of view (FOV), aperture number and laser energy were set. At this point, the field of view (FOV) was checked to ensure it was homogeneously illuminated by laser sheets. This was achieved by checking that the double-frame exposures of the laser were of the same intensity. The number of seeding particles per interrogation area was ensured to be between 8 and 10 for better cross-correlation. Following this, the time between the two light pulses, laser trigger rate and number of images to be captured per iteration were set. Steady and unsteady data were then acquired and analysed using DynamicStudio software for the determination of velocity field. Flow chart for data acquisition and processing stages in two-dimensional PIV system are shown in Figure 3-9.

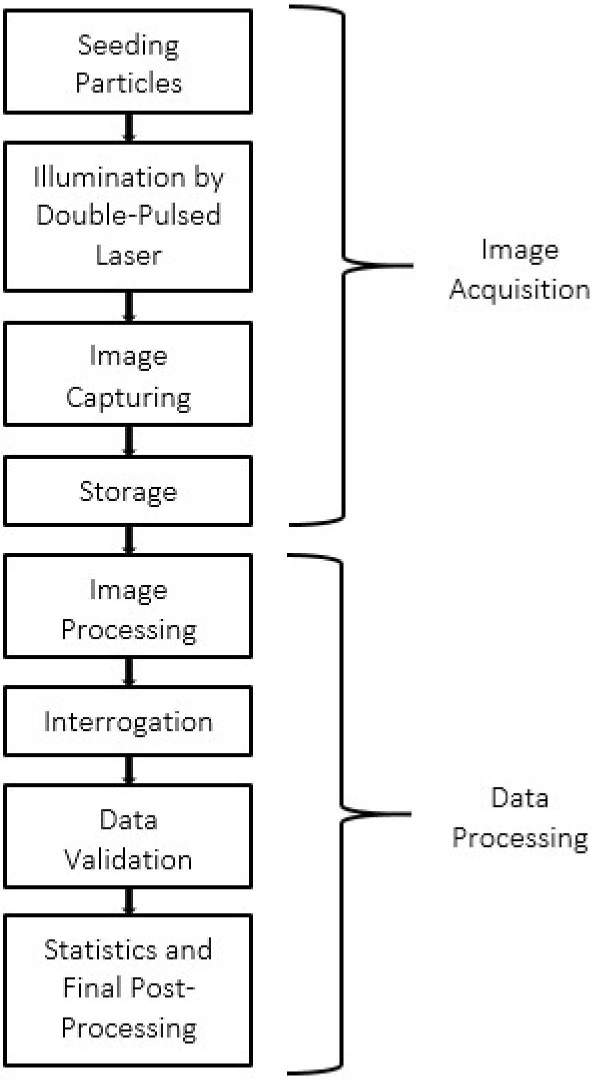

***Figure 3-9: Flow Chart of Data Acquisition and Processing in Two-Dimensional PIV.***

### 3.5.5 DynamicStudio software version 3.41

In PIV system, DynamicStudio software is commonly used for raw image acquisition and analysis by synchronising camera and laser. DynamicStudio is used for camera calibration, image pre-processing, image processing, vector post processing, vector evaluation and data export in comma separated value (CSV) format. It is also used to calculate the velocity vector from the displacement ($\Delta x$) of seeding particles and the known value of the time between the two light pulses. The process of such image acquisition and analysis is as follows. First, raw images captured during data acquisition are saved and pre-processed in order to improve the images' quality before PIV processing. Pre-processing is done by performing image background subtraction and image balancing on the raw images captured to improve the quality of the raw images. During image processing, the images from frame A and frame B are divided into a number of interrogation areas which are specified during the conversion of image maps into vector maps. In each interrogation area, groups of particles are visible. The group of particles in each interrogation area in frame A produce a unique thumbprint and this unique thumbprint is used to search in frame B. Cross-correlation is calculated pixel by pixel at each location within the interrogation area for a correlation function to be obtained. Thus, when a thumbprint is detected in frame B, a maximum correlation is obtained. The length of the displacement vector is then measured from the offset of the thumbprint in the interrogation area of frame B. As the length of the displacement vector is known, the velocity vector is obtained by dividing the length of displacement vector by the time between the two light pulses, and the procedure is therefore repeated for all the remaining interrogation areas.

A better PIV measurement has the following criteria: 1) the whole Field of View (FOV) must be illuminated as homogeneously as possible; 2) seeding particles must not affect the flow of fluid; 3) the intensity of the double-frame exposures (Frame A and Frame B) must be the similar; 4) the camera must be focused and aligned perpendicular to the laser sheets; 5) each interrogation area must contain between 8-10 seeding particles; and 6) the maximum displacement ($\Delta x$) of seeding particles must be less than one-quarter (1/4) of the interrogation area.

Three inherent assumptions must be made when using the PIV measuring technique. It is assumed that 1) the seeding particles perfectly follow the flow motion in the channel; 2) the seeding particles are homogeneously distributed in the channel; and 3) the displacement ($\Delta x$) of the seeding particles, which is used to calculate the velocity field, is uniform within the interrogation areas.

## 3.6 Measurement technique

The measurements of velocity field were obtained using two different camera-laser orientations. These two measuring techniques were used for all the data acquisition in this current study. The first orientation enabled the laser to fire from the top of the test channel (vertical-PIV) and the second orientation enabled the laser to fire from the side of the test channel (horizontal-PIV). During the first orientation, the CCD camera was mounted on the camera tripod which was positioned on the traverse system; the laser was placed on the hanger on the top of the test channel. In the second orientation of the camera-laser, the CCD camera was suspended from the hanger on the top of the test channel while the laser was mounted directly on the traverse system. The wall-normal velocity field (x-y direction) was obtained from vertical-PIV and horizontal-PIV measured spanwise velocity (x-z direction). Figure 3-10 shows the two laser-camera orientations that were used to measure the velocity field during the experiments.

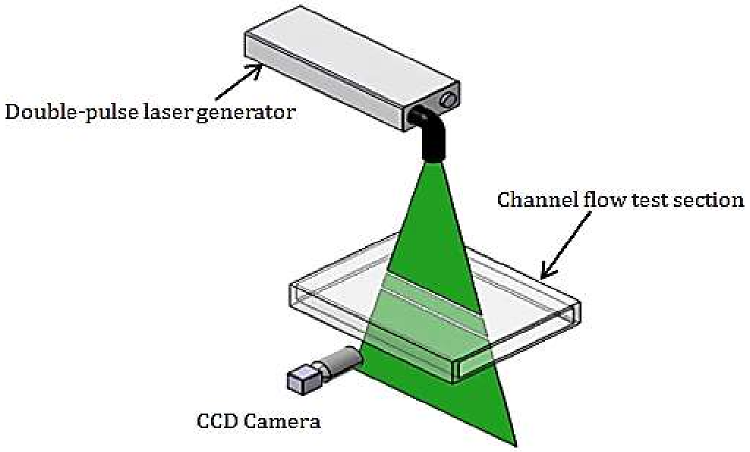

(a)

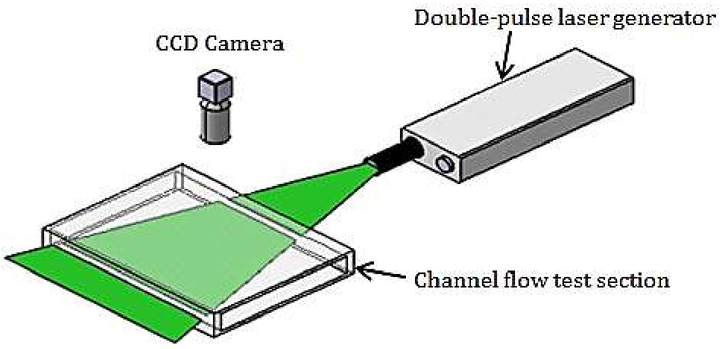

(b)

***Figure 3-10: The two camera-laser orientations for the PIV measurements: (a) vertical-PIV (x-y direction) and (b) horizontal-PIV (x-z direction).***

The following factors have been proven to contribute substantially to better results of Particle Image Velocimetry measurements: interrogation areas, calibration of CCD camera to determine the field of view (FOV), time between the two light pulses, the particle's fidelity to the flow, the position of the light sheet optics, and the position of the camera. Keane and Adrian (1990; 1991) and Raffel et al. (2007) have suggested certain rules of thumb for PIV measurements. They suggest that, for effective cross-correlation to be achieved, the number of seeding particles within one interrogation area must be within the range of 5 to 15. The authors also suggest that the highest displacement ($\Delta x$) of the seeding particles between the two frames, which is caused by the time between the two light pulses, must not exceed 25% of the width of the interrogation area, as this improves the process of thumbprint identification. It is also suggested that the diameter of the seeding particles be more than three pixels for accurate determination of displacement ($\Delta x$) of the seeding particles to be obtained. These suggestions were all applied to the experiments conducted here. The number of seeding particles between 8-10 guaranteed that they stayed within each interrogation area. However, it should be noted that, for unsteady flow measurements, the highest displacement ($\Delta x$) of the particles between the pulses can be massively different for the initial and final flow conditions, and this resulted in a challenge. And whilst the distribution of seeding particles within the interrogation area is uniform in an ideal situation, this is not the case in wall shear flows. To account for this, Keane and Adrian (1992) suggested that gradients in the flow must be calculated in accordance with Eq. (3.1) below:

$$\frac{Mdt\Delta U_y}{d_{PIV}} < 0.03 \tag{3.1}$$

where $M$ is the magnification factor, $dt$ is the time between the two light pulses, $d_{PIV}$ is the length of the interrogation area and $\Delta \mathrm{U_y} = \left({}^{\partial \mathrm{U}}\!/_{\partial \mathrm{y}}\right)\left({}^{\mathrm{d_{PIV}}}\!/_{2}\right)$ is the velocity gradient. One effect of using this equation for calculation of gradients is that it limits the validity of measurements in the wall region location of high flow conditions. It has been shown that at high flow condition ($Re_b = 20000$), the flow measurements are considered valid when $\mathrm{y}^+ \geq 50$, $\mathrm{M} = 2.20$, interrogation area = 32 × 32 pixels and time between the two light pulses = 300μs. For a low flow condition ($Re_b = 2800$), flow measurements above $y^+ = 12$ are regarded as valid providing the value of magnification factor is 2.2 with interrogation area of 32 × 32 pixels and time between the two light pulses = 900μs. The time between the two light pulses used during the investigations of unsteady flows was equivalent to that of higher Reynolds number because of the late response associated with the stages of the transient flow.

There are several methods that can be used to analyse the displacement ($\Delta x$) of individual particles inside the interrogation areas. An adaptive correlation analysis method using an iterative procedure was applied to calculate the velocity vectors for all the investigations carried out in this current study. This is a multi-step process where the interrogation area size changes, as shown in Figure 3-11. With this method, velocity vectors were computed iteratively with an initial bigger interrogation area size, which then reduced to the final smaller interrogation area size. The number of refinements determined the number of iterations performed. The processing parameters of initial and final interrogation areas, overlap, number of refinements, peak validation, neighbourhood validation, and acceptance factor were selected during data analysis. For all the investigations carried out in both laser-camera orientations, the same size of the initial bigger interrogation area size (256×256 pixels) and final smaller interrogation area size (32×32 pixels) were used, with 3 being the number of refinements. By using a peak validation parameter for the adaptive correlation, spurious velocity vectors were detected and removed. Keane and Adrian (1992) showed that the peak validation, which is the ratio of the two maximum consecutive correlation peaks, must not exceed 1.2 or the vectors would be rejected. In this study, a peak validation of 1.15 and 50% overlap were set for vertical-PIV while a peak validation of 1.2 and 50% overlap were selected for horizontal-PIV. Moving average parameters, which are the neighbourhood, acceptance factor and iteration, were selected for the replacement of the spurious vectors. For all the investigations using vertical-PIV orientation, a moving average was performed on 3 × 3 neighbourhood vectors, an acceptance factor of 0.11, and 3 iterations. The moving average was performed on 5×5 neighbourhood vectors and an acceptance factor of 0.12 was used for all investigations involving horizontal-PIV orientation. The fields of view (FOV) for vertical-PIV and horizontal-PIV were $30.60 \times 30.60\ mm^2$ and $110 \times 110\ mm^2$, respectively.

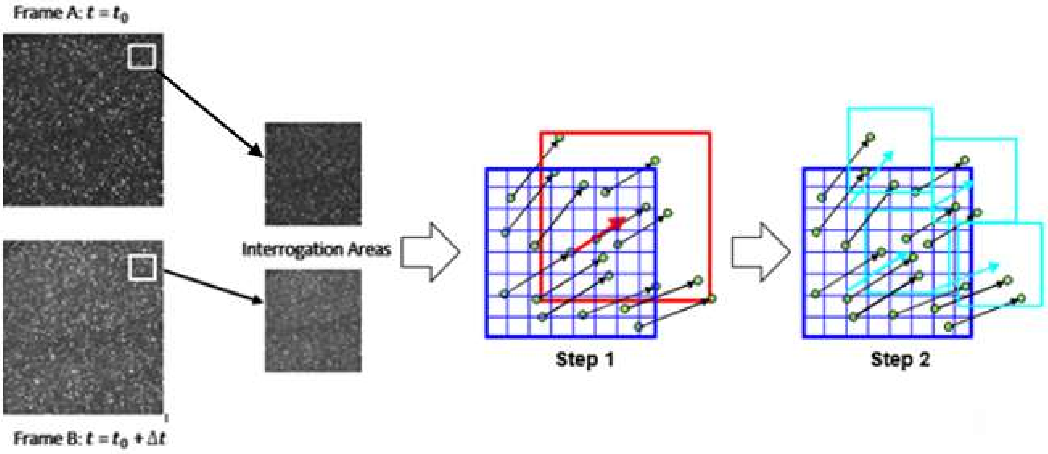

*Figure 3-11: Adaptive correlation method.*

## 3.7 Constant Temperature Anemometry (CTA)

Constant-Temperature Anemometry (CTA) is an intrusive measurement technique used for measuring velocity and wall shear stress in fluid flows. The usage of this technique can be traced to the late 1800s when scientists in the field of fluid mechanics built constant temperature anemometers that supplied a constant heating current to the sensor when the velocity of the flow varied in order to maintain constant sensor resistance and temperature during their experiments (Lomas, 1986). Although the benefits of constant temperature anemometers were recorded at this early stage, the highly stable and integrated-circuit amplifier was not supplanted with this technique until the mid-1960s (Weske, 1943; Ossofsky, 1948).

The working principle of constant temperature anemometry is illustrated in Figure 3-12. The technique is based on the cooling effect of a flow on a heated body. The two main components of constant temperature anemometer are Wheatstone bridge and a servo amplifier. The probe of the sensor is connected to one arm of the Wheatstone bridge. As the sensor is heated by the current, the servo amplifier helps to keep the bridge in balance by controlling the current to the sensor and causing the resistance and temperature of the sensor to remain constant. The rate of cooling of the sensor depends on the velocity of the flow and thus, an increase in velocity of the flow causes the temperature of the sensor to be cooled by the fluid, thereby causing the bridge to be unbalanced. A servo amplifier senses any imbalance in the bridge and stabilises it by increasing the sensor's heating current. The procedure continues throughout the experiment.

The Wheatstone bridge is used in different electronics packages. It outputs an error as the difference between a variable signal and a reference signal. The Wheatstone bridge configuration used in constant temperature anemometer of this current study consists of a bridge voltage $E$, an output current $i$, four resistors and one adjustable resistance. The bridge voltage, $E$, as shown in Figure 3-12, denotes the amount of heat transfer; and $i$ is an output current that is inversely proportional to the change in resistance of the sensor. Other variables include $R_k$, which is the operating resistance of the sensor, and $R_L$, which is the sensor cable resistance. Both $R_1$ and $R_2$ are known as the fixed resistances. The ratio of the fixed resistances ($R_1/R_2$) in the anemometer is referred to as the bridge ratio. ($R_3$), which is the adjustable resistance, is varied to set the operating temperature of the sensor above the ambient temperature of the fluid. When the flow becomes unsteady, the temperature and sensor's resistance change. Due to the fluctuation of the flow conditions, the bridge becomes unbalanced and the bridge is balanced by increasing the sensor heating current. The difference between the error voltages $(e_1 - e_2)$ is equivalent to the corresponding change in the sensor resistance and forms the input to the operational amplifier. The error voltages across the bridge throughout the experiment is proportional to the fluid velocity (Lomas, 1986; Bruun, 1995).

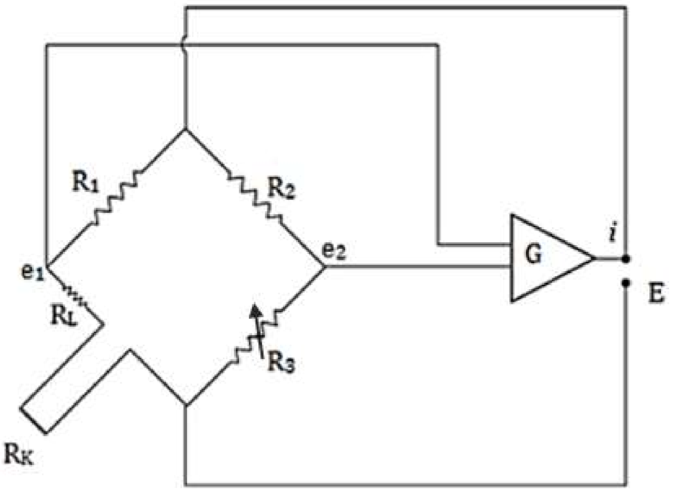

***Figure 3-12: Circuit diagram of a constant temperature anemometer.***

In this current study, skin friction measurements were taken in unsteady flow using a constant temperature anemometer. Winter (1977) first provided in-depth reviews of the four techniques by which skin friction can be obtained and outlined problems associated with each technique. Subsequently, Gasser, Thomann and Dengel (1993) provided a comprehensive study of the four techniques. The four techniques studied by the authors are as follows: 1) Clauser plot technique; 2) Preston tube method; 3) Surface fence method; and 4) Surface-mounted sensors. For this current study, the surface-mounted sensor technique was adopted.

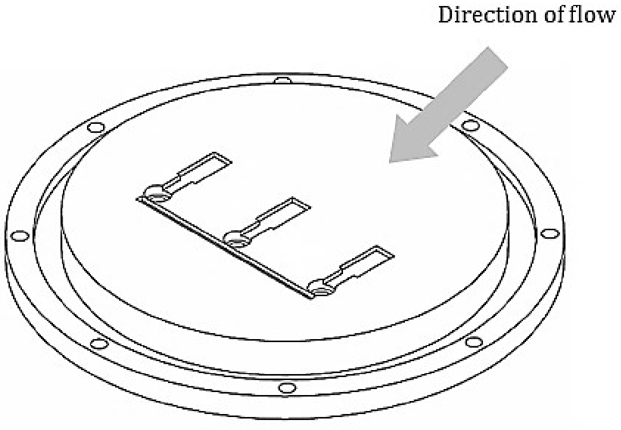

***Figure 3-13: Hot-film sensors panel.***

Figure 3-13 shows the top Perspex plate that has three pockets created in the mid-span for the installation of the three Dantec 55R48 glue-on probes. The plate was installed on the channel test session at a distance slightly greater than 7,850 $mm$ from the inlet of the test session.

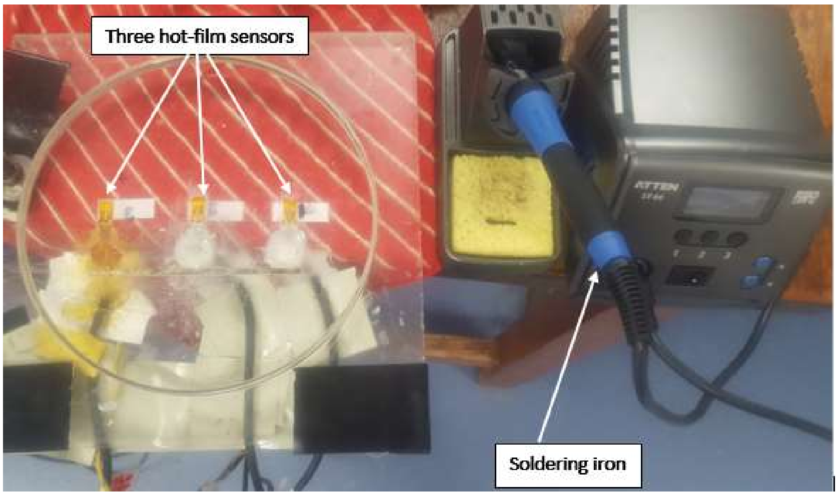

***Figure 3-14: Installation of hot-film sensors.***

Figure 3-14 shows the procedure for the installation of the three hot-film sensors (Dantec 55R48 glue-on probes) that were used for the measurement of instantaneous wall shear stress in this current study. The three Dantec 55R48 glue-on probes were installed in the pockets created on the mid-span of the top perplex plate 50 $mm$ apart. On the top of the Perspex plate, a groove for the 108 $mm$-long brass rods used to ground the probes was made. The size of the brass rod was reduced by machining so that it could be accommodated by the groove of

$2mm \times 1mm$. The Dantec 55R48 glue-on probes used in this current study are shown in Figure 3-15. They comprise a nickel heating film of dimensions $0.9mm \times 0.1mm \times 0.001mm$ which was deposited on a polyimide foil (resistant to wear and high temperature) of dimensions $8mm \times 16mm \times 0.05mm$. Each polyimide foil was glued onto the wall of the Perspex plate at the required measuring points of 50 $mm$ apart. For a protective coating, quartz coating of 5 $\mu m$ thickness was deposited over the film probes.

The film probes – copper wires of dimensions $0.7mm$ in diameter and 55 $mm$ long – were joined to the two nickel/gold-plated areas using a soldering iron (see Figure 3-14). A thin layer of Loctite 495, which is transparent, colourless and has a fast bonding time, was used to glue the hot-film sensors onto the surface of the Perspex plate. The leading copper wires of the probes were then joined to RG59 BNC cables using the soldering iron. The joints that were soldered were finally prevented from being exposed to working fluid (water) using Araldite.

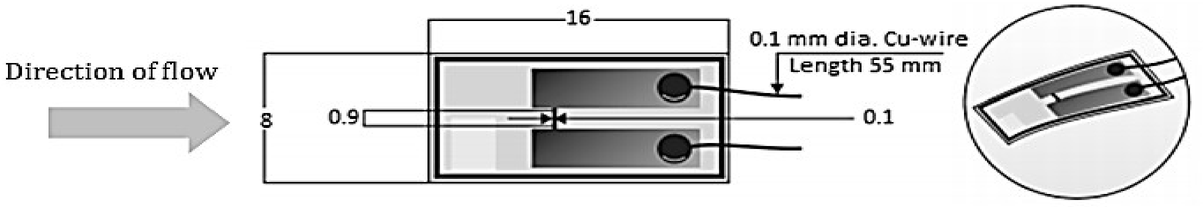

***Figure 3-15: Dantec 55R48 glue-on film probe (Dantec Inc).***

A Multichannel CTA system was used to provide measurements of instantaneous wall shear stress. This system consists of six velocity channels, a temperature channel, and a velocity reference channel. The Dantec Dynamics Multichannel CTA model with these features is the 54N81 Multichannel CTA. The bridge ratio of the Multichannel CTA system is 1:20 and the sensor resistance ranges between 4 Ω and 20 Ω.

In this current study, three hot-films sensors were installed but only two worked. Only one sensor was eventually used for the measurements of the instantaneous wall shear stress as the second sensor later stopped working. DIP switches of the Multichannel CTA were adjusted based on the MiniCTA overheat calculator spreadsheet from Dantec Dynamics. The values of sensor resistance, sensor lead resistance, sensor cable resistance, and sensosr temperature coefficient resistance provided from each hot-film sensor were input to the spreadsheet and the directions of the DIP switches were then automatically displayed. The output signal of the Multichannel CTA was connected to National Instruments Data Acquisition (DAQ) device.

The empirical correlation between skin friction and the rate at which heat transfers from a heated platinum strip embedded in a groove in a surface was derived by Fage and Falkner (1931) using a laminar boundary layer. Following this, Ludweig (1950) designed the first measuring device that used the analogy between flush-mounted skin friction sensors and heat transfer. The author used the heated element method for the shear measurement of turbulent flow and also obtained an analytical solution to the heat transfer equations that govern skin friction sensors. In later experiments, Leipmann and Skinner (1954), Bellhouse and Schultz (1966; 1968) and Menendez and Ramaprian (1985) obtained skin friction using the heated element method. Leipmann and Skinner (1954) stated that heat loss from the embedded sensor is proportional to the cube root of wall shear stress, and the constants of proportionality can be obtained by calibration. By assuming that the thermal boundary layer is within the laminar boundary layer, a statistically steady state analysis is represented by Eq. (3.2) below.

$$\frac{I^2\,R_k^2}{\Delta T} = A\tau_w^{1/3} + B \tag{3.2}$$

where $\Delta T$ is the temperature difference between the sensor element and the working fluid; A and B are calibration constants; $I$ is the heating current, and $R_K$ is the heating element resistance. If the sensor resistance is held constant and the heating current or voltage drop $E = IR$ is obtained (Goldstein, 1996). Eq. (3.2) can thus be re-written as follows:

$$E^2 = A\tau_w^{1/3} + B \tag{3.3}$$

An alternative Eq. (3.4) reported by He et al. (2011) and was found to relate the data better. As a result, this equation was adopted in this current study. The estimated wall shear stress values were fitted to the values of hot-film voltage from constant temperature anemometer for the determination of the calibration constants.

$$\log(\tau_w) = A' + B'E \tag{3.4}$$

where $A'$ and $B'$ are calibration constants. The constants $A'$ and $B'$ are obtained when the anemometer output voltage, $E$, of the CTA and the wall shear stress are known.

A dynamic calibration technique was used in this current study in order to calculate the calibration constants. The initial Reynolds number and final Reynolds number of the unsteady flows were maintained for 60 seconds each to attain steadiness and the output voltage of constant temperature anemometer was recorded. The output voltage at the steady flow rates together with the flow rates measured by flowmeter or integral of the PIV measurement was used for the calibration for that individual run. The wall shear stress for a particular flow rate was obtained using the relationship between the bulk Reynolds number and the Reynolds number based on friction velocity obtained using the DNS of He and Seddighi (2013), Abe, Kawamura and Matsuo (2001) and Moser, Kim and Mansour (1999) as shown in Figure 3-16. For each realisation, the wall shear stresses of initial and final Reynold numbers were dynamically determined from the power law that was obtained by curve fitting of DNS data in Table 3-1.

The procedure for calibration for a typical transient shown in Figure 3-17 is as follows:

1) Calculate the mean initial flow ($Re_0$) and final statistically steady flow ($Re_1$) based on flow rate obtained using PIV integration or flow meter;
2) Use Figure 3-16 to find the wall shear stress expected for these two flows ($\tau_{w0}$ and $\tau_{w1}$);

3) Calculate mean voltage readings from constant temperature anemometer (CTA) for the two flow rates ($E_0$ and $E_1$);
4) Substitute ($\tau_{w0}$ and $E_0$ ) and ($\tau_{w1}$ and $E_1$ ) to Eq. (3.4) to determine the calibration constants $A'$ and $B'$.

In the experiment, the wall shear stress $\tau_w$ for the transient flow was obtained using Eq. (3.4) with the $A'$ and $B'$ obtained in step (4) and the values of the output voltage were measured using CTA during the transient flow experiment.

Experimental challenges had to be overcome to ensure the repeatability of the results. One such was the ageing or pre-contamination of the flush-mounted skin friction sensors. According to Jimenez, Martinez-Val and Rebollo (1981), there is always a slight difference between data of the first realisation and the final realisation due to surface contamination. In this current study, the working fluid (water) was changed every three days to solve the problem of contamination of the hot-film sensors. The dynamic calibration of the hot-film sensors helped to reduce the error.

***Table 3-1: $Re_\tau$ and $Re_b$ obtained from direct numerical simulations (DNS)***

| $Re_b$ | $\mathrm{Re}_\tau$ | *DNS* |
|---|---|---|
| 2825 | 178.12 | (Moser et al., 1999) |
| 2825 | 178.6 | (He & Seddighi, 2013) |
| 2857 | 182 | (Lee & Moser, 2015) |
| 7404 | 418 | (He & Seddighi, 2013) |
| 6990.5 | 395 | (Abe et al., 2001) |
| 10000 | 544 | (Lee & Moser, 2015) |
| 20000 | 1000 | (Lee & Moser, 2015) |

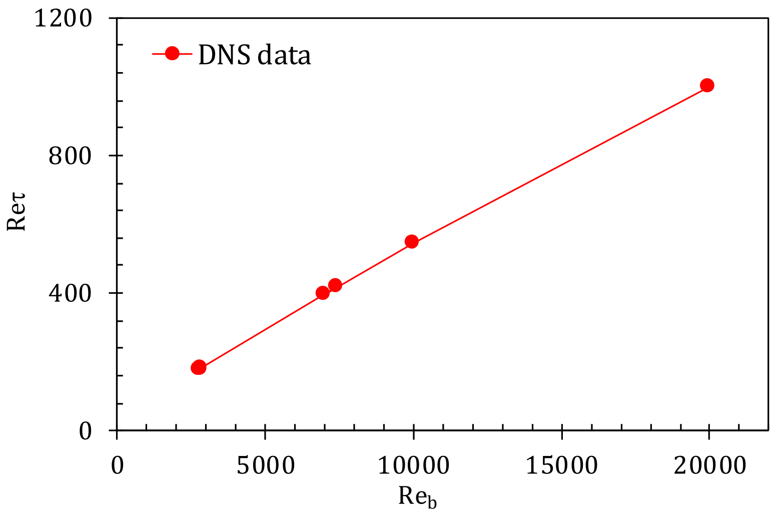

***Figure 3-16:Interpolation of friction Reynolds number and bulk Reynolds number for DNS data of Moser et al. (1999), Abe et al. (2001) and He and Seddighi (2013).***

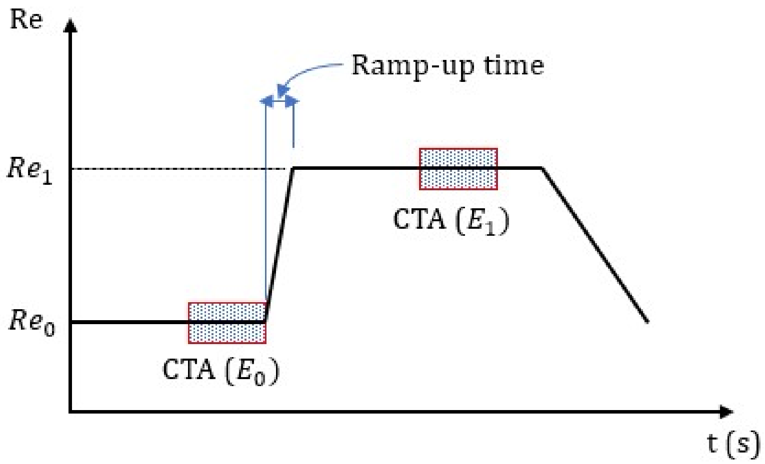

***Figure 3-17: The procedure for a dynamic calibration.***

## 3.8 Data processing

To determine streamwise mean velocity and turbulence statistics, ensemble, spatial and temporal averages were performed on the data obtained through PIV and CTA techniques. DynamicStudio software was used to obatin and process the raw images during vertical-PIV and horizontal- PIV measurements. The acquired and processed data were saved to the database of the DynamicStudio software in comma-separated values (CSV) format. To obtain the time-average quantities and their derivatives on the acquired data, MATLAB scripts were used to perform spatial, temporal and ensemble averages on the data that was saved in CSV format. LabVIEW software (version 18.0) and National Instruments DAQ card were used for the acquisition of the anemometer output voltage. The recording rate of the LabVIEW scripts was set to a frequency of 100 $Hz$. MATLAB codes were used to read the acquired data and calibrate the constant temperature anemometer (CTA) signal using the ensemble averaged velocity obtained from particle image velocimetry (PIV) for the determination of the unsteady wall shear stress. In this current study, the results of each case of the unsteady flows were obtained from 80 repeated experimental runs. The statistical quantities of unsteady data were then obtained from streamwise spatial and ensemble averaging. The equations used to obtain unsteady wall shear stress, Reynolds shear stress, r.m.s fluctuating velocities and streamwise mean velocity are shown below.

Unsteady wall shear stress is given by:

$$\bar{\phi}(t) = \frac{1}{K}\sum_{j=1}^{K}\phi(j,t) \tag{3.5}$$

where $K$ is the total number of repeated realisations used to perform ensemble average and $\phi(j,t)$ is the quantity at any time instant, t, for j<sup>th</sup> repeated realisation.

Averaged velocities are given by:

$$\bar{U}(p,t) = \frac{1}{KN}\sum_{l=1}^{K}\sum_{i=1}^{N}[u(i,l,p,t)] \tag{3.6}$$

$$\bar{V}(p,t) = \frac{1}{KN}\sum_{l=1}^{K}\sum_{i=1}^{N}[v(i,l,p,t)] \tag{3.7}$$

R.M.S fluctuating velocities are given by:

$$\overline{u'_{rms}}(p,t) = \sqrt{\frac{1}{KN}\sum_{l=1}^{K}\sum_{i=1}^{N}[u(i,l,p,t) - U(p,t)]^2} \tag{3.8}$$

$$\overline{v'_{rms}}(p,t) = \sqrt{\frac{1}{KN}\sum_{l=1}^{K}\sum_{i=1}^{N}[v(i,l,p,t) - V(p,t)]^2} \tag{3.9}$$

Reynolds shear stress is given by:

$$\overline{u'v'}(p,t) = \frac{1}{KN}\sum_{l=1}^{K}\sum_{i=1}^{N}[u(i,l,p,t) - U(p,t)].[v(i,l,p,t) - V(p,t)] \tag{3.10}$$

where $K$ is the total number of data points in the x-direction, p is any location in the y-direction, and $N$ is the number instants of time utilised for temporal-averaging for statistically steady state cases or the number of repeated realisations for ensemble-averaging for unsteady flow cases.

## 3.9 Steady and unsteady data acquisition

For the purpose of this current study, a removable panel that contained three hot-film sensors was installed at a location slightly above 7850 mm downstream of the inlet of the channel. Hot-film sensors controlled by constant temperature anemometry (CTA) were used to measure wall shear stress of transient flows during the experiments. Measurements of mean and turbulence statistics using particle image velocimetry (PIV) were obtained at a distance of 87.5 $mm$ ($3.5\delta$) from the edge of the channel width (w), where $\delta$ is the half-height of the channel, the dimension of the height ($h$) of the channel was 50 $mm$, and the channel width was 350 $mm$. The distance of 87.5 $mm$ from the edge of the channel width (w) was chosen for laser sheet in order to attain better resolutions of all the wall-normal measurements (Gorji, 2015). During the vertical-PIV orientation experiments, the camera was attached to the traverse system and the laser was fired from the top of measuring section of the channel, as shown in Figure 3-18. Care was taken to ensure that the camera was perpendicular to the laser sheets during experiments. If the laser sheets and camera were not perpendicular, the entire results would have been error-strewn. The reverse was the arrangement during the

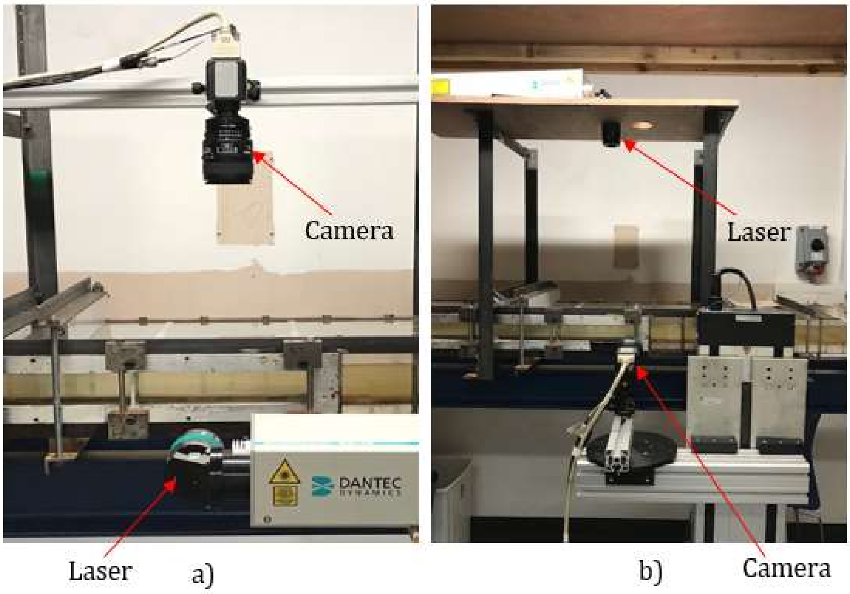

***Figure 3-18: Laser-Camera orientation photos (a) horizontal-PIV and (b) vertical-PIV.***

horizontal-PIV orientation experiments where the laser was attached to the traverse system and the camera was attached to the hanger installed on top of the wall of the measuring section as presented in § 3.6.

## 3.10 Steady flow comparison

Three cases of statistically steady turbulent flow experiments were carried out and the results obtained from the measurements are here compared with the direct numerical simulations (DNS) results of Lee and Moser (2015), as shown in Table 3-2. The experimental data obtained, and DNS data are in close agreement. The three experimental cases studied are $Re_b = 2826$ *(K1)*, $Re_b = 10459$ *(K2)* and $Re_b = 20890$ *(K3)* which have been compared with the Lee and Moser' (2015) simulation at $Re_\tau = 182$, $Re_\tau = 544$ *and* $Re_\tau = 1000$. The authors referred to $\mathrm{Re}_\tau = 182$, 544 and 1000 as LM 180, LM 550 and LM 1000, respectively. The Reynolds numbers, $Re_b(= \frac{U_b\delta}{v})$, where $U_b$ is the bulk velocity and $\delta$ is the half-height of the channel. Friction Reynolds number was calculated as $Re_\tau(= \frac{u_\tau\delta}{v})$ where $u_\tau$ is the friction velocity, $y$ is the distance from the wall, and $v$ is the kinematic viscosity of the working fluid. The streamwise mean velocity ($U$), streamwise fluctuating velocity ($u'_{rms}$), wall-normal fluctuating velocity ($v'_{rms}$) and turbulence shear tress ($\overline{u'v'}$) of the outer scaled profiles are normalised by centreline velocity ($U_c$) while the distance from the all is normalised by half-height of the channel ($\delta$), as shown in the Figure 3-19. It is clear from the analysis of the data the experimental data in the region $y/_\delta < 0.045$ are not dependable.

***Table 3-2: $Re_\tau$ obtained from the experiments and that of Lee and Moser (2015)***

| Case | $Re_b$ | U<sub>b</sub> (m/s) | $(\overline{u'v'})$ $Re_\tau$ | Log law $Re_\tau$ | Lee & Moser $Re_b$ | Lee & Moser $Re_\tau$ |
|---|---|---|---|---|---|---|
| K1 | 2826 | 0.115 | 179 | 193 | 2857 | 182 |
| K2 | 10459 | 0.414 | 558 | 571 | 10000 | 544 |
| K3 | 20890 | 0.860 | 989 | 1044 | 20000 | 1000 |

Accurate measurement of wall shear stress during steady channel flow experiments is difficult using particle image velocimetry (PIV) due to the large velocity gradients near the wall. The wall shear stress can be obtained by utilising one of the indirect methods suggested below.

Blasius' law of friction can be written as:

$$C_f = \frac{0.079}{(4Re_b)^{0.25}} \tag{3.11}$$

where $Re_b$ *is* the bulk Reynolds number and $C_f$ is the skin friction coefficient.

Dean (1978) has suggested another empirical method to calculate the skin friction coefficient as follows:

$$C_f = \frac{0.073}{(4Re_b)^{0.25}} \tag{3.12}$$

The wall shear stress and skin friction coefficient are related in the equation below:

$$2 * \left(\frac{u_\tau}{U_b}\right)^2 = C_f = \frac{2\tau_w}{\rho {U_b}^2} \tag{3.13}$$

where $\rho$ is the density of the working fluid, $u_\tau$ is the friction velocity, $C_f$ is the skin friction coefficient, and $\tau_w$ $(= u_\tau^2\rho)$ is the wall shear stress.

Other indirect methods for obtaining wall shear stress in channel and pipe flows are by curve-fitting of streamwise mean velocity profiles in the viscous sublayer of the flow or line-fitting of the curve of the turbulence shear stress in the core region of the flow, as suggested by Durst et al. (1996) in order to obtain the friction velocity $(u_\tau)$. In the viscous sublayer of the flow, $y^+ \leq 5$.

$$U^+ = y^+ \tag{3.14}$$

where $U^+ = \frac{\bar{U}}{u_\tau}$ and $y^+ = \frac{u_{\tau * y}}{v}$

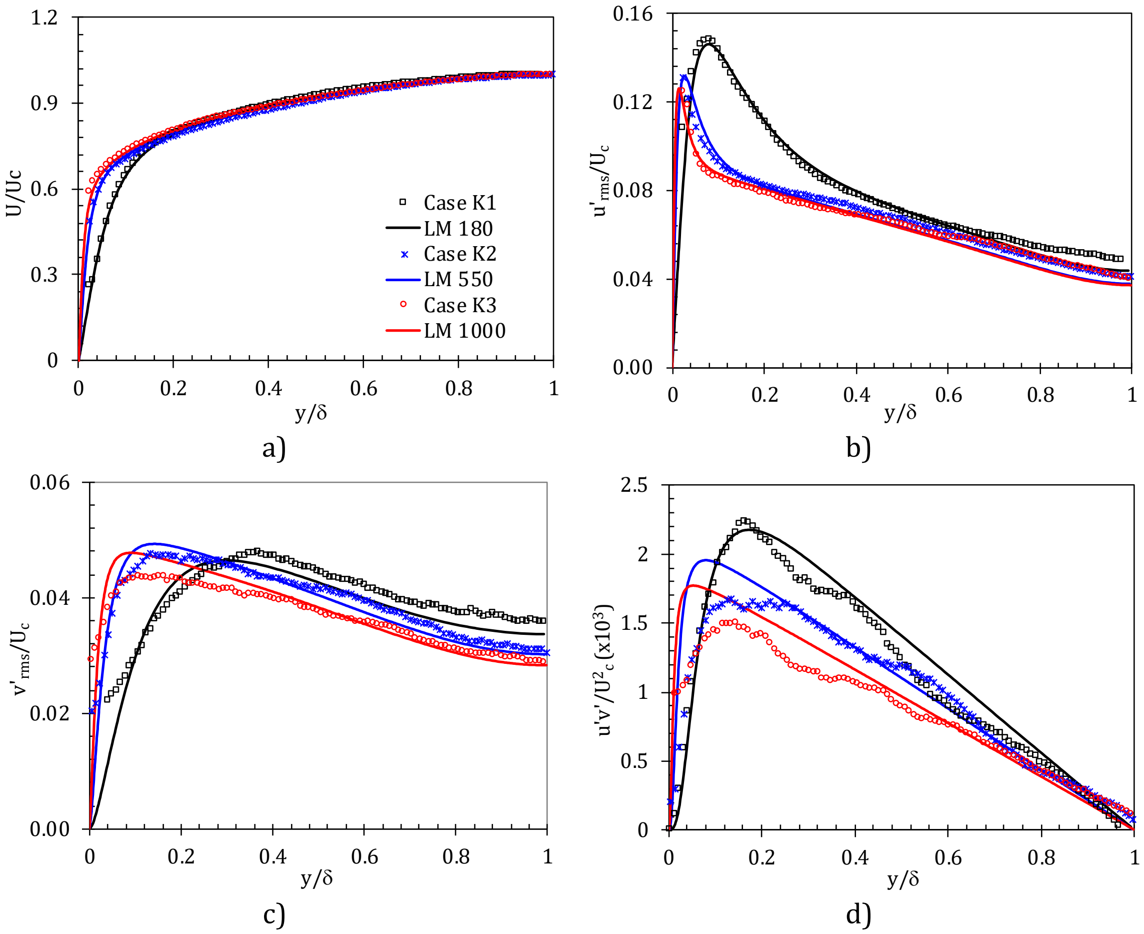

***Figure 3-19: Comparison of outer scaled vertical-PIV measurements at $Re_b$ =2826, 10469 and 20890 with the DNS Data of Lee and Moser (2015) of $Re_b$=2857, 10000 and 20000.***

The friction velocity ($u_\tau$) can also be obtained from the polynomial curve-fitting of streamwise mean velocity profile in the buffer region ($5 < y^+ < 30$) of the flow, as presented by Spalding (1961) and Musker(1979). This method requires velocity measurement in the wall region where the velocity gradient is high. In this current study, data acquisition in a location in the near wall could not be obtained due of high velocity gradient.

Polynomial curve fitting of the streamwise mean velocity in the logarithmic region of the flow can also be used to obtain the friction velocity. Wall shear stress is then determined in the logarithmic region of the flow where $y^+ > 30$ (von Kármán, 1930).

$$U^+ = \frac{1}{k}\ln(y^+) + C \tag{3.15}$$

Eq. (3.15) can be re-written as follows:

$$\frac{\bar{U}}{u_\tau}=\frac{1}{k}\ln(\frac{u_{\tau*y}}{v})+C \tag{3.16}$$

where $k$ and $C$ are empirical constants. The accepted values of $k$ and $C$ for the channel flow are 0.41 and 5.17, respectively.

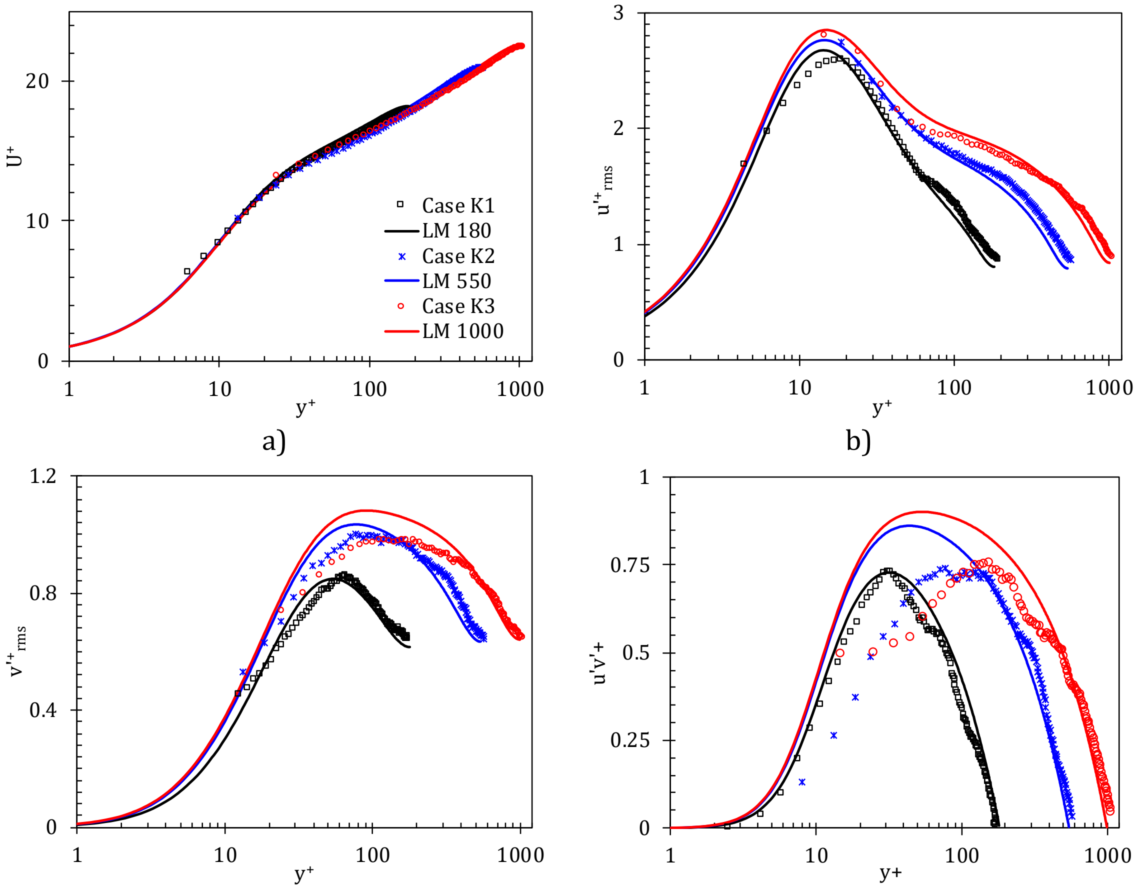

a) b)

c) d)

***Figure 3-20: Comparison of inner scaled vertical-PIV measurements at $Re_b$ = 2826, 10469 and 20890 with the DNS Data of Lee and Moser (2015)of $Re_b$=2857, 10000 and 20000.***

In this current study, the friction velocity was obtained using DNS interpolation of Figure 3-16. Friction velocity can alternatively be obtained in square form when the Reynolds stress $(\overline{u'v'})$ in the centre region of the flow is linearly extrapolated in the direction of the wall. Additionally, the friction velocity was obtained from curve fitting of streamwise mean velocity profile in the logarithmic region of the flow. The values of friction Reynolds number calculated from the friction velocities obtained from the three methods are shown in Table 3-1. Figure 3-19 shows the comparison of experimental data and the DNS data for outer-scaled flow profiles. In a comparison of streamwise mean velocity $(U)$ and root mean square streamwise velocity $(u'_{rms})$ of the experimental results with the direct numerical simulation results, there is a close agreement. However, the experimental data of wall-normal fluctuating velocity $(v'_{rms})$ and Reynolds shear stress $(\overline{u'v'})$ agree with the DNS data except that the experimental data fails to follow the trend of the direct numerical simulation data in a region close to the wall for cases K2 $(Re_b = 10469)$ and K3 $(Re_b = 20890)$. At the low Reynolds number (K1) there is a small difference between the wall normal fluctuating velocities $(v'_{rms})$ of the experimental data and the direct numerical simulation. This difference is partly to low pulsation frequency $(Hz)$ of the laser utilised during the experimentation. The inner-scaled flow profiles in Figure 3-20 were normalised by the friction velocity $(u_\tau)$ obtained from the log-law curve fitting, and the normalised wall distance $y^+$ was calculated as $\frac{u_{\tau*y}}{v}$. The trends of the inner-scaled follow the DNS data except that of Reynolds shear stress for case K3 $(Re_b = 20890)$. The slight deviation between DNS and experimental data is due to camera's resolution. Finally, the friction velocity$(u_\tau)$ obtained through the log-law is higher than that the value of friction velocity $(u_\tau)$ through the Reynolds stress $(\overline{u'v'})$ extrapolation. .The repeatability of the three steady cases is better than 3.5%.

### 3.10.1 Investigations to determine time between the two light pulses

A series of measurements with different time between the two light pulses were carried out in order to select the best time between the two light pulses for each flow condition and for the results to be used in the optimisation of steady and unsteady flows measurements. In the unsteady flows, the initial and final flow conditions vary and the best time needs to be chosen for good transient flow results to be obtained.

***Table 3-3: PIV measurements at different time between the two light pulses and Reynolds numbers***

| Case | $Re_b$ | U<sub>b</sub> (m/s) | DNS (Interpolation) | (u′v′) $Re_\tau$ | Log law $Re_\tau$ | $t$ (μsec) |
|---|---|---|---|---|---|---|
| S1 | 2813 | 0.098 | 179 | 167 | 191 | 400 |
| S2 | 2841 | 0.104 | 186 | 164 | 198 | 600 |
| S3 | 2818 | 0.101 | 185 | 158 | 197 | 800 |
| S3 | 2826 | 0.115 | 186 | 163 | 198 | 900 |
| S5 | 2792 | 0.098 | 184 | 177 | 190 | 1100 |
| SS1 | 20890 | 0.860 | 1025 | 989 | 1044 | 300 |
| SS2 | 19514 | 0.834 | 966 | 957 | 1016 | 400 |
| SS3 | 19447 | 0.830 | 963 | 969 | 1013 | 500 |
| SS4 | 19448 | 0.831 | 963 | 1000 | 1012 | 600 |

All the test cases in Table 3-2 were carried out at the same field of view (FOV) of 30.6 $mm \times$ 30.60 $mm$ with a trigger frequency of 2 $Hz$. Measurements of the test cases were taken from two different Reynolds numbers. The initial and final Reynolds number of the transient flow of the current study were close to the Reynolds numbers of the test cases. The results obtained from the tests are shown in Figure 3-21 and Figure 3-22.

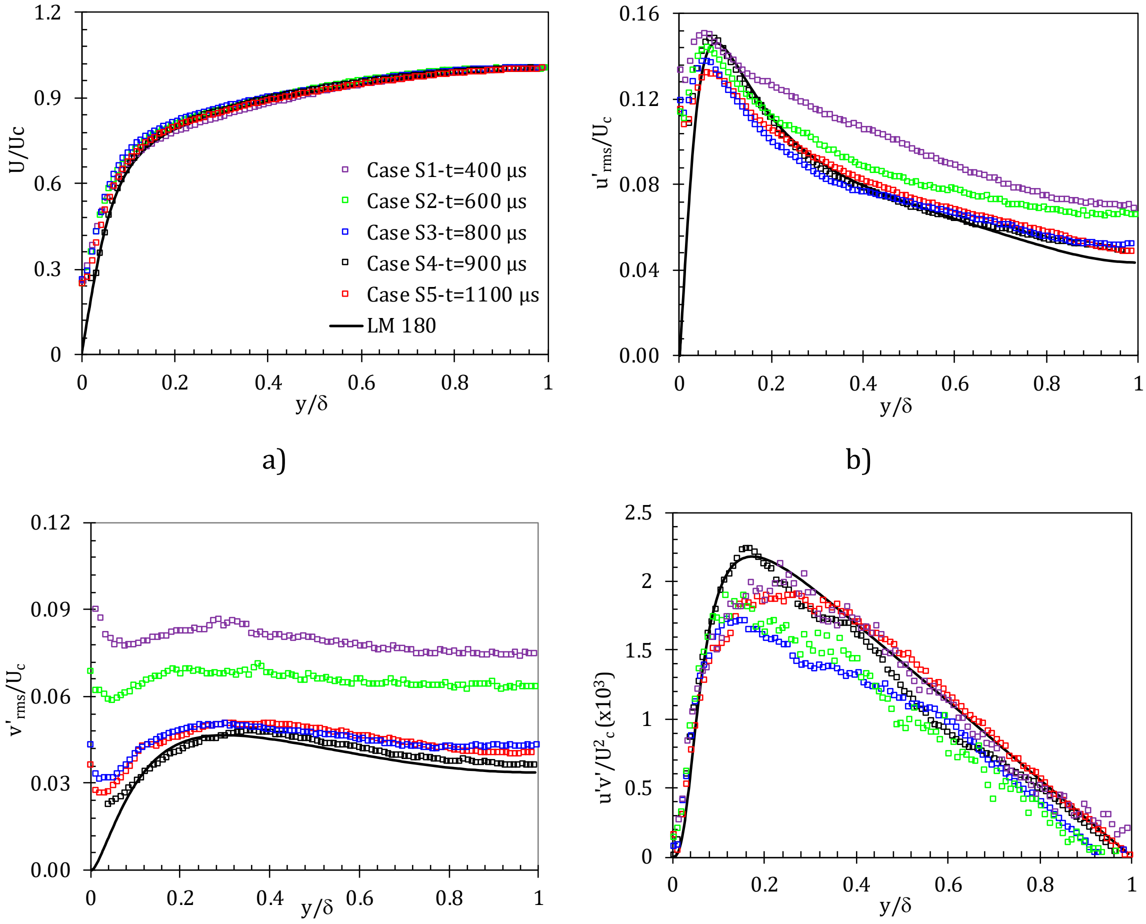

a) b)

c) d)

***Figure 3-21: PIV measurements at different times between the two light pulses for $Re_b$~2800. Legend is the same for the four subplots.***

For the low Reynolds number cases, the streamwise mean velocity profiles follow the tread of the DNS data of Lee and Moser (2015). The data of the three cases with higher times between the two light pulses agrees with the streamwise fluctuating velocity of DNS data while the two cases with the lower time between the two light pulses of 400 $\mu s$ and 600 $\mu s$ overshot at both core and wall of the channel. The same two data of the lower time between the two light pulses of400 $\mu s$ and 600 $\mu s$ overshot the DNS data of wall-normal fluctuating velocity. It is revealed from the analysis that wall-normal fluctuating velocity is very sensitive to the choice of time between the two light pulses. The data of time between the two light pulses of 900 $\mu s$ follows the trend of Reynolds shear stress, streamwise fluctuating velocity, wall-normal fluctuating velocity and streamwise mean velocity profiles of the DNS data perfectly compared to other low Reynolds number cases investigated. In this current study, the best time found between the two pulses for the low statistically steady turbulent test case is 900 $\mu s$.

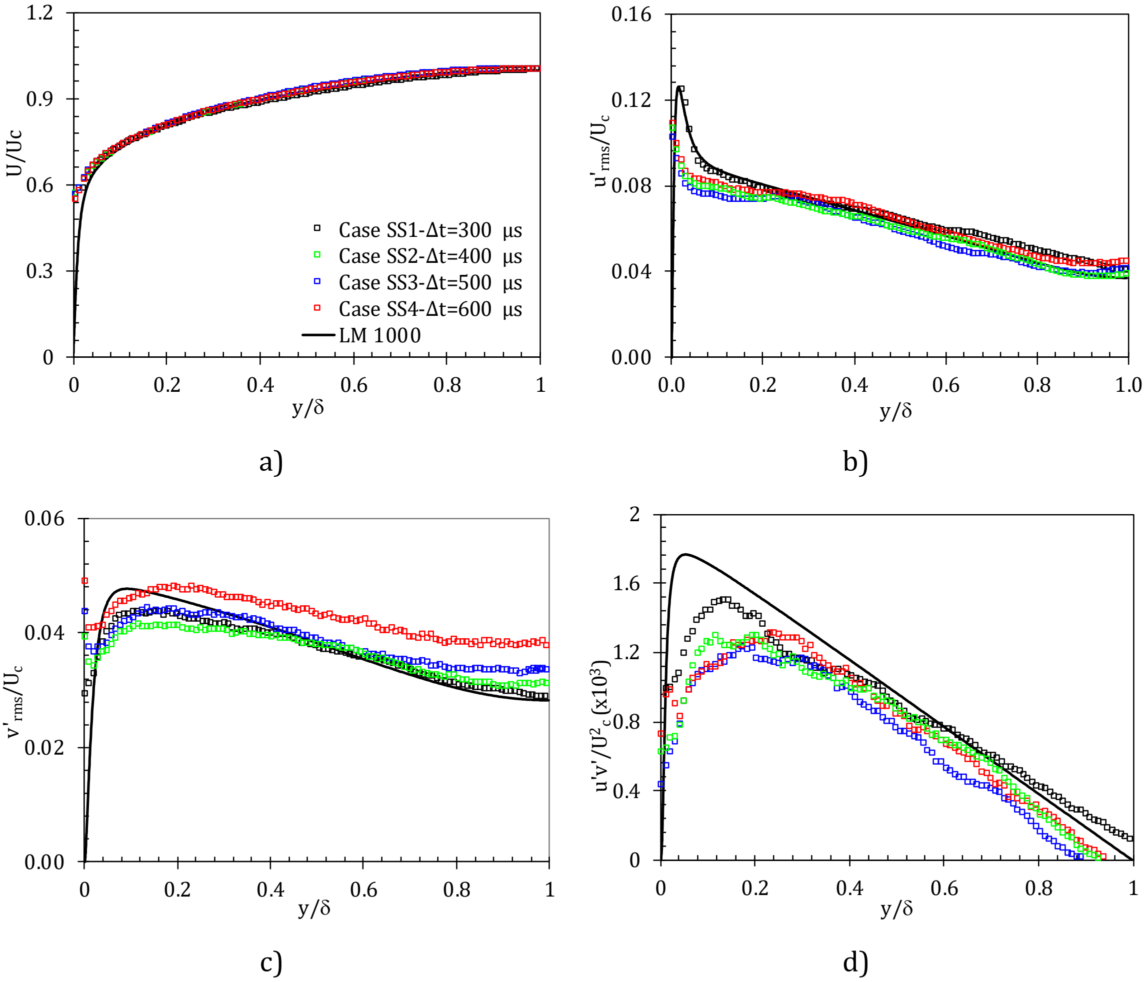

***Figure 3-22: PIV measurements at different time between the two light pulses for $Re_b$~20000.***

There were four test cases investigated for a higher Reynolds number of approximately $\mathrm{Re_b} \approx 20000$. The best time between the two light pulses is vital as if a wrong time is chosen, all results will be in error. The time between the two light pulses determines the quantities of seeding particles in the interrogation area size for a better cross-correlation, as discussed in § 3.5.5. The responses of time between the two light pulses of $300, 400, 500\ and\ 600\ \mu s$ were investigated on $\mathrm{Re_b} \approx 20000$ and the results compared with the DNS data of Lee and Moser (2015). The data of time between the two light pulses $= 300\ \mu s$ is the best among all the cases investigated as it follows the DNS data. The sensitivity of wall-normal fluctuating velocity to the choice of the time between the two light pulses is also revealed. At the higher time between the two light pulses of 600 $\mu s$, fewer seeding particles were captured by the frames for cross-correlation and the data overshoots that of DNS. For a higher flow rate, the time between the two light pulses must be small for a range of 5 and 15 seeding particles to be within the interrogation. It has been suggested by Keane and Adrian (1990; 1991) and Raffel et al. (2007), for a strong cross-correlation to be attained on PIV measurements, the range of seeding particles within the interrogation area should be between 5 and 15.

The right choice of time between the two light pulses is important in PIV measurements and it must be chosen correctly for every flow condition; otherwise, all results will be in error. It is revealed from Figure 3-21 that 900 $\mu s$ is the best time between the two light pulses for the lower Reynolds number test cases investigated while 300 $\mu s$ is the best for all the higher Reynolds number test cases, as shown in Figure 3-22. During the flow acceleration, the initial flow condition is different from the final flow condition and this becomes a significant challenge in the choice of the best time between the two light pulses. This current study is concerned with the procedure of transition of transient channel flow. The best time (300 $\mu s$) reported for the higher Reynolds number test case was utilised for all the transient cases investigated due to late response associated with stages of transient flow.

## 3.11 Comparison of transient turbulent flows in channel

The transient turbulent flow of this current study is compared with Mathur's (2016) case E2 ($Re_b$=2800-15500) to check the precision of the experiments. It is advisable to check the repeatability of the investigations because uncertainties in measurements are inevitable. At the new location, the rig was redesigned, and different investigations were carried out. The case N1 ($Re_b$=2759-14973) of the current study was compared with the case E2 ($Re_b$=2800-15500) of Mathur (2016) that was obtained at the old location of the rig (Mappin Building, the University of Sheffield). The comparison of the two flow cases was done to check the repeatability of the experimental rig in the new location. During the experiments, transient flow was produced due to sudden opening of the pneumatic control valve. As the initial flow was increased suddenly to the final flow condition, an acceleration period was obtained. This time is equivalent to the time of 90% of the final stage of the flow. For the current case N1 ($Re_b$=2759-14973), the acceleration period was 2.12 seconds and that of Mathur's (2016) case E2 ($Re_b$=2800-15500) was reported as 1.90 seconds at 80% of the final stage of the flow.

***Table 3-4: Transient flow of present N1 case in comparison with Mathur (2016)'s case E2***

| | Case | $Re_0$ | $Re_1$ | $U_b$ $(^m/_s)$ | $\Delta t$ $(s)$ | $t_{cr}(sec)$ | $t_{turb}(sec)$ |
|---|---|---|---|---|---|---|---|
| Present | N1 | 2759 | 14973 | 0.10-0.54 | 2.12 | 1.82 | 2.82 |
| Mathur (2016) | E2 | 2800 | 15500 | 0.11-0.64 | 1.90 | 2.05 | 3.30 |

*Note: Acceleration period ($\Delta t$) is defined here to the amount of time for an initial bulk velocity ($U_{b0}$) to reach 90% of the final bulk velocity ($U_{b1}$).*

The results of the current case N1 ($Re_b$=2759-14973) are consistent with that of case E2 ($Re_b$ =2800-15500). The responses of the two flows were observed at the same wall location, as shown in Figure 3-23, but there are slight variations. These variations are due to the difference in time period and the slight difference in the initial and final Reynolds numbers. Moreover, the two investigations were carried out at different temperatures. The resemblance of the two flows shows the duplicability of unsteady flow using the experimental rig at the new location.

Another area of analysis was the repeatability of the constant temperature anemometry (CTA) with hot-film sensors. The development of skin friction coefficient ($C_f$) of the current case N1 ($Re_b$ = 2759-14973) and that of case E2 ($Re_b$ = 2800-15500) were compared. When the transient flow was initiated in both cases, the skin friction coefficient ($C_f$) increased rapidly in fractions of a second to its maximum value before decreasing to its minimum value. It then increased again and approached the statistically steady state. The responses of the skin friction coefficient in the two flows are consistent, as shown in Figure 3-24. The slight variations are due to the differences in the transient flow period, initial Reynolds number, final Reynolds number and temperature.

It can be concluded that the responses of the two flow cases using flow development at the different wall locations and skin friction coefficient ($C_f$) provide evidence of duplicability of unsteady flow using the experimental rig at the new location.

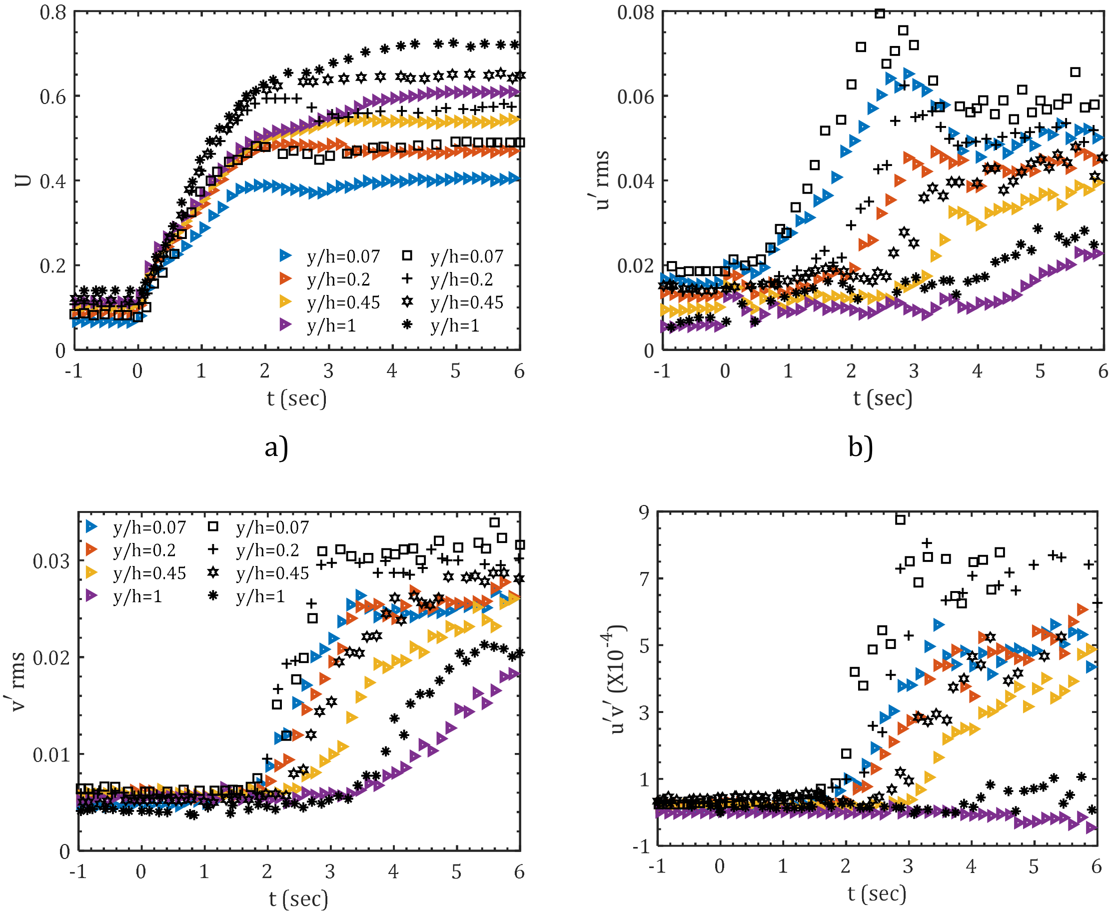

a)
b)
c)
d)

***Figure 3-23:Flow development comparison of case N1 ($Re_b$ = 2759-14973) with Mathur 's (2016) case $Re_b$ = 2800-15500. The present case's symbols are in colour and Mathur's (2016) case E2 symbols are in black. The half-channel height, $h = \delta$.***

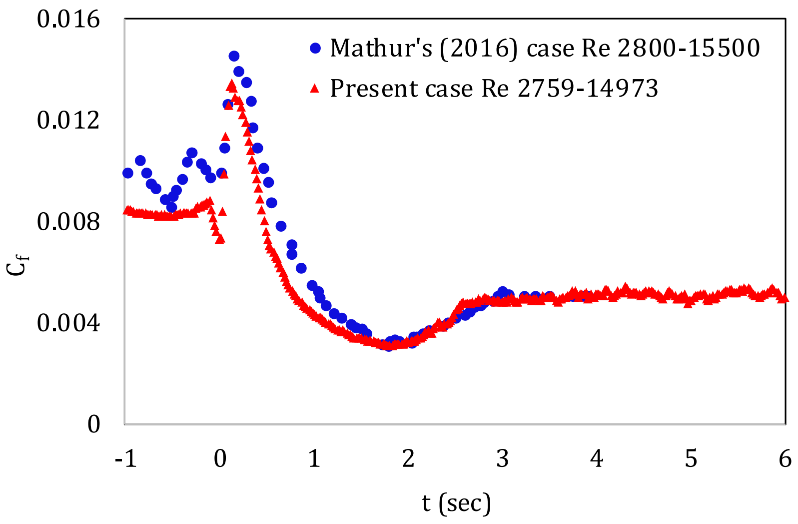

***Figure 3-24: Comparison of skin friction coefficient the present case N1 with Mathur's (2016) cases $Re_b$ = 2800-15550.***

## 3.12 Uncertainty analysis in repeated measurements

Experimental uncertainty determines the amount of errors that might be in measurements; all measurements are subject to different levels of uncertainty that may come from a range of sources during experiments. No matter how carefully the measurement is taken, it cannot be completely free from such uncertainties. These different levels of uncertainty can be classified as one of the following two types: the uncertainty associated with measured values, and that associated with the measuring equipment. The estimation of uncertainty in measured values and measuring equipment can be obtained using error analysis or uncertainty analysis. In order to evaluate experimental uncertainty in measurements, the errors between the measured values and accepted values must be assessed by determining the accuracy and precision of the measurements, with accuracy depending on the degree to which the measured values and the accepted values agree and precision showing the degree of agreement of repeated measurements. In order to access the repeatability and uncertainty of the current study, two means were used:

1) The measurements were compared with reference data (Lee & Moser 2015);
2) The repeatability was assessed directly, as shown below.

Experimental data of this current study was compared with DNS data. Since the accepted values could not be known, the determination of the accuracy was impracticable. The repeatability of the present experimental data was established under the same measuring procedure, measuring equipment and conditions for both steady and unsteady flows. This was achieved by calculating the standard deviation ($\sigma$) of the bulk velocity (an estimate of uncertainty in measurements), ($U_b$) from multiple realisations measured by particle image velocimetry (PIV) system, and constant temperature anemometry (CTA). The uncertainty in the flow measurements under steady and unsteady conditions was calculated using Eq. (3.17).

$$\sigma = \sqrt{\frac{\sum \delta x_i^2}{N}} \tag{3.17}$$

*where* $\delta x_i = x_i - \bar{x}$*, for i = 1, 2, 3, 4, 5,…N.*

The repeatability of the Particle Image Velocimetry (PIV) system was obtained by calculating the standard deviation of the bulk velocity ($U_b$) on 120 images captured by Charge-Coupled Device (CCD) camera. The statistically steady data acquisition was carried out at a frequency of 2 $Hz$ for 60 seconds. As is shown in Figure 3-25, the uncertainty of the PIV system for all statistically steady data is below 3.5%.

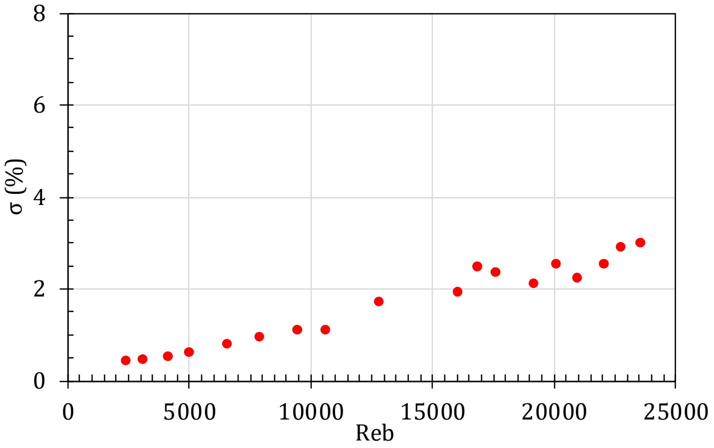

***Figure 3-25: Repeatability of bulk velocity of stationary flows against Reynolds numbers.***

Standard deviation was calculated on 80 realisations of time-average data to determine the repeatability of the control valve. The repeatability of the statistically steady data is better than 2%, as shown in Figure 3-26. This shows that the control valve produced almost the same flow.

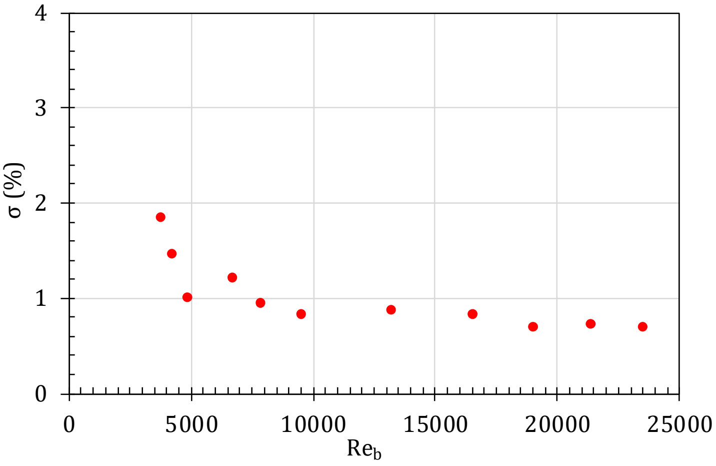

***Figure 3-26: Repeatability of bulk velocity of several realisations against Reynolds numbers.***

The repeatability of statistically steady data obtained through hot-film method is presented in Figure 3-27. Standard deviation was calculated on bulk velocity ($U_b$) obtained at different flow conditions and at frequency of 100 $Hz$. The duration of data acquisition for each flow condition was 80 seconds and it is clear from the results that the repeatability of the hot-film measurements for stationary flow is better than 1%.

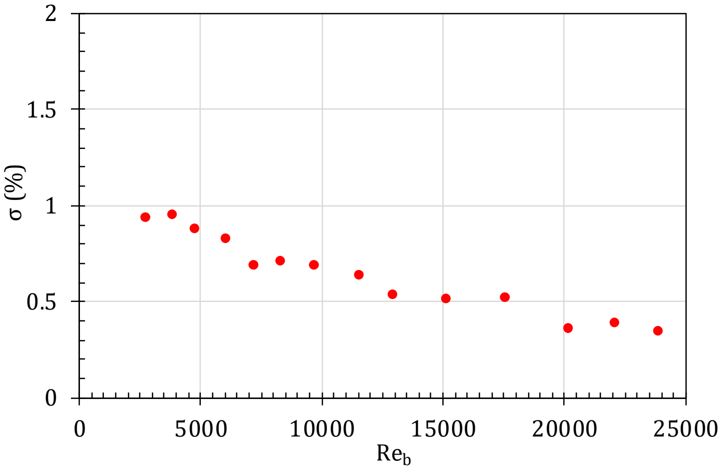

***Figure 3-27: Repeatability of bulk velocity of hot-film measurements for stationary flow against Reynolds numbers.***

Standard deviation was calculated on 20 different realisations of time-averaged of hot-film measurements to determine the repeatability of the stationary flow at different flow conditions and at frequency of 100 $Hz$. It is shown in Figure 3-28 that the repeatability of the hot-film measurements is better than 20% for several realisations. The poor repeatability can be attributed to dirt in the working fluid (water) and drift in calibration constants. In this measuring technique, a dynamic method that used different calibration constants for each repeated run was employed.

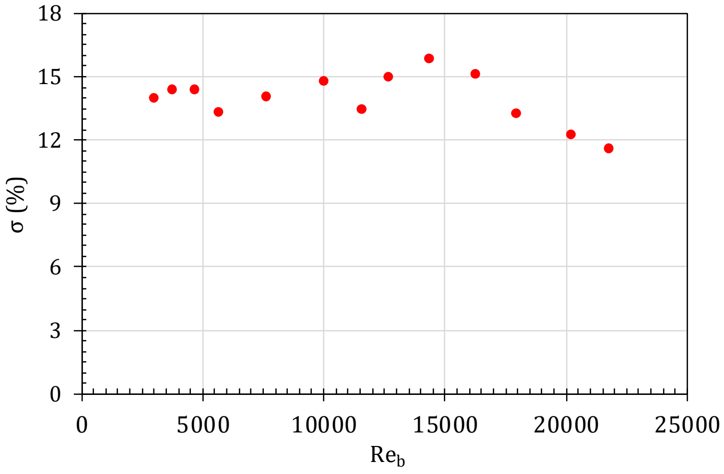

***Figure 3-28: Repeatability of bulk velocity of hot-film measurements for several realisations against Reynolds numbers.***

## 3.13 Summary

This chapter provides a full description of the experimental channel flow facility, flow control, particle image velocimetry (PIV), constant temperature anemometry (CTA) and data processing. Uncertainty analysis is performed on the repeated measurements to determine the repeatability of the data obtained from PIV and CTA. The statistically steady turbulent data is compared with the data of Lee and Moser (2015). The data of the transient turbulent channel flow is compared with the case E2 of Mathur (2016) to test the repeatability of the measurement equipment. A dynamic calibration technique is adopted to calculate the calibration constants. The detailed description of how to obtain the calibration constants is discussed and the results from all experiments are presented in the next chapters.

## Chapter 4

# Turbulent to Turbulent Transition in Rapidly Accelerating Flows

---

## 4.1 Introduction

In this chapter, the experimental investigation of the response of turbulence in transient turbulent flow using Particle Image Velocimetry (PIV) and Constant Temperature Anemometry (CTA) techniques is presented. Turbulent flow in a statistically steady state is accelerated rapidly to the final flow condition using pneumatic control valve. During this ramping up period, data is recorded using a Constant Temperature Anemometer and DynamicStudio of Particle Image Velocimetry. The data acquired from PIV is saved in a comma-separated value (csv) format and that of CTA is saved in a LabVIEW measurement (lvm) file. The saved files in csv and lvm are exported to MATLAB for post processing. Moreover, both spatial and ensemble averaging are performed for 80 repeated experimental runs for the determination of streamwise mean velocity and turbulence statistics for each case of transient turbulent flow studied. Experimental cases of accelerating turbulent flow from initial flow condition to a higher one are presented. First, initial Reynolds numbers are varied while the final Reynolds number is fixed. Second, the initial Reynolds number is fixed while the final Reynolds numbers are varied. The Reynolds number at which transition to turbulence occurs is known as the critical Reynolds number. In flat plate boundary layer flow, it has been shown that the value of the transitional Reynolds number depends on Free-Stream Turbulence ($FST$) (Andersson et al., 1999; Brandt et al., 2004; Fransson et al., 2005). He and Seddighi (2015) have shown that in a boundary layer that develops temporally, the critical Reynolds number also depends on $FST$ which exhibits as initial turbulence intensity. The authors observed the occurrence of progressive changes in channel transient flow transition and reported that the transition that occurs in transient channel flow resembles that of bypass transition, even though the initial flow rate is turbulent. This current study aims at expanding these concepts. The results of the experimental investigations carried out and presented in this chapter show similar transition process to that of the experimental study of Mathur et al. (2018) and the numerical study of He and Seddighi (2015). In this current study, the initial Reynolds number $Re_0$ is higher than that of Mathur et al. (2018), and the pneumatic control valve is opened suddenly. On the other hand, Mathur et al. (2018) opened the control valve in a slower controlled fashion in order to generate a "smooth" flow increase. In step-change in flow rate reported by He and Seddighi (2015), the authors obtained an increase in flow rate following a sudden increase in pressure gradient. Experimental cases studied

In this current study, the acceleration of the transient turbulent flow from initial statistically steady state to the final turbulent flow is obtained by suddenly opening the pneumatic control valve of the flow facility. The time period at which the acceleration occurs in the flow is subject to the sudden opening of the pneumatic control valve and the final flow condition. During the sudden opening of the valve, the flow rate increase, which is referred to as positive acceleration. The study of the effect of deceleration on the fluid flow is beyond the scope this current study. Experimental studies are thus carried out to investigate effects of different Reynolds number ratios on streamwise mean velocity and turbulence statistics, as shown in Tables 4-1 and 4-2.

***Table 4-1: Experimental cases showing different Reynolds number ratios.***

| Group | Case | $Re_0$ | $Re_1$ | $\frac{Re_1}{Re_0}$ | $U_b$ $({m}/{s})$ | 90% $U_{b1}$ | Temp. (°C) | $\Delta t$ $(s)$ | $\Delta t_{ac}$ ${m}/{s^2}$ |
|---|---|---|---|---|---|---|---|---|---|
| 1 | T1 | 3298 | 24047 | 7.29 | 0.110-0.804 | 0.724 | 28 | 1.72 | 0.356 |
| | T2 | 4234 | 24155 | 5.71 | 0.142-0.808 | 0.727 | 28 | 1.65 | 0.354 |
| | T3 | 5100 | 24324 | 4.77 | 0.171-0.814 | 0.732 | 28 | 1.61 | 0.348 |
| 2 | U1 | 2845 | 7560 | 2.66 | 0.092-0.245 | 0.221 | 29.4 | 1.52 | 0.085 |
| | U2 | 2852 | 9557 | 3.35 | 0.093-0.310 | 0.279 | 29.4 | 1.36 | 0.137 |
| | U3 | 2838 | 12069 | 4.25 | 0.092-0.392 | 0.353 | 29.4 | 1.56 | 0.167 |

*Note: Acceleration period ($\Delta t$) denotes the amount of time for an initial bulk velocity ($U_{b0}$) to reach 90% of the final bulk velocity ($U_{b1}$). Acceleration rate ($\Delta t_{ac}$) is calculated as* ${(90\%(U_{b1}) - U_{bo})}/{\Delta t}$.

The flow parameters in Table 4-1 are divided into two groups. The first group required a variation of the initial Reynolds numbers while the final Reynolds number is fixed in order to produce different values of initial turbulence intensity ($T_{u0}$). In the second group of the investigation, the initial Reynolds number is fixed while the final Reynolds numbers are varied, and different values of initial turbulence intensity ($T_{u0}$) are produced. Each group comprises three different cases with different Reynolds number ratios at a constant temperature. Measurements are obtained through vertical-PIV and horizontal-PIV orientations during the flow acceleration and the procedure of transition to turbulence is studied during the flow acceleration of the cases in the two groups.

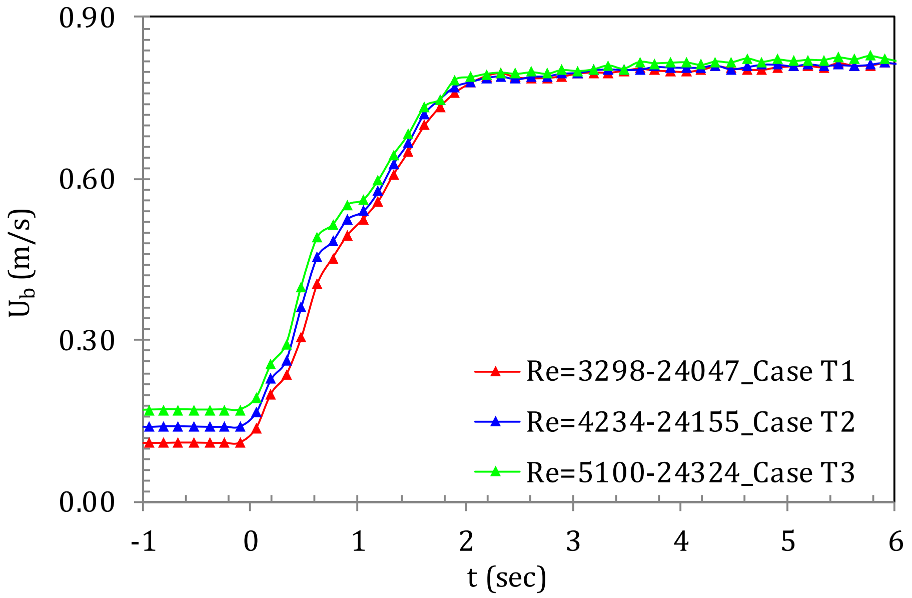

***Figure 4-1: Bulk velocity variation for the cases of different initial Reynolds numbers and a fixed final Reynolds number.***

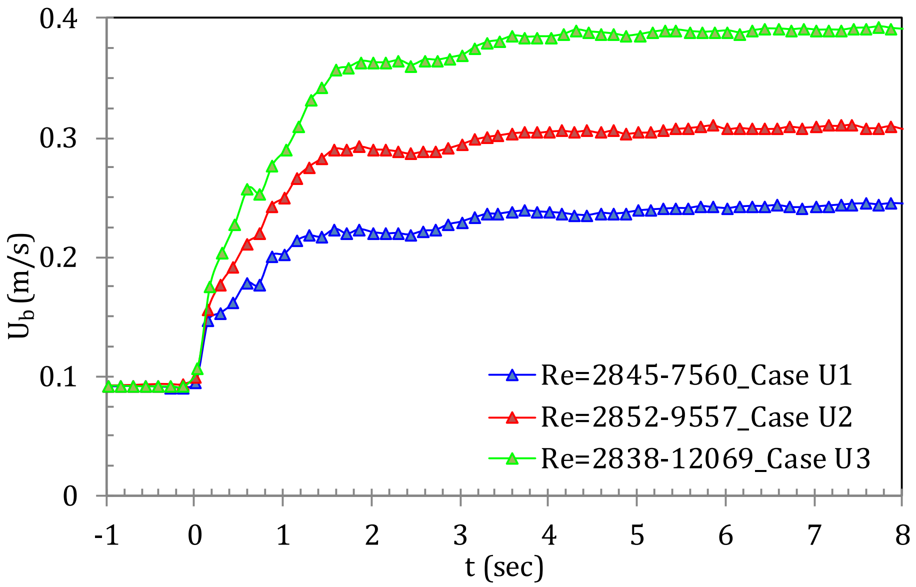

***Figure 4-2: Bulk velocity variation for the cases of a fixed initial Reynolds number and different final Reynolds number.***

Figure 4-1 shows the bulk velocity variation when the pneumatic control valve is opened suddenly from $Re_b$ = 3298-24047 (T1), $Re_b$ = 4234-24155 (T2) and $Re_b$ = 5100-24324 (T3) at a constant temperature. Both initial and final Reynolds numbers are indicated with subscripts 0 and 1, respectively. Figure 4-2 shows all the U cases studied, $Re_b$ =2845-7560 (U1), $Re_b$ = 2852-9557 (U2) and $Re_b$ =2838-12069 (U3) during the flow acceleration. The bulk Reynolds number for all the experimental cases is calculated as $Re_b = {}^{\delta U_b}/_{v}$ where $\delta$ is the half-height of the channel, $U_b$ is the bulk velocity of the flow and $v$ is the kinematic viscosity of the working fluid. $\Delta t$ denotes the time period of ramping up the flows which is determined as the amount of time for an initial bulk velocity ($U_{b0}$) to reach 90% of the final bulk velocity ($U_{b1}$). The variation in bulk flow with time up to 90% is rapid while the variation of bulk flow with time is much slower during the remaining period. It can be concluded, based upon the results, that the acceleration rate ($\Delta t_{ac}$) reduces as the initial Reynolds number increases while the final Reynolds number remains fixed. The acceleration rate ($\Delta t_{ac}$) increases as the final Reynolds number increases while the initial Reynolds number is fixed. Other normalised parameters used in the subsections of this chapter are $t^{+0}$, $y^{+}$ and $t^{*}$. Each dimensionless parameter is calculated as follows: $t^{+0}(= tu_{\tau 0}^{2}/v)$, $y^{+}(= yu_{\tau}/v)$ and $t^{*}(= tU_{b1}/\delta)$ where $u_{\tau}$ is the friction velocity, $t$ is the time of flow acceleration, $\delta$ is the half-height of the channel, $U_{b1}$ is the bulk velocity of the final stage of the flow, $y$ is the distance from the wall, $v$ is the kinematic viscosity, $t^{*}$ and $t^{+}$are normalised time, and $y^{+}$ is the normalised wall distance. "0" refers to initial state and "1" refers to final state.

Measurements of streamwise mean velocity, turbulence statistics and wall shear stress during the flow acceleration for all experimental cases presented in this chapter are obtained using PIV and CTA. PIV is used to measure the instantaneous velocity while measurements of wall shear stress during the acceleration of transient turbulent flow are obtained through CTA. As earlier explained in § 3.7, a dynamic calibration technique is adopted and wall shear stress calculated.

The cases of different initial Reynolds numbers and temperatures with a fixed final Reynolds number are also presented as the third group of the cases investigated. Table 4-2 presents the flow conditions for all such cases. The final fixed Reynolds number for all the cases investigated is approximately $Re_b = 22400$.

***Table 4-2: Experimental cases showing different Reynolds number ratios at different temperatures***

| Case | $Re_0$ | $Re_1$ | $\frac{Re_1}{Re_0}$ | $U_b$ $\left({}^{m}/_{s}\right)$ | 90% $U_{b1}$ | Temp. (°C) | $\Delta t$ $(s)$ | $\Delta t_{ac}$ ${}^{m}/_{s^2}$ |
|---|---|---|---|---|---|---|---|---|
| P1 | 4192 | 22481 | 5.36 | 0.147-0.789 | 0.711 | 25.8 | 1.69 | 0.33 |
| P2 | 5096 | 22282 | 4.37 | 0.179-0.784 | 0.705 | 25.7 | 1.66 | 0.32 |
| P3 | 6127 | 22514 | 3.67 | 0.214-0.787 | 0.708 | 26 | 1.60 | 0.31 |
| P4 | 7348 | 22250 | 3.03 | 0.267-0.810 | 0729 | 24.2 | 1.52 | 0.30 |
| P5 | 8947 | 22224 | 2.48 | 0.306-0.760 | 0.684 | 27 | 1.50 | 0.25 |
| P6 | 10375 | 22468 | 2.17 | 0.355-0.768 | 0.691 | 25.9 | 1.38 | 0.24 |
| P7 | 12455 | 22347 | 1.79 | 0429-0.767 | 0.692 | 26.7 | 1.26 | 0.21 |

*Note: Acceleration period ($\Delta t$) denotes the amount of time for an initial bulk velocity ($U_{b0}$) to reach 90% of the final bulk velocity ($U_{b1}$). Acceleration rate ($\Delta t_{ac}$) is calculated as* ${}^{(90\%(U_{b1})\,-\,U_{bo})}/_{\Delta t}$.

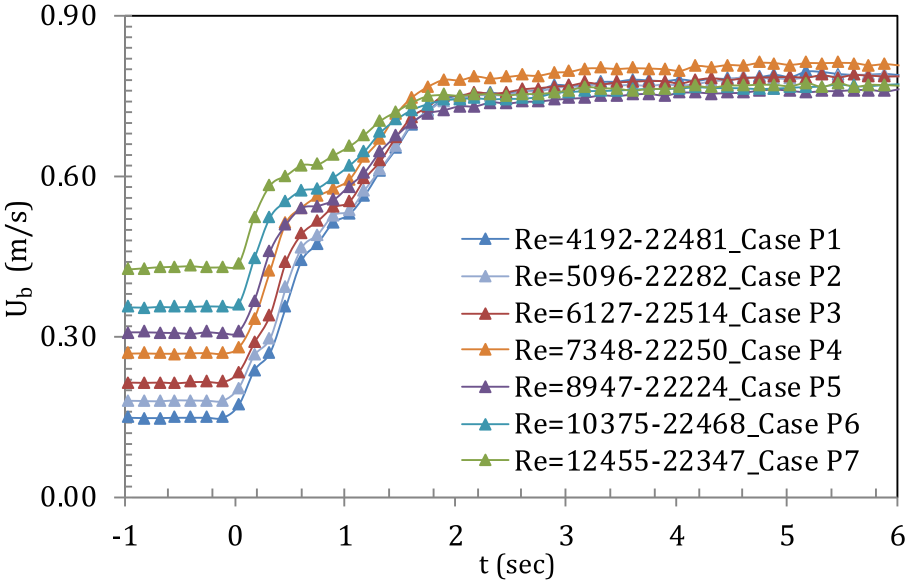

***Figure 4-3: Bulk velocity variation for the cases of different initial Reynolds numbers and a fixed final Reynolds number at different temperatures.***

Figure 4-3 shows the variation of the bulk velocity for all the cases studied. The trend of the case $Re_b$ =7348-22250 at temperature 24.2°C with a final bulk velocity $U_{b1} = 0.81\,m/s$ overshoots in the final bulk flow due to temperature difference. The variation of the bulk velocity is similar to that of the T cases at same the temperature as presented earlier.

***Table 4-3: The onset and completion times for different cases investigated at the same temperature.***

| Group | Case | $t_{cr}(sec)$ | $t_{turb}(sec)$ | $t_{cr}^{*}$ | $t_{turb}^{*}$ | $t_{cr}^{+0}$ | $t_{turb}^{+0}$ |
|---|---|---|---|---|---|---|---|
| 1 | T1 | 1.71 | 2.66 | 55 | 86 | 99 | 154 |
|  | T2 | 1.34 | 2.18 | 43 | 70 | 121 | 197 |
|  | T3 | 0.88 | 1.37 | 29 | 45 | 110 | 171 |
| 2 | U1 | 2.51 | 4.61 | 25 | 45 | 108 | 199 |
|  | U2 | 2.37 | 4.42 | 29 | 55 | 103 | 192 |
|  | U3 | 2.29 | 3.81 | 36 | 60 | 98 | 164 |

***Table 4-4: The onset and completion times for different cases investigated at different temperatures.***

| Case | Temp. (°C) | $t_{cr}(sec)$ | $t_{turb}(sec)$ | $t_{cr}^{*}$ | $t_{turb}^{*}$ | $t_{cr}^{+0}$ | $t_{turb}^{+0}$ |
|---|---|---|---|---|---|---|---|
| P1 | 25.8 | 1.13 | 2.02 | 36 | 64 | 105 | 187 |
| P2 | 25.7 | 0.97 | 1.53 | 30 | 48 | 127 | 200 |
| P3 | 26 | 0.88 | 1.34 | 28 | 42 | 158 | 240 |
| P4 | 24.2 | 0.78 | 1.09 | 25 | 35 | 200 | 279 |
| P5 | 27 | 0.67 | 0.88 | 20 | 27 | 227 | 298 |
| P6 | 25.9 | 0.55 | 0.66 | 17 | 20 | 241 | 289 |
| P7 | 26.7 | 0.37 | 0.45 | 11 | 14 | 223 | 272 |

## 4.2 Instantaneous behaviour in rapidly accelerating flows

This section focuses on the visualisation of the transition procedure of channel transient flow using the instantaneous behaviour of the flow. The instantaneous behaviour of the flow is described using the contour plots of fluctuating streamwise velocity in a plane adjacent to the bottom wall of the channel at different times, as shown in Figures 4-4, 4-5, 4-6 and 4-7. The arrangement of laser-camera has been previously described in § 3.6 for horizontal-PIV where the camera is installed on top of the measuring section and the laser fired at the side. In the following experiments, the horizontal-PIV orientation is used to capture velocities in streamwise and spanwise directions for the six cases (T1, T2 & T3) and (U1, U2 & U3) investigated. The field of view (FOV) utilised during the measurement is 110 $mm$ × 110 $mm$

and the captured images are processed using a final interrogation area (IA) of $32\,pixels \times 32\,pixels$ and initial interrogation size of $256\,pixels \times 256\,pixels$ with three being the number of refinements, as described earlier in § 3.6. The time between the two light pulses used for the cases reported is $600\mu s$ for the determination of instantaneous behaviour of transient channel flow due to a bigger field of view (FOV). Based on the field of view of $110\,mm\,x\,110\,mm$, the experimental measurement area used to describe the instantaneous behaviour of the flow is $4\delta \times 4\delta$, where $\delta$ is the half-height of the channel. The instantaneous fluctuating velocities are determined when the mean velocities averaged in both streamwise and spanwise directions of the field of view (FOV) are subtracted from the instantaneous velocities, as shown in Eq. (4.1).

$$\overline{u'}(t) = u(t) - \bar{u} \tag{4.1}$$

where $u$ represents the instantaneous velocity and $\bar{u}$ represents the streamwise mean velocity of the flow averaged in both streamwise and spanwise directions.

All measurements made below 2 mm above the bottom wall of the channel are blurred and showed the surface of the wall. For all the cases investigated in this section, measurements are made at a distance of $2\,mm$ above the bottom wall of the channel. The value of wall distance is equivalent to the dimensionless wall distance of ${}^{y}/_{\delta} = 0.08$ or $y_0^+ = \left({}^{yu_{\tau 0}}/_{\nu}\right) \approx 14$ where $y$ represents for the distance from the channel bottom wall, $\delta$ is the half-height of the channel, $u_{\ \tau 0}$ is the initial friction velocity of the steady turbulent flow and $v = ({}^{\mu}/_{\rho})$ is the kinematic viscosity. Measurements below $2\,mm$ above the bottom wall of the channel were blurred.

Moreover, for all T cases investigated, the initial flow of each case is maintained as statistically steady turbulent flow before ramping up to the final stage of the flow. The initial Reynolds number is varied while the final Reynolds number ($Re_b \approx 24200$) is fixed to produce different Reynolds number ratios, as shown in Table 4-1. Figure 4-4, 4-5 and 4-6 show the elongation, amplification and breakdown of streaks in the streamwise direction during the flow acceleration at a wall distance of $y = 2\ mm$ ($y_0^+ = 14$) from the channel. The initial flow is characterised by small pre-streaky structures with a small degree of streamwise fluctuations at $t = 0.0\ sec$, as seen in the first frames of all T cases before the commencement of the flow acceleration. Immediately following the start of the transient flow, the pre-streaky structures in the flow are stretched. The amplification of the elongated streaks of both positive and negative streamwise fluctuating velocity becomes stronger with time during the early (pre-transitional) stage of the transient flow for case T1 (up to about $t < 1.7$ sec), for case T2, (up to about $t < 1.3$ sec) and for case T3 and (up to about $t < 0.9$ sec), as shown in Figures 4-4, 4-5 and 4-6. The sky blue sections of the early frames of contour plots of fluctuating streamwise velocity are referred to as negative jets by Jacobs and Durbin (2001), and these negative jets denote the primary disturbances in flat plate boundary layer flow subjected to $FST$.

As with the flat plate boundary layer flow, the pre-streaky structure in the initial flow acts as primary disturbances in transient channel flow. The numerical investigation of He and Seddighi (2013) showed that transition to turbulence also occurs in a channel transient. The authors termed the initial stage of the transient flow the pre-transitional time frame. This pre-transitional stage is also referred to as the buffeted laminar boundary layer by Jacobs and Durbin (2001) in their numerical investigation on bypass transition. Further, during the transitional time frame, the streaky structures brakes up and the formation of isolated turbulence spots occurs. The isolated turbulence spots, which initially appear as turbulence burst, grow downstream over time combine with each other. The transitional time frames for the three cases occurs between $1.7 < t < 2.7$ for case T1, $1.3 < t < 2.2$ for case T2 and $0.9 < t < 1.3$ for case T3, as shown in Figures 4-4, 4-5 and 4-6. The transition completes, and the flow then becomes fully developed turbulent flow once the entire wall-bounded surface has been filled with newly generated turbulence structures. The newly generated turbulence structures cover the entire wall surface from $t > 2.7$ for case T1, $t > 2.2$ for case T2 and $t > 1.3$ for case T3. It can be observed from the contour plots that as the Reynolds number ratio reduces as the initial Reynolds increases, the onset of transition reduces from 1.7 s in case T1 to 0.9 s in case T3, as shown in Figures 4-4, 4-5 and 4-6.

For brevity, only case U3 is presented, as shown in Figure 4-7. In the U cases, the initial Reynolds number ($Re_b \approx 2800$) is fixed while the final Reynolds numbers are varied to produce different Reynolds number ratios, as shown in Table 4-1. The procedure for the transition to turbulence is similar to T cases presented earlier but the time frame of the pre-transitional is longer. It is revealed that at $t = 0.0\ sec$, the initial flow contains small-amplitude streamwise fluctuations as characteristics of a fully developed turbulent flow. As the transient flow commences, the pre-streaky structures in the initial flow are amplified and increases in magnitude with time. The amplification of the structures is revealed in the pre-transitional stage up to about $t < 2.3$ secs. In the transitional stage between $(2.3 < t < 3.8)$, the elongated streaks brakes, and the formation of isolated turbulence spots occurs. On the completion of transition, from $t > 3.8\ secs$, the whole wall-bounded surface has been filled with the newly generated turbulence and the flow has become fully developed turbulent flow.

The flow structures for the two groups investigated in this current study are similar to that of the numerical and experimental findings of Mathur et al. (2018) and the experimental flow structures of Gorji (2015). Though their experimental flow measurement area $(3\delta \times 3\delta)$ is smaller than that of the current experimental measurement area at $(4\delta \times 4\delta)$, the results look alike. The flow structures at the different stages of transition to turbulence are similar to that of direct numerical simulation of step-increase in flow rate by He and Seddighi (2013), the linear flow acceleration of Seddighi et al. (2014) on channel transient flow, and with the direct numerical simulation of Jacobs and Durbin (2001) on bypass transition.

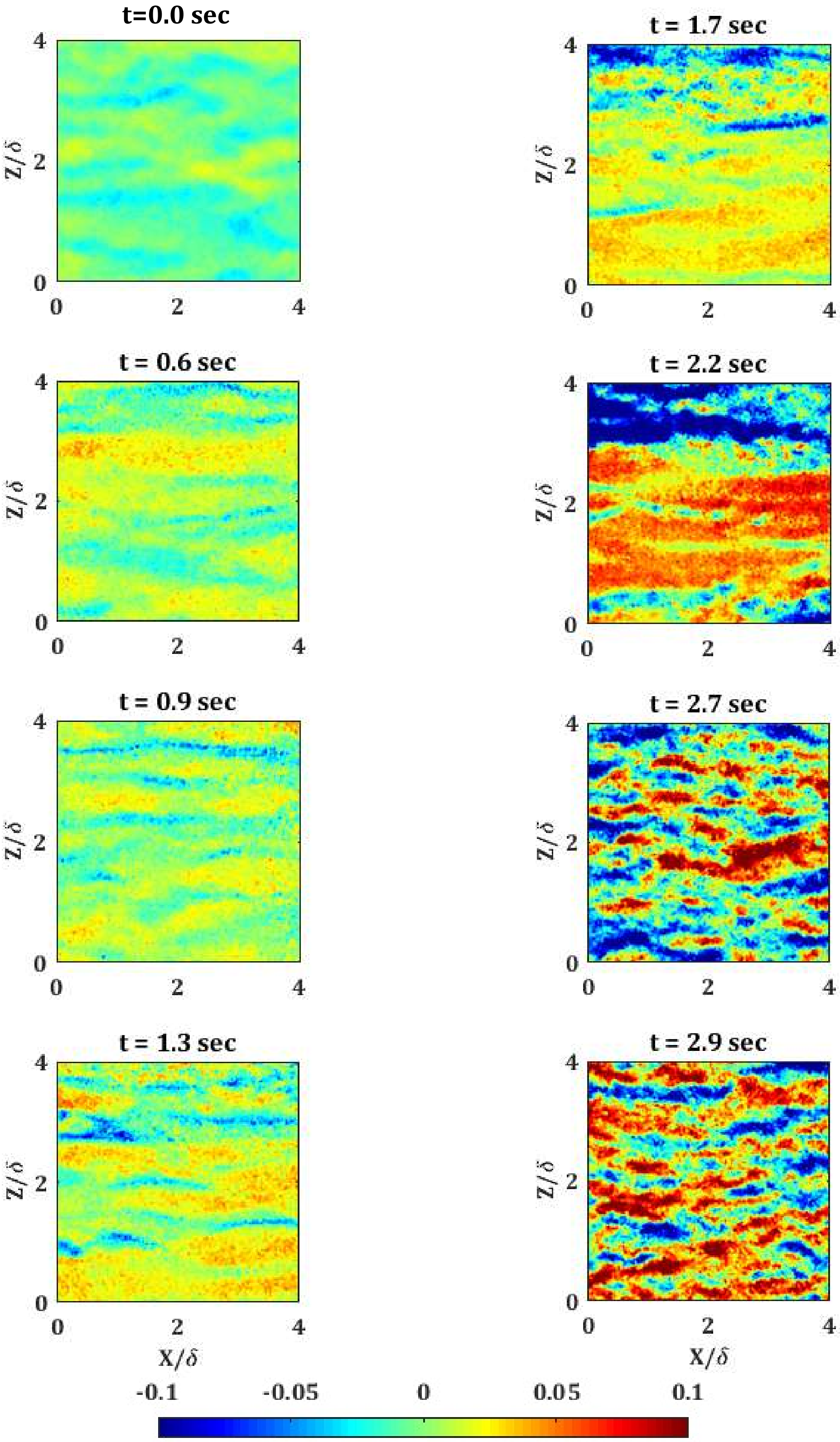

***Figure 4-4: Contour plots at a distance of 2 mm ( $y_0^+ = 14$ ) from the channel bed showing streamwise fluctuating velocity, u' (m/s) for unsteady flows at different time frames for case T1 ($Re_b$ = 3298-24047).***

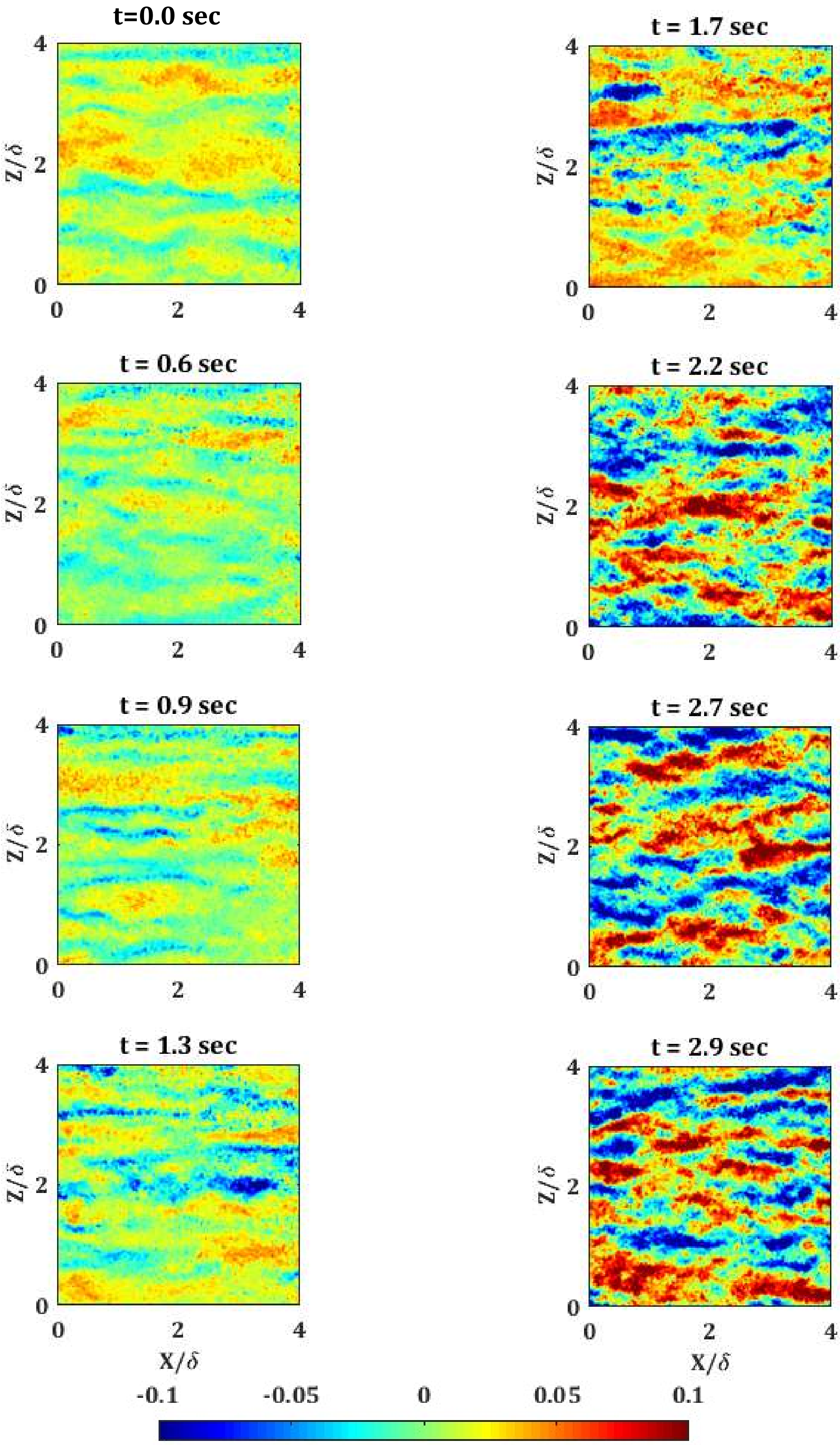

*Figure 4-5- Contour plots at a distance of 2 mm ($y_0^+ = 14$) from the channel bed showing streamwise fluctuating velocity, u' (m⁄s) for unsteady flows at different time frames for case T2 ($Re_b$ =4234-24155).*

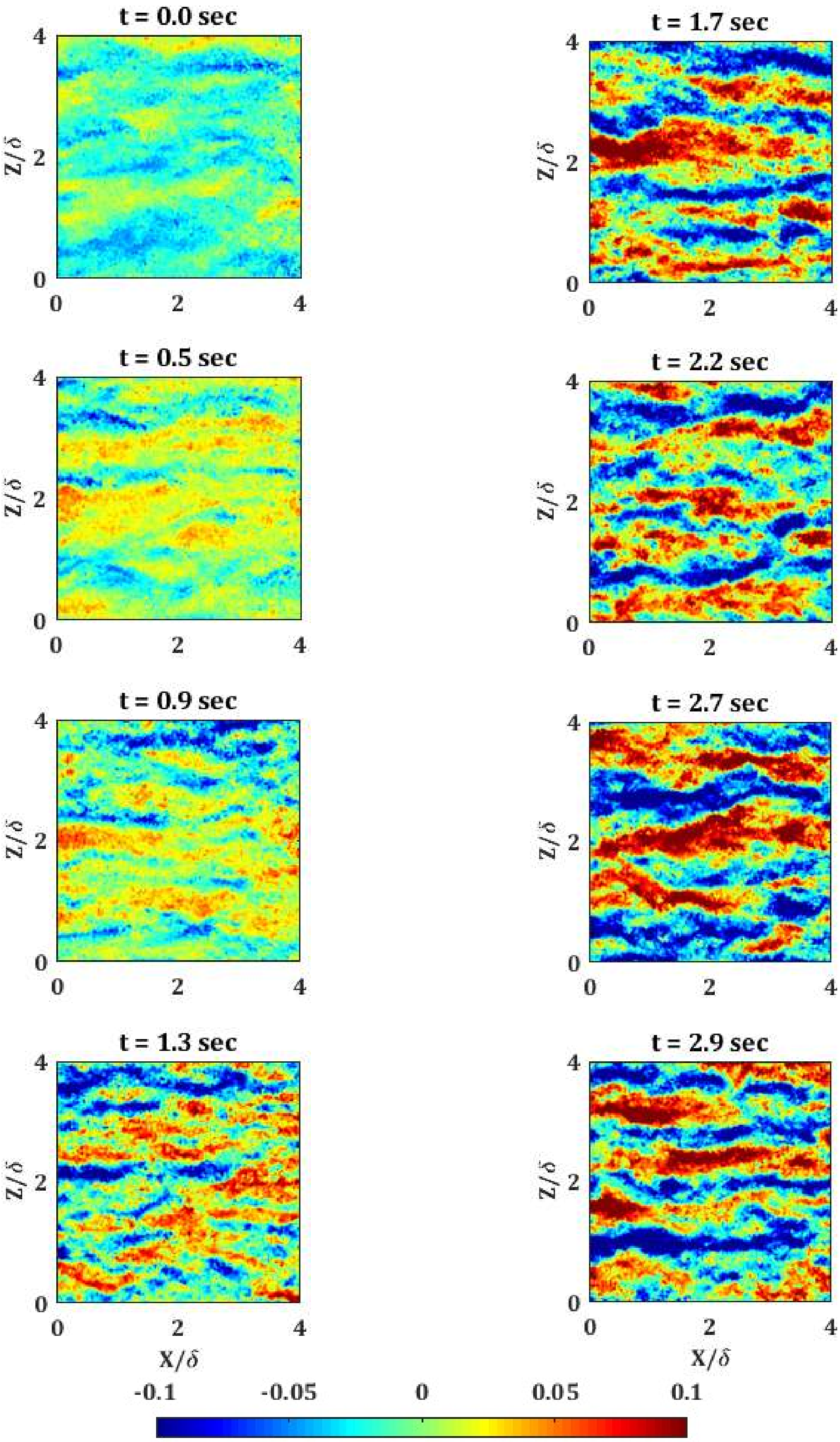

***Figure 4-6- Contour plots at a distance of 2 mm ( $y_0^+ = 14$ ) from the channel bed showing streamwise fluctuating velocity, u' (m/s) for unsteady flows at different time frames for case T3 ($Re_b$ = 5100-24324).***

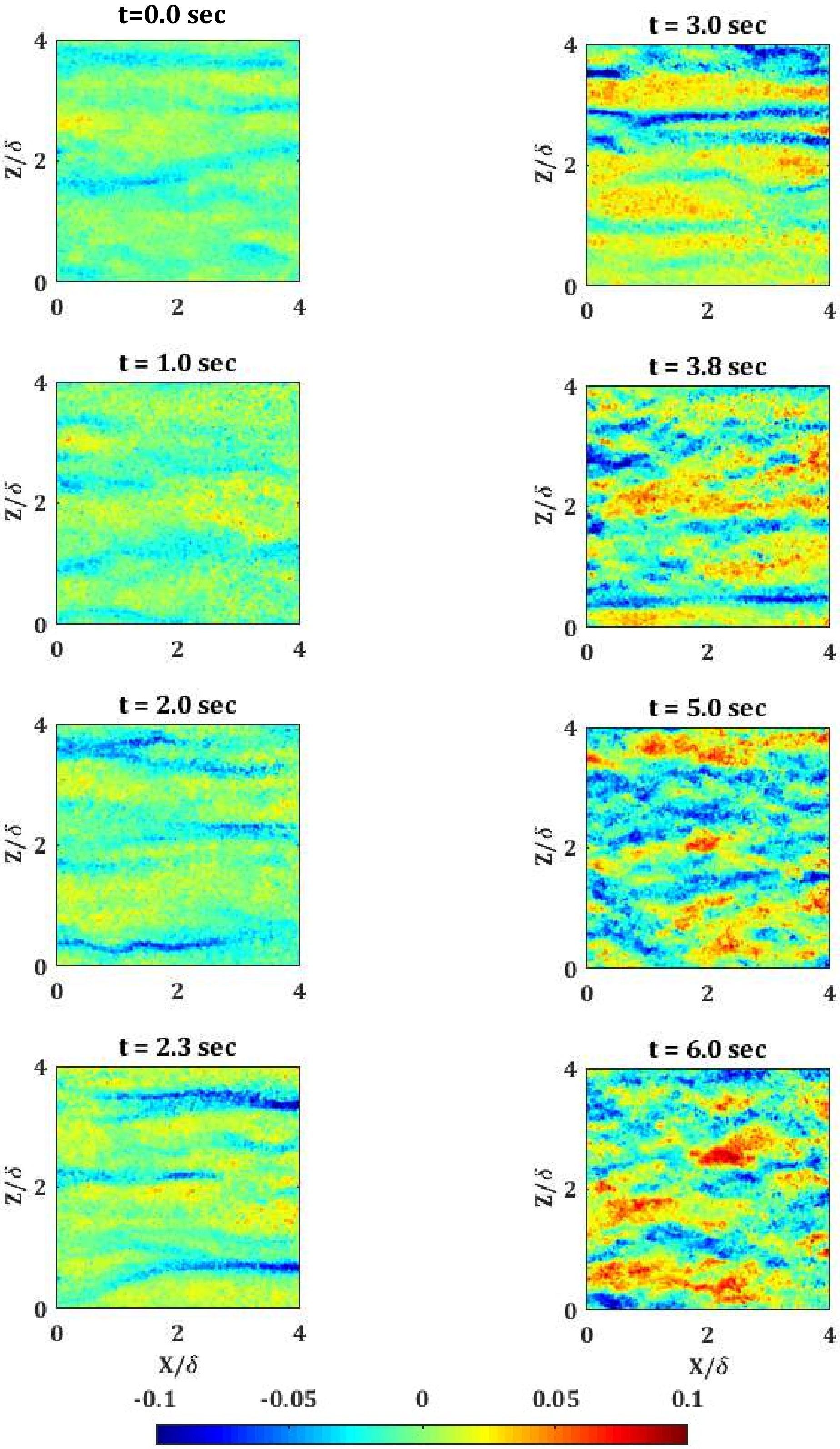

***Figure 4-7- Contour plots at a distance of 2 mm ( $y_0^+ = 14$ ) from the channel bed showing streamwise fluctuating velocity, u' (m/s) for unsteady flows at different time frames for case U3 ( $Re_b$ = 2838-12069).***

## 4.3 Ensemble-averaged flow behaviour

In the experiments described in this section, vertical-PIV orientation is adopted for data acquisition. Ensemble-average calculation is performed on the repeated experimental runs acquired from all transient flow cases presented in Tables 4-1 and 4-2 in order to obtain streamwise mean velocity, streamwise fluctuating velocity, wall-normal fluctuating velocity and Reynold shear stress. Unlike steady flow analysis, where spatial and temporal averages are performed on the acquired data, ensemble and spatial averages are performed on the unsteady flow data. A longer observation of 80 repeated experimental runs is adopted for each of the cases as this procedure allows wiggles to be reduced in the plots. The PIV measurements are made through the field of view (FOV) of $30.60\,mm \times 30.60\,mm$, and an adaptive correlation is used to process the data in the final interrogation area size of $32 \times 32$ pixels and initial interrogation area size of $256 \times 256$ pixels with three of refinements, as previously described in § 3.6. The response of wall shear stress is recorded using hot-film sensors of CTA. Ensemble-averaging is then performed on all the repeated experimental runs acquired from CTA for the determination of wall shear stress of all the cases investigated in this section.

### 4.3.1 Behaviour of skin friction coefficient of varying Reynolds numbers ratio in channel flow

The development of the skin friction is reported in three groups: First, when the initial Reynolds numbers are varied with a final fixed Reynolds number at the same temperature; second, the development of skin friction coefficients for cases of different initial Reynolds numbers and temperatures with a final fixed Reynolds number. Finally, the initial Reynolds number is fixed while the final Reynolds numbers are varied at the same temperature. The skin friction coefficient of the flow is obtained as;

$$C_f(t) = \frac{2\tau_w(t)}{\rho(U_b(t))^2} \tag{4.2}$$

where $\tau_w(t)$ is the wall shear stress of the flow at time, $t$ and $U_b(t)$ is the bulk velocity at time, $t$ of the flow.

As earlier reported He and Seddighi (2013;2015), the procedure of transition to turbulence of transient turbulent flow in a channel that is subjected to a rapid or slow acceleration resembles a laminar-turbulent transition due to free-stream turbulence ($FST$) even though the initial flow condition is turbulent. The process of transition to turbulence consists of three stages; namely, pre-transition, transition and fully turbulence (He & Seddighi, 2013; Seddighi et al., 2014; He & Seddighi, 2015). The development of the skin friction coefficient of all the cases investigated in this section reflects the three stages of transition to turbulence and is similar to that of bypass transition in a flat plate boundary layer flow. The time of onset of transition and when the transition is completed can be determined using the development of skin friction coefficient ($C_f$). The time which is equivalent to the minimum value of skin friction coefficient ($C_f$) where the turbulence spots are first seen is referred to the critical time ($t_{cr}$). In addition, the time which is equivalent to the skin friction coefficient when it increases to the first peak from its minimum position due to the formation of "new" turbulence structures in the flow is referred to as the time of completion of transition process ($t_{turb}$). Immediately following commencement of the flow excursion, the skin friction coefficient increases sharply, reaching the maximum value rapidly. This results in the creation of a thin boundary layer near the wall that increases both viscous force and velocity gradient. Near the wall, the viscous force reduces the velocity of fluid, leading to a high strain rate. The formation of the thin boundary layer near the wall is due to the no-slip boundary condition. It is noted that the growth of the thin boundary layer with time during the pre-transitional time frame causes the skin friction coefficient to reduce and reach minimum values for the different cases investigated at t = 1.71s (T1), t = 1.34s (T2), t = 0.88s (T3), t = 2.51s (U1), t = 2.37s (U2), t = 2.29s (U3), t = 1.13s (P1), t = 0.97s (P2), t = 0.88s (P3), t = 0.78s (P4), t = 0.67s (P5), t = 0.55s (P6), t = 0.37s (P7), as shown in Figures 4-8a, 4-8b and 4-8c, respectively.

At the minimum value of skin friction coefficient, which marks the onset of transition, turbulence spots are first seen. Subsequently, a prompt increase of the skin friction coefficient is observed due to the creation of "new" turbulence structures at the beginning of the transitional period. The skin friction coefficient increases to the final statistically steady values which marked the end of transition for all the cases investigated at t = 2.66s (T1), t = 2.18s (T2), t = 1.37s (T3), t = 4.61s (U1), t = 4.42s (U2), t = 3.81s (U3), t = 2.02s (P1), t = 1.53s (P2), t = 1.34s (P3), t = 1.09s (P4), t = 0.88s (P5), t = 0.66s (P6) and t = 0.45s (P7). At these times listed, the transition procedure has completed and the whole wall-bounded surface of the channel has been filled with the "new" turbulence structures. The trend of the skin friction coefficient development reported is the same as that of numerical studies of He and Seddighi (2013; 2015). Figures 4-4a, 4-4b, 4-4c show the development of skin friction coefficient for all the cases investigated in this section. Figure 4-4a presents the cases of different initial Reynolds numbers in a turbulent statistically steady state accelerated to final turbulent flow with Reynolds number ratios of 7.29, 5.71 and 4.77 for cases T1, T2 and T3, respectively. It is observed that as the Reynolds number ratio increases, as the initial Reynolds number reduces, the time of onset of transition to turbulence increases. However, the time of onset of transition decreases as the Reynolds number ratio decreases. Figure 4-4b shows the cases with a fixed initial Reynolds number and different final Reynolds numbers. The three cases U1, U2 and U3 are equivalent to Reynolds number ratios of 2.66, 3.35 and 4.25, respectively. The response of skin friction coefficient ($C_f$) for all the U cases conforms to that of P and T cases, and follows the three stages of transition to turbulence earlier reported. It is observed that the minimum value of the skin friction coefficient ($C_f$) reduces as the final Reynold number increases. Another interesting observation of U cases is that the initial turbulence intensity ($T_{u0}$) reduces as the final Reynolds number increases. The case U1 has the smallest value of final Reynolds number with the highest value of the time of onset of transition. However, the critical time of transition for case U3 with a higher value of the final Reynolds number has the smallest value for the time of onset of transition among the U cases investigated. Comparing the onset of transition identified here using $C_f$ with the visualisations presented in Figures 4-4, 4-5, 4-6 and 4-7, it is revealed that the onset of transition closely coincides with the stage at which turbulence spots are generated.

P cases have a fixed final Reynolds number of approximately $Re_b$ = 22400. The Reynold number ratios range from 1.79 to 5.36 and the critical time for Reynolds number ratios range between 1.13s and 0.37s, as shown in Table 4-2. It is observed that the largest Reynolds number ratio of 5.36 has the highest critical time of 1.13s and process of transition becomes strong. The lowest Reynolds number ratio of 1.79 has the lowest critical time of 0.37s and the process of transition to turbulence appears to be subtle, as shown in Figure 4-8 (c).

Considering all the cases investigated, as the difference between the final Reynolds number and the initial Reynolds number increases, the transition procedure becomes prominently noticeable; however, it becomes undetectable when the difference between the final Reynolds number and the initial Reynolds number decreases in case P7. This conforms with the investigations previously reported by He and Seddighi (2015) and Jung and Kim (2017b) that the process of transition to turbulence becomes noticeable when the Reynolds number difference is large and the transition process resembles that of bypass transition of flat plate boundary layer flow.

The responses of skin friction coefficient for all the three groups investigated have revealed the three stages of transition earlier described. Table 4-3 and Table 4.4 show the actual and normalised times for both the onset of transition and completion of transition procedure. The trend of the skin friction development of all the cases investigated is similar to that of Mathur et al. (2018) and He and Seddighi (2013) with these authors suggesting that normalised time $t^{+0}$ is an important parameter in characterising the time when transition begins. In the direct numerical simulations of transient flow following a step increase carried out by the authors, it is reported that the normalised time $t^{+0}$ is between $80 < t^{+0} < 110$.

Furthermore, Gorji (2015) utilised wall-normal fluctuating velocity ($v'_{rms}$) and streamwise fluctuating velocity ($u'_{rms}$) in the determination of the onset of transition to turbulence and when the transition has been completed in his experimental investigations. The normalised time $t^{+0}$ reported by the author ranges from between $80 < t^{+0} < 130$. In all the cases investigated, the values of the normalised time $t^{+0}$ are similar except for some of the P cases with very high initial Reynolds numbers. Some of the initial Reynolds numbers reported in this current study are higher than the previous studies. P cases has normalised times $t^{+0}$ between 105 to 241 ($105 < t^{+0} < 241$). This suggests that $t^{+0}$ is not approximately constant whilst the normalised time $t^{+0}$ for T and U cases ranges between 79 and 121 ($80 < t^{+0} < 110$), similar to that reported by Gorji (2015). Overall, the development of skin friction coefficient for all the cases investigated is similar to that of He and Seddighi (2013; 2015) and Mathur et al. (2018), and similar to that of skin friction coefficients during transition to turbulence in flat plate boundary layer flow reported by Jacobs and Durbin (2001) and Nagarajan et al. (2007).

By focusing on Figures 4-1and 4-3, it can be observed that transition to turbulence of transient channel flow that occurs within the time the flow is still accelerating for all the cases presented. Figure 4-2 shows the cases with different final Reynolds numbers and a fixed initial Reynolds number. This shows that when the final Reynolds number is small, it takes a longer time before the transition to turbulence can occur. It also takes a shorter time to attain the onset of transition when the final Reynolds number is high, as shown from the U cases investigated.

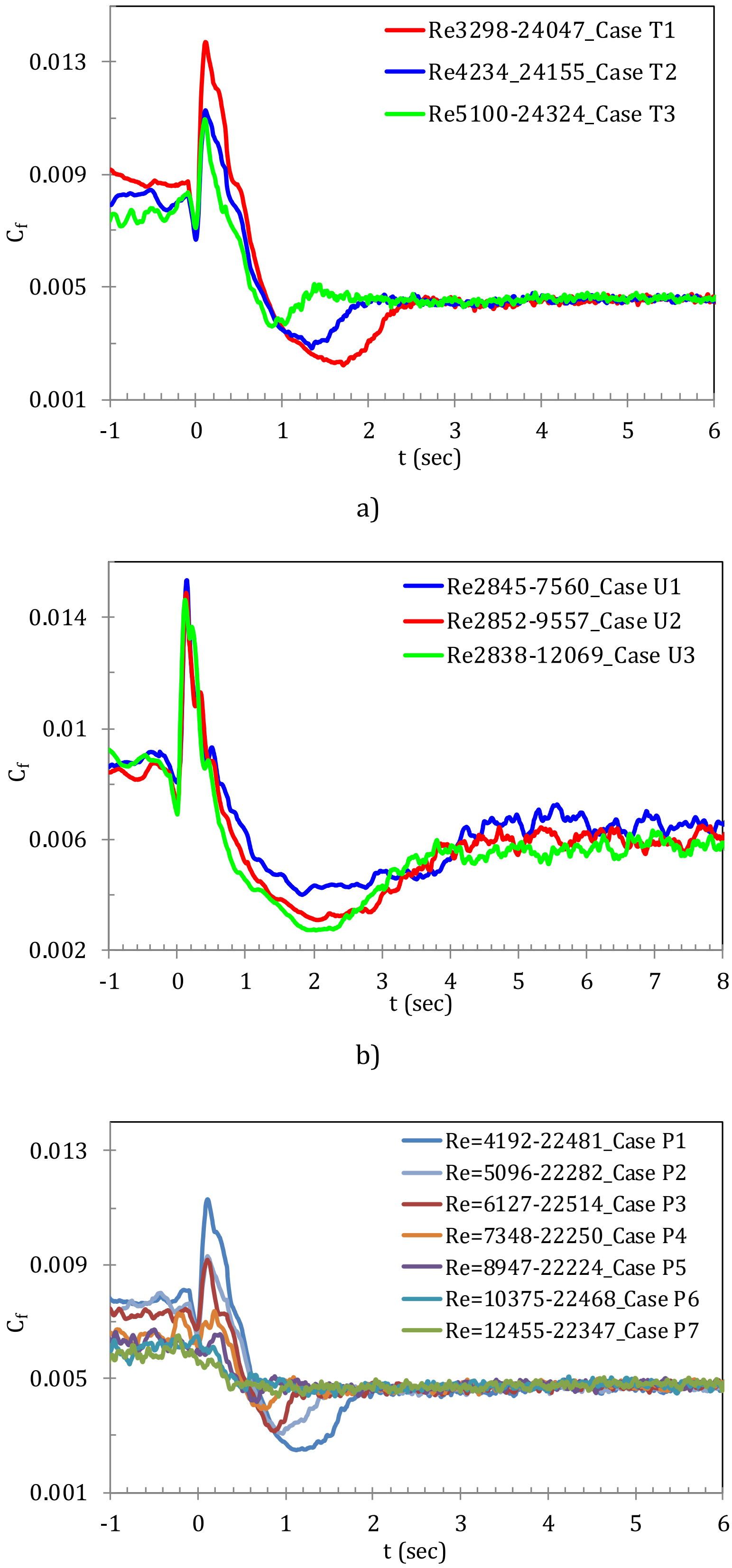

a)

b)

c)

***Figure 4-8: Development of skin friction coefficient for a) T cases, b) U cases and c) P cases.***

#### 4.3.1.1 Effect of Reynolds number ratio on transient channel flow using equivalent Reynolds number and skin friction coefficient

The investigations carried out by Andersson et al. (1999) and Fransson et al. (2005) on flat plate boundary layer flow have shown that free-stream turbulence ($FST$) influences the transition to turbulence. As with flat plate boundary layer flow, turbulence intensity produced by Reynolds number ratio influences the process of transition to turbulence in transient channel flow. In flat plate boundary layer flow, the Reynolds number is given as:

$$Re_x = {}^{xU_\infty}/_{v} \tag{4.3}$$

where $x$ is the distance from the leading edge, $U_\infty$ is the free-stream velocity, and $v$ is the kinematic viscosity of the fluid flow.

***Table 4-5: The transient flow cases showing equivalent Reynolds number at different Reynolds number ratios.***

| Case | $Re_0$ | $Re_1$ | $Re_{t,cr}$ | $Re_{t,turb}$ |
|---|---|---|---|---|
| T1 | 3298 | 24047 | $1.32 \times 10^6$ | $2.06 \times 10^6$ |
| T2 | 4234 | 24155 | $1.05 \times 10^6$ | $1.70 \times 10^6$ |
| T3 | 5100 | 24324 | $0.7 \times 10^6$ | $1.08 \times 10^6$ |
| U1 | 2845 | 7560 | $1.36 \times 10^5$ | $3.42 \times 10^5$ |
| U2 | 2852 | 9557 | $2.46 \times 10^5$ | $5.24 \times 10^5$ |
| U3 | 2838 | 12069 | $4.33 \times 10^5$ | $7.20 \times 10^5$ |
| P1 | 4192 | 22481 | $0.80 \times 10^6$ | $1.43 \times 10^6$ |
| P2 | 5096 | 22282 | $0.68 \times 10^6$ | $1.07 \times 10^6$ |
| P3 | 6127 | 22514 | $0.62 \times 10^6$ | $0.95 \times 10^6$ |
| P4 | 7348 | 22250 | $0.56 \times 10^6$ | $0.79 \times 10^6$ |
| P5 | 8947 | 22224 | $0.45 \times 10^6$ | $0.59 \times 10^6$ |
| P6 | 10375 | 22468 | $0.38 \times 10^6$ | $0.46 \times 10^6$ |
| P7 | 12455 | 22347 | $0.25 \times 10^6$ | $0.31 \times 10^6$ |

In order to study the behaviour of transient channel flow using skin friction coefficient ($C_f$), He and Seddighi (2015) re-defined Eq.(4.3), representing the distance ($x$) from the leading edge as the distance at which a seeding particle travels, starting from the beginning of the transient flow. The distance at which the seeding particle travels is given as $x = tU_{b1}$, where $U_{b1}$, the final bulk flow, is the characteristic convective velocity, and $t$ is time stamp for a step increase transient flow. He and Seddighi (2015) obtained an equivalent Reynolds number after the substitution for $x = tU_{b1}$ to Eq. (4.3) as follows:

$$Re_t = \frac{tU_{b1}^2}{\nu} \tag{4.4}$$

It has been revealed by He and Seddighi (2015) that equivalent Reynolds number ($Re_t$) in unsteady transient flow has the same impact that $Re_x$ has on the transition to turbulence in flat plate boundary layer flow. Table 4-5 presents the parameters for all the cases presented.

Focusing on all the cases in the three groups, immediately after the start of the flow acceleration, the skin friction coefficient ($C_f$) increases sharply and reaches the peak for each of the cases in fractions of a second. The $C_f$ then decreases to its minimum value at critical equivalent Reynolds number $Re_{t,cr} = 1.32 \times 10^6$ for case T1, $Re_{t,cr} = 1.05 \times 10^6$ for case T2 and $Re_{t,cr} = 0.7 \times 10^6$ for case T3, as shown in Figure 4-9(a). For the T cases, the initial Reynolds number varied while the final Reynolds number ($Re_b \approx 24200$) remains fixed. As the initial Reynolds number increases, the critical equivalent Reynolds number $Re_{t,cr}$ decreases, increasing as the initial Reynolds number decreases. For the three T cases investigated, $Re_{t,cr}$ decreases from $1.32 \times 10^6$ to $0.7 \times 10^6$ as the initial Reynolds number ($Re_0$) increases from 3298 to 5100, as shown in Table 4-5.

For U cases, where the initial Reynold number is fixed to $Re_b \approx 2800$, the minimum value of $C_f$ occurs at $Re_{t,cr} = 1.86 \times 10^5$ for case U1, $Re_{t,cr} = 2.81 \times 10^5$ for case U2 and $Re_{t,cr} = 4.33 \times 10^5$ for case U3. An interesting observation during the analysis of results is that the value of $Re_{t,cr}$ increases as the final Reynolds number increases and decreases as the final Reynolds number decreases. Thus, it should be noted that the Reynolds number ratio has a significant impact on the process of transition to turbulence in transient channel flow. Figure 4-9(b) shows another important characteristic behaviour of $C_f$ during the transition to turbulence. The levels of undershooting of $C_f$ for the three U cases are large compared to that of T cases and P cases. For the U cases, the level of undershooting of $C_f$ is large for the case U3 with a higher Reynolds number ratio and the undershooting becomes smaller as the Reynolds number ratio decreases when the final Reynolds number decreases, as in the case of U1.

Furthermore, the minimum values of $C_f$ for P1 and P7 occurs at $Re_{t,cr} = 0.80 \times 10^6$ and $Re_{t,cr} = 0.25\times 10^6$, as shown in Table 4-5. In these cases, the final Reynolds number is fixed $Re_b \approx 22400$ while the initial Reynolds number varied between $Re_b = 4192$ and $Re_b = 12455$ at different temperatures. As with T cases, the critical equivalent Reynolds number $Re_{t,cr}$ decreases as the initial Reynolds number increases and vice versa, as shown in Figure 4-9(c). The trend of $C_f$ shows a small undershoot as the Reynolds number ratio reduces, becoming subtle for the last case (P7) investigated.

The response of $C_f$ during acceleration of transient channel flow for all cases investigated is similar to that of flat plate boundary layer flow reported by Jacobs and Durbin (2001) and Nagarajan et al. (2007) and can be used to determine the onset of transition (minimum value of $C_f$) and the completion of transition process (the first peak attained when $C_f$ increases again). The minimum value of $C_f$ corresponds, in comparison with the flow the visualisation of Figure 4-4, 4-5, 4-6 & 4-7, to the point where turbulence spots are first seen initially. The completion of the transition procedure corresponds to the point where the wall-bounded channel surface has been filled with newly generated turbulence. The overall $C_f$ development for the cases when the initial Reynolds number varied with a final fixed Reynolds number and the cases with a fixed initial Reynolds number with different final Reynolds numbers is similar to that of the numerical study of He and Seddighi (2015). The variation of the skin friction coefficient ($C_f$) with equivalent Reynolds number ($\mathrm{Re}_\mathrm{t}$) reveals the effect of critical Reynolds number on the ratio of initial Reynolds number ($Re_0$) and the final Reynolds number ($Re_1$). By considering T and P cases, the results obtained show that critical Reynolds number ($Re_{t,cr}$) decreases as the Reynolds number ratio decreases; that is $Re_{t,cr}$ decreases as the initial Reynolds number is increases, as shown in Table 4-5. On the other hand, $Re_{t,cr}$ increases as the Reynolds number ratio increases for the U cases, which means $Re_{t,cr}$ increases as the final Reynolds number increases. These observations have shown that the process of transition to turbulence is affected by Reynolds number ratio. Thus, the results are consistent with the numerical findings previously presented by He and Seddighi (2015). As can be seen in Figure 4-9, more wiggles are visible in the plots due to the limited number of realisations. For complete eradication of the wiggles in the plots, the number of realisation needs to be increased far above the present 80 repeated experimental runs.

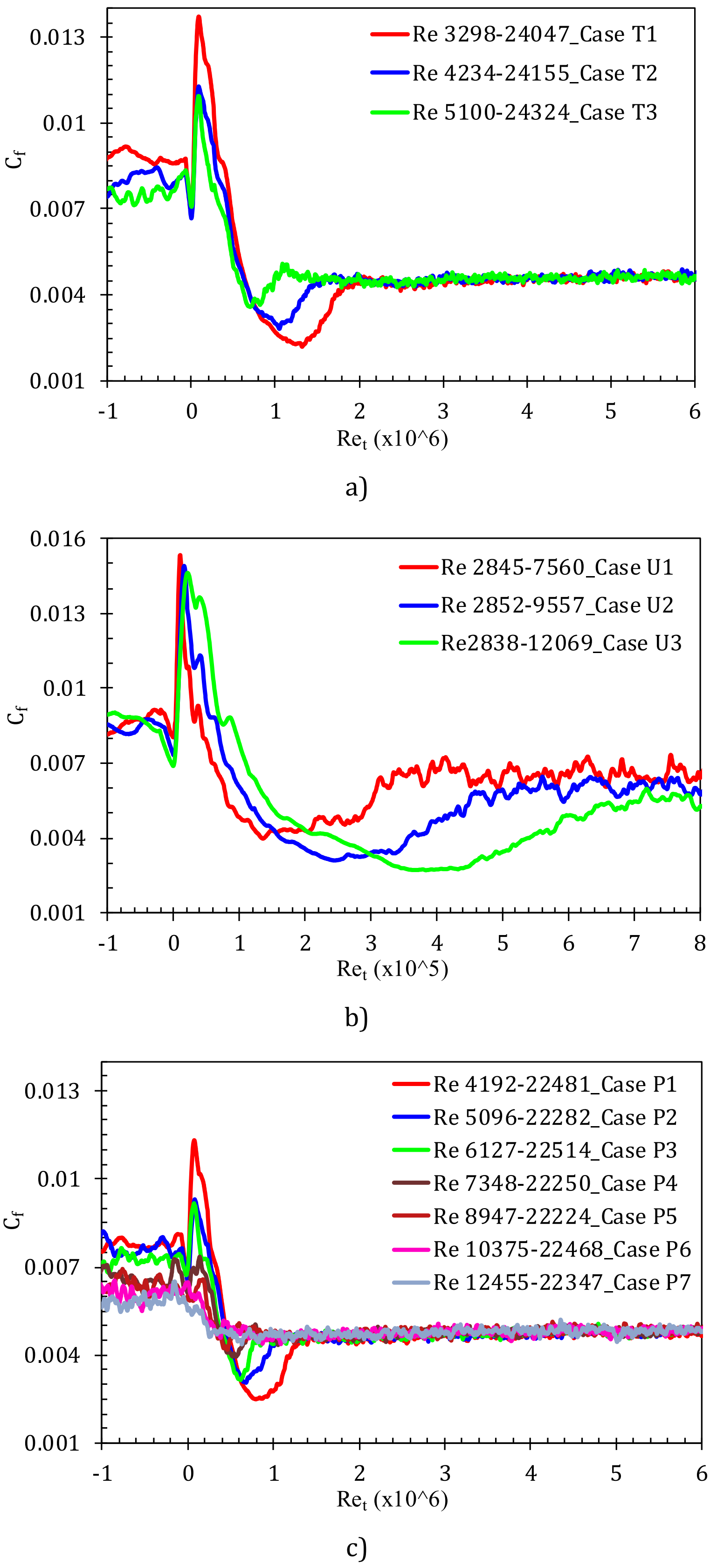

***Figure 4-9: Variation of skin friction coefficient ($C_f$) with equivalent Reynolds number ($Re_t$). a) T cases, b) U cases and c) P cases.***

### 4.3.2 Behaviour of wall shear stress of varying Reynolds numbers ratio in channel flow

Wall shear stress is an expedient integral flow parameter that reveals the overall behaviour of flow during the flow acceleration. The wall shear stress of this present research is obtained through constant temperature anemometry (CTA) utilising flush-mounted hot-film sensors. The procedure for data acquisition of the wall shear stress has previously been described in § 3.7 and the responses of wall shear stress for all the cases investigated are presented here. Table 4-1 and Table 4-2 show the flow conditions for all the three groups investigated. The variation of wall shear stress with time during the transient flow for cases T1-T3 is presented in Figure 4-10. The response of wall shear stress during the transient flow for cases U1-U3 is shown in Figure 4-11. For brevity, the response of wall shear stress for cases P1-P3 is presented in Figure 4-12. Moreover, the results of quasi-steady flow are derived by the following procedures: 1) obtain the steady results of wall shear stress and the Reynolds number over the range that covered all the transient flow cases, 2) perform interpolation on the steady wall shear stress and Reynolds number obtained in order to determine the quasi-steady value for each flow condition. The equivalent quasi-steady results obtained are plotted with wall shear stress results on a single figure for comparison. The transient responses of wall shear stress of the current investigations have been shown to occur in a three-stage development similar to the trend of wall shear stress previously reported by He et al. (2008, 2011), He and Ariyaratne (2011), Seddighi et al. (2011, 2014) and Sundstrom and Cervantes (2017). For all cases investigated, at stage one of the transient flows, immediately after the start of the flow acceleration, the wall shear stress increases rapidly and overshoots the quasi-steady flow then undershoots the quasi-steady flow, as shown in Figures 4-10, 4-11 and 4-12,.

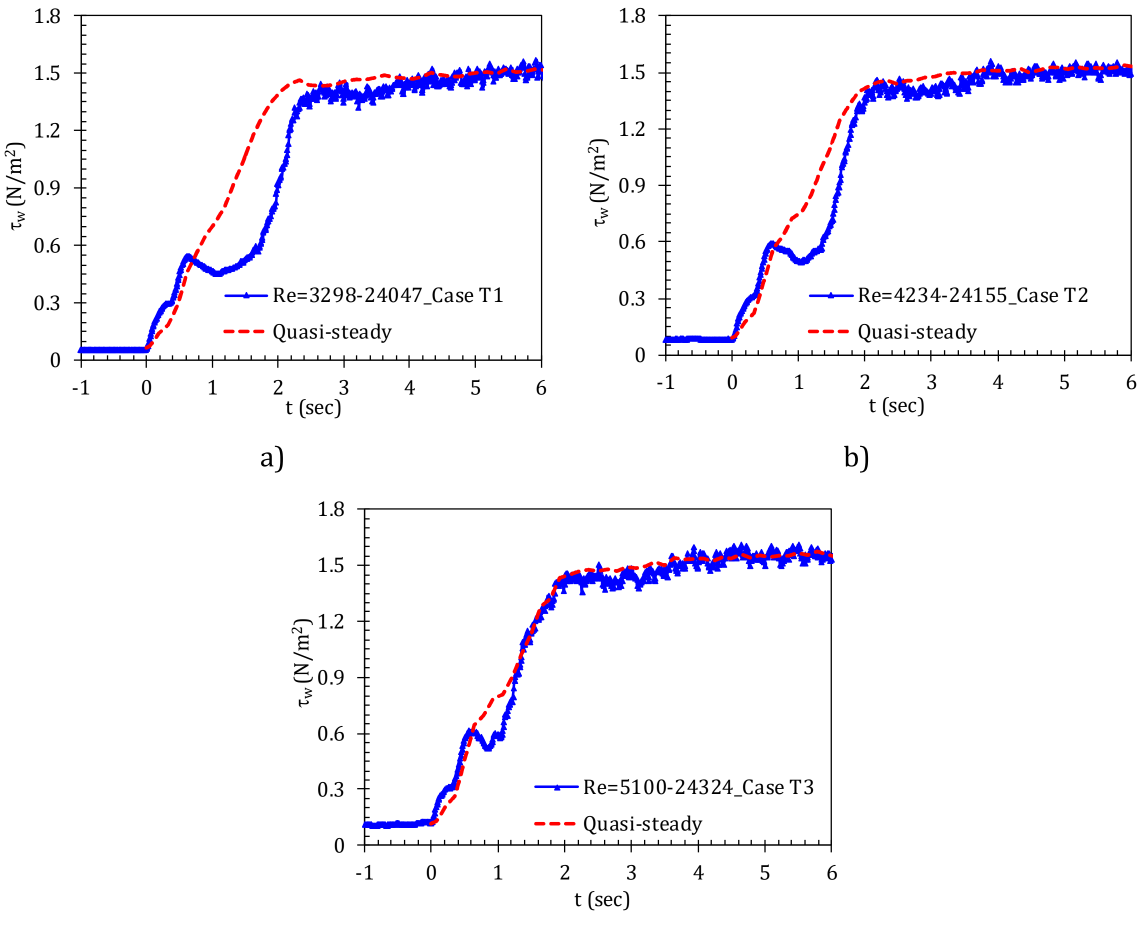

a)

b)

c)

***Figure 4-10: Wall shear stress development for cases (T1, T2 & T3) during transient flow.***

As with the response of skin friction coefficient previously reported, a sharp increase in wall shear stress resulted from the formation of a thin boundary layer with high viscous force and velocity gradient. During this period, turbulence is “frozen” near the wall. As the thin boundary layer increases with time to the flow, both viscous force and velocity gradient decrease, then the wall shear stress decreases and undershoots the quasi-steady flow. Stage two, which is the onset of transition, is characterised by the formation of “new” turbulence that causes the wall shear stress to increase rapidly to a quasi-steady flow. At stage three, wall shear stress approaches the quasi-steady-value and fluctuates around that value, as shown in Figure 4-10, 4-11 and 4-12 for all cases investigated. An impressive characteristic behaviour of the response of wall shear stress to different Reynolds number ratios is revealed, as shown in all the cases presented; the level of undershooting of wall shear stress reduces when the Reynolds number ratio reduces and it increases as the Reynolds number ratio increases. The response of wall shear stress in U cases shows a bigger undershoot compared to T and P cases because of the low final Reynolds numbers of the U cases, but the procedure of transition to turbulence is the same.

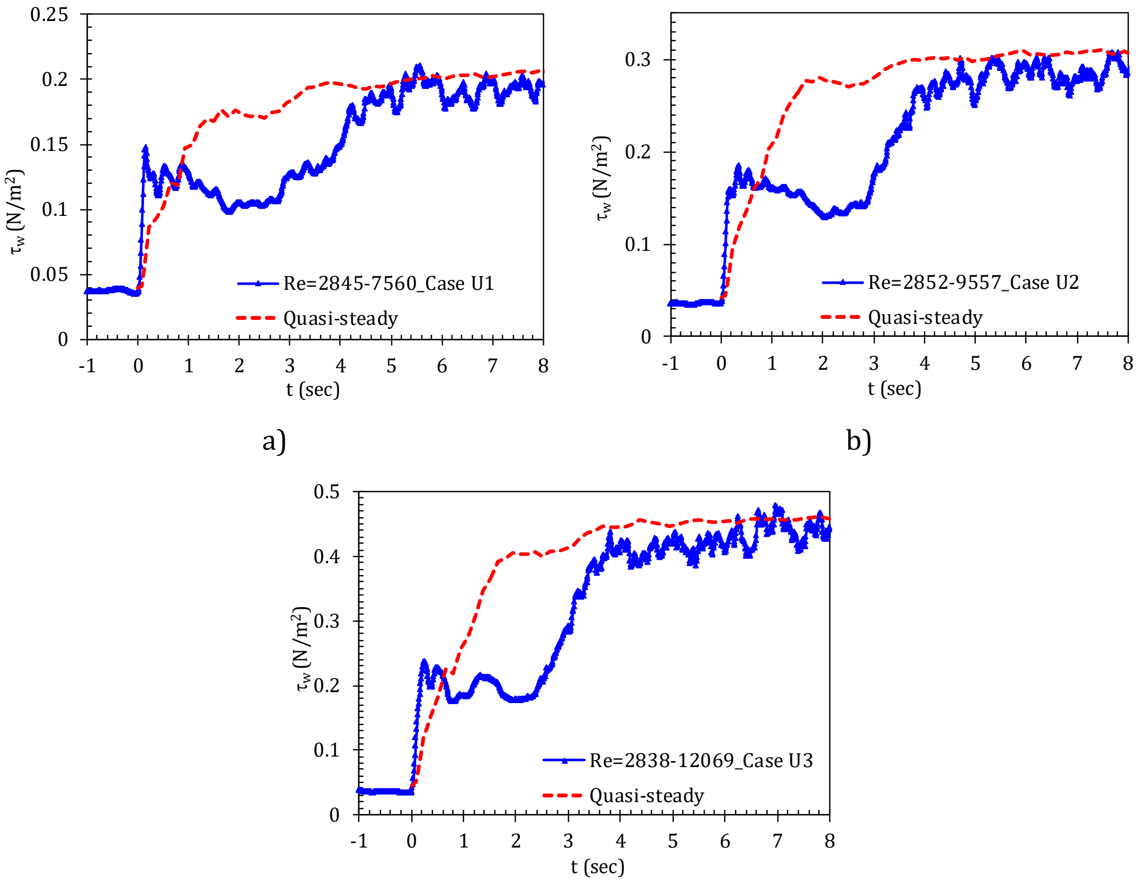

a)

b)

c)

*Figure 4-11: Wall shear stress development for cases (U1, U2 & U3) during transient flow.*

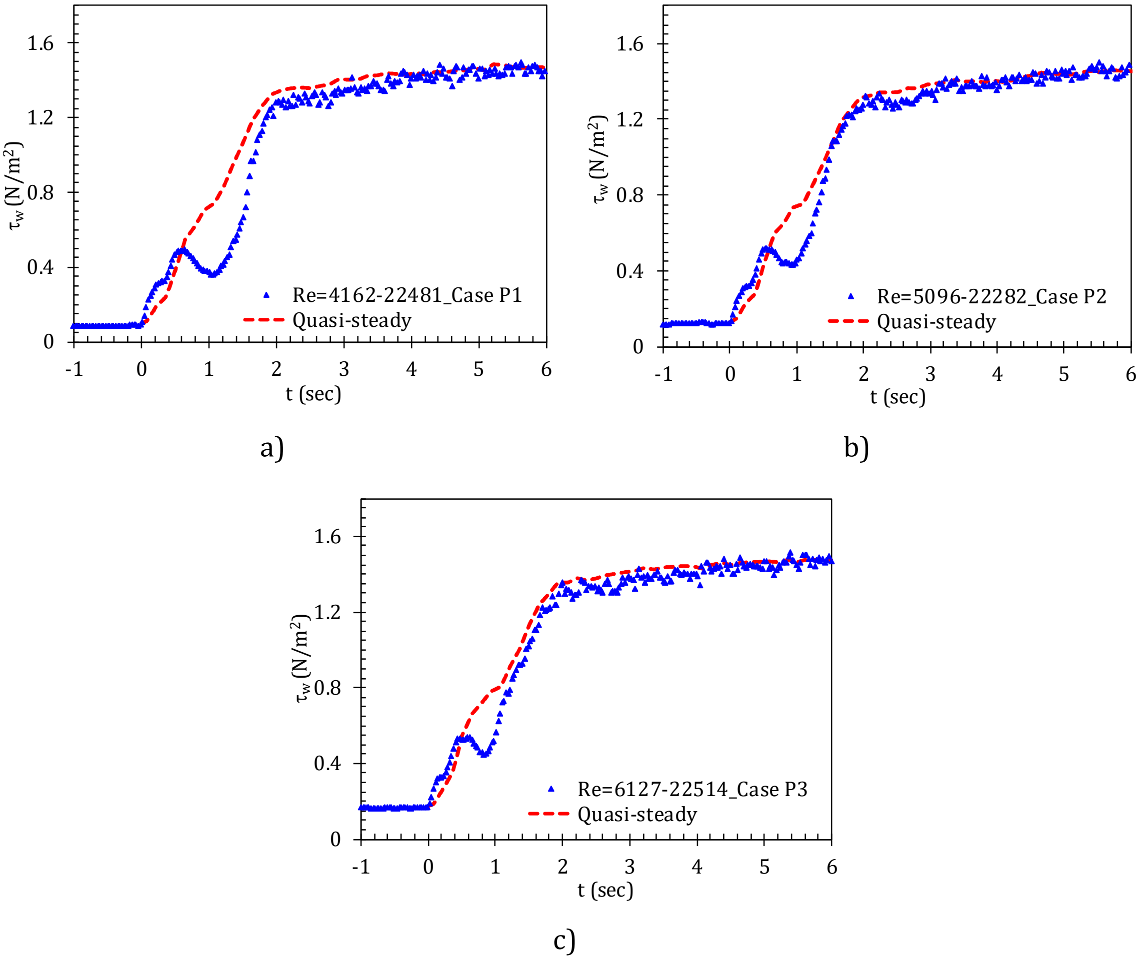

a) b) c)

*Figure 4-12: Wall shear stress development for cases (P1, P2 & P3) during transient flow.*

### 4.3.3 Behaviour of mean velocity and turbulence statistics of varying Reynolds numbers ratios in channel flow

In this section, the behaviours of streamwise mean velocity, streamwise fluctuating velocity (r.m.s), wall-normal fluctuating velocity (r.m.s), and turbulence stresses of the flow subjected to different Reynolds number ratios are discussed. The discussion of this section is based on two groups for brevity: in group one, there are three cases with a fixed final Reynolds number and different intial Reynolds; group two comprises the cases with a fixed initial Reynolds number and different final Reynolds numbers, as shown in Table 4-1.

The required flow variation for all the cases presented in Table 4-1 is obtained when the pneumatic control valve is opened suddenly from the initial flow condition to the final flow condition. In these experiments, vertical-PIV orientation is used for data acquisition. Ensemble and spatial averages are performed on the acquired data for the determination of mean, r.m.s fluctuating velocities and Reynold shear stress. The growth of the transient turbulent flow is studied at different wall locations $y/_h$=0.07, 0.2, 0.45 and 1 and at different time instants.

### *4.3.3.1 Development of mean velocity and turbulence statistics at different wall locations*

The response of streamwise mean velocity $(U)$, streamwise fluctuating velocity $(u'_{rms})$, wall-normal fluctuating velocity $(v'_{rms})$ and the Reynolds shear stress $(\overline{u'v'})$ during the transient turbulent flow is investigated. Immediately following the commencement of transient turbulent flow, the streamwise mean velocity $(U)$ at the selected wall locations responds in a plug-like fashion, as shown in Figures 4-13a, 4-14a and 4-15a for cases T1, T2 and T3, respectively. There are four subplots that are used to describe the development of streamwise mean velocity and turbulence statistics $(u'_{rms}, v'_{rms}$ and $\overline{u'v'})$ for each of the cases - all the subplots in each case share the same legend. During the pre-transtional time frame the streamwise fluctuating velocity $(u'_{rms})$ responds near the wall of the channel immediately after the commencement of the flow acceleartion, but it experiences a delay in the centre of the flow, as shown in Figures 4-13b, 4-14b and 4-15b for cases T1, T2 and T3, respectively. The transportation of turbulence from the wall to the centre of the flow reveals a diffusion mechanism that is associated with the unsteady flow's feature, which was reported by He and Jackson (2000). For all three cases investigated, a small jump of streamwise fluctuating velocity $(u'_{rms})$ in the centre region occurs immediately after the start of the transient turbulent flow. The small jump is due to the finite repeatability of the quick opening of the pneumatic control valve. In the experimental investigation of transient turbulent flow of Gorji (2015) using particle image velocimetry (PIV) and laser dropper velocimetry (LDV) for data acquisition, it is established by Gorji (2015) that a controlled valve opening does not suffer from this shortcoming. The quick response of $u'_{rms}$ near the wall region is caused by the elongation of the initial streaky structures during the pre-transitional time frame. This establishes the fact that the elongation of the pre-existing streaky structures occurs first in the near wall region. The elongation of the streaky structures is equivalent to the rapid development of the energy of the perturbations in the buffeted laminar region before the start of transition to turbulence in a flat plate boundary layer flow (Jacobs & Durbin, 2001; Nagarajan et al., 2007). Another interesting observation to note during the pre-transitional time frame is that the wall-normal fluctuating velocity ($v'_{rms}$) and and the Reynolds shear stress ($\overline{u'v'}$) neither respond to the response of the streamwise fluctuating velocity ($u'_{rms}$), nor to the quick opening of the pneumatic control valve. The lack of response of both $v'_{rms}$ and $\overline{u'v'}$ during the pre-transitional time frame reveals that no ''new'' turbulence is generated during that period.

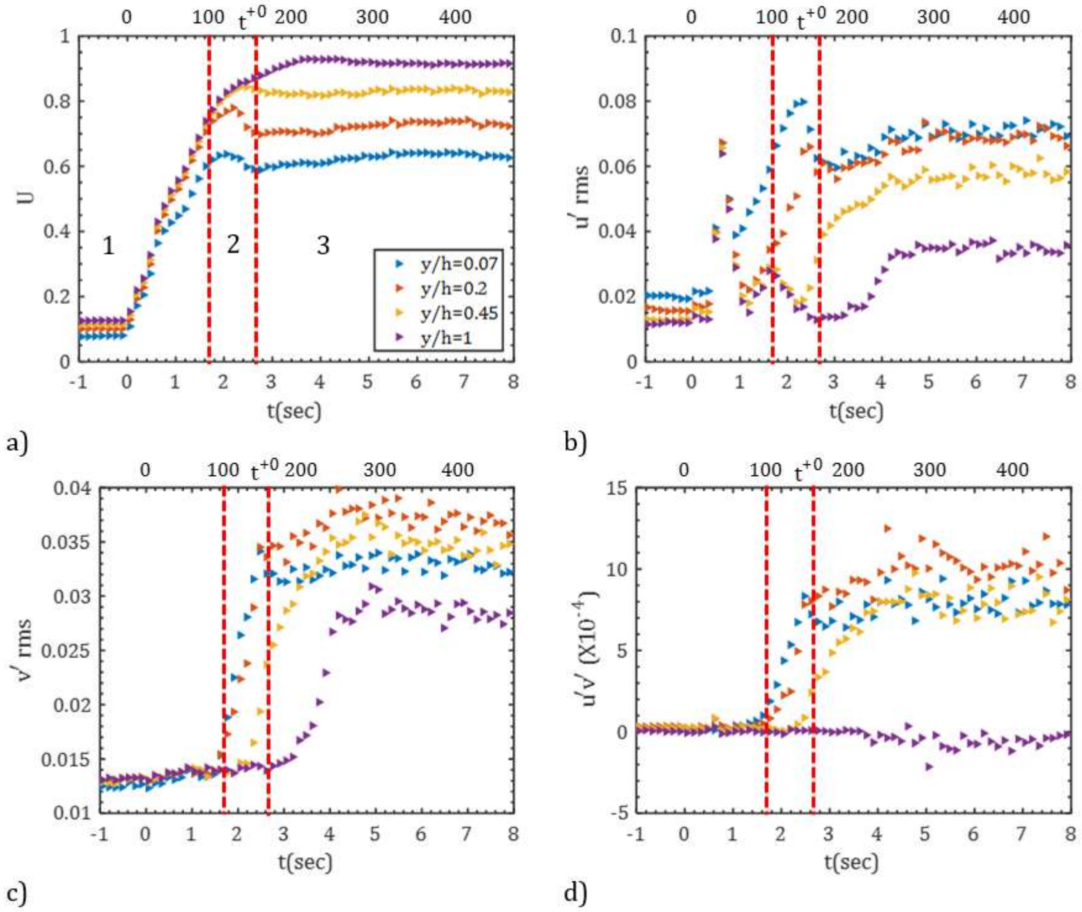

***Figure 4-13: Temporal growth of streamwise mean velocity ($U$), streamwise fluctuating velocity ($u'_{rms}$), wall-normal fluctuating velocity ($v'_{rms}$) and Reynolds shear stress ($\overline{u'v'}$) for case T1 ($Re_b = 3298 - 24047$). Legend is the same for the four subplots and all quantities are not normalised. The unit of subplots (a)-(c) is m/s and that of subplot (d) is $m^2/s^2$. 1) pre-transition, 2) transition and 3) fully turbulence. Channel half-height δ=h.***

Furthermore, it is revealed by the data that during the transitional time frame both wall-normal fluctuating velocity ($v'_{rms}$) and the Reynolds shear stress ($\overline{u'v'}$) start to respond, as shown in Figures 4-13(c,d), 4-14(c,d) and 4-15(c,d) for cases T1, T2 and T3, respectively. The start of the response of $v'_{rms}$ and $\overline{u'v'}$ near the wall marks the onset of transition (at $t^* = 52$ for case T1, $t^* = 43$ for case T2 and $t^* = 29$ for case T3). The onset of transition recorded using $v'_{rms}$ coincides with the previous onset of transition reported using skin friction coefficient ($C_f$) ( $t^* = 55$ for case T1, $t^* = 43$ for case T2 and $t^* = 29$ for case T3), as presented in Table 4-3. Gorji (2015) used the value of $v'_{rms}$ near the wall when it begins to respond to flow acceleration to determine the critical time, $t_{cr}$, for the calculation of the critical Reynolds number.

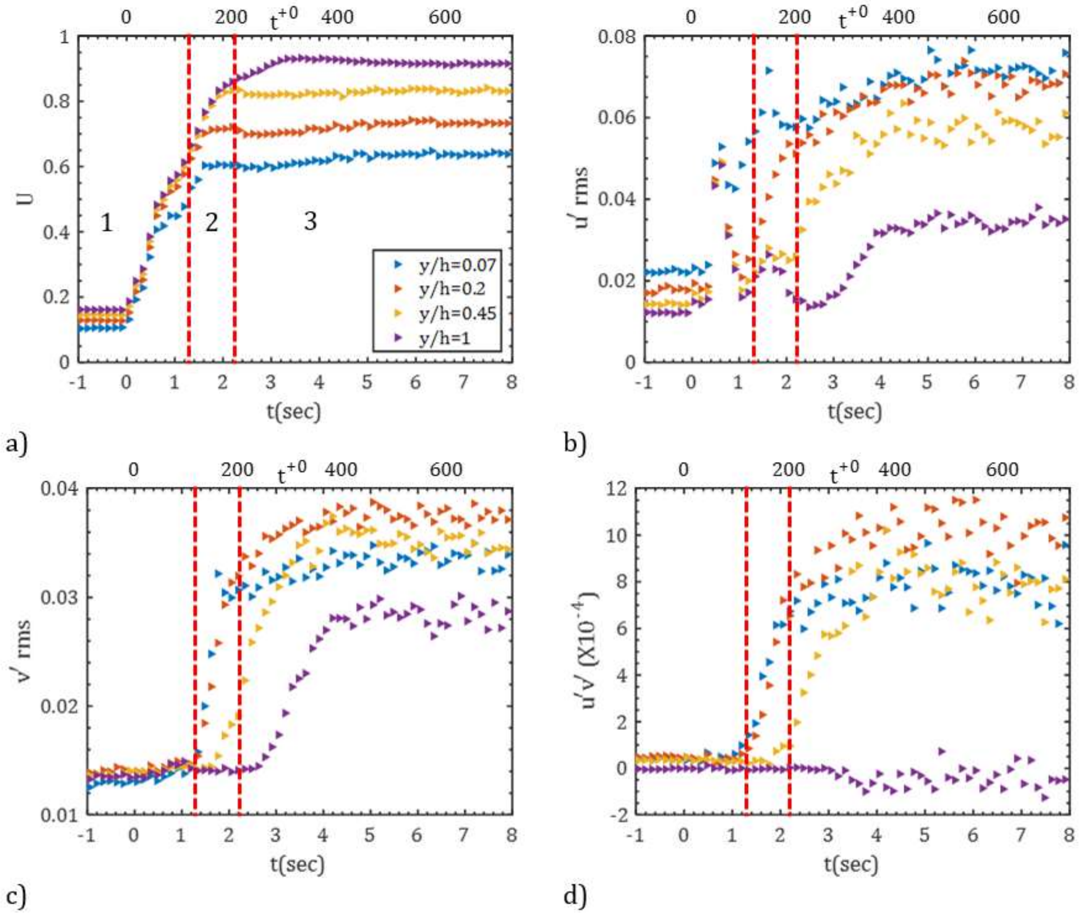

***Figure 4-14: Temporal growth of streamwise mean velocity ($U$), streamwise fluctuating velocity ($u'_{rms}$), wall-normal fluctuating velocity ($v'_{rms}$) and Reynolds shear stress ($\overline{u'v'}$) for case T2 ($Re_b = 4234 - 24155$). Legend is the same for the four subplots and all quantities are not normalised. The unit of subplots (a)-(c) is m/s and that of subplot (d) is m$^2$/s$^2$. 1) pre-transition, 2) transition and 3) fully turbulence. Channel half-height δ=h.***

In the transitional time frame, $u'_{rms}$ increases to its maximum peak, approaches or slightly overshoots the statistically steady values and then decreases to the final statistically steady values. The obvious decrease at the location near the wall can be attributed to the breakdown of streaky structures and the formation of turbulence spots in the flow. This process of breaking down of the streaky structures and the generation of turbulence spots results in the turbulence kinetic energy redistribution to the wall-normal fluctuating velocity ($v'_{rms}$). It is revealed that, as the Reynolds number ratio reduces (due to an increase of the initial Reynolds number while the final Reynolds number remains fixed) from 7.29 (case T1) to 4.77 (case T3), as shown in Table 4-1, the onset of transition to turbulence also reduces from $t^* = 52$ to $t^* = 29$ for cases T1 and T3, respectively. It is also noted that as the Reynolds number ratio reduces, the turbulence characteristic in the flow becomes subtle. For instance, in the case T3 with a smallest value of Reynolds number ratio, the slight reduction of $u'_{rms}$ in transitional time frame responsible for the formation of turbulence spots does not appear, as shown in Figure 4-15b. The transitional period is very short in case T3, even at the completion of transition using $C_f$, the wall -normal fluctuating velocity $v'_{rms}$ increases. It shows that more turbulence generates near the wall after the completion of turbulence and propagtes to the flow with time for case T3. It can been seen that the transitional period decreases as the initial Reynolds number increases and vice versa.

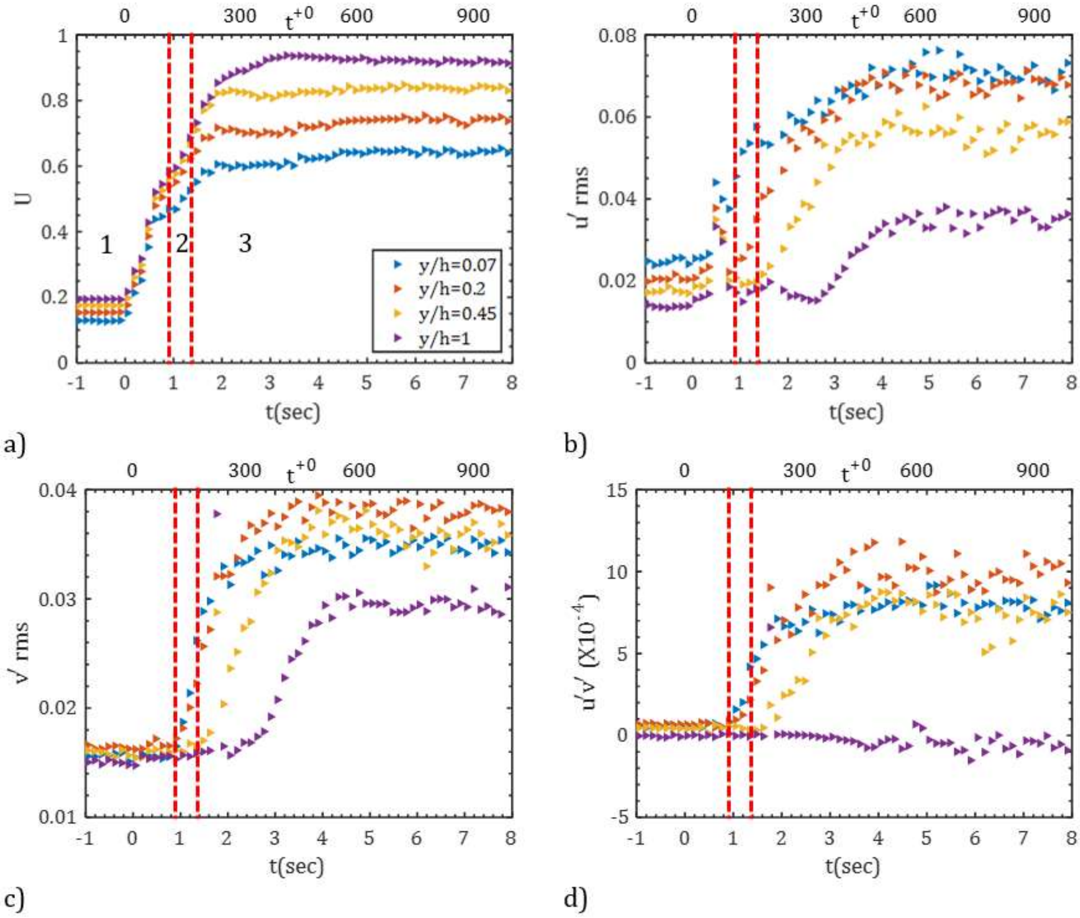

***Figure 4-15: Temporal growth of streamwise mean velocity ($U$), streamwise fluctuating velocity ($u'_{rms}$), wall-normal fluctuating velocity ($v'_{rms}$) and Reynolds shear stress ($\overline{u'v'}$) for case T3 ($Re_b = 5100 - 24324$). Legend is the same for the four subplots and all quanties are not normalised. The unit of subplots (a)-(c) is m/s and that of subplot (d) is $m^2/s^2$. 1) pre-transition, 2) transition and 3) fully turbulence. Channel half-height δ=h.***

The growth of streamwise mean velocity ($U$) and turbulence statistics ($u'_{rms}$ $v'_{rms}$ & $\overline{u'v'}$) of the rapid accelerating flow presented in Figures 4-13, 4-14 and 4-15 is similar to the rapid accelerating flow of Gorji (2015) and Mathur et al. (2018), and the slow accelerating flow of Seddighi et al. (2014). From the figures, it is evident that the onset of transition to turbulence decreases as the initial Reynolds number increases. The flow behaviours described above are based on the new theory relating transient flow to boundary layer bypass transition by He and Seddighi (2013; 2015). The data at the location near the wall ($^{y}/_{h} = 0.07$) for wall-normal fluctuating velocity ($v'_{rms}$) and the Reynolds shear stress ($\overline{u'v'}$) in three T cases (Figures 4-13, 4-14 and 4-15) dropped and mixed with the data of other locations due to higher values of initial Reynolds numbers of the T cases and the experimental uncertainty during the experiments. Moreover, the data of Reynolds shear stress ($\overline{u'v'}$) for the three T cases at the wall location of ($^{y}/_{h} = 1$ (centreline)) fluctuates between negative and positive values. This is due to experimental uncertainty during the experiments.

The second group (U cases) tests the effect of changing the final Reynolds number. The response of streamwise mean velocity and the turbulence statistics ($u'_{rms}$ $v'_{rms}$ & $\overline{u'v'}$) is similar to that of cases T1, T2 and T3 previously discussed. The flow development for each of the cases investigated is observed at the selected wall locations of $^{y}/_{\delta} = 0.07, 0.2. 0.45$ and 1. The response of the wall-normal fluctuating velocity ($v'_{rms}$) during the transitional time frame is used to determine the onset of transition, and the values are compared with the onset of transition obtained using skin friction coefficient ($C_f$). Immediately after the commencement of the transient turbulent flow, when the pneumatic control valve opens suddenly, streamwise mean velocity ($U$) responds like a plug flow (that is the flow responds as a solid body everywhere in the flow region apart from the location near the wall) and increases uniformly across all the selected wall locations, as shown in Figures 4-16a, 4-17a and 4-18a for cases U1, U2 and U3, respectively. The streamwise fluctuating velocity ($u'_{rms}$) responds near the wall during the pre-transitional time frame but experiences a delay in the centre of the flow of the three cases investigated, as shown in Figures 4-16b, 4-17b and 4-18b. It is observed during the pre-transitional time frame that both wall-normal fluctuating velocity ($v'_{rms}$) and Reynolds shear stress ($\overline{u'v'}$) remain unchanged to sudden opening of pneumatic control valve and the response of streamwise fluctuating velocity ($u'_{rms}$). As the distance from the wall increases, the delay of $u'_{rms}$, $v'_{rms}$ and $\overline{u'v'}$at the centre of the flow appears alike. The rapid increase of $u'_{rms}$ during the pre-transitional time frame is due to the elongation of the initial streaky structures in the flow.

Moreover, at the onset of transition, $v'_{rms}$ and $\overline{u'v'}$ components start to respond to the flow acceleration, as shown in Figures 4-16(c,d), 4-17(c,d) and 4-18(c,d), and at the transitional time frame, $u'_{rms}$ increases and attains its maximum peak then decreases to its statistically steady value. As previously stated, the sudden decrease from its peak to the statistically steady value at the location near the wall is due to the breakdown of the streaky structure in the flow and the formation of turbulence spots. The point where $u'_{rms}$ decreases to the statistically steady value near the wall marks the end of transition. As the final Reynolds number increases, the time at which $v'_{rms}$ responds decreases.

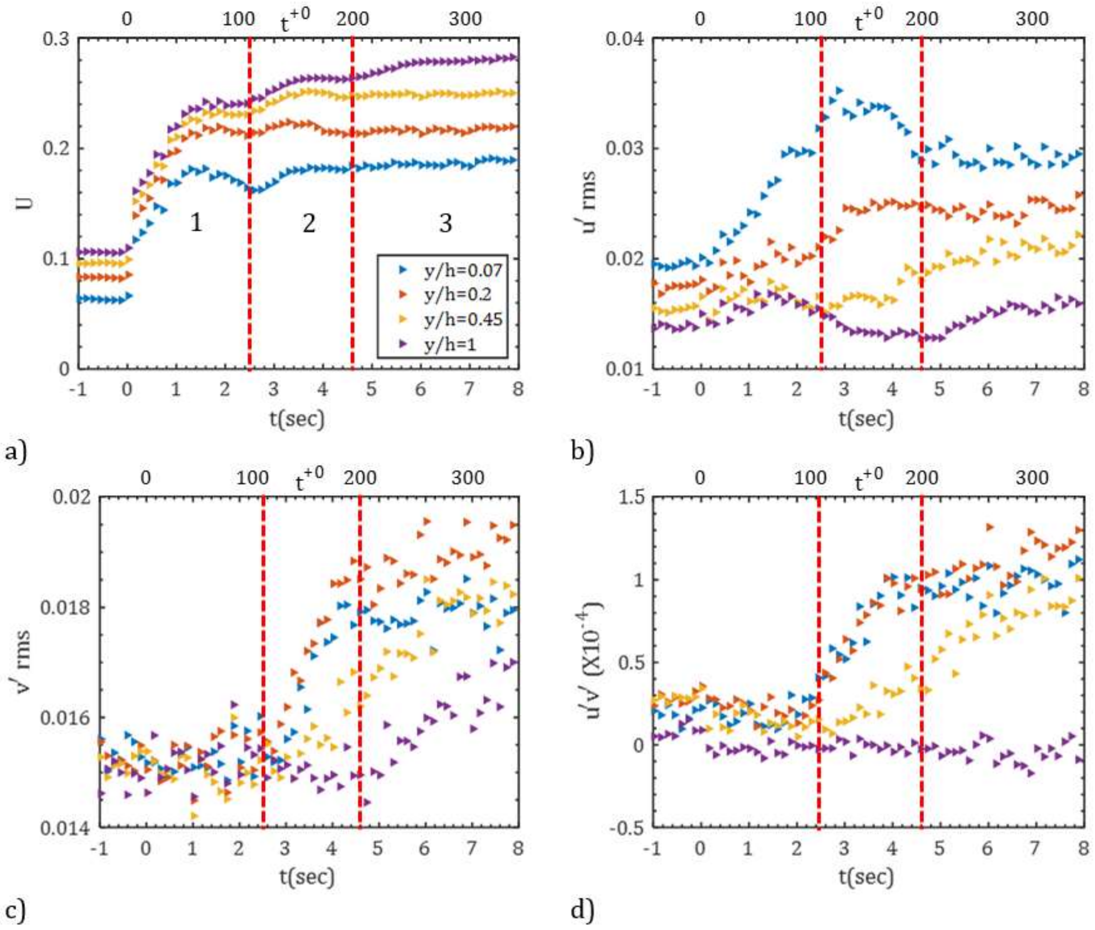

***Figure 4-16: Temporal growth of streamwise mean velocity ($U$), streamwise fluctuating velocity ($u'_{rms}$), wall-normal fluctuating velocity ($v'_{rms}$) and Reynolds shear stress ($\overline{u'v'}$) for case U1 ($Re_b = 2845 - 7560$). Legend is the same for the four subplots and all quantities are not normalised. The unit of subplots (a)-(c) is m/s and that of subplot (d) is m²/s².: 1) pre-transition, 2) transition and 3) fully turbulence. Channel half-height δ=h.***

The onset of transition obtained using $v'_{rms}$ in this section is compared here with that obtained using minimum value of skin friction coefficient ($C_f$) for the same experimental cases (U1, U2 and U3). As previously presented in section §4.4.1, the onsets of transition are 2.51 secs ($t^* = 25$), 2.37 secs ($t^* = 29$).and 2.29 secs ($t^* = 36$) for cases U1, U2 and U3, respectively. The values of the onset of transition obtained using $v'_{rms}$ are 2.58 secs ($t^* = 25$), 2.44 secs ($t^* = 30$) and 2.30 secs ($t^*$ =36). The times coincide with each other with a slight variation due to the frequency ($7Hz$) pulsation of the laser used during the experiments.

The effect of varying Reynolds number ratios on the transient process of an initially turbulent flow is here examined. The results obtained show that the onset of transition decreases as the

Reynolds number ratio (due to an increase in initial Reynolds number) decreases for the T cases. However, when the initial Reynolds number remains fixed while the final Reynolds number changes, the onset of transition decreases as the Reynolds number ratio increases, as shown in U cases.

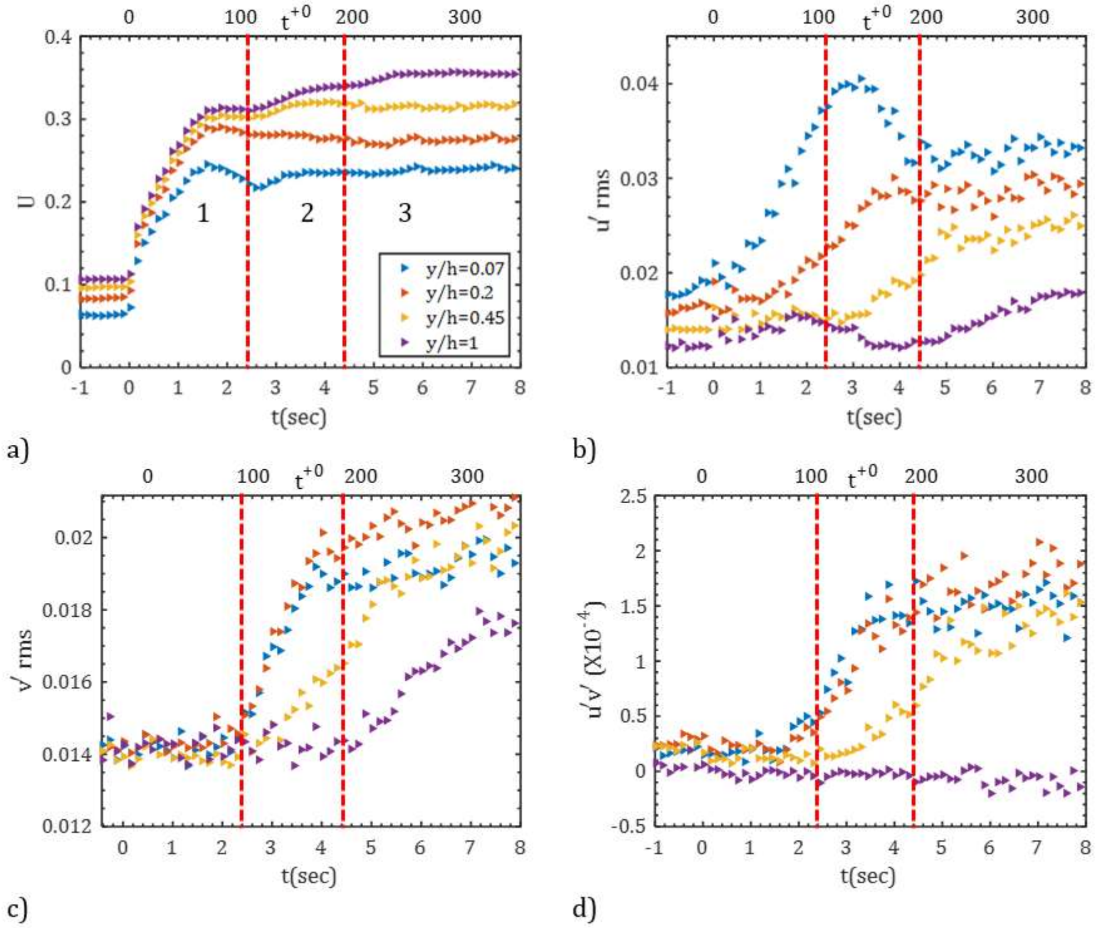

***Figure 4-17: Temporal growth of streamwise mean velocity $(U)$, streamwise fluctuating velocity $(u'_{rms})$, wall-normal fluctuating velocity $(v'_{rms})$ and Reynolds shear stress $(\overline{u'v'})$ for case U2 $(Re_b = 2852 - 9557)$. Legend is the same for the four subplots and all quanties are not normalised. The unit of subplots (a)-(c) is m/s and that of subplot (d) is m$^2$/s$^2$. 1) pre-transition, 2) transition and 3) fully turbulence. Channel half-height δ=h.***

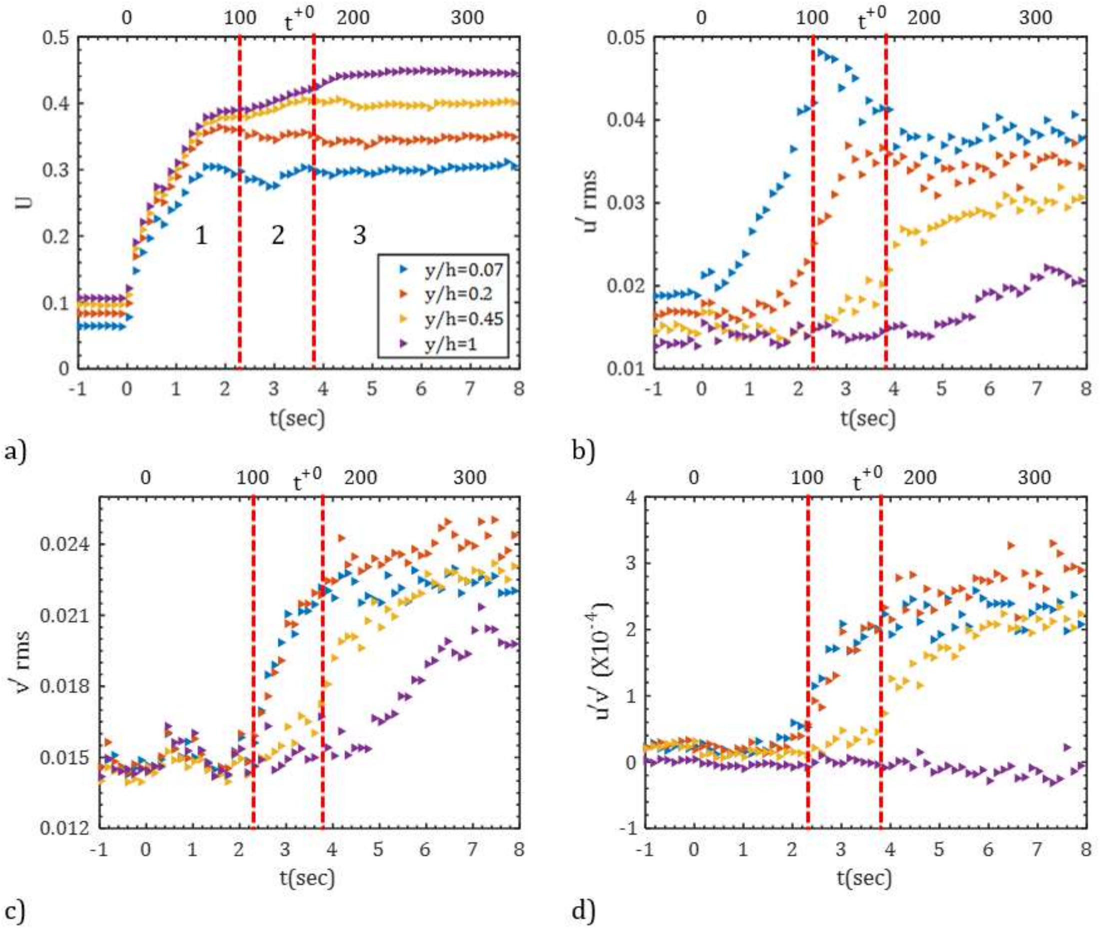

***Figure 4-18: Temporal growth of streamwise mean velocity $(U)$, streamwise fluctuating velocity $(u'_{rms})$, wall-normal fluctuating velocity $(v'_{rms})$ and Reynolds shear stress $(\overline{u'v'})$ for case U3 $(Re_b = 2838 - 12069)$. Legend is the same for the four subplots and all quanties are not normalised. The unit of subplots (a)-(c) is m/s and that of subplot (d) is m²/s². 1) pre-transition, 2) transition and 3) fully turbulence. Channel half-height δ=h.***

### 4.3.3.2 Time development of wall normal profiles of the mean velocity and turbulence statistics

In this section, the time development of the profile in cases T1-T3 and cases U1-U3 are discussed. The flow conditions for each of the cases has been previously discussed in §4.2 and are presented in Table 4-1. Figures 4-19 - 4-24 show the time development of the profiles of the streamwise mean velocity $(U)$, streamwise fluctuating velocity $(u'_{rms})$, wall-normal fluctuating velocity $(v'_{rms})$ and Reynolds shear stress $(\overline{u'v'})$ for all the cases investigated. Each figure comprises four subplots that are used to describe the development of streamwise mean velocity and turbulence statistics $(u'_{rms}, v'_{rms}$ and $\overline{u'v'})$. In each case, all the subplots share the same legend. The transient procedures, as described previously, are revealed during the flow acceleration for all the cases examined. The streamwise mean velocity ($U$) respond in a plug-like fashion and increases uniformly when the acceleration commences at all the instant times selected. The development of streamwise mean velocity is shown in Figures 4-19a, 4-20a and 4-21a for cases T1, T2 and T3, respectively, and Figures 4-22a, 4-23a and 4-24a for cases U1, U2 and U3, respectively. As shown from the figures, streamwise mean velocity increases and becomes flatter during the transitional period.

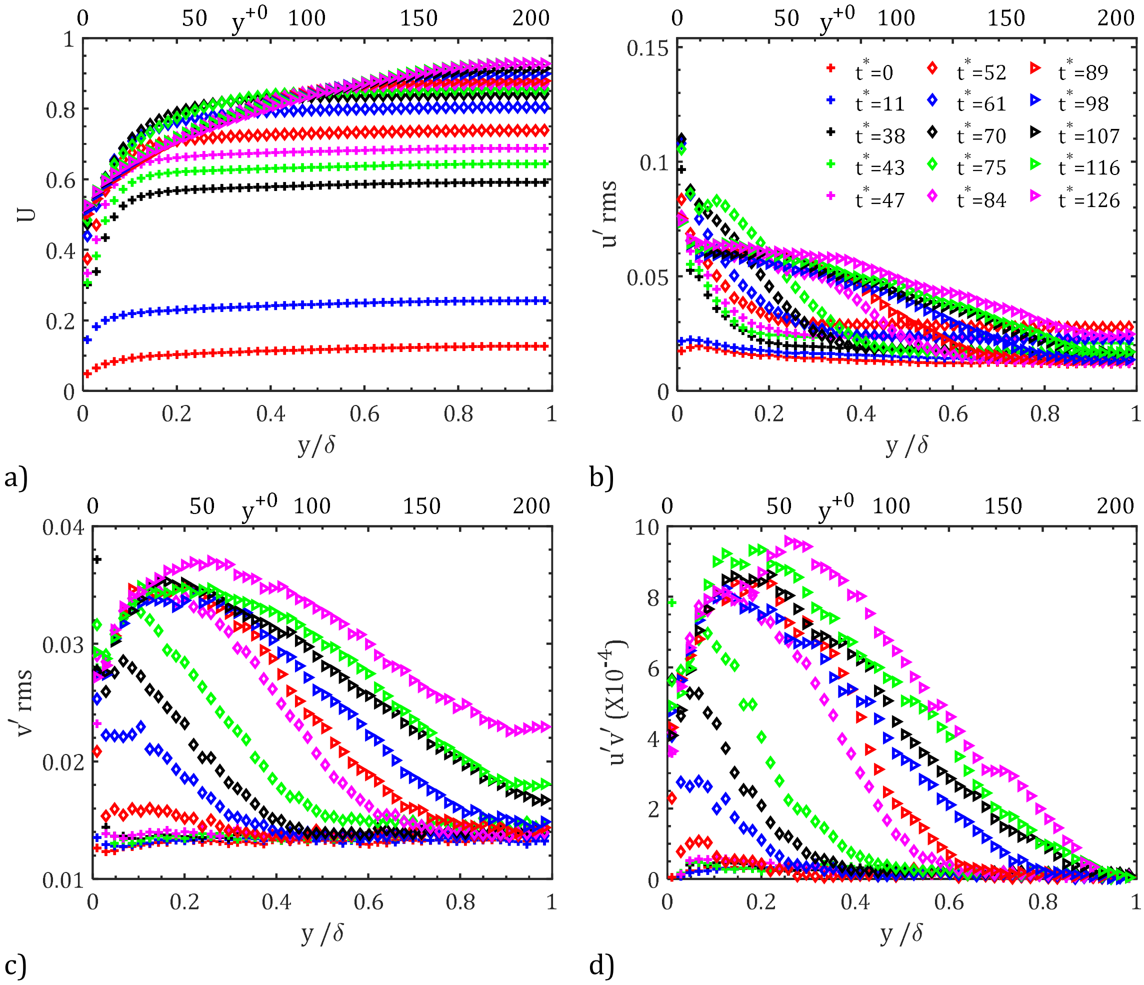

***Figure 4-19: Time development of streamwise mean velocity ($U$), streamwise fluctuating velocity ($u'_{rms}$), wall-normal fluctuating velocity ($v'_{rms}$) and Reynolds shear stress ($\overline{u'v'}$) for case T1 ($Re_b = 3298 - 24047$). Legend is the same for the four subplots. The unit of subplots (a)-(c) is m/s and that of subplot (d) is m$^2$/s$^2$.***

The profiles are observed to overlap each other when the flow has become fully developed turbulent flow for all the cases investigated. The profiles of streamwise mean velocity for all the cases are similar to those in the experimental study of Greenblatt and Moss (2004) on the transition to turbulence, and the investigation of transient turbulent transition using the large-eddy simulation (LES) by He et al. (2015). During the pre-transitional time frame, the streamwise fluctuating velocity ($u'_{rms}$) increases rapidly near the wall, as shown in Figures 4-19b, 4-20b and 4-21b for cases T1, T2 and T3, respectively and Figures 4-22b, 4-23b and 4-24b for cases U1, U2 and U3, respectively. At this time period, both wall-normal fluctuating velocity ($v'_{rms}$) and Reynolds shear stress ($\overline{u'v'}$) remain unchanged everywhere in the flow field as shown in Figures 4-19(c,d), 4-20(c,d) and 4-21(c,d) for cases T1, T2 and T3, respectively, and Figures 4-22(c,d), 4-23(c,d) and 4-24(c,d) for cases U1, U2 and U3, respectively. The rapid increase of $u'_{rms}$ during the pre-transitional time frame can be attributed to the modulation and elongation of the initial streaky structures in the flow. Further, the procedure of the streak elongation is equivalent to the growth of energy of the perturbations in the buffeted laminar region of the flat plate boundary layer flow Jacobs and Durbin (2001) and Nagarajan et al. (2007). It is revealed that no turbulence generation during the pre-transtional time frame, as both $v'_{rms}$ and $\overline{u'v'}$ remain unchanged. The time equivalent to when both $v'_{rms}$ and $\overline{u'v'}$ start responding to flow acceleration can be used to determine the onset of transition.

The wall-normal fluctuating velocity ($v'_{rms}$) and Reynolds shear stress ($\overline{u'v'}$) start to respond during the transitional time frame and increase to its peak. The time equivalent to when the two components ($v'_{rms}$ and $\overline{u'v'}$) start to respond to the flow acceleration marks the onset of transition. The onset of transition is obtained for each case using $v'_{rms}$, as $t^* = 52$ ($t = 1.62s$) for case T1 , $t^* = 43$ ($t = 1.33s$) for case T2 , $t^* = 29$ ($t = 0.90s$) for case T3 , $t^* = 25$ ($t = 2.58s$) for case U1 , $t^* = 30$ ($t = 2.44s$) , for case U2 and $t^* = 36$ ($t = 2.30s$) for case U3. At the transitional time frame, $u'_{rms}$ increases further to its peak near the wall then decreases slightly and overlaps at the completion of transition. This turbulence feature is seen clearly in the case T1 and is not very obvious as the Reynolds number ratio decreases due to an increase in the value of the initial Reynolds number for cases T2 and T3. This feature is seen clearly in all the U cases reported. The transitional time frames ($52 < t^* < 84$ for case T1, $43 < t^* < 71$ for case T2, $29 < t^* < 43$ for case T3, $25 < t^* < 45$ for case U1, $30 < t^* < 48$ for case U2, and $36 < t^* < 58$ for case U3 , obtained using $v'_{rms}$ and $u'_{rms}$ coincide with the onset of transition obtained using skin friction coefficient ($C_f$), as presented in Table 4-3. There is a slight variation between the time obtained by $v'_{rms}$ and $C_f$ due to the pulsation frequency ($Hz$) of the laser utilised during the experiments.

The time development reported for all the cases investigated shows a similar transition process to that of the numerical study of He et al. (2015) as both wall-normal fluctuating velocity ($v'_{rms}$) and Reynolds shear stress ($\overline{u'v'}$) start to respond to flow acceleration at the onset of transition . The effect of varying Reynolds number ratios on the transient process has been revealed from the T and U cases investigated. In cases T1, T2 and T3 with a fixed final Reynolds number and Reynolds number ratios of 7.29, 5.71 and 4.77, respectively, the results from the investigations using wall-normal fluctuating velocity ($v'_{rms}$), skin friction coefficient ($C_f$) and flow visualization have revealed that the onset of transition decreases as the Reynolds number ratio decreases. Further, for cases U1, U2 and U3 with the Reynolds number ratios of 2.66, 2.35 and 4.25, respectively, the onset of transition decreases as the final Reynolds number increases.

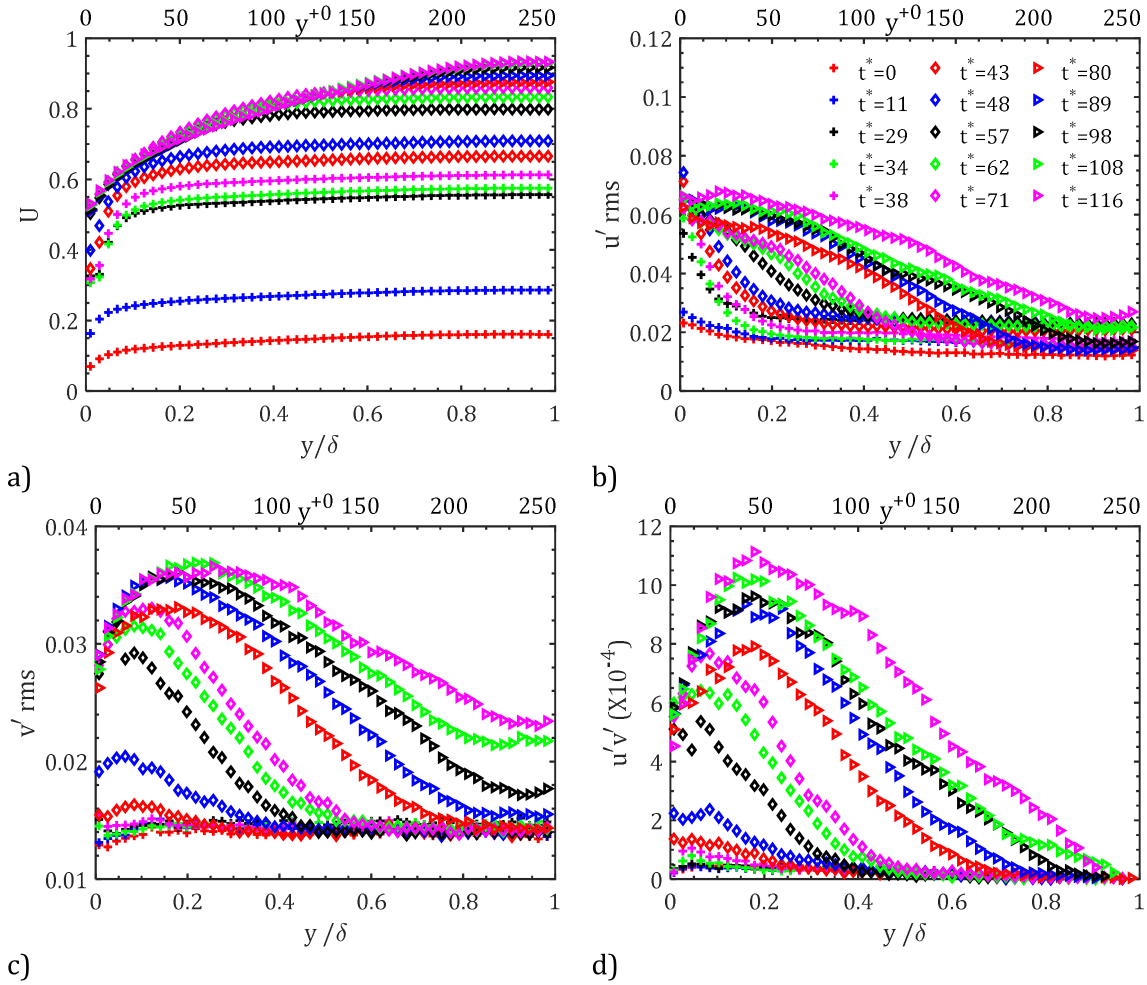

***Figure 4-20: Time development of streamwise mean velocity ($U$), streamwise fluctuating velocity ($u'_{rms}$), wall-normal fluctuating velocity ($v'_{rms}$) and Reynolds shear stress ($\overline{u'v'}$) for case T2 ($Re_b = 4234 - 24155$). Legend is the same for the four subplots. The unit of subplots (a)-(c) is m/s and that of subplot (d) is m²/s².***

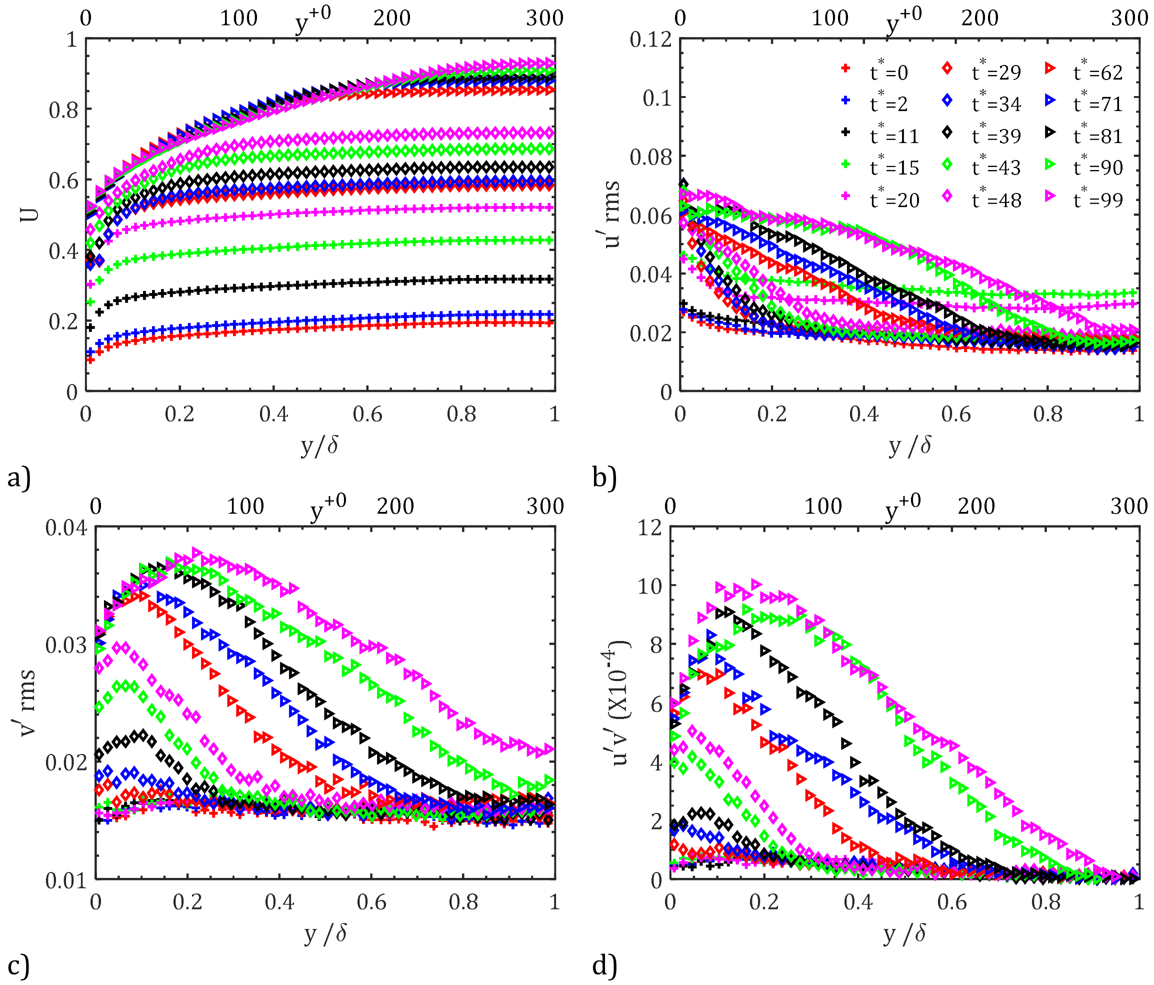

***Figure 4-21: Time development of streamwise mean velocity ($U$), streamwise fluctuating velocity ($u'_{rms}$), wall-normal fluctuating velocity ($v'_{rms}$) and Reynolds shear stress ($\overline{u'v'}$) for case T3 ($Re_b = 5100 - 24324$). Legend is the same for the four subplots. The unit of subplots (a)-(c) is m/s and that of subplot (d) is m²/s².***

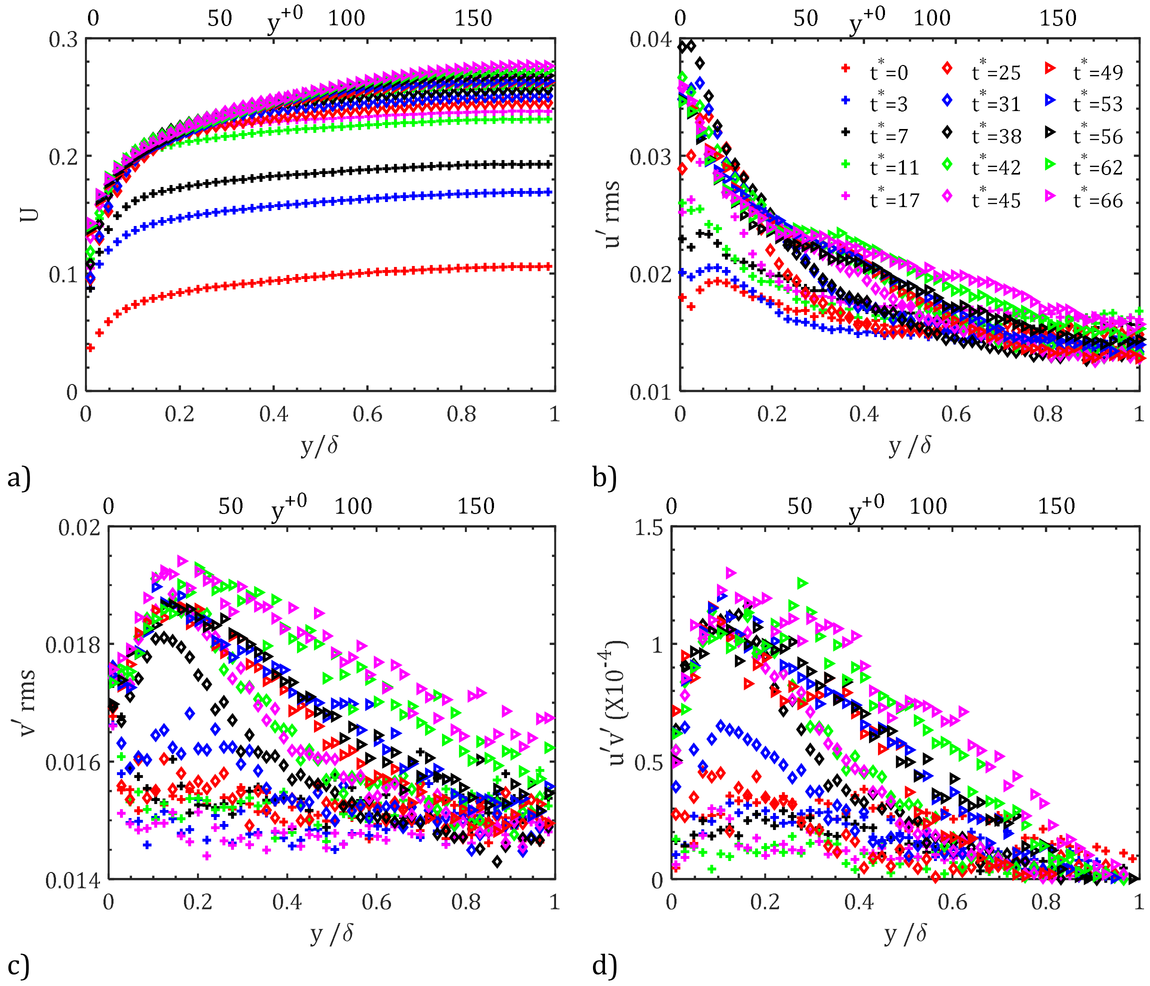

***Figure 4-22: Time development of streamwise mean velocity ($U$), streamwise fluctuating velocity ($u'_{rms}$), wall-normal fluctuating velocity ($v'_{rms}$) and Reynolds shear stress ($\overline{u'v'}$) for case U1 ($Re_b = 2845 - 7650$). Legend is the same for the four subplots. The unit of subplots (a)-(c) is m/s and that of subplot (d) is $m^2/s^2$.***

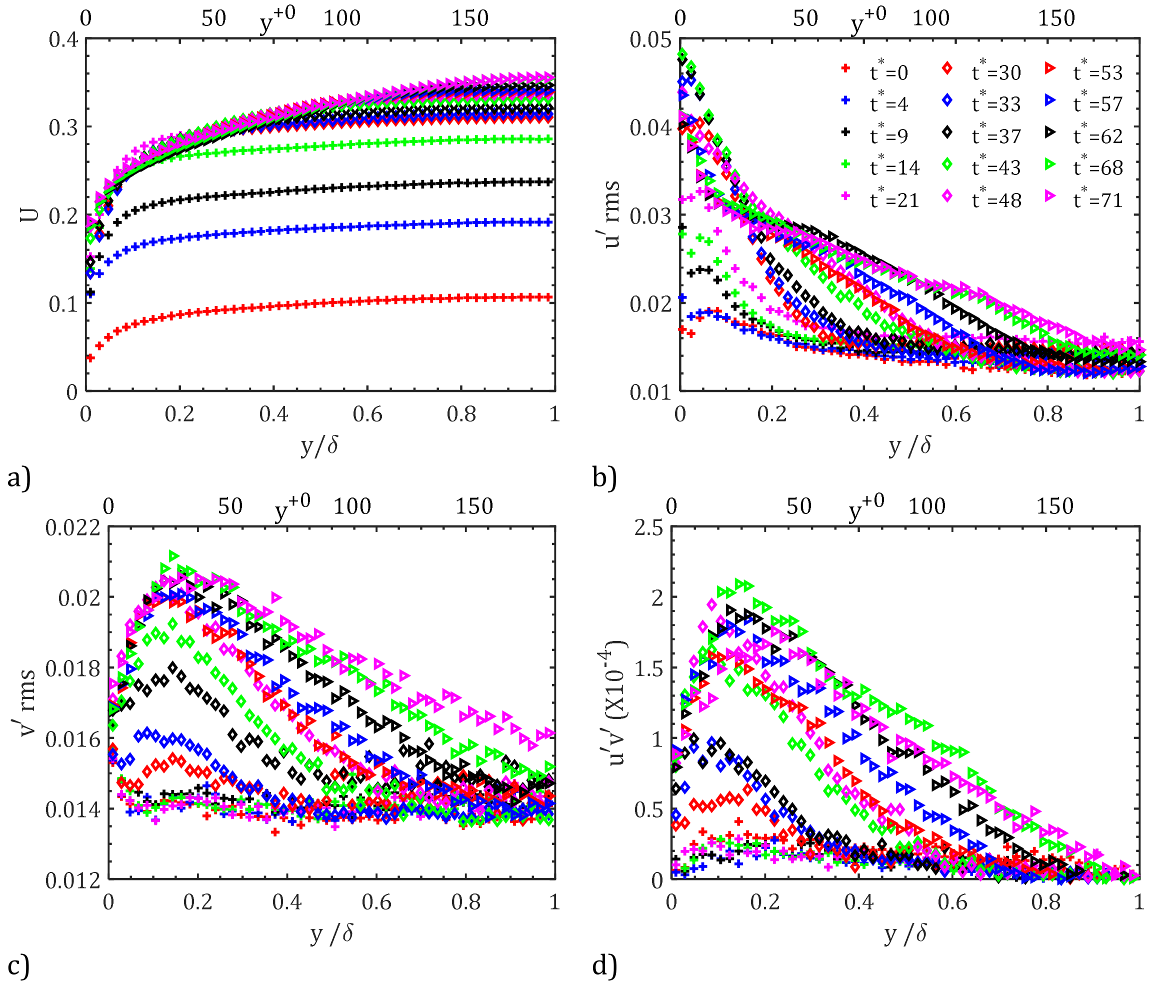

***Figure 4-23: Time development of streamwise mean velocity ($U$), streamwise fluctuating velocity ($u'_{rms}$), wall-normal fluctuating velocity ($v'_{rms}$) and Reynolds shear stress ($\overline{u'v'}$) for case U2 ($Re_b = 2852 - 9557$). Legend is the same for the four subplots. The unit of subplots (a)-(c) is m/s and that of subplot (d) is m$^2$/s$^2$.***

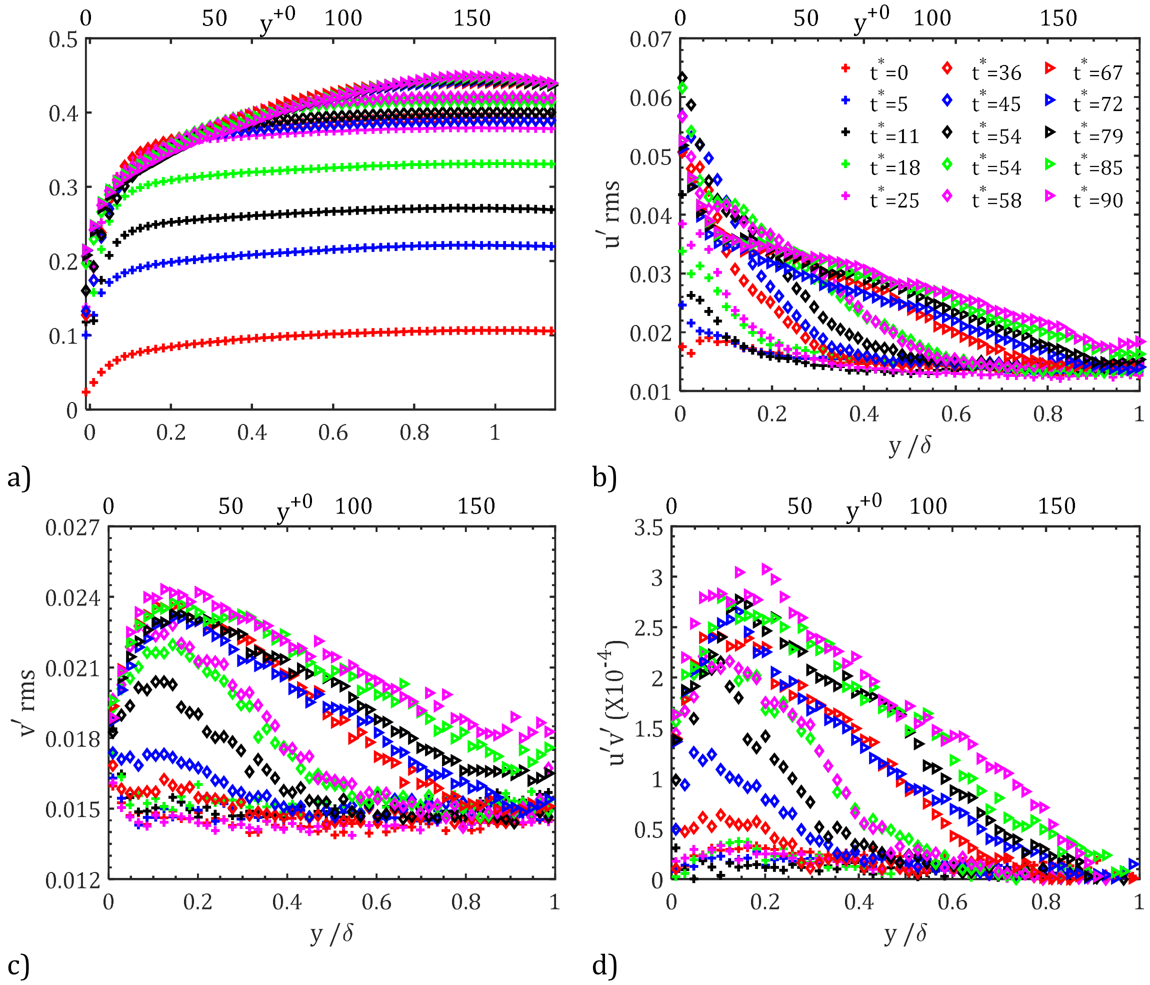

***Figure 4-24: Time development of streamwise mean velocity ($U$), streamwise fluctuating velocity ($u'_{rms}$), wall-normal fluctuating velocity ($v'_{rms}$) and Reynolds shear stress ($\overline{u'v'}$) for case U3 ($Re_b = 2838 - 12069$). Legend is the same for the four subplots. The unit of subplots (a)-(c) is m/s and that of subplot (d) is m²/s².***

### 4.3.4 Temporal development of boundary layer

It has previously been shown that the transient turbulent flow in a channel which is subjected to a step increase of flow rate is effectively a laminar-turbulent bypass transition despite the fact the initial flow condition is turbulent. The response of transient turbulent flow during the rapid increase of flow rate has shown three-stage development which are referred to as the pre-transitional stage, transitional stage and fully developed turbulent stage. These stages of flow development have been shown to closely resemble the three stages of the boundary layer bypass transition, which are the buffeted laminar flow, the intermittent turbulence spot generation and the fully turbulence (He & Seddighi, 2013; 2015). It has been revealed from

DNS studies that after the commencement of the transient flow in a channel, a thin boundary layer of high-velocity gradient and high shear is formed near the wall during the pre-transitional stage, and that this thin boundary layer grows with time to the centre of the flow. This temporal development of boundary layer is responsible for the change of structures in the transient channel flow and closely resembles that of the spatial development of laminar boundary layer flow on a flat plate before the start of transition

For a quantitative description of temporal development of boundary layer, He and Seddighi (2013) introduced perturbation velocity equation in order to measure the time-developing boundary layer in the flow. The dimensionless measurement of change of velocity is referred to as the perturbation velocity, and it is obtained when the initial flow values are deducted from the transient flow values. The results obtained are then normalised by the difference between the transient velocity ($\bar{U}_c(t)$) at the centre and the initial velocity ($\bar{U}_c(0)$) at the centre. The perturbation velocity equation is represented as follows:

$$\bar{U}^{\wedge}\left({}^{y}/_{h},t\right) = \frac{\bar{U}\left({}^{y}/_{h},t\right) - \bar{U}\left({}^{y}/_{h},0\right)}{\bar{U}_c(t) - \bar{U}_c(0)} \tag{4.5}$$

where $\bar{U}_c(t)$ is the centreline velocity at time $t$, and $\bar{U}\left({}^{y}/_{h},t\right)$ is the ensemble-averaged streamwise mean velocity at the distance ${}^{y}/_{h}$ from the wall and at time $t$. It has been shown previously by He and Seddighi (2015) that the profiles of perturbation velocity in a step increase of flow rate collapse on top of each other during the pre-transitional time frame and these velocity profiles during the initial stage of the transient flow frame are represented closely by the solution of Stokes' first problem. In this section, the cases of different Reynolds number ratios are demonstrated.

In unsteady flow cases, the growth of the perturbation velocity can be represented by the development of the laminar boundary layer. The laminar flow near the wall of a flat plate that is subjected to a sudden constant velocity can be solved by Stokes' first problem. The solution to this problem is the same as that of the heat conduction equation for one-dimensional unstable temperature fields. Stokes' first problem is concerned mainly with a sudden movement of a solid boundary, and that is why it easier to represent the evolution of step increase in the flow (Schlichting, 2000). However, the temporal development of the cases reported is slower than that of step increase of flow rate and can be best represented using an extension of the Stokes' solution to temporally varying velocity. As the temporally varying velocity is considered as a multi-step function with small steps, the whole solution comprises superposition of elementary solutions for all velocity steps. The function $U(t)$ is replaced with a multi-step function with small steps $dU_b$ (Schlichting, 2000).

The velocity at wall distance, y and at any time, t is represented as:

$$U(y,t) = \int_0^t dU_b \, erfc(\eta) \tag{4.6}$$

where $erfc$ is the complementary error function.

A dimensionless similarity variable is introduced as:

$$\eta = \frac{y}{2\sqrt{v(t-\tau)}} \tag{4.7}$$

The equation for velocity at wall distance, y and at time difference $(t-\tau)$ becomes

$$U(y,t) = \int_0^t \frac{dU_b}{dt} erfc\left(\frac{y}{2\sqrt{v(t-\tau)}}\right) d\tau \tag{4.8}$$

where $y$ is the wall distance, $v$ is the kinematic viscosity, $t$ is the actual time, $\tau$ is the small time step, $erfc$ is the complementary error function, and $U_b(t)$ is the temporally varying velocity function with small steps $dU_b$ in a range of small time step $d\tau$.

In these present cases of varying Reynolds number ratios, the accelerating flow is divided into small steps then the temporal development of the laminar boundary layer of each of the cases investigated is obtained by integrating the Eq. (4.8). The $dU_b/dt$ in Eq. (4.8) is obtained from the measured bulk velocity $U_b$ from the integration of the velocity profiles measured using the PIV, which are shown in Figures 4-1 and 4-2 for the T and U cases, respectively. It is noted that the extended Stokes solution is very sensitive to the early flow acceleration. Moreover, such flow measurement with the PIV integration is sparse due to the limited laser pulsation frequency with a maximum value of $7Hz$. In order to improve the results, the raw data is represented using curve fitting to smooth data by removing the scatters.

As previously explained, T cases comprise variation of the initial Reynolds number while the final Reynolds number is fixed. In U cases, the initial Reynolds number is fixed while the final Reynolds number varied. The profiles of the temporal development of laminar boundary layer and that of perturbation velocity are compared in Figures 4-25 and 4-26 for T and U cases, respectively.

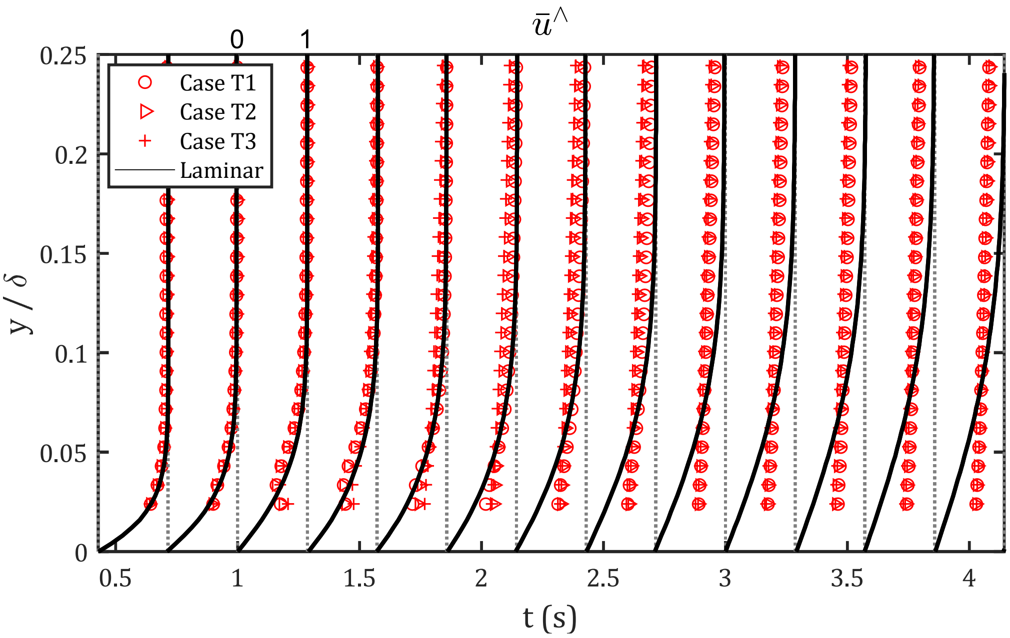

***Figure 4-25: Comparison of the development of the perturbation velocity profiles and the extended Stokes laminar boundary layer of cases T1, T2 and T3.***

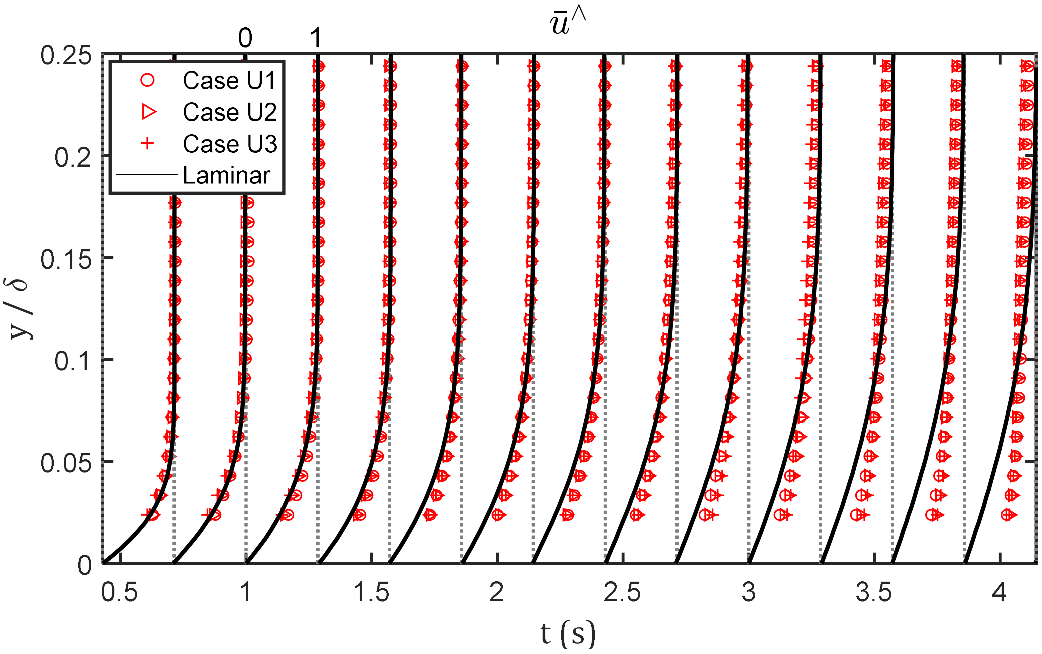

***Figure 4-26: Comparison of the development of the perturbation velocity profiles and the extended Stokes laminar boundary layer of cases U1, U2 and U3.***

Considering cases T1, T2 and T3 with the Reynolds number ratio of 7.29, 5.71 and 4.77 as shown in Table 4.1, it has been previously shown that the onset of transition to turbulence for the three cases reduces as the Reynolds number ratio reduces. As shown from Figure 4-25, the temporal development of the perturbation velocity for the three cases collapses with each other and overlaps the laminar boundary layer up to the transitional stage of the case with a smaller Reynolds number ratio; case T3, $t^{+0} < 110$ $(0.88s)$. The U cases consist of Reynolds number ratios of 2.66, 3.35 and 4.25 for cases U1, U2 and U3, as shown in Table 4.1. It can also be observed that the temporal perturbation velocity profiles for three cases collapses with each other and overlaps the laminar boundary layer development up to the transitional stage of the case with the highest Reynolds number ratio, case U3 $t^{+0} < 98$ $(2.29s)$. The divergence between the perturbation velocity profiles and the laminar boundary layer development starts to occur when the flow of each case undergoes transition. It can be seen that the divergence between the two profiles occurs earlier as the Reynolds number ratio decreases for T cases. The divergence occurs earlier as the Reynolds number ratio increases for U cases. As can been seen from Figures 4-25 and 4-26, the perturbation velocity profiles and solution of extended Stokes' first problem overlap each other until the onset of transition for all the cases presented. The results of these present cases are similar to the previous experimental and numerical investigations on transient turbulent flow of Gorji (2015), He and Seddighi (2015) and Mathur et al. (2018).

In order to describe the temporal development of the transient turbulent flows, a skin friction coefficient based on perturbation flow is described by He and Seddighi (2015) as:

$$C_{f,du} = \frac{2 * \tau_{w,du}}{\rho(U_{b1} - U_{b0})^2} \tag{4.9}$$

where $\tau_{w,du} = \mu[\partial\{\bar{u}\left({}^{y}/_{h}, t\right) - \bar{u}({}^{y}/_{h}, 0)\}/\partial y]_{y=0} = \tau_w - \tau_{w,0}$ is the wall shear stress of perturbation flow, $\tau_w$ is the wall shear stress of the flow at time, $t$, $\tau_{w,0}$ is the wall shear stress of the flow at time, $t = 0$. The theoretical wall shear stress of the solution of Stokes' first problem is given as $\tau_{w,stokes} = \mu(U_{b1} - U_{b0})/\sqrt{\pi v t}$ (Schlichting, 2000). Moreover, the skin friction coefficient for the solution of the Stokes' first problem is given as:

$$C_{f,Stokes} = \frac{2}{\sqrt{\pi}} \frac{1}{\sqrt{\frac{(U_{b1} - U_{b0})^2 t}{v}}} \tag{4.10}$$

Eq. (4.9) can be re-written as follows:

$$C'_{f,du} = C_{f,du}\frac{(U_{b1} - U_{b0})}{u_{\tau 0}} = \frac{2 * \tau_{w,du}}{\rho(U_{b1} - U_{b0})u_{\tau 0}} \tag{4.11}$$

Immediately as the transient flow commences in a channel following a step increase of flow rate, the initial bulk velocity ($U_{b0}$) increases and reaches the final bulk flow ($U_{b1}$), and the modified skin friction coefficient are calculated using Eq. (4.11). In contrast to the transient flow due to step-increase of flow rate, in ramp-type flow of the present cases, the flow acceleration occurs at a slower rate and the initial bulk velocity ($U_{b0}$) changes continuously to the final bulk flow ($U_{b1}$) in a longer period during the transient flow.

For the ramp-type cases, the change in bulk velocity from the initial flow to the final stage of the flow in Eq. (4.11) is replaced with the difference between temporally varying velocity ($U_b(t)$) and the initial bulk velocity ($U_{b0}$). Thus, the modified skin friction coefficient from

extended Stokes' first problem for all the cases investigated is given as:

$$C''_{f,du} = \frac{2 * \tau_{w,du}}{\rho\{U_b(t) - U_{b0}\}u_{\tau 0}} \tag{4.12}$$

By differentiating Eq. (4.8), then the equation that is used to calculate the laminar wall shear stress based on temporally varying perturbation is obtained as:

$$\tau_{w,lam} = \rho \int_0^t \frac{dU_b}{dt} \sqrt{\frac{v}{\pi(t-\tau)}}\, d\tau \tag{4.13}$$

He and Seddighi (2015) found that the DNS data for friction in the pre-transition phase can be represented by:

$$C'_{f,du} = \frac{2}{\sqrt{\pi}} \frac{1}{(t^{+0})^{0.47}} \tag{4.14}$$

The authors re-cast Eq. (4.14) in terms of $C_{f,du}$ to produce a slight modification of the solution of extended Stokes' first problem in step-change flow as:

$$C'_{f,du} = \frac{2}{\sqrt{\pi}} \frac{(t^{+0})^{0.03}}{\sqrt{\frac{(U_{b1} - U_{b0})^2 t}{v}}} = C_{f,Stokes}\ (t^{+0})^{0.03} \tag{4.15}$$

As can be seen during the pre-transitional period, all the present data follows the trend of the extended Stokes laminar solution $C''_{f,du}$ Eq. (4.12) well. The following equation based on the dimensionless time of the initial flow ($t^{+0}$) provides correction to the extended Stokes laminar solution Eq. (4.12):

$$C''_{f,du(corrected)} = C''_{f,du}\ (t^{+0})^{0.03} \tag{4.16}$$

Figure 4-27 (a, c & e) shows $C_f$ defined using of Eq. (4.2) for T cases plotted together with the extended Stokes laminar solution obtained from Eq. (4.13). Those of the U cases are shown in Figure 4-28 (a, c & e). Moreover, Figure 4-27 (b, d & f) and Figure 4-28 (b, d & f) show the development of the modified skin friction coefficient $C''_{f,du}$ Eq.(4.12) for T cases and U cases, respectively, in comparison with that of the extended Stokes laminar solution and the correction from Eq. (4.16). All the data of $C_f$ during the pre-transitional stage for both T cases and U cases collapse with the extended Stokes laminar solution. Furthermore, the data in terms of $C''_{f,du}$ of the present cases follows the extended Stokes laminar solution and the Eq. (4.16) provides an improvement for the slight deviation. The same deviation was observed by He and Seddighi (2015) during their numerical investigations of transient channel flow but the data was well represented when Eq. (4.15) was used.

Another important feature to note from Figures 4-27 and 4-28 is that the onset of transition decreases as the initial Reynolds number of the T cases increases, while the timing for the onset of transition decreases as the final Reynolds number increases for the U cases. Moreover, the present data of the two groups presented deviates from the extended Stokes obtained from Eq.

(4.13) at the onset of transition. For the T cases investigated, the onset of transition is $t^{+0} = 99\ (1.71s)$ for case T1, $t^{+0} = 121\ (1.34s)$ for case T2 and $t^{+0} = 110\ (0.88s)$ for case T3. The onset of transition from the figure of U cases is $t^{+0} = 108\ (2.51s)$ for case U1, $t^{+0} = 103\ (2.37s)$ for case U2, and $t^{+0} = 98\ (2.29s)$ for case U3. As with step increase of flow, the temporal development of boundary of the accelerating flow cases reported in this section closely resembles the laminar boundary layer development of flat plate boundary layer flow during the pre-transitional time frame.

Equations (4.13), (4.13)and (4.16) can be used to predict the skin friction coefficient in transient flow during the pre-transitional time frame. The development of both extended Stokes laminar solution and that of the slight correction is similar to the numerical and experimental studies of He and Seddighi (2015) and Mathur (2016).

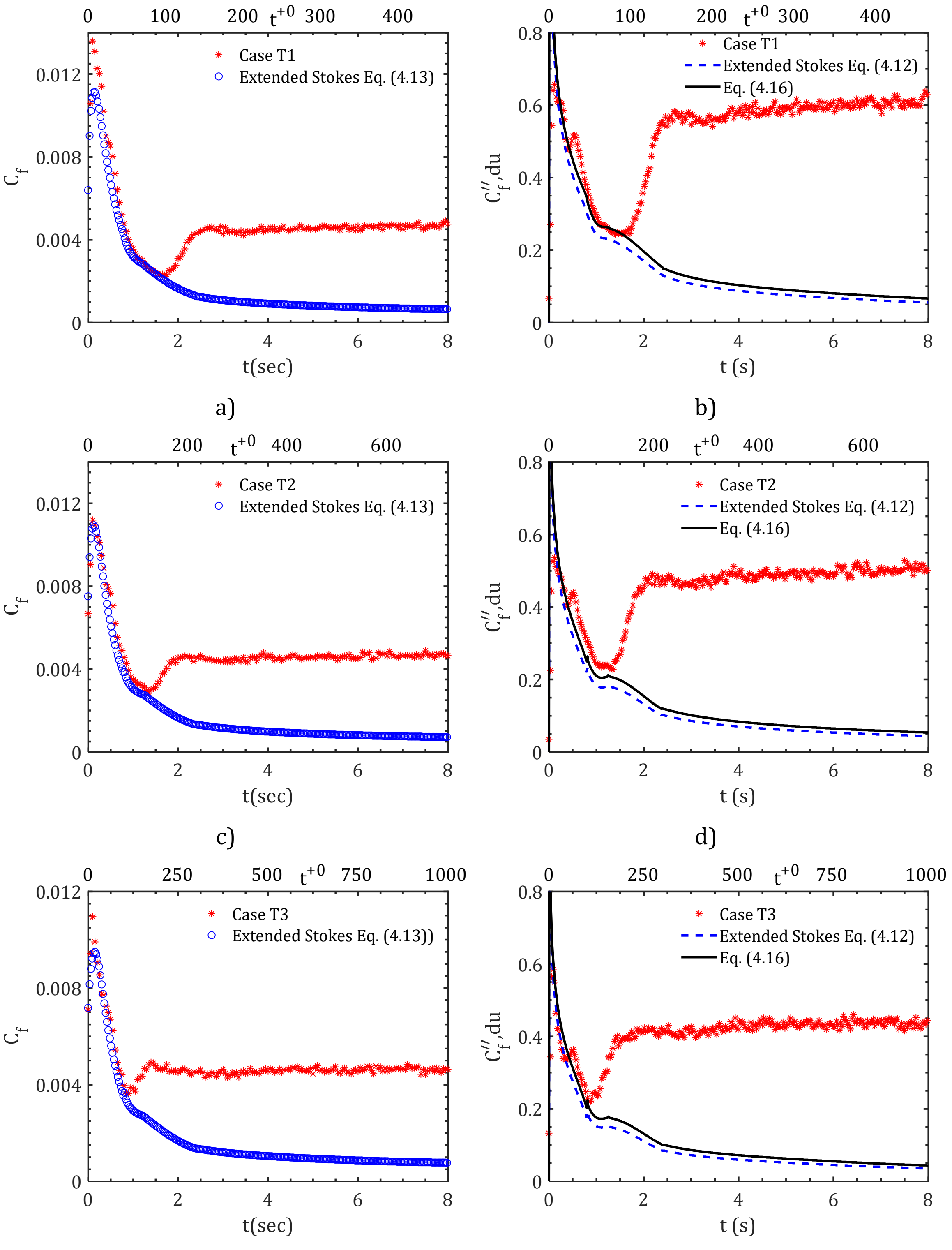

a)

b)

c)

d)

e)

f)

***Figure 4-27: Development of the skin friction coefficient $C_f$ Eq. (4.2) for cases T1 (a), T2 (c) and T3 (e) and the development of the modified skin friction coefficient coefficient $C''_{f,du}$ Eq.(4.12) for cases T1 (b), T2 (d) and T3 (f).***

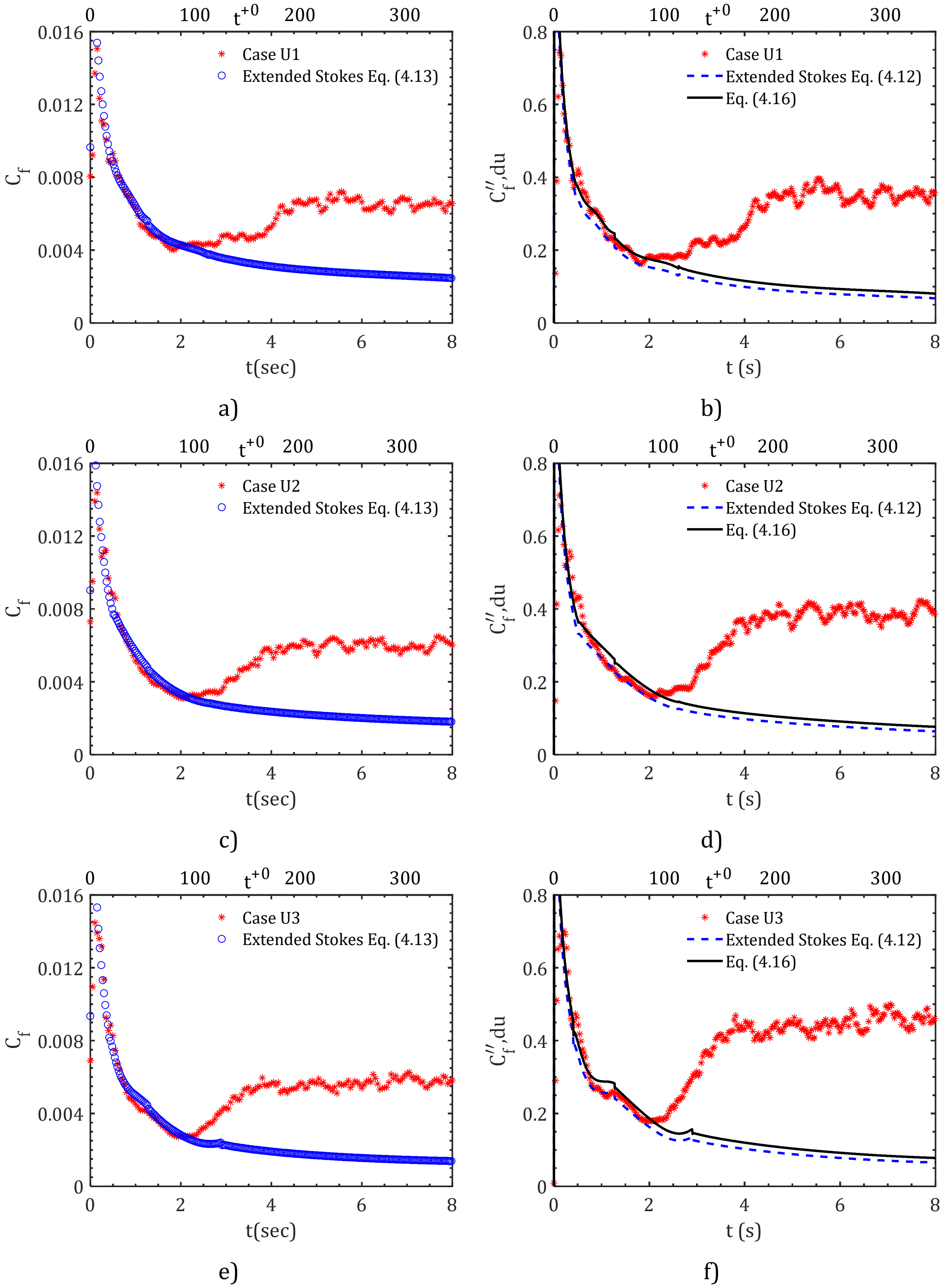

a) b) c) d) e) f)

***Figure 4-28: Development of the skin friction coefficient $C_f$ Eq. (4.2) for cases U1 (a), U2 (c) and U3 (e) and the development of the modified skin friction coefficient $C''_{f,du}$ Eq.(4.12) for cases U1 (b), U2 (d) and U3 (f).***

The momentum thickness ($\theta_{du}$), the shape factor ($H$) and the displacement thickness ($\delta_{du}$) for fluctuating boundary layer in unstable channel flow are re-defined by He and Seddighi (2013) as:

$$\theta_{du}(t) = \int_0^1 \bar{U}^{\wedge}({}^{y}/_{\delta}, t)(1 - \bar{U}^{\wedge}({}^{y}/_{\delta}, t))d({}^{y}/_{\delta}) \tag{4.17}$$

$$\delta_{du}(t) = \int_0^1 (1 - \bar{U}^{\wedge}({}^{y}/_{\delta}, t))d({}^{y}/_{\delta}) \tag{4.18}$$

$$H(t) = \frac{\delta_{du}(t)}{\theta_{du}(t)} \tag{4.19}$$

The momentum-thickness Reynolds number is calculated as $Re_{\theta} = \theta\bar{U}_c/v$ where $\theta$ is the momentum thickness, $\bar{U}_c$ is the centreline velocity and $v$ is the kinematic viscosity of the working fluid. Figure 4-29 shows the development of the momentum-thickness Reynolds number and the shape factor for cases U1, U2 and U3. The two subplots share the same legend in Figure 4-29b. These experimental cases are compared with the step increase of flow rate of He and Seddighi (2013) and the experimental cases of Mathur (2016). Moreover, direct comparison of the U cases with the T3A and T3B cases of Roach and Brierley (1992) of spatially developing boundary layer is done. Before the data of the spatially developing boundary layer flow can be compared with the time-developing boundary layer of the channel flow, there is a need for a correlation between the two data to be established. The distance from the leading edge ($x$) of the boundary layer flow on a flat plate has been re-defined by He and Seddighi (2013) as $x = t * U_{conv}$ where $U_{conv}$ is known as convective velocity. The authors obtained the velocity, $U_{conv} = 0.74U_{b1}$ from the best curve-fitting of the transient turbulent flow with the Blasius solution in the initial stage of the transient. The data of Roach and Brierley (1992) has been used as benchmark data in the studies of bypass transition induced by free-stream turbulence carried out by several researchers; for instance, Jacobs and Durbin (2001) and Ovchinnikov et al. (2008).

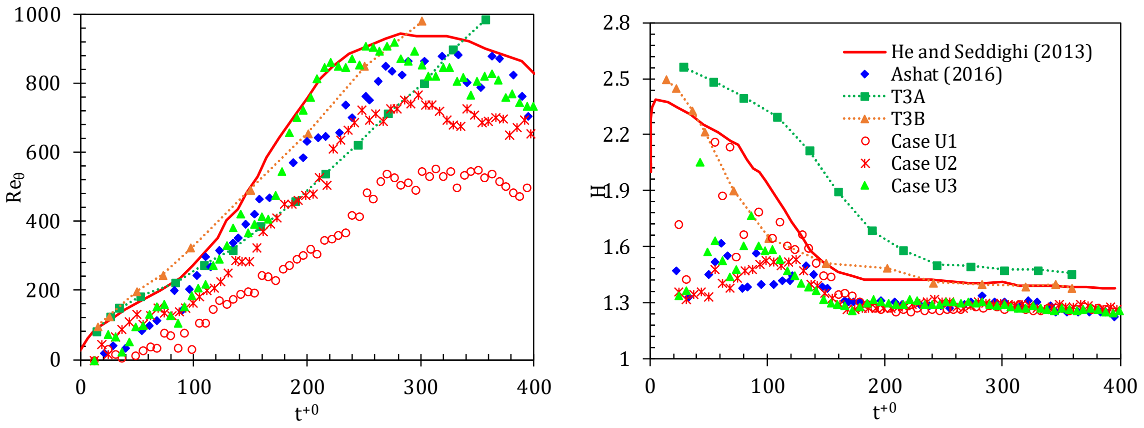

a) b)

***Figure 4-29: Development of momentum-thickness Reynolds number ($Re_\theta$) and shape factor (H) of the present cases (U1-U3) with 1) step increase of flow rate of He and Seddighi (2013), 2) accelerating flow of Mathur (2016) and 3) flat plate boundary layer flow of Roach and Brierley (1992) cases (T3A and T3B). For present cases; a) momentum-thickness Reynolds number ($Re_\theta$), b) shape factor (H).***

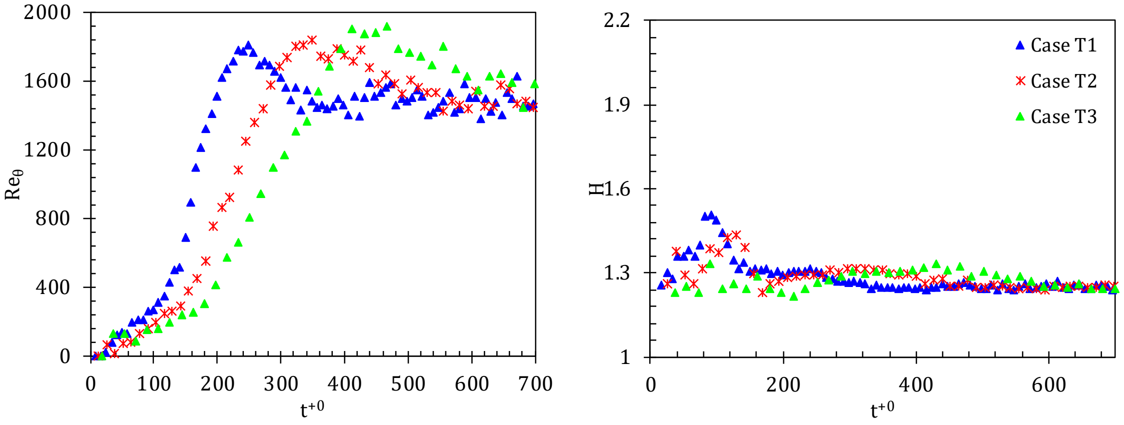

a) b)

***Figure 4-30: Development of momentum-thickness Reynolds number ($Re_\theta$) and shape factor (H) of the present cases (T1-T3): a) momentum-thickness Reynolds number ($Re_\theta$), b) shape factor (H).***

The present cases that are compared with the previous data in Figure 4-29 are $Re_b = 2845 - 7560$ for case U1, $Re_b = 2852 - 9557$ for case U2 and $Re_b = 2838 - 12069$ for case U3. In these cases, the initial Reynolds number is fixed to an approximate the same Reynolds number of $Re_b = 2800$ while the final Reynolds number varied. He and Seddighi (2013) obtained the onset of transition to turbulence at dimensionless time, $t^{+0}$~90 which is equivalent to the momentum-thickness Reynolds number, $Re_\theta$~250. In the experimental case reported by Mathur (2016), the author obtained the time of the onset transition to turbulence and the momentum-thickness Reynolds number as $t^{+0}{\sim}120$ and $Re_\theta{\sim}225$ , respectively. The acceleration rates of these present cases are slower in comparison with the step-increase of flow rate of He and Seddighi (2013), which is $\Delta t^* = 0.22$ ($t = 0.019s$). This caused the onset of transition to turbulence to be delayed. The onset of transition and momentum-thickness Reynolds number for the three cases reported are $t^{+0}{\sim}108$ and $Re_\theta{\sim}106$ for case U1, $t^{+0}{\sim}103$ and $Re_\theta{\sim}209$ for case U2 and $t^{+0}{\sim}98$, and $Re_\theta{\sim}187$ for case U3. The rate of development and the magnitude of the changes are responsible for the delay of the present cases in comparison with the step increase of flow rate of He and Seddighi (2013). The development of the three cases is similar to that of Mathur (2016), but the variation is due to the slight difference in the initial flow condition, the final flow condition, and the temperature. The difference in the flow acceleration of He and Seddighi (2013) and the present U cases causes the variation. Figure 4-29b presents the development of the shape factor in comparison with the previous data of step increase in terms of flow rate, accelerating flow and the spatial development of boundary layer flow. The flow development is seen to flow according to same trend. By considering the case U2, the value of shape factor increases during the initial stage of the transient flow to a maximum value of 1.53 at time $t^{+0}{\sim}99$ before reducing again which indicates laminarising flow effect during the flow acceleration. He and Seddighi (2013) reported a maximum shape factor of 2.4 at $t^{+0}{\sim}10$ during their step increase of flow rate investigation. The values of shape factor at point of transition for the three cases presented are, H~1.74, H~1.59 and, H~1.52 for U1, U2 and U3, respectively. It is revealed that as the Reynolds number ratio increases, the value of shape factor at the point of onset transition reduces. The trends of the present cases are similar to those of step increase of flow rate reported by He and Seddighi (2013), in which the value of shape factor is presented as $H{\sim}2$ at the point of onset of transition. It should be noted that the difference in the values of shape factor $H$ is the due to the the difference in the flow acceleration and the delay in the present flow cases. The values of shape factor ($H$) in statistically steady turbulent flow for all T and U cases are less than 1.4 in comparison with that of step increase of flow rate of He and Seddighi

(2013). This is due to the different flow acceleration and experimental errors during data acquisition.

Figures 4-30a and 4-30b present the development of the momentum-thickness Reynolds number and the shape factor, respectively for cases T1-T3. The response of $\mathrm{Re}_\theta$ and H is similar to the U cases earlier reported and also similar to the development of the cases reported by of He and Seddighi (2013) and Mathur (2016). The onset of transition and momentum-thickness Reynolds number are $t^{+0}\sim 99$ (1.71s) and $\mathrm{Re}_\theta\sim 269$, $t^{+0}\sim 121$ (1.34s) and $\mathrm{Re}_\theta\sim 245$ and $t^{+0}\sim 110$ (0.88s) and $\mathrm{Re}_\theta\sim 158$ for cases T1, T2 and T3, respectively. It is interesting to note that as the Reynolds number ratio reduces from 7.29-4.77 as shown in Table 4-1, the time of onset of transition and the momentum-thickness Reynolds number also reduces. The development of the shape factor for the three T cases presented in Figure 4-30b is similar to the U cases previously presented and with the cases reported by He and Seddighi (2013) and Mathur (2016). In the early stage of transient flow the maximum value of shape factor that indicates laminarising effect is noted for the T cases investigated. The values are 1.5 at $t^{+0}\sim 91$ for case T1, 1.44 at $t^{+0}\sim 129$ for case T2 and 1.29 at $t^{+0}\sim 161$ for case T3. The value of the shape factor reduces as the Reynolds number ratio reduces for the three cases presented. The values of shape factor corresponding to the point of transition for the three cases are also reported. For cases T1, T2 and T3, the shape factor at the point of transition is approximately 1.50, 1.42 and 1.24, respectively. The values also reduces as the Reynolds number ratio reduces.

### 4.3.5 Correlations of flow transition in channel flow

In the numerical studies of He and Seddighi (2015), the significance of Reynolds number ratio ($^{Re_1}/_{Re_0}$) to the initial turbulence intensity in channel flow has been shown. The importance of the initial turbulence intensity ($Tu_0$) in the procedure of transition to turbulence in channel flow just like the free-stream turbulence ($FST$) intensity in boundary layer flow over a flat plate has been revealed. The authors described the initial turbulence intensity ($Tu_0$) as the ratio of the peak turbulence of the initial flow before the start of the transient turbulent flow to the final stage of the flow velocity. The equation of the initial turbulence intensity is written as:

$$Tu_0 = \frac{(u'_{rms,0})_{max}}{U_{b1}}) = \left(\frac{U_{b0}}{U_{b1}}\right)\frac{(u'_{rms,0})_{max}}{U_{b0}} \tag{4.20}$$

The derivation of the above equation is based on the early stage of the flow. At that stage, turbulence does not change from its initial value and the streamwise mean velocity is equivalent to the velocity of the final stage of the flow. From the reported DNS data, it has been shown that $(u'_{rms,0})max/U_b \propto Re^{-0.1}$ and the authors re-formulated a new equation as:

$$Tu_0 = 0.375\left(\frac{U_{b0}}{U_{b1}}\right)\left(\frac{1}{(Re_{b0})^{0.1}}\right) \tag{4.21}$$

The concept of equivalent Reynolds number for transient flows which corresponds to the Reynolds number of a flat plate boundary layer flow has been previously described in §4.4. In a flat plate boundary layer flow, the Reynolds number is denoted as $Re_x = {}^{xU_\infty}/_{v}$ where $x$ is the distance from the leading edge, $U_\infty$ is the free-stream velocity and $v$ is the kinematic viscosity of the working fluid flow. He and Seddighi (2015) has re-defined the Reynolds number equation's of a flat plate boundary layer flow to be equivalent to the Reynolds number in a fully developed channel flow by replacing the distance from the leading edge to an equivalent characteristic length as $x = tU_{b1}$. Thus, the equivalent Reynolds number is obtained as $Re_t = {}^{tU_{b1}^2}/_{v}$, where the final bulk velocity ($U_{b1}$) is equal to the characteristic convective velocity in the step-accelerating flow.

In order to study the procedure of transition to turbulence, a critical equivalent Reynolds number ($Re_{t,cr}$) is essential and it needs to be described. He and Seddighi (2015) showed that both Reynolds number of a flat plate boundary layer flow ($Re_x$) and equivalent Reynolds number ($Re_t$) of a fully developed channel flow have the same impact in the procedure of transition to turbulence. In spatial-developing boundary layer, transition from laminar to turbulent is observed to commence as the skin friction coefficient ($C_f$) deviates from the curve of Blasius solution. As with the spatially developing boundary layer, the time that corresponds to the minimum value of ($C_f$) in a step-acclerating flow has been shown to be the time at which the first burst occurs and the onset of transition. The time is known as the critical time ($t_{cr}$)of onset of transition to turbulence, and the first peak attains by the $C_f$ when it recovers from its minimum value corresponds to the end of transition ($t_{turb}$) (He & Seddighi, 2013 ;2015). Moreover, the critical equivalent Reynolds number for a fully developed channel flow is obtained as $Re_{t,cr} = {t_{cr}U_{b1}^2}/{\nu}$.

The results presented here show that the flow acceleration is slower in comparison with the step-accelerating flow previously discussed. During transient turbulent flow, the flow velocity increases continuously at a slower rate from the initial value to the final value, and the transition occurs before the end of the ramping period. The velocity of the final stage of the flow can not be used as the characteristic velocity in this slower accelerating flow because the transition to turbulence may have occurred before the ramping period is completed. The data of all cases reported in this chapter has shown that the onset of transition occurs before the ramping time is completed.

For the correlation of the time of onset of transition to turbulence with the initial turbulence intensity, the bulk velocity that is equivalent to the onset of transition is assumed to be the characteristic convective velocity instead of the bulk velocity of the final stage of the flow. The bulk velocity at the onset of transition to turbulence in this present accelerating flow is donated as $U_{b,tcr}$. Equations (4.20) and (4.21) are re-defined based on ($U_{b,tcr}$) as the characteristic convective velocity. Equation (4.20) becomes:

$$Tu_0 = \frac{(u'_{rms,0})_{max}}{U_b(t_{cr})}) = \left(\frac{U_{b0}}{U_b(t_{cr})}\right)\frac{(u'_{rms,0})_{max}}{U_{b0}} \tag{4.22}$$

And Eq. (4.21) becomes,

$$Tu_0 = 0.375\left(\frac{U_{b0}}{U_b(t_{cr})}\right)\left(\frac{1}{(Re_{b0})^{0.1}}\right) \tag{4.23}$$

The equivalent Reynolds number earlier presented as $Re_t = {tU_{b1}^2}/{\nu}$ in step-accelearting flow is adjusted for the present flow cases, where $x = tU_{b1}$ and is the distance at which each particle in the flow travels. In this current investigation, the distance is given in an integral form as $x(t) = \int_0^t U_b(t)dt$ and it is calculated using trapezoidal numerical integration. Based on the representation of the distance at which the flow particle travel, the equivalent Reynolds number is re-presented in a general form as:

$$Re_t(t) = \frac{U_b(t)}{\nu}\int_0^t U_b(t)dt \tag{4.24}$$

As previously described, the skin friction coefficient ($C_f$) is used by He and Seddighi (2013; 2015) to determine the onset of transition ($t_{cr}$) and the end of transition ($t_{turb}$). In these present cases, $C_f$ is also used to determine the onset of transition ($t_{cr}$) and the end of transition ($t_{turb}$). The times of onset of transition and the end of transition obtained for T cases and U cases in these current studies are presented in Table 4-3. The time that corresponds to the minimum value of $C_f$ is denoted as $t_{cr}$. Due to the generation of "new" turbulence structures in the flow, the $C_f$ recovers from its minimum value and attains the first peak which is assumed to be the end of transition. The time that corresponds to the end of transition is denoted as $t_{turb}$.

Equation (4.24) is re-presented based on the critical time ($t_{cr}$) to determine critical equivalent Reynolds number as:

$$Re_{t,cr} = \frac{U_b(t_{cr})}{\nu}\int_0^{t_{cr}} U_b(t)dt \tag{4.25}$$

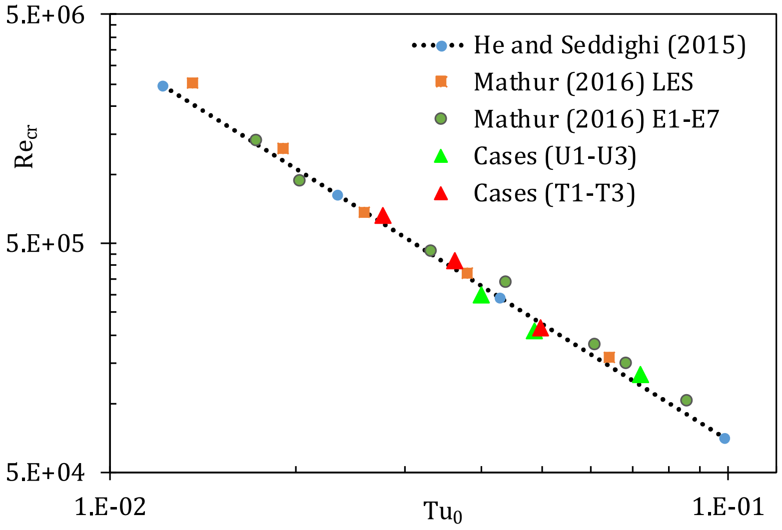

***Figure 4-31: Critical equivalent Reynolds number ($Re_{t,cr}$) as a function of initial Turbulence intensity ($Tu_0$) for case (T1-T3) and case (U1-U3) in comparison with He and Seddighi (2015), Mathur (2016) E1-E7, Mathur (2016) LES.***

Figure 4-31 shows the critical equivalent Reynolds number ($Re_{t,cr}$) plotted against the initial turbulence intensity ($Tu_0$) for cases T and U, and the previous data of He and Seddighi (2015) and Mathur (2016) are also plotted for comparison. The results are shown to be consistent with the previous findings and that the critical equivalent Reynolds number ($Re_{t,cr}$) is a function of the initial turbulence intensity ($Tu_0$). The correlation of critical equivalent Reynolds number ($Re_{t,cr}$) and the initial turbulence intensity ($T_{uo}$) for unsteady flows is first defined by He and Seddighi (2015). The data of both groups presented by the authors consists of different cases and the results are reported to be well represented along a straight line. A best-fit power law of the following equation is obtained from their data:

$$Re_{t,cr} = 1.34 \times 10^3 Tu_0^{-1.71} \tag{4.26}$$

The data of case (T1-T3) and cases (U1-U3) are seen to be on the straight line with the previous data reported using a best-fit power law equation of $Re_{t,cr} = 1.319 \times 10^3 Tu_0^{-1.71}$, which is almost the same as that of He and Seddighi (2015). This close correlation implies a strong dependence of $Re_{t,cr}$ on $Tu_0$. The similarity of the power law equations has established the fact that Eq. (4.22) and (4.25) can be used to provide an estimation of the start of onset transition in flow acceleration that is based on the ramping-up of flow rate. The exponent of the power law of the present cases is the same as that reported by He and Seddighi (2015), with a small different in the value of their constants. In this current study, the velocity at the onset of transition $U_b(t_{cr})$ is used as a characteristic convective velocity instead of the velocity of the final stage of the flow ($U_{b1}$). The results of the present correlation has revealed that the choice of velocity at the onset of transition, $U_b(t_{cr})$ instead of $U_{b1}$ that is used in the step-accelerating flow is right.

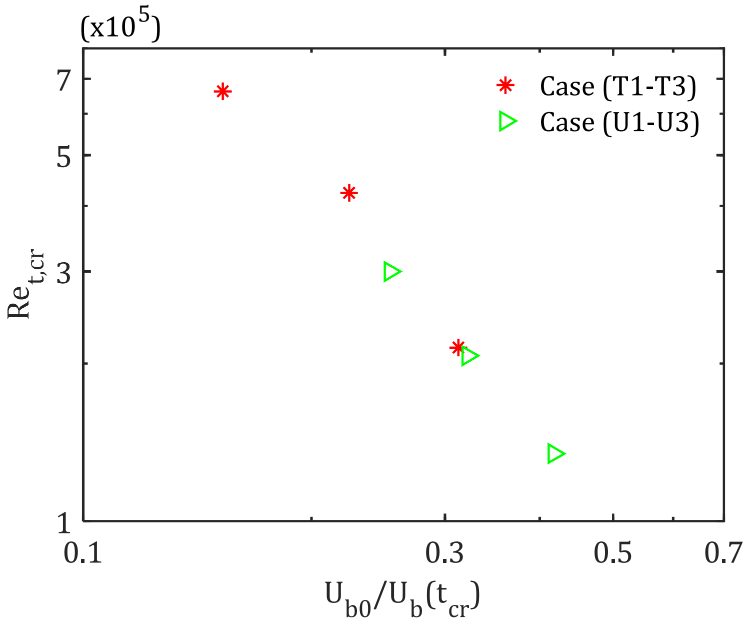

***Figure 4-32: Dependence of critical equivalent Reynolds number on the ratio of initial bulk velocity and the bulk velocity at the onset of transition for cases (T1-T3) and cases (U1-U3).***

The double logarithmic scale of Figure 4-32 presents the critical equivalent Reynolds number ($Re_{t,cr}$) versus the ratio of initial bulk velocity and the bulk velocity at the onset of transition to turbulence (${}^{U_{b0}}/_{U_b}\,(t_{cr})$) for the present cases. It can be seen from the figure that the data of U cases lie perfectly on a straight line, which signifies the existence of power-law relationship between $Re_{t,cr}$ and ${}^{U_{b0}}/_{U_b}\,(t_{cr})$. However, case T2 deviates slightly from the straight line, but $Re_{t,cr}$ still shows a dependence on ${}^{U_{b0}}/_{U_b}\,(t_{cr})$. The trend of the data of the present cases is similar to the numerical results reported by He and Seddighi (2015) which shows that the critical equivalent Reynolds number is a function of velocity ratio.

The transitional length is another important feature during the transition to turbulence of a flat plate boundary layer flow. For the determination of the length of transition in boundary layer flow over a flat plate, several researchers have established different empirical relationships, amongst which is the linear empirical relationship presented by Fransson et al. (2005) that calculates the length of transition as the difference between the final transitional Reynolds number and the initial transitional Reynolds number as:

$$\Delta Re_{x,cr} = Re_{x,\gamma_2} - Re_{x,\gamma_1} \tag{4.27}$$

where $\gamma_2 = 0.9$ and $\gamma_1 = 0.1$. The distance from the leading edge is referred to as $x$, and $\gamma$ is the level of intermittency. The flow appears as fully developed turbulent flow when the intermittency ($\gamma$) is equal to 1, and it resembles a laminar when the intermittency ($\gamma$) is equal to 0. Narasimha, Narayanan and Subramanian (1984) determined the length of transition from their experimental data obtained through low-turbulence wind tunnel. The authors used intermittency levels at the initial transitional flow (onset of transition) as $\gamma = 0.25$, and $\gamma = 0.75$ was used as the intermittency for the final transitional flow (completion of transition). At the location of intermittency ($\gamma = 0.50$), which is the midway point between the initial transitional flow and final transitional flow, the length of transition for flat plate boundary layer flow has been revealed to be well-related (Fransson et al., 2005). The power-law correlation between the transitional length and the critical Reynolds number was proposed by Narasimha et al. (1984) using intermittency, $\gamma = 0.50$ as:

$$\Delta Re_{x,cr} = 9Re_{x,\gamma=0.5}^{0.75} \tag{4.28}$$

Recently, Fransson et al. (2005) suggested an alternative empirical relationship between the length of transition and the critical Reynolds number from their experimental data as:

$$\Delta Re_{x,cr} = A + BRe_{x,\gamma=0.5} \tag{4.29}$$

where $A = 3.9 \times 10^4$ and $B = 0.33$.

The transitional time frame is the time between the transition starts and the completion of it. As explained previously, the time at which the transition has completed ($t_{turb}$.) is defined as the time when $C_f$ reaches the first peak after the recovery from its minimum value. The time also corresponds to the time when the whole flow region has been covered by the newly generated turbulence.

He and Seddighi (2015) determined the transitional period Reynolds number as:

$$\Delta Re_{t,cr} = {U_{b1}^2 t_{turb}}/{v} - {U_{b1}^2 t_{tcr}}/{v} \tag{4.30}$$

where $U_{b1}$ is a characteristic convective velocity in their step-increase investigation, $t_{cr}$ is critical time, and $t_{turb}$ is the time when the flow becomes fully developed turbulent flow. For comparisons of unsteady flow with the spatially developing boundary layer flow that has a different definition of critical Reynolds number, He and Seddighi (2015) replaced the transitional length Reynolds number at the halfway point, $Re_{x,\gamma=0.5}$ of Eq. (4.28) and (4.29) by $Re_{x,cr} + 0.5\Delta Re_{x,cr}$.

In this current study, the transitional period Reynolds number for each of the cases investigated is determined using the following modified equation:

$$\Delta Re_{t,cr} = \frac{U_b(t_{turb})}{v} \int_{t_{cr}}^{t_{turb}} U_b(t)dt \tag{4.31}$$

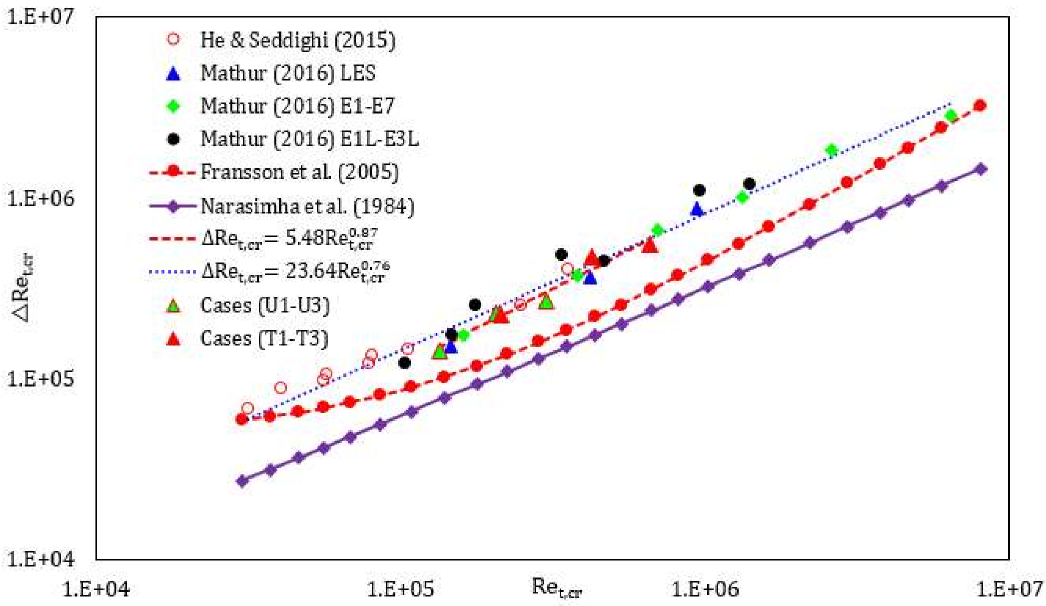

***Figure 4-33: Relationship between the transitional period Reynolds number ($\Delta Re_{t,cr}$) and the critical Reynolds number ($Re_{t,cr}$)of the present experimental cases. Symbol: Cases U1-U3 ($*$) and cases T1-T3 ($*$).***

Figure 4-33 presents the relationship between the transitional period Reynolds number ($\Delta Re_{t,cr}$) and the critical Reynolds number ($Re_{t,cr}$) of the present experimental cases with the direct numerical simulation results of He and Seddighi (2015) and both experimental and numerical cases of Mathur (2016). The data of the spatially developing boundary layer flow at $Re_{x,\gamma=0.5}$, which represent the halfway point of the transition length Reynolds number is plotted on the figure. Based on the comparison, the present data follow the trend of the data of the flat plate boundary layer flow. The present experimental cases are similar with the results of He and Seddighi (2015) and Mathur (2016). It is seen that the present data is predicted reasonably by the correlations of the spatially developing boundary layer flow when a factor of 0.5 is applied as a constant of $\Delta Re_{t,cr}$. The power-law relation of $\Delta Re_{t,cr} = 5.48Re_{t,cr}^{0.87}$ is established with the present cases but the constants of the power law are different from those of Narasimha et al. (1984) in Eq. (4.28) due to the present cases are temporally developing boundary layer flows. It can be seen that the power-law relation of the present cases is close to that of Mathur (2016), which is $\Delta Re_{t,cr} = 13.5Re_{t,cr}^{0.81}$. The slight variation in the constants of the power in comparison with the current cases is due to differences in the initial and final flow conditions. In addition, a best power law relation of $\Delta Re_{t,cr} = 23.64 Re_{t,cr}^{0.76}$ is obtained from the data of He and Seddighi (2015) and Mathur (2016) and the current T & U cases. The constants of the power law are different from those in Eq. (4.28) because of the spatially developing boundary layer flow of Narasimha et al. (1984). The regime of the experimental data in Figure 4-33 can be extended further by increasing the final Reynolds number of each case.

## 4.4 Summary

The response of turbulence in a transient flow reported in this section has been shown to resemble that of laminar-turbulent transition induced by free-stream turbulence ($FST$) even though the initial flow is turbulent. As with the spatially developing boundary layer flow, three stages of transition to turbulence are observed from the all the cases reported. These are pre-transition, transition and fully turbulence. The response of the present accelerating flow is observed to be similar to that of the direct numerical simulation of He and Seddighi (2013; 2015) and Mathur et al. (2018).

Three groups of cases are investigated to study the procedure of transition to turbulence in transient turbulent flows. The flow conditions of T cases and P cases are similar except that P cases are investigated at different temperatures. Comparing P cases and T cases, it is clear that different temperatures only affect the flow velocity during the investigations. For brevity, discussion is streamlined into two groups (T cases and U cases, as presented in Table 4-1). In T cases, initial Reynolds number is varied while the final Reynolds number is fixed. The initial Reynolds number of U cases is fixed while the final Reynolds number is varied.

In comparison the present T and P cases with Mathur et al. (2018), the initial $Re_0$ in T and P cases are much greater. Moreover, in the current experiments, the pneumatic control valve is opened suddenly, whereas in that of Mathur et al. (2018), the pneumatic control valve is opened in a slower controlled fashion to generate a smooth flow increase.

Skin friction coefficient ($C_f$) is used to determine the onset of transition and the completion of it. The time equivalent to the minimum value of $C_f$ is used to determine the onset of transition and the time equivalent to the first peak of the $C_f$ after its recovery from the minimum value is used to mark the end of transition. The recovery of the skin friction coefficient starting from the onset of transition is due to the generation of "new" turbulence structures near the wall. The times obtained are compared with that of the flow visualisation, the response of wall-normal fluctuating velocity ($v'_{rms}$) and the Reynolds shear stress ($\overline{u'v'}$), and the critical times obtained from these different methods are almost the same.

The responses of streamwise mean velocity and that of the turbulence statistics are also studied. It is observed that the streamwise mean velocity responses like a plug flow to the sudden opening of the pneumatic control valve at every location except to near the wall while the streamwise fluctuating velocity ($u'_{rms}$) only responded at the locations close to the wall. At the initial stage of the transient flow, the streamwise fluctuating velocity ($u'_{rms}$) does not response at the core while both wall-normal fluctuating velocity ($v'_{rms}$) and the Reynolds shear stress ($\overline{u'v'}$) do not respond at every location of the flow. The time equivalent to when both $v'_{rms}$ and $\overline{u'v'}$ respond to flow marks the onset of transition. This is used by Gorji (2015) to determine the onset of transition in his experimental investigations.

The data of all the cases presented are well represented by laminar solution during the pre-transitional time frame using the extended solution to Stokes' first problem. For all the cases presented, the flow acceleration is slower in comparison with the previous step increase of flow rate reported. In order for the multi-step increase of bulk velocity of the present flow cases to account for the slower acceleration, the extended Stokes' solution is used. It is revealed that the results of T and U cases collapse with the extended Stokes solution obtained from Eq (4.2). The data of present cases deviates from the extended Stokes laminar solution obtained from Eq. (4.13) but well represented by the correction of Eq. (4.16).

A modification is made on the critical equivalent Reynolds number ($Re_{t,cr}$) and the initial turbulence intensity ($Tu_0$) proposed by He and Seddighi (2015) in order to account for the present slower accelerating flow cases in comparison with step increase of flow rate. He and Seddighi (2015) obtained a power-law relation of $Re_{t,cr} = 1340Tu_0^{-1.71}$ when the critical equivalent Reynolds number ($Re_{t,cr}$) is plotted against the initial turbulence intensity ($Tu_0$). Similar to the power-relation of He and Seddighi (2015), the data of the present cases produces a power-law relation of $Re_{t,cr} = 1319Tu_0^{-1.71}$. It is noted that the slight difference in constants in comparison with the step increase of flow rate reported by He and Seddighi (2015) is due to different flow accelerations. The increase of flow rate of the present flow cases is slower compared to the step increase of flow rate. The transitional period Reynolds number of the step increase of flow rate is also modified for the present flow cases and the power-law relation of $\Delta Re_{t,cr} = 5.48Re_{t,cr}^{0.87}$ is obtained similar to that of Narasimha et al. (1984) of spatially developing boundary layer flows. The difference in constants is due to the fact that the present flow cases being temporally developing boundary layer flows.

The variation of the initial Reynolds number while the final Reynolds number is fixed and vice versa changes the values of the initial turbulence intensity ($Tu_0$). As the Reynolds number ratio reduces for the cases with a fixed final Reynolds number, the time of onset to transition reduces and the process of transition to turbulence appears to be subtle and the transition feature not clearly seen. The process of transition to turbulence becomes strong when the Reynolds number ratio is large and the transition features becomes more visible. Moreover, the time of onset to transition reduces as the Reynolds number ratio increases for the cases with a fixed initial Reynolds number but different final Reynolds numbers.

# Chapter 5

# Systematic change of Flow Acceleration

## 5.1 Introduction

In this chapter, an explanation is provided of the experimental investigation carried out to study the effects of different acceleration periods on the response of turbulence in transient turbulent flow. Particle Image Velocimetry (PIV) is used to measure the instantaneous velocity during slower flow acceleration than those reported in Chapter Four, and the measurements of the wall shear stress of the transient flows are obtained through hot-film anemometry. In Chapter Four, the valve is opened suddenly while in this present chapter, the valve is opened in a controlled fashion that causes the flow acceleration to be slower. The acceleration of initial statistically steady turbulent flow is slower, and the onset of transition is delayed in this chapter in comparison with the cases reported in Chapter Four. Ensemble average is performed on the data acquired by both techniques for the determination of mean and turbulence statistics of the transient flows. A pre-determined flow variation is obtained through a pneumatic control valve in order to produce a systematic change of flow acceleration. The acceleration of the cases presented in this chapter is slower in comparion with that of step increase in flow rate of He and Seddighi (2013; 2015), hence they are referred to ''slow acceleration''. The initial increase of wall shear stress among the cases investigated can be categorised as faster (D1, D2 D3 and E1), medium (D4, D5 and E2) and slower (D6 and E3) within the slow accelerating flow. Moreover, during the slow acceleration of the transient channel flow, the initial Reynolds number based on half-height of the channel and bulk velocity is increased linearly to the final Reynolds number. The response of slow accelerating turbulent flow has been investigated numerically by Seddighi et al. (2014) and the results of their findings are compared with the results of step increase of flow rate reported by He and Seddighi (2013). The turbulence characteristics of the two flows are similar and three stages (pre-transition, transition and fully turbulence) of transition to turbulence are reported. They reported that the transition of turbulent channel flow due to increase in flow rate has striking similarity to bypass transition of a flat plate boundary layer flow. This current study is carried out to demonstrate experimentally the transition procedure established in the slow accelerating flow investigations of Seddighi et al. (2014) and to expand the concept proposed by He and Seddighi (2013) to a wider flow conditions as shown in Table 5.1. The flow behaviour of this current study will be compared with the recent numerical investigation of Jung and Kim (2017b) on temporal accelerating channel flow.

## 5.2 Experimental cases studied

The response of turbulence in a slow accelerating flow is investigated in this current study. A range of acceleration periods are applied to a fixed initial Reynolds number ramping up to a fixed final Reynolds number to elucidate the effects of changing transient periods on the transition procedure in the transient channel flows. Other cases of fixed initial Reynolds number with different final Reynolds numbers and acceleration periods are also investigated. For each case, the flow acceleration is produced by a controlled opening of the pneumatic control valve. The time of flow excursion depends on the control valve operating curve (as shown in Figure 3-7) and the final flow rate and is referred to as the acceleration period ($\Delta t$), which is defined as the time needed for the initial flow condition to attain 90% of the final flow condition. Flow variation before 90% of the final stage of the flow appears to be rapid while the flow above 90% towards the final flow condition is much slower. The Reynolds numbers for all the cases are obtained as $Re_b(= {}^{\delta U_b}/_{v})$, where $U_b$ is bulk velocity of the flow, $\delta$ is the half-height of the channel and $v$ is the kinematic viscosity of the water.

Measurements of mean and turbulence statistics using particle image velocimetry (PIV) are taken using two laser-camera orientations as previously described in §3.6. The two orientations are designated as vertical-PIV and horizontal-PIV. The wall-normal measurements for all cases studied are taken through vertical-PIV orientation while the measurements of flow fields parallel to the bottom wall of the channel are taken through horizontal-PIV orientation. For better resolutions of wall-normal measurements, a laser sheet is positioned to penetrate the wall of the channel at a distance of 87.5 $mm$ from the edge of the channel width (w). A high-power laser (Class 4), which is hazardous, is placed in a closed room during the experiments. The PIV system is positioned in the closed room downstream of the channel for the wall-normal and instantaneous flow field measurements. Downstream of the channel, the flow had already become streamwise fully developed and free from air bubbles before it is ramped up by a pneumatic control valve. Furthermore, downstream near the exit of the channel are positioned three hot-film sensors. The installation procedure has previously been described in §3.7. CTA with hot-film sensors is used to measure wall shear stress during the slow accelerating flow for all the cases studied. The data acquired by PIV and CTA is saved in the common-separated values (csv) format and LabVIEW measurement (lvm) files, respectively, before being exported to MATLAB for post processing.

***Table 5-1: Experimental parameters for two groups at different acceleration periods.***

| Group | Case | $Re_0$ | $Re_1$ | $U_b$ ($^m/_s$) | 90% $U_{b1}$ | Temp. (°C) | $\Delta t$ ($s$) | $\Delta t_{ac}$ ($^m/_{s^2}$) |
|---|---|---|---|---|---|---|---|---|
| D | D1 | 2799 | 15601 | 0.091-0.507 | 0.456 | 29.4 | 1.87 | 0.20 |
|  | D2 | 2874 | 15560 | 0.093-0.505 | 0.455 | 29.5 | 2.06 | 0.18 |
|  | D3 | 2850 | 15522 | 0.092-0.501 | 0.451 | 29.7 | 2.81 | 0.13 |
|  | D4 | 2813 | 15319 | 0.093-0.506 | 0.455 | 28.6 | 4.26 | 0.08 |
|  | D5 | 2863 | 15644 | 0.093-0.507 | 0.456 | 29.5 | 5.56 | 0.07 |
|  | D6 | 2865 | 15584 | 0.093-0.505 | 0.455 | 29.5 | 6.94 | 0.05 |
| E | E1 | 2755 | 7440 | 0.096-0.259 | 0.233 | 26.2 | 2.73 | 0.05 |
|  | E2 | 2766 | 15121 | 0.098-0.537 | 0.483 | 25.3 | 3.23 | 0.12 |
|  | E3 | 2769 | 24010 | 0.097-0.839 | 0.755 | 26.0 | 4.73 | 0.14 |

*Note: Acceleration period ($\Delta t$) denotes the amount of time for an initial bulk velocity ($U_{b0}$) to reach 90% of the final bulk velocity ($U_{b1}$). Acceleration rate ($\Delta t_{ac}$) is calculated as* $^{(90\%(U_{b1}) - U_{bo})}/_{\Delta t}$.

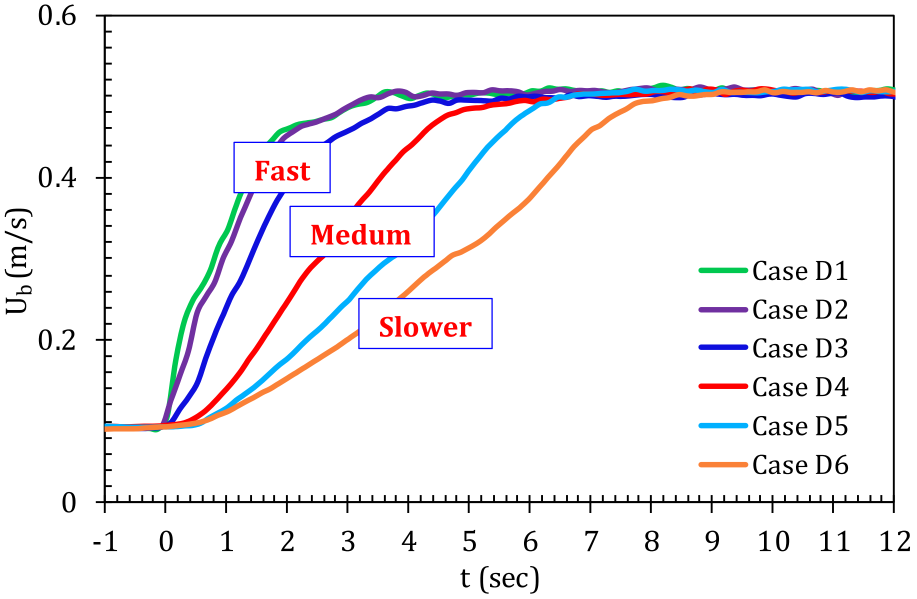

***Figure 5-1:Variation of bulk velocity for a fixed initial Reynolds number and final Reynolds number with different acceleration periods.***

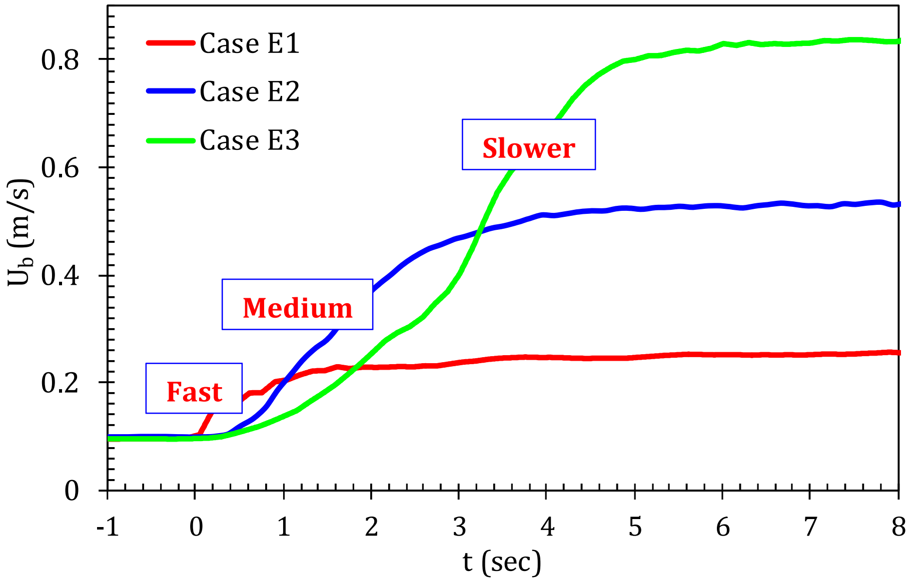

***Figure 5-2: Variation of bulk velocity for a fixed initial Reynolds number with different final Reynolds numbers and acceleration periods.***

Two different groups (group D and E) contain all the flow parameters investigated; with 6 cases in group D and 3 cases in group E. In each of the cases studied, transient turbulent flow is accelerated from the initial flow condition to the final flow condition at different acceleration periods. The acceleration periods in group D vary from 1.87 s to 6.94 s while both initial and final Reynolds numbers are fixed to approximately $Re_b = 2800$ and $Re_b = 15600$, respectively. In the second group of the investigation, the initial Reynolds number is fixed while the final Reynolds number and acceleration period are varied, as shown in Table 5-1. Figure 5-1 displays the actual bulk velocity variation obtained from the integral of velocity profile obtained from PIV measurements during the accelerating flow of the cases in group D, and the actual variation of bulk velocity for cases in group E is shown in Figure 5-2.

***Table 5-2: The onset and completion times for slow accelerating cases.***

| Group | Case | $t_{cr}(sec)$ | $t_{turb}(sec)$ | $t_{cr}^{*}$ | $t_{turb}^{*}$ | $t_{cr}^{+0}$ | $t_{turb}^{+0}$ |
|---|---|---|---|---|---|---|---|
| D | D1 | 1.91 | 3.01 | 39 | 61 | 79 | 125 |
|  | D2 | 2.07 | 3.09 | 42 | 62 | 92 | 137 |
|  | D3 | 2.71 | 3.54 | 54 | 71 | 117 | 153 |
|  | D4 | 3.35 | 5.05 | 68 | 102 | 146 | 220 |
|  | D5 | 4.35 | 5.20 | 88 | 105 | 193 | 231 |
|  | D6 | 4.45 | 6.05 | 90 | 122 | 198 | 269 |
| E | E1 | 2.83 | 4.78 | 29 | 50 | 121 | 205 |
|  | E2 | 2.85 | 3.70 | 61 | 79 | 127 | 166 |
|  | E3 | 3.72 | 4.15 | 125 | 139 | 164 | 183 |

## 5.3 Instantaneous behaviour of slow accelerating flow

In this section, the instantaneous behaviour of slow accelerating flow is described using contour plots of streamwise fluctuating velocity on the bottom wall of the channel. Measurements of streamwise and spanwise velocities for all cases presented in Table 5-1 are obtained using horizontal-PIV orientation. The description on laser-camera orientations has previously been discussed in § 3.6. To briefly repeat, the field of view (FOV) used during the horizontal-PIV measurements is 110 $mm\ x$ 110 $mm$. Dantec DynamicStudio software, version 3.41 is used to process the acquired data before exporting to MATLAB for post-processing. During the processing of the data using DynamicStudio, the initial interrogation area size (IA) is set to 256 $pixels \times 256\,pixels$ with a final interrogation area size (IA) of 32 $pixels \times 32\,pixels$ with three refinements. For all the cases studied, the time between the two light pulses is set to $600\mu s$. A pneumatic control valve is used to produce the near-linear accelerating flow based on the acceleration periods presented in Table 5-1, and instantaneous velocities are obtained during the flow acceleration for all cases. The Reynolds decomposition equation ($u'(t) = u(t) - \bar{u}$) is applied for the determination of the instantaneous fluctuating velocities; the mean velocities are averaged in the streamwise and spanwise direction, and the instantaneous fluctuating velocities are obtained by subtracting the mean velocities from the instantaneous velocities.

The dimensionless wall distance $y_0^+ = ({}^{yu_{\tau 0}}/_{\nu})$, where $y$ is the distance from the channel bottom wall, $\delta$ is the half-height of the channel, and $u_{\tau 0}$ is the initial friction velocity of the steady turbulent flow is used to determine the distance above the bottom wall of the channel from which the measurements of instantaneous velocities are obtained. It should be noted that the measurements below the actual wall distance of $y = 2\ mm$ (equivalent to ${}^{y}/_{\delta} = 0.08$) or dimensionless wall distance of $y_0^+ \approx 14$ are considered blurred during post-processing. An experimental measurement area of $4\delta \times 4\delta$ is used to describe the instantaneous behaviour of the slow accelerating flows investigated.

In this chapter, the cases investigated are divided into two groups as shown in Table 5-1. For brevity, the discussion of the instantaneous behaviour of the flow in this section is focused mainly on three cases in the first group (D1, D4 and D6). Flow unsteadiness is produced for the three cases presented as the pneumatic control valve is opened in a controlled manner and the flow accelerated from an initial statistically steady turbulent flow to the final stage of the flow at different acceleration periods.

Figures 5-3, 5-4 and 5-5 show the contours of streamwise fluctuating velocities at a wall distance of y=2 mm from the bed of the channel for cases D1, D4 and D6, respectively. The fundamental transition procedure of these transient flows is similar to that of step increase of flow rate of He and Seddighi (2013; 2015), and the slow accelerating flow of Seddighi et al. (2014) and Jung and Kim (2017b). The flow development occurs at a slow rate as will be seen later in Figure 5-6a, for example but again it consists of three stages; namely, pre-transition, transition and fully turbulence, resembling that of bypass transition of boundary layer flow on a flat plate. At $t = 0.0\ sec$, the initial fully-developed turbulent flow is characterised by pre-streaky structures (dark blue) with a small degree of streamwise fluctuations, as shown in the first frames of cases D1, D4 and D6 before the beginning of the flow acceleration. Immediately following the commencement of the transient flow when the pneumatic control valve is opened in a controlled manner, the elongation of the pre-streaky structures in the initial turbulent flow is seen. The amplification of the elongated streaks of both positive and negative streamwise fluctuating velocity becomes stronger in magnitude with time during the pre-transitional stage of the transient flow (up to about $t < 1.9$ s) for case D1, (up to about $t < 3.3$ s) for case D4 and (up to about $t < 4.4$ s) for case D6. The formation and stretching of these streaky structure are seen in the pre-transitional stage and the time of pre-transitional stage increases as the acceleration period increases, as shown in Figures 5-3, 5-4 and 5-5. During the transitional stage, the stretched streaks (dark blue deeper) break and the formation of isolated turbulence spots appear. These isolated turbulence spots, which appear initially as turbulence bursts, then grow with time and combine with each other in the downstream of the flow. The transitional time frames for the three cases occurs between $1.9 < t < 3.01$ for case D1, $3.3 < t < 5.05$ for case D4 and $4.40 < t < 6.05$ for case D6, as shown in Figures 5-3, 5-4 and 5-5. The flow becomes fully developed turbulent flow and the transition completes as the entire wall-bounded surface has been filled with newly generated turbulence structures. The newly generated turbulence structures are seen to cover the entire wall surface from $t > 3.0$ for case D1, $t > 5.0$ for case D4 and $t > 6.0$ for case D6. The times of the onset of transition, as shown in Table 5-2, are obtained using the skin friction coefficient ($C_f$) for cases D1, D4 and D6 and are similar to that of the flow visualisation of this section. It can be seen from the contour plots of the streamwise fluctuating velocity that as the acceleration period increases, the onset of transition increases from 1.9 s in case D1 to 4.4 s in case D6, as shown in Figures 5-3, 5-4 and 5-5.

The trend of case D1 is the same as that of the numerical and experimental findings of Mathur et al. (2018) and the experimental flow structures of Gorji (2015). However, the trends of cases D4 and D6 are not the same to that of Gorji (2015) and Mathur et al. (2018) because the flow development delays as the acceleration period increases. The elongation of the pre-streaky structures occurs slowly in cases D4 and the time of transition delays. In case D6, the elongation of pre-streaky is weaker resulting in a delay in transition to turbulence. In addition, the duration of the pre-transitional stage is longer. It should be noted that the flow measurement area ( $4\delta \times 4\delta$ ) of the present experimental flow cases is bigger than the experimental studies of Gorji (2015) and Mathur et al. (2018) but smaller in comparison with the flow domains of the previous numerical studies. Despite the difference in flow domains, the fundamental procedures of transition to turbulence are similar. The flow structures described above are similar to that of the flat plate boundary layer flow reported by Jacobs and Durbin (2001) in which the boundary layer flow develops spatially.

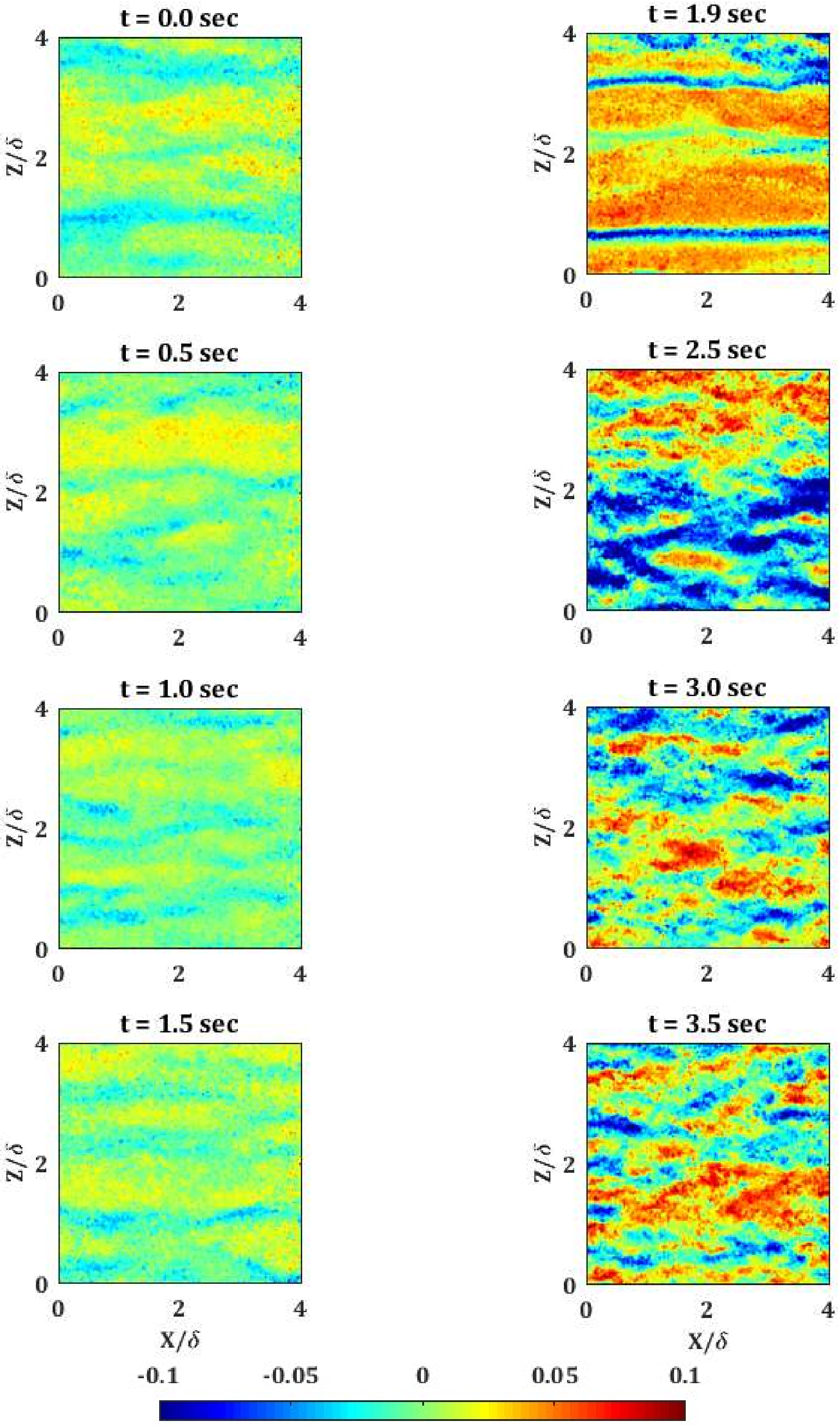

*Figure 5-3: Temporal variation of contour plots of streamwise fluctuating velocity, u' (m⁄s) for case D1 ($Re_b$ = 2799-15601) at a distance of 2 mm from the channel bed.*

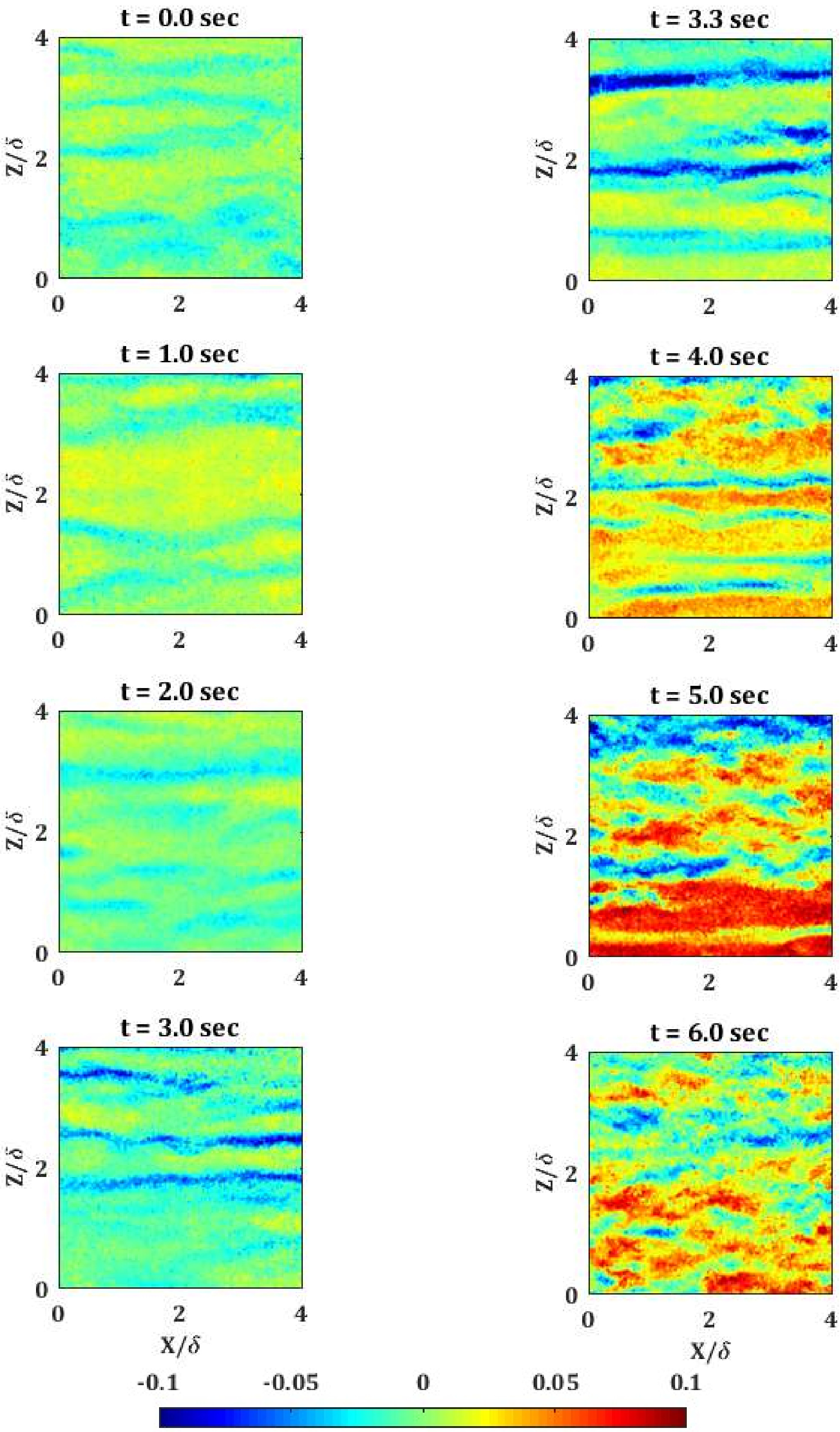

*Figure 5-4: Temporal variation of contour plots of streamwise fluctuating velocity, u' (m/s) for case D4 ($Re_b$ = 2813-15319) at a distance of 2 mm from the channel bed.*

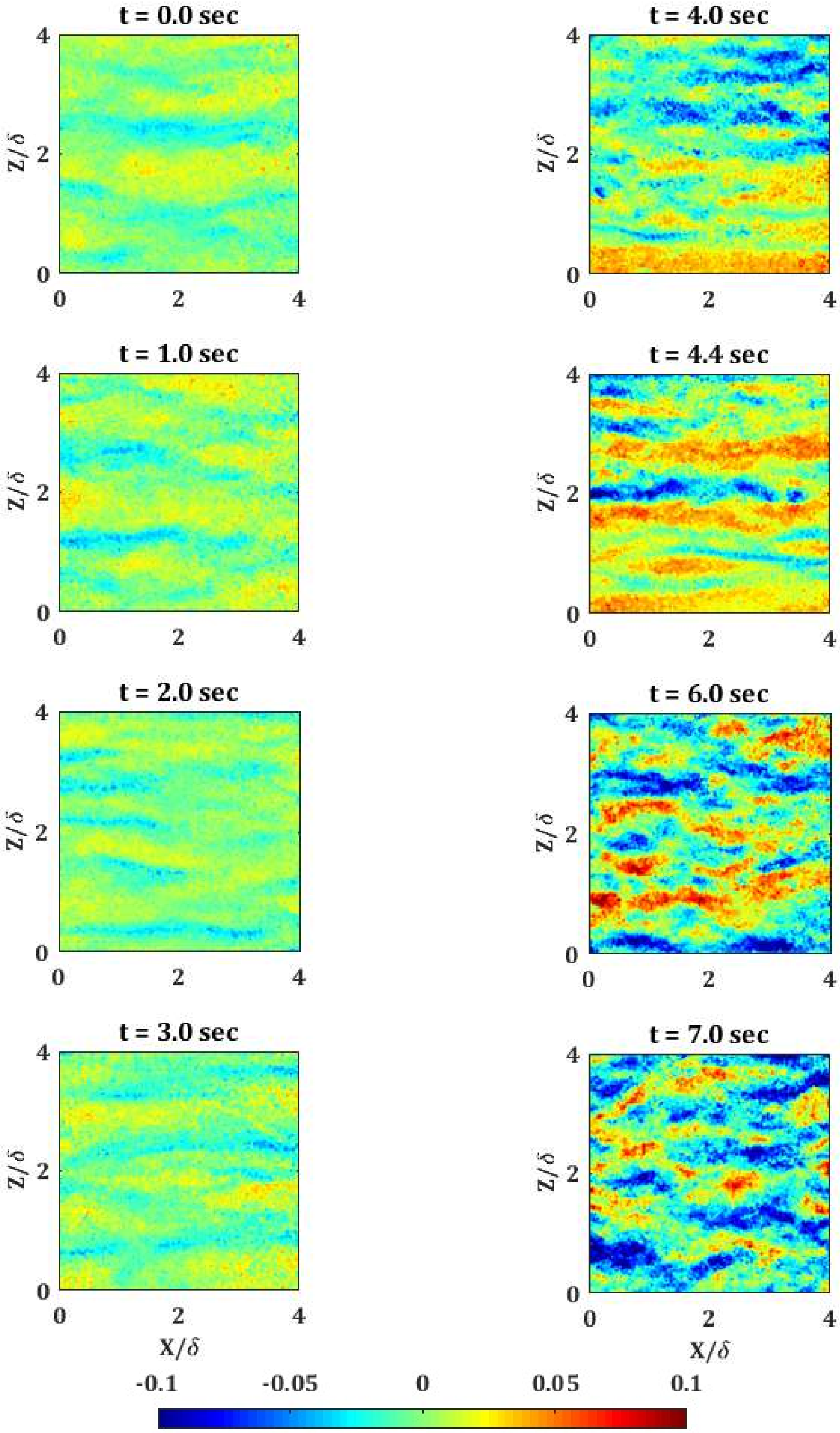

*Figure 5-5: Temporal variation of contour plots of streamwise fluctuating velocity, u' (m/s) for case D6 ($Re_b$ = 2865-15584) at a distance of 2 mm from the channel bed.*

## 5.4 Ensemble-averaged behaviour in slow accelerating flow

In this section, the response of transient turbulent flow accelerated at different acceleration periods is investigated with the help of ensemble-averaged calculation. The data acquisition described in this section is done with a vertical-PIV orientation. PIV measurements are taken through the field of view (FOV) of 30.60 $mm \times 30.60\ mm$. Dantec DynamicStudio software, version 3.41 is used to process the data obtained by PIV using an adaptive correlation method. The final interrogation area size is 32 × 32 pixels and the initial interrogation area size is 256 × 256 pixels, with 3 being the number of refinements as are utilised during the data processing. For ensemble-averaging to be performed, 80 repeated experimental runs are performed for each experimental case investigated. The response of wall shear is recorded by CTA with hot-film sensors. Ensemble-averaging is performed on all the repeated experimental runs acquired in order to determine wall shear stress for each of the cases investigated.

### 5.4.1 Response of skin friction coefficient in a slow accelerating flow

The behaviour of $C_f$ between two transient flows is important as it helps to reveal the overall characteristics of the flow. Equation (4.2) was used in Chapter Four to calculate the skin friction coefficient and the same equation is adopted in this chapter as follows:

$$C_f(t) = \frac{2\tau_w(t)}{\rho(U_b(t))^2} \tag{5.1}$$

where $\tau_w(t)$ is the wall shear stress of the flow at time, $t$ and $U_b(t)$ is the bulk velocity at time, $t$ of the flow. Investigations in this section are divided into two groups as presented in Table 5-1. Focusing first on D cases, transient turbulent flow is accelerated from approximately the same Reynolds number ($Re_0$) of 2800 to the final approximate Reynold number ($Re_1$) of 15600 at different acceleration periods. Figure 5-6a shows the development of the skin friction coefficient ($C_f$) during the transient channel flow for all the D cases investigated. Immediately after the start of the transient flow, $C_f$ increases and reaches its maximum peak. This is due to the creation of thin boundary layer near the wall that increases both viscous force and velocity gradient. The growth of the thin boundary layer in the flow during the pre-transitional time frame causes the skin friction coefficient to decrease and reach a minimum value for cases D1, D2, D3, D4, D5 and D6 at 1.91s, 2.07s, 2.71s, 3.35s, 4.35s, and 4.45s, respectively. Thus, the reduction in $C_f$ occurs at a slow rate as the acceleration period increases. The time at which the skin friction coefficient reaches the minimum value marks the start of the transition and has been referred to as the critical time by He and Seddighi (2013).

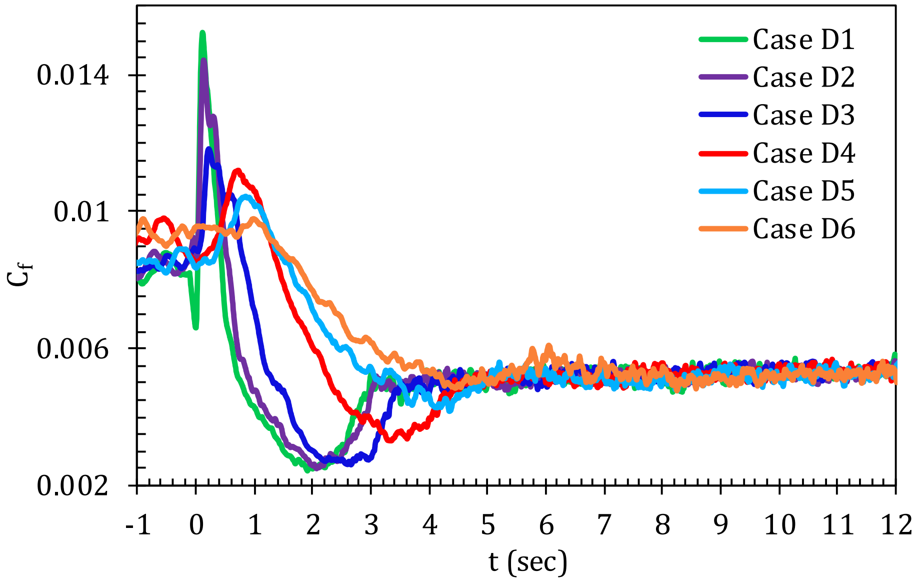

a)

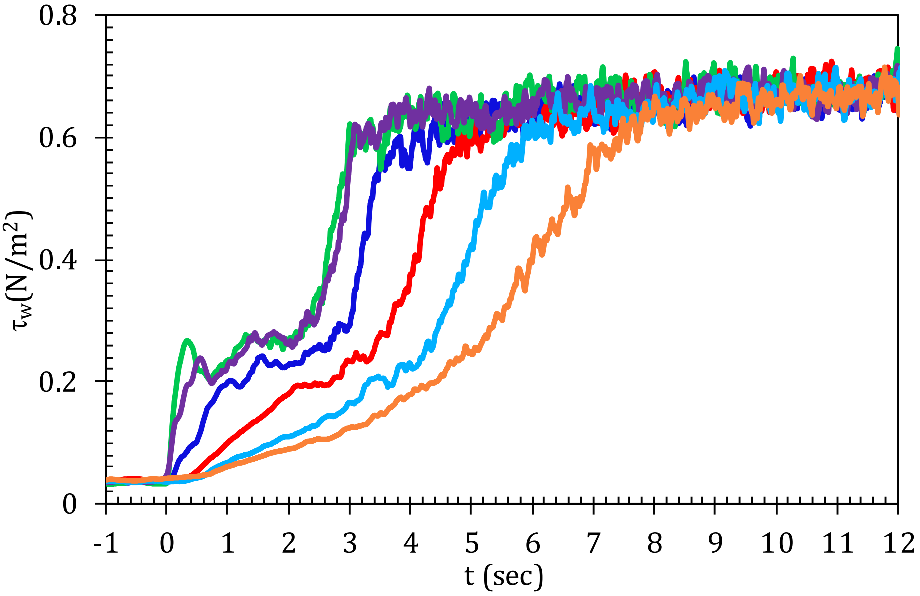

b)

***Figure 5-6: Development of skin friction coefficient ($C_f$) and wall shear stress ($\tau_w$) during slow accelerating flow: a) skin friction coefficient ($C_f$), b) wall shear stress.***

The skin friction coefficient increases again following this initial reduction, which is due to the creation of ''new'' turbulence structures at the start of the transition. It approaches the final statistically steady values marking the end of transition for cases D1, D2, D3, D4, D5 and D6 at 3.01s, 3.09s, 3.54s, 5.05s, 5.20s, and 6.05s, respectively. Other normalised times that indicate the onset and completion of transition are shown in Table 5-2. The development of the skin friction coefficient ($C_f$) elucidated above resembles the $C_f$ development reported on flat plate boundary layer flow by Jacobs & Durbin (2001) and Nagarajan et al. (2007). The growth of $C_f$ of the current cases investigated is also similar with that of slow accelerating flow numerically investigated by Seddighi et al. (2014) and Jung and Kim (2017b). The development of $C_f$ occurs in three stages, similar to the previous channel transient flow reported by He and Seddighi (2013), Seddighi et al. (2014) and Mathur et al. (2018), but due to a slow acceleration, the details are different. It is shown from Figure 5-6a that as the acceleration period increases, the time equivalent to the minimum value of $C_f$ that marks the onset of transition to turbulence in the slow accelerating cases increases. For all the D cases examined, as the acceleration period increases, the critical time of transition increases from 1.91s ($t_{cr}^{+0} = 80$) to 4.45s ($t_{cr}^{+0} = 195$), as shown in Table 5-2.

By comparing the responses of $C_f$ in all the D cases, the effects of varying acceleration period on transient flow are revealed. It can be seen that the response of the initial $C_f$ to the flow acceleration for case D1 is the fastest of all cases. The trend of the $C_f$ in the flow is similar to that of step increase of flow rate reported by He and Seddighi (2013) and the experimental studies of Mathur et al. (2018). The peak reduces slightly in the case D2 and a significant reduction of the peak can be seen in cases D2-D6 as the acceleration period increases. Moreover, as the acceleration period increases, the minimum $C_f$ increases from significant undershooting to a very minimal undershooting in D6, as shown in Figure5-6a. The transitional period reduces as the acceleration period increases, but this become less clear in case D6, similar to the results published by Seddighi et al. (2014) and Jung and Kim (2017b). Figure 5-6a shows wiggles in the initial flow before the flow acceleration; this is due to an insufficient number of realisations for all D cases investigated. For the eradication of the wiggles in the initial flow, the number of realisations must be increased far above the current 80 repeated experimental runs.

The development of skin friction coefficient of $(C_f)$ of E cases is presented Figure 5-7a. In each of the E cases investigated, both final Reynolds number and acceleration period varied while the initial Reynolds number is maintained at approximately the same Reynolds number $(Re_0)$ of 2800. Table 5-1 shows the flow parameters for E cases. The response of $C_f$ is similar to that of D cases previously presented. During the accelerating flow, $C_f$ increases reaching its maximum value then reducing slowly to the minimum value of $C_f$ that marks the onset of transition to turbulence. $C_f$ then increases again due to the generation of turbulence structures in the flow to the final statistically steady value that marks the end of the transition, as shown in Figure 5-7a. The onset of transition for the three E cases examined occurs at 2.83s, 2.85s and 3.72s for E1, E2, and E3, respectively, while the time of completion of turbulence occurs at 4.78s for E1, 3.70s for E2, and 4.15s for E3.

It is interesting to note that the initial increase of $C_f$ in E1 is much faster than that in the other cases (E2 and E3), despite the final flow in E1 being much slower than in the other two flows. This is likely due to the fact that the initial acceleration in E1 is much stronger than in other two flows, as shown in Figure 5-2. On the other hand, the transitional period is much longer in E1 than in E2 and E3. Moreover, the undershooting in E1 in comparison with other cases is much more pronounced. This may be linked to the fact that the final Reynolds number in E1 is lower than in other cases. Another interesting finding to note is that the peak $C_f$ achieved in cases E2 and E3 are effectively the same – slightly lower than that in E1. This is despite the fact that the acceleration, final Reynolds number and transient period are all very different in these cases. However, this may not bear much physical significance and further study should be carried out to ascertain whether this assumption is correct. These scenarios will be discussed further in relation to the response of $\tau_w$ later in § 5.4.2. As shown in Figure 5-7a, the minimum value of $C_f$ increases as the acceleration period and final Reynolds number increases for the three flows, and the onset of transition is longer in case E3. Moreover, the minimum $C_f$ varied from very large undershooting to a small one in E3. The final $C_f$ for E1, E2 and E3 decreases with an increase of the final Reynolds number and acceleration period.

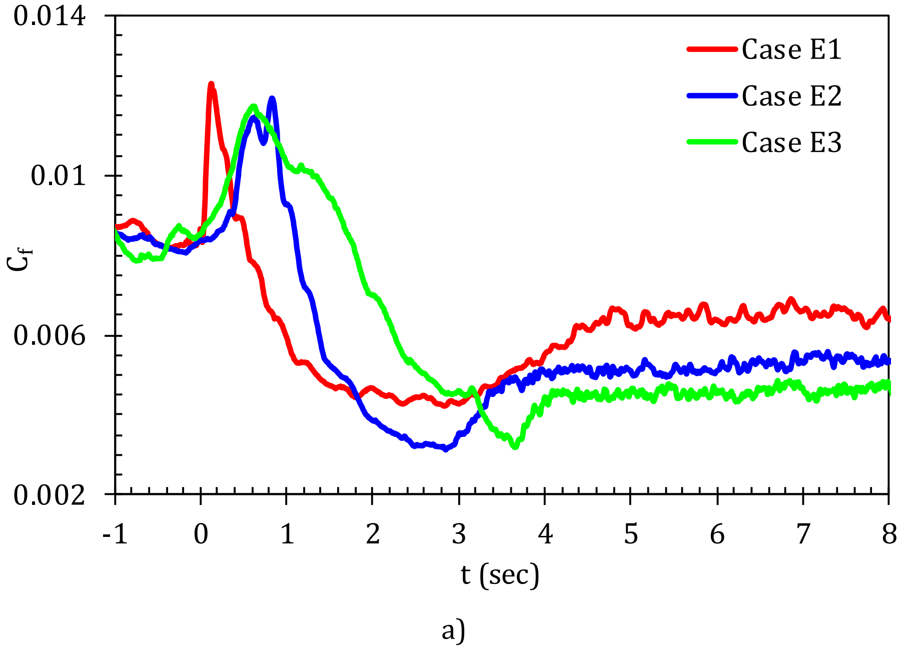

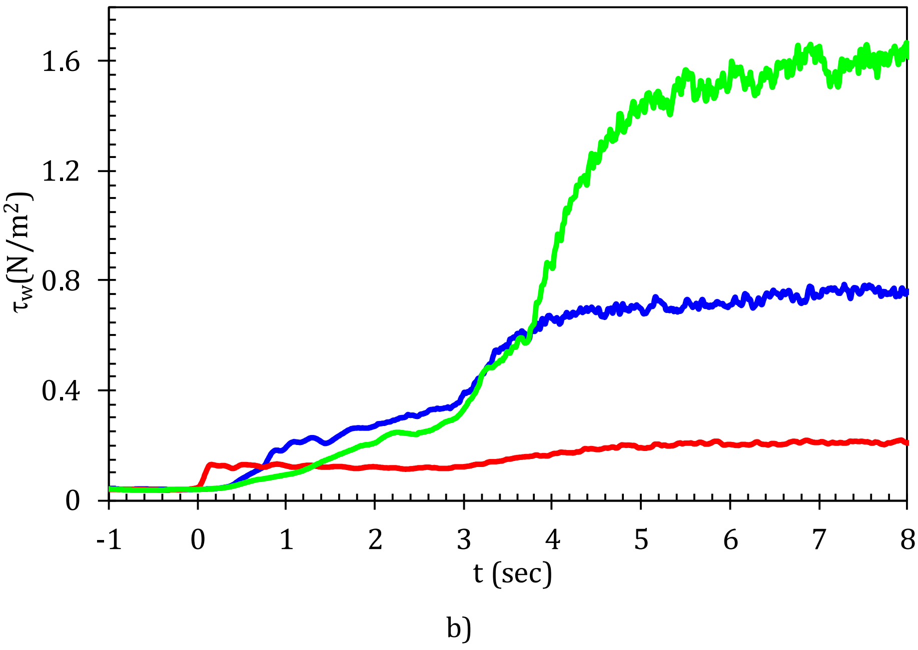

***Figure 5-7: Development of skin friction coefficient ($C_f$) and wall shear stress ($\tau_w$) during slow accelerating flow: a) skin friction coefficient ($C_f$), b) wall shear stress.***

### 5.4.2 Response of wall shear stress in a slow accelerating flow

In this section, the development of wall shear stress is described. The wall shear stress developments for the first and second groups are shown in Figure 5-6b and 5-7b and the figures share the same legend as Figure 5-6a and 5-7a, respectively. During the initial flow acceleration, a thin boundary layer of high velocity gradient and strain rate is formed near the wall, leading to a sharp increase in wall shear stress ($\tau_w$). As the thin boundary layer transports into the flow, it reduces both velocity gradient and strain rate and causes the sharp wall shear stress that is earlier generated to reduce. However, in this slow accelerating flow, the mean flow continues to accelerate at this time, as shown in Figure 5-1 and 5-2, which causes an additional boundary layer to be generated and spread into the flow. This leads to a temporally developing boundary layer that is responsible for further changes in the structure of the flow and additional wall shear stress is formed. The development of the $\tau_w$ for the D cases within the slow accelerating flow can be classified as faster (D1, D2 and D3), medium (D4 and D5) and slower (D6), as shown in Figure 5.8 (a,b&c).

The response of wall shear stress ($\tau_w$) in D cases exhibits interesting characteristics and a four-stage development is observed in faster cases which are (D1, D2 and D3), as shown in Figures 5-6b. The four-stage development for the three faster cases is shown in Figure 5.8 (a,b&c). In this description, the pre-transition is split into two stages as seen below. During the initial increase of flow rate, a sharp increase of wall shear stress ($\tau_w$) is observed in D1, D2 and D3 might due to the formation of a thin boundary layer near the wall in stage 1. This sharp increase of $\tau_w$ in D1, D2 and D3 is due to a high acceleration rate. The same sharp increase is observed in the bulk velocity profiles, as shown in Figure 5-1. As previously elucidated, $\tau_w$ reduces as the thin boundary layer generated transports into the flow. It can be seen during the stage 2, the reduction of the $\tau_w$ is noticeable in D1, D2and D3 as the mean flow continues to increase, as shown in Figure 5-1, and an additional boundary layer continues to form and transports into the flow, which causes the $\tau_w$ to increase gradually until the onset of transition at stage 3 ($t = 1.91s$ for case D1, $t = 2.07s$ for case D2 and $t = 2.71s$for case D3). At the beginning of stage 3, the transition of the time-developing boundary layer occurs, leading to an increment in $\tau_w$ to stage 4 and the start of stage 4 marks the end of transition. The $\tau_w$ increases slightly during stage 4 and attained a statistically steady flow. As the acceleration period increases, the length of stage 2 starts to decrease and vanishes in case D6. The response of the $\tau_w$ in D6 appears to be different from that in the faster cases, such as D1, D2 and D3. As shown in Figure 5-8f, the $\tau_w$ largely follows the quasi-steady values throughout the transient, except over a small period in the middle. Based on this observation, we may refer this flow as quasi-steady. However, we will see later, the turbulent development (especially wall-normal fluctuating velocity, $v'_{rms}$) indicates that, a distinct transition also occurs in the slow acceleration. Moreover, it can be seen in Figure 5-9, the $\tau_w$ in E1 is similar to that in D1, D2 and D3, and hence it is a fast transient flow. Case E2 and E3 behave as medium and a slow transient, respectively.

The development of wall shear stress with the corresponding quasi-steady values are presented in Figure 5-8 & 5-9 for D cases and E cases, respectively. For the determination of quasi-steady values, the statistically steady values of several Reynolds numbers and wall shear stress that cover the whole range of the accelerating flow cases investigated are obtained. Quasi-steady values are then derived from the power law of the curve fitting of the steady values of Reynolds numbers and wall shear stress. The response of $\tau_w$ of the medium (D4, D5 and E2) and slower (D6 and E3) transient cases is shown to be different from that of faster transient cases (D1, D2, D3 and E1). The $\tau_w$ increases following the commencement of the flow acceleration and it increases above the quasi-steady value due to the formation a thin boundary layer. The transportation of the the boundary layer to the flow causes the $\tau_w$ to reduce below the quasi steady value. It increases again due to the generation of "new" turbulence structures in the flow and attains the quasi-steady value as the flow become fully developed turbulent flow. As shown in Figures 5-8 and 5.9, the undershooting of $\tau_w$ becomes smaller as the acceleration period increases.

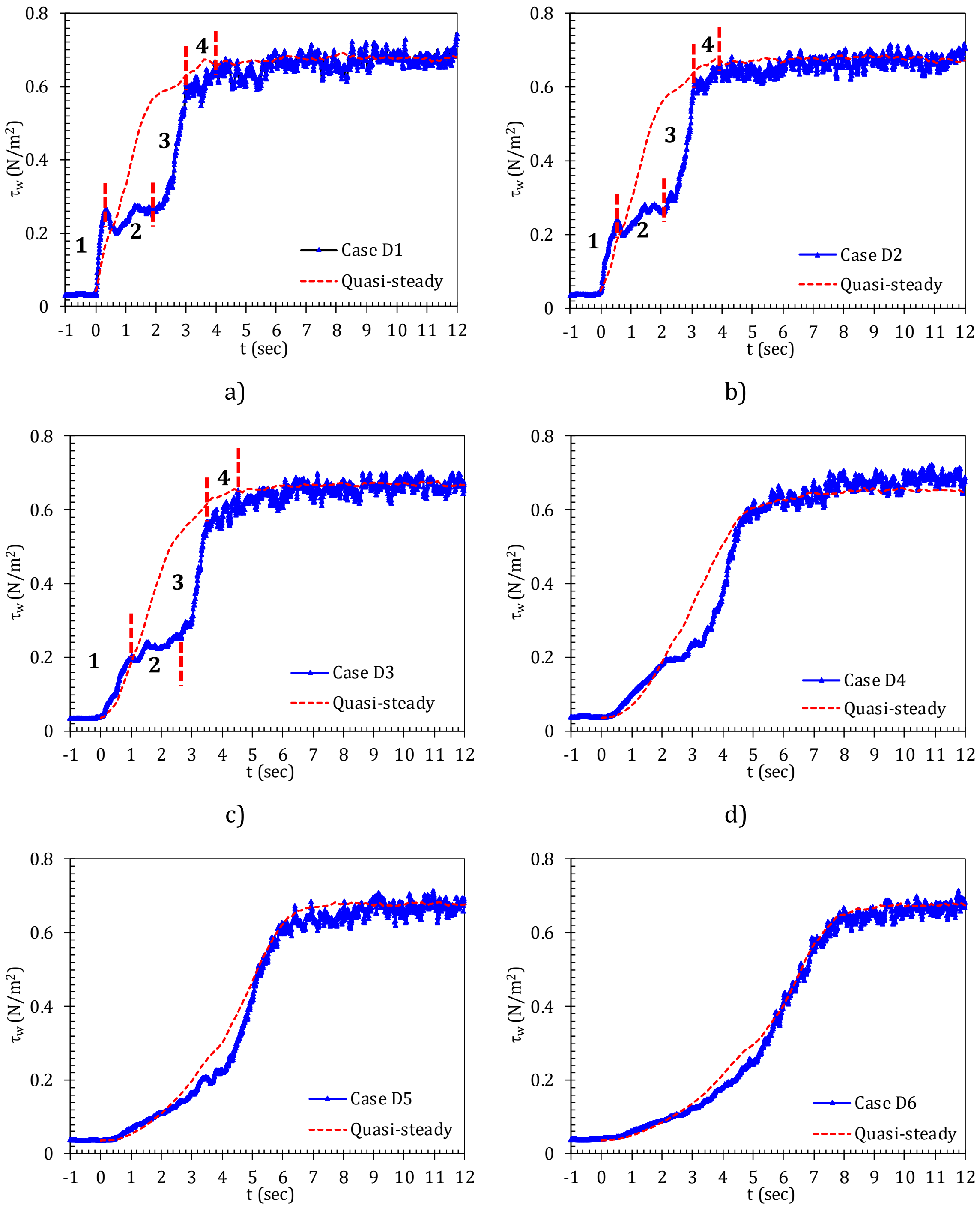

a) b) c) d) e) f)

***Figure 5-8: Development of wall shear stress in slow accelerating flows with different acceleration periods showing quasi-steady flow values for cases D1 (a), D1 (b), D3 (c) D4 (d), D5 (e) and D6 (f).***

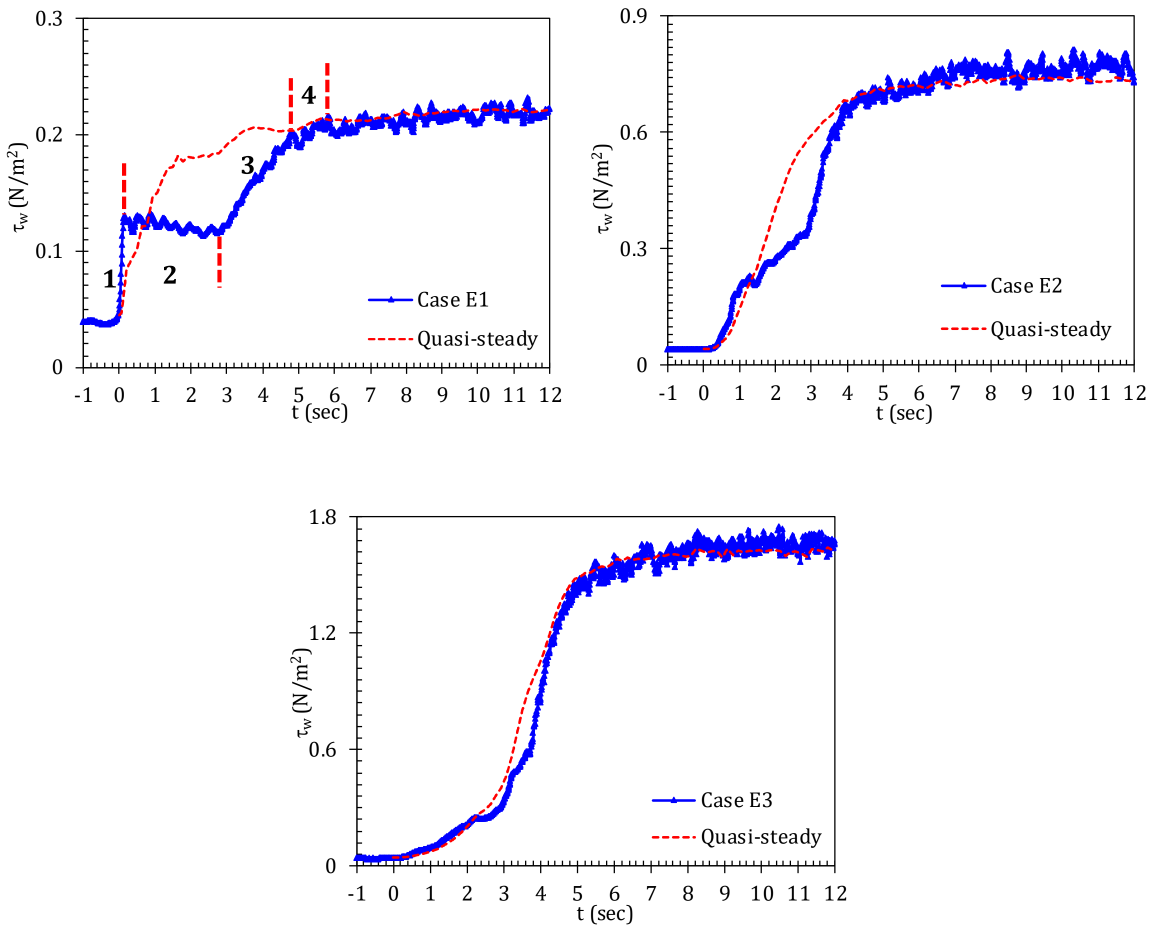

***Figure 5-9: Development of wall shear stress in slow accelerating flows with different acceleration periods showing quasi-steady flow values for cases E1 (a), E2 (b) and E3 (c).***

## 5.4.3 Response of mean velocity and turbulence statistics in a slow accelerating flow

The behaviour of streamwise mean velocity, streamwise fluctuating velocity, wall-normal fluctuating velocity and Reynolds shear stress are discussed in this section. The discussion of this section focuses on three cases from group D and two cases from group E. The cases to discuss in group D are $Re_b$ = 2799-15601 (D1), 2813-15319 (D4) and 2865-15584 (D6) while cases $Re_b$ = 2755-7440 (E1) and 2769-24010 (E3) are discussed in group E. The ensemble-averaged statistics are obtained from 80 repeated experimental runs on each of the cases examined. As previously described in §3.8, spatial averaging is performed on the experimental data in the streamwise direction then averaged through the total repeated experimental runs in order to obtain mean and turbulence quantities for each case.

#### 5.4.3.1 Development of mean velocity and turbulence statistics at different wall locations

The transient development of the slow accelerating flow is pesented at wall locations of ${}^{y}/_{\delta} = 0.07, 0.2. 0.45$ and $1$ which are equivalent to dimensionless wall distance, $y^{+0}(= {}^{yu_{\tau o}}/_{v})$ =12.94, 35.73, 80.40 and 178.66, respectively. The dimensionless wall distance ($y^{+0}$), is based on the initial friction velocity ($u_{\tau o}$), actual wall distance ($y$) and kinematic viscosity ($v$) of the working fluid. There are four subplots used to show the variation of streamwise mean velocity ($U$) and the turbulence statistics, that is ($u'_{rms}, v'_{rms}$ and $\overline{u'v'}$). Figures 5-10, 5-11 and 5-12 present the temporal growth for cases D1, D4, and D6, respectively while Figures 5-13 and 5-14 show the transient development for cases E1 and E3, respectively.

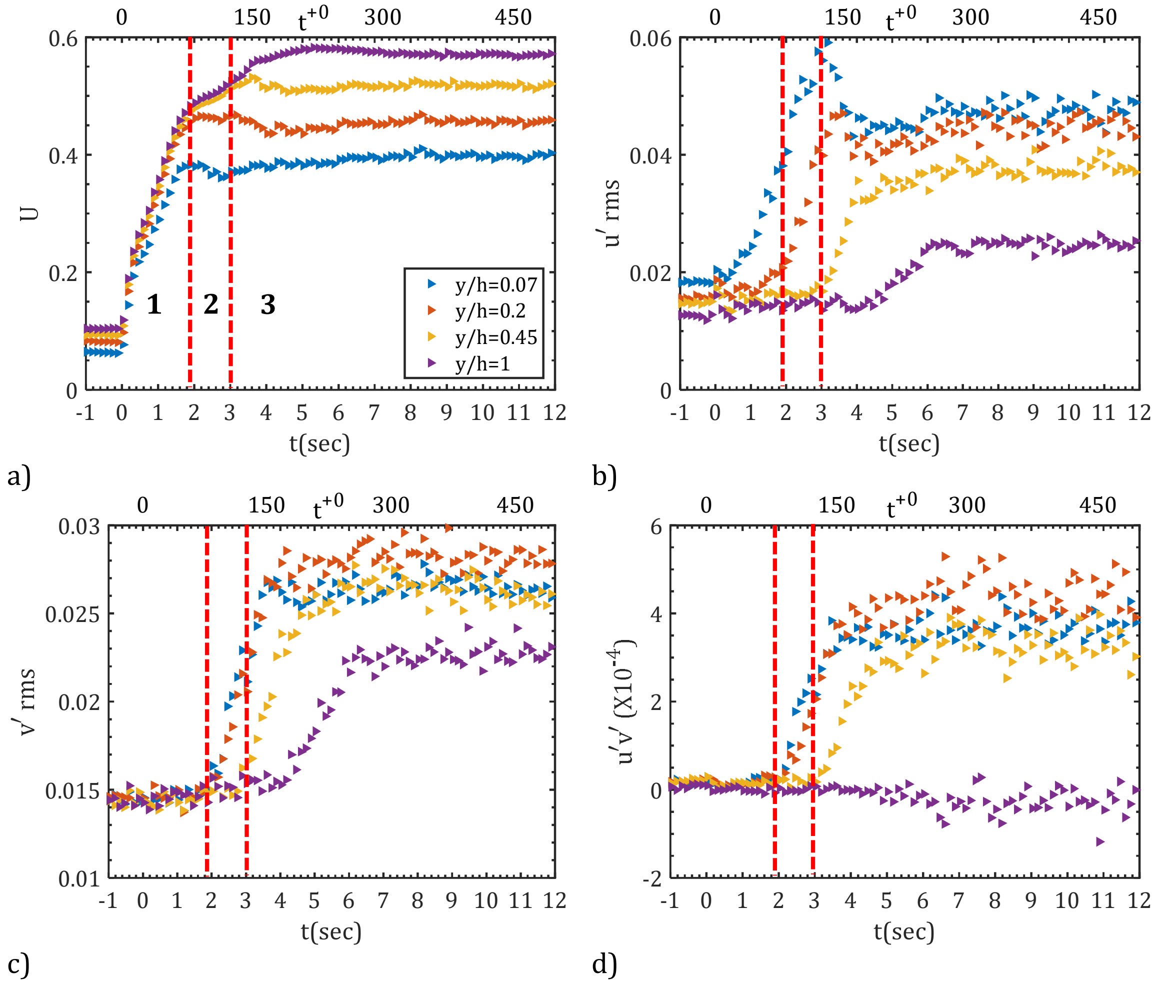

***Figure 5-10: Temporal growth of streamwise mean velocity ($U$), streamwise fluctuating velocity ($u'_{rms}$), wall-normal fluctuating velocity ($v'_{rms}$), and Reynolds shear stress ($\overline{u'v'}$) for case D1 ($Re_b = 2799 - 15601$) with acceleration period of 1.87s. Legend is the same for the four subplots and all quantities are not normalised. The unit of subplots (a)-(c) is m/s and that of subplot (d) is m$^2$/s$^2$. 1) pre-transition, 2) transition and 3) fully turbulence. Channel half-height δ=h.***

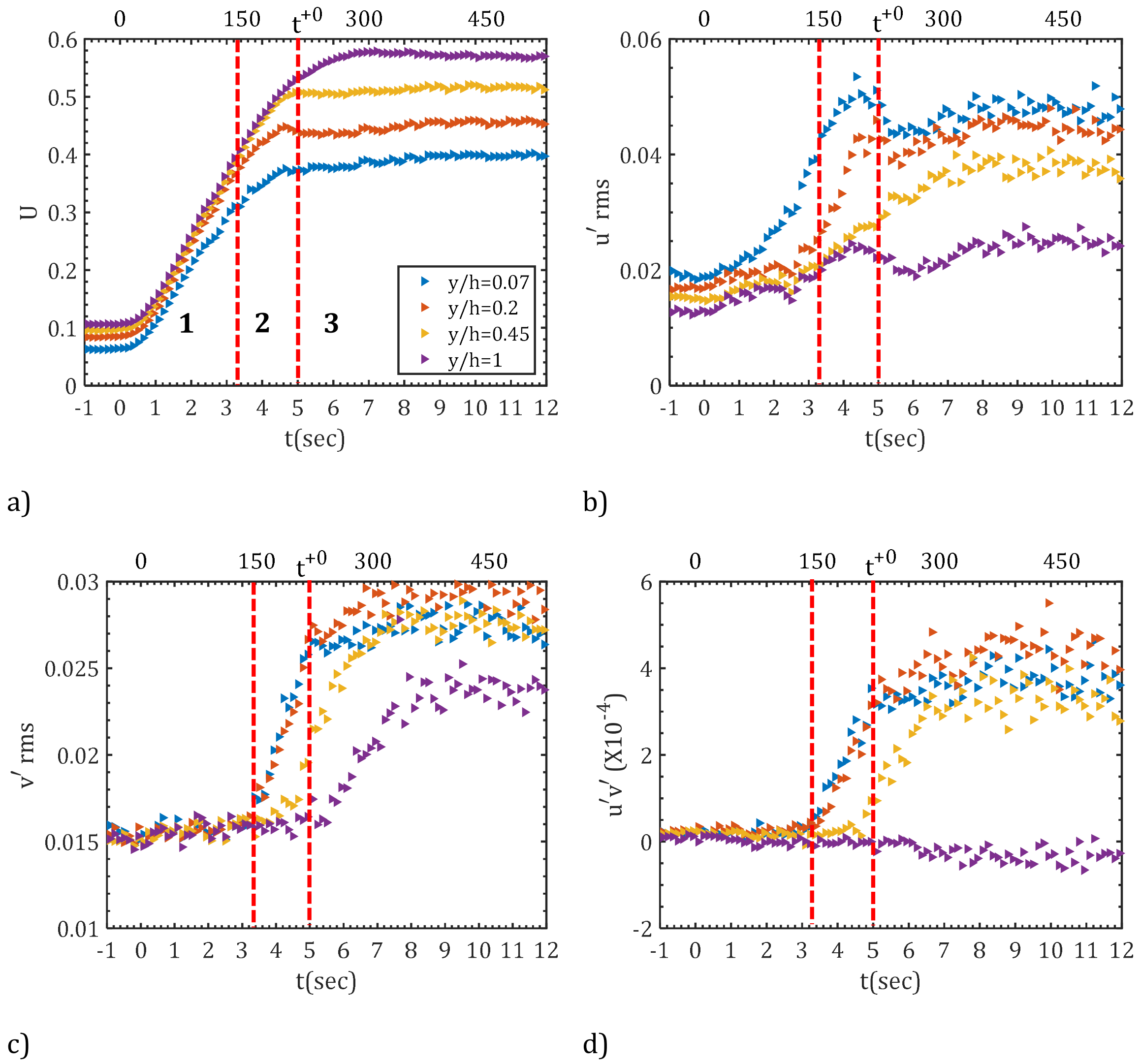

***Figure 5-11: Temporal growth of streamwise mean velocity ($U$), streamwise fluctuating velocity ($u'_{rms}$), wall-normal fluctuating velocity ($v'_{rms}$), and Reynolds shear stress ($\overline{u'v'}$) for case D4 ($Re_b = 2813 - 15319$) with acceleration period of 4.26 secs. Legend is the same for the four subplots and all quantities are not normalised. The unit of subplots (a)-(c) is m/s and that of subplot (d) is m²/s². 1) pre-transition, 2) transition and 3) fully turbulence. Channel half-height δ=h.***

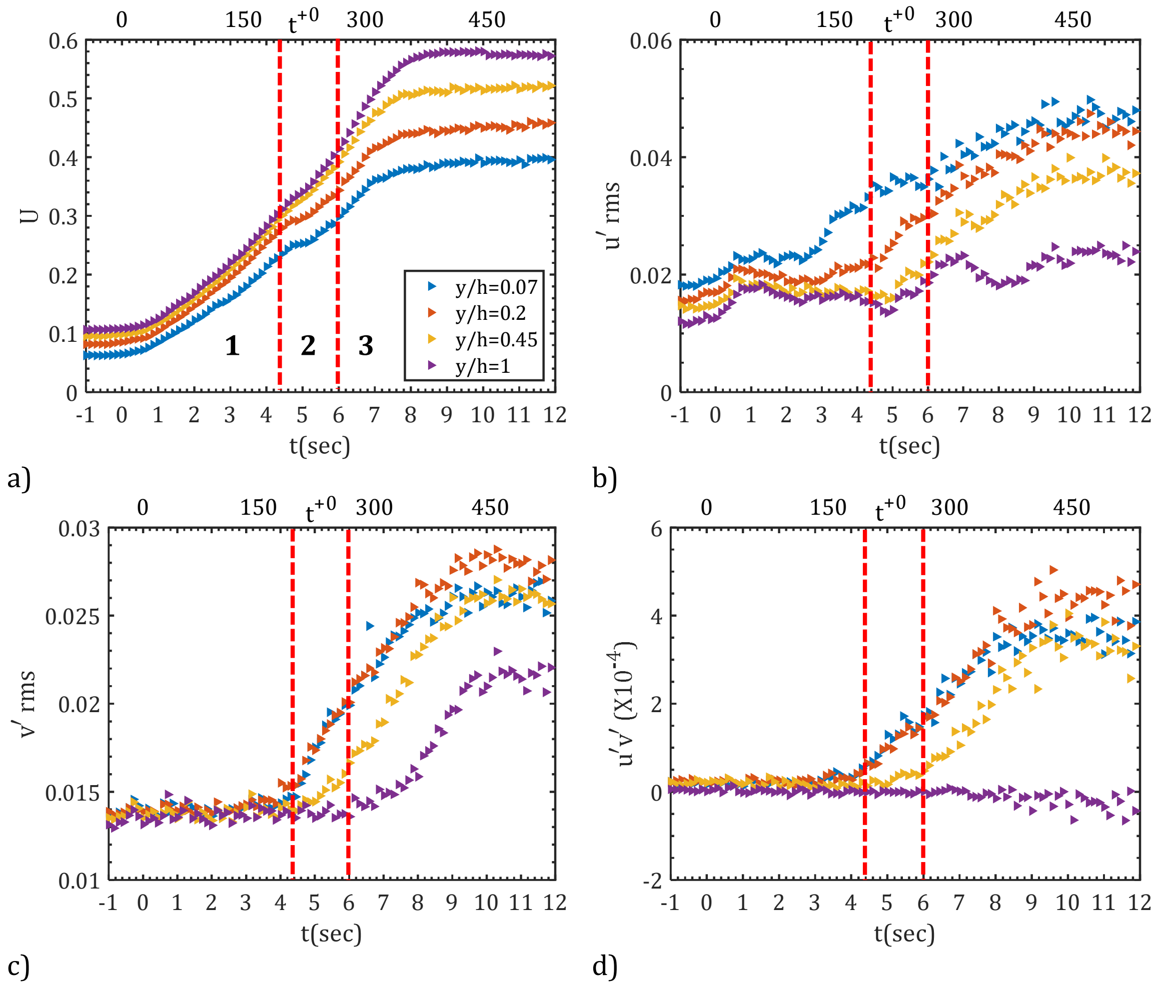

***Figure 5-12: Temporal growth of streamwise mean velocity ($U$), streamwise fluctuating velocity ($u'_{rms}$), wall-normal fluctuating velocity ($v'_{rms}$), and Reynolds shear stress ($\overline{u'v'}$) for case D6 ($Re_b = 2865 - 15584$) with acceleration period of 6.94 secs. Legend is the same for the four subplots and all quantities are not normalised. The unit of subplots (a)-(c) is m/s and that of subplot (d) is $m^2/s^2$. 1) pre-transition, 2) transition and 3) fully turbulence. Channel half-height δ=h.***

It should be noted noted that the streamwise mean velocity responds like a 'plug flow' (that is the flow responds as a solid body everywhere in the flow region apart from the location near the wall) immediately after the commencement of the slow acceleration. It increases uniformly across all the locations but at a slow rate as the acceleration period increases. The development of the streamwise mean velocity for cases D1, D4, and D6 is shown in Figures 5-10a, 5-11a and 5-12a, respectively. During the pre-transitional time frame, the streamwise fluctuating velocity ($u'_{rms}$) responds immediately in the viscous wall region but a delay is experienced in the centre of the flow, as shown in Figures 5-10b, 5-11b and 5-12b. At this pre-transitional stage, both wall-normal fluctuating velocity ($v'_{rms}$) and Reynolds shear stress ($\overline{u'v'}$ ) exhibit a significant delay and remain unaltered in all the wall locations, as shown in Figures 5-10(c,d), 5-11(c,d) and 5-12(c,d).This pre-transitional stage has been reported to be equivalent to buffeted laminar region in the transition to turbulence of a flat plate boundary layer flow subjected to $FST$ (He & Seddighi, 2013; Seddighi et al., 2014; He & Seddighi, 2015).

At the centre of the channel, the behaviour of the streamwise fluctuating velocity ($u'_{rms}$), wall-normal fluctuating velocity ($v'_{rms}$) and Reynolds shear stress ($\overline{u'v'}$ ) are found to be similar in delayed response as the distance from the wall increases. This is a common attribute associated with temporal accelerating turbulent flow in that the transportation of turbulence from the wall to the centre of the flow is caused by a diffusion mechanism (He & Jackson, 2000). The rapid increase of streamwise fluctuating velocity ($u'_{rms}$) near the wall can be attributed to the stretching, enhancement and elongation of the initial streaky structures. In addition, the increment is equivalent to the growth of energy of the perturbations before the onset of transition in the buffeted laminar region of the flat plate boundary layer flow (Jacobs & Durbin, 2001; Nagarajan et al., 2007). The increase of $u'_{rms}$ establishes the fact that the enhancement and elongation of the streaky structures occurs first in the wall region before transporting to the centre of the flow. The lack of response of wall-normal fluctuating velocity ($v'_{rms}$) to both accelerating flow and the initial response of the streamwise fluctuating velocity ($u'_{rms}$) provide clear evidence that no "new" turbulence formation occurs during the pre-transitional stage.

Furthermore, at the onset of transition to turbulence, both wall-normal fluctuating velocity ($v'_{rms}$) and Reynolds shear stress ($\overline{u'v'}$ ) that do not initially respond to flow acceleration, begin to respond at the location near the wall, as shown in Figures 5-10(c,d), 5-11(c,d) and 5-12(c,d).The delay of $v'_{rms}$ and $\overline{u'v'}$ increases as the acceleration period increases in D1, D4 and becomes very long in case D6. The response of the two quantities shows the formation of "new" turbulence structures in the channel accelerating flow. The time at which $v'_{rms}$ and $u'v'$

starts to respond marks the onset of transition, which is equivalent to the time of the minimum value of skin friction coefficient of $(C_f)$ reported in §5.4.1. Using the wall-normal fluctuating velocity $(v'_{rms})$, the time almost coincides with the time of minimum $C_f$ for cases D1, D4 and D6 as 1.90s, 3.36 and 4.50s, respectively.The slight variation is due to low pulsation frequency of laser used during the experiments. In the experimental investigation of turbulence in a channel flow carried out by Gorji (2015), the author determined the time of onset of transition to turbulence using wall-normal fluctuating velocity $(v'_{rms})$ at a location near the wall. Sundstrom and Cervantes (2017) reported a rapid increase of $u'_{rms}$ during the pre-transitional time frame while both $v'_{rms}$ and $\overline{\mathrm{u'v'}}$ remained unchanged. It was reported by the authors that onset of transition initiates when both $v'_{rms}$ and $\overline{u'v'}$ start to respond to flow acceleration. In this transitional time frame, it is noted that streamwise fluctuating velocity $(u'_{rms})$ increases to its maximum peak, approaches or slightly overshoots the statistically steady values, and then decreases to the final statistically steady values. The obvious decrease at a location near the wall ($y^{+0}$=12.94) is ascribed to the breakdown of streaky structures and the formation of turbulence spots in the flow.

The development of streamwise mean velocity $(U)$, streamwise fluctuating velocity $(u'_{rms})$, wall-normal fluctuating velocity $(v'_{rms})$ and the Reynolds shear stress $(\overline{u'v'})$ of case D1 presented in Figure 5-10, D1 is similar with the previous investigations of Gorji (2015) and Mathur et al. (2018). As the acceleration period increases, the delay of $v'_{rms}$ and $\overline{u'v'}$ increases for cases D4 and D6 as shown in Figures 5-11 and 5-12 which is similar to that of Seddighi et al. (2014). From the figures, it is shown that the onset of transition to turbulence in the slow acceleration increases as acceleration period increases.

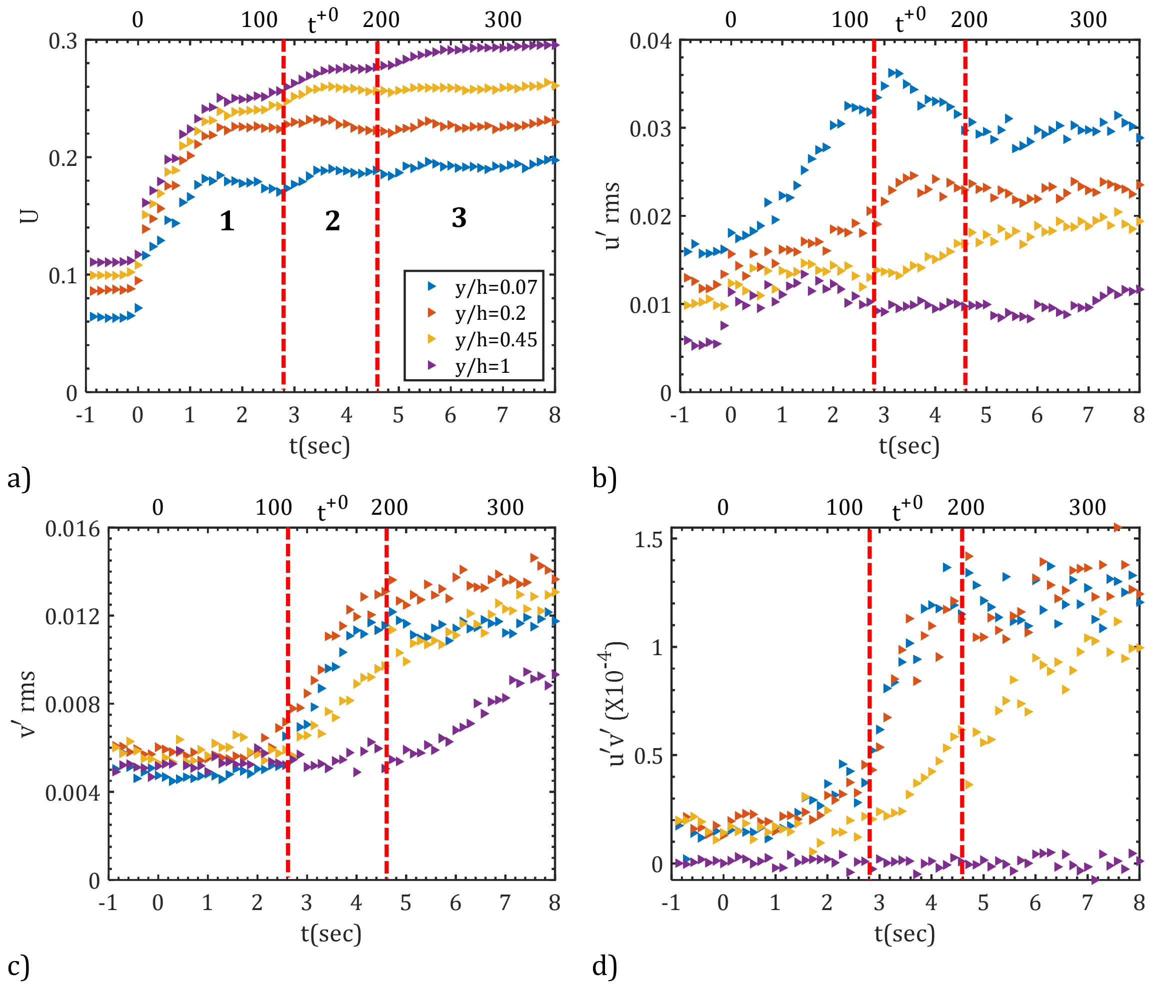

***Figure 5-13: Temporal growth of streamwise mean velocity ($U$), streamwise fluctuating velocity ($u'_{rms}$), wall-normal fluctuating velocity ($v'_{rms}$), and Reynolds shear stress ($\overline{u'v'}$ ) for case E1 ($Re_b = 2755 - 7440$) with acceleration period of 2.73s. Legend is the same for the four subplots and all quantities are not normalised. The unit of subplots (a)-(c) is m/s and that of subplot (d) is $m^2/s^2$. 1) pre-transition, 2) transition and 3) fully turbulence. Channel half-height δ=h.***

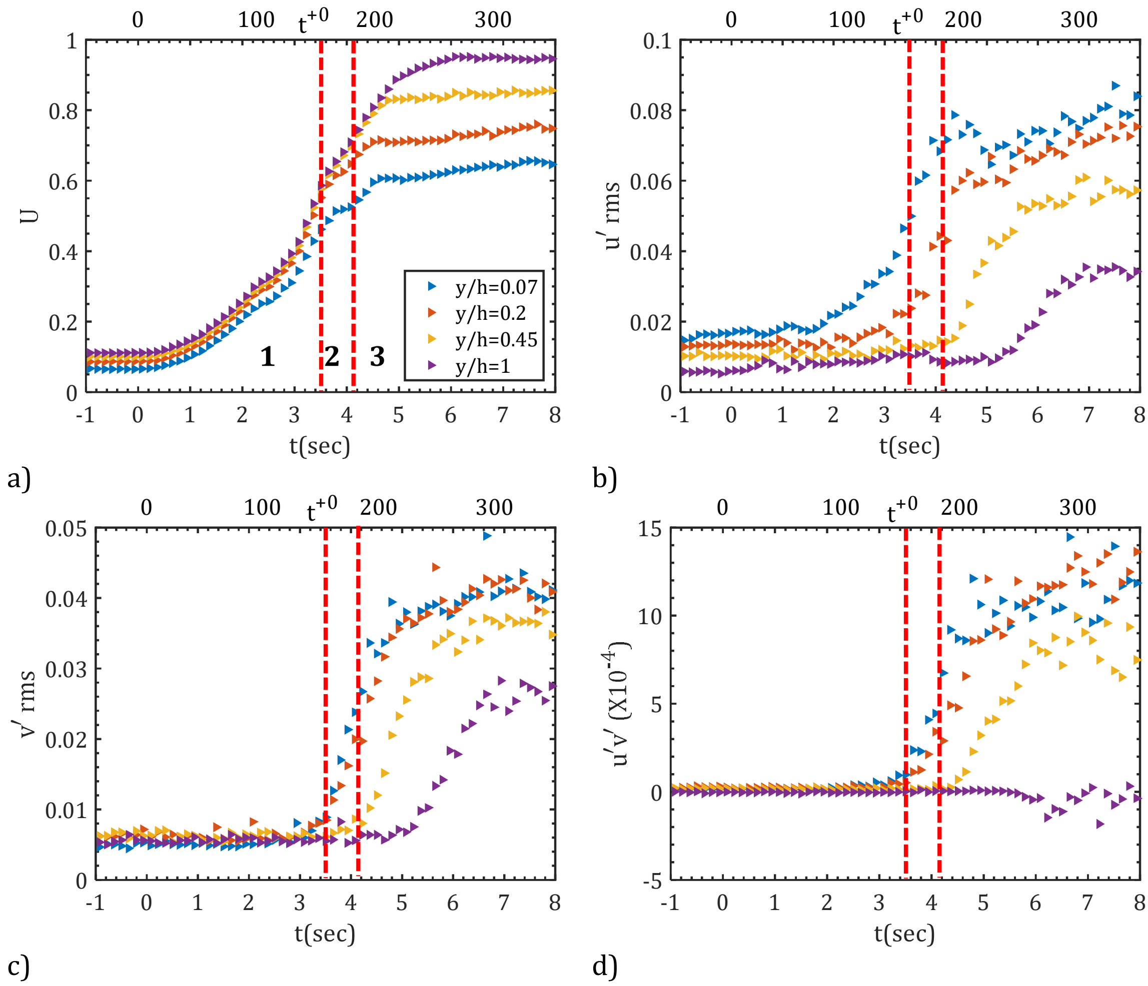

***Figure 5-14: Temporal growth of streamwise mean velocity (U), streamwise fluctuating velocity ($u'_{rms}$), wall-normal fluctuating velocity ($v'_{rms}$), and Reynolds shear stress ($\overline{u'v'}$) for case E3 ($Re_b = 2769 - 24010$) with acceleration period of 4.73. Legend is the same for the four subplots and all quantities are not normalised. The unit of subplots (a)-(c) is m/s and that of subplot (d) is m²/s². 1) pre-transition, 2) transition and 3) fully turbulence. Channel half-height δ=h.***

Two cases, E1 and E3, are presented in group E for brevity. The flow development during the slow acceleration is obtained at different wall locations of $^{y}/_{\delta} = 0.07, 0.2. 0.45$ and 1. The development of streamwise mean velocity ($U$) and turbulence statistics ($u'_{rms}, v'_{rms}$ and $\overline{u'v'}$) is similar to that of D cases previously presented. Figures 5-13 and 5-14 show the temporal growth of streamwise mean velocity and the turbulence statistics for cases E1 and E3, respectively. It should be noted that the two subplots of cases E1 and E3 share the same legend. As with the D cases, the streamwise mean velocity ($U$) and streamwise fluctuating velocity ($u'_{rms}$) responds during the pre-transitional time frame with a delay of $u'_{rms}$. at the centre of the flow while the wall-normal fluctuating velocity ($v'_{rms}$) and Reynolds shear stress ($\overline{u'v'}$) do not change during the transitional time frame. The delay of $v'_{rms}$ and $\overline{u'v'}$ becomes long as the acceleration period final Reynolds number increase in E cases. The same long delay of both $v'_{rms}$ and $\overline{u'v'}$ occurs in laminar flow cases accelerated to turbulent flow in Appendix A.

The time at which both $v'_{rms}$ and $\overline{u'v'}$ start responding to the flow acceleration is expedient, as it is used to determine the onset of transition. In §5.4.1, the time of onset of transition reported using skin friction coefficient ($C_f$) is 2.83s ($t^* = 29$) and 3.72s ($t^* = 125$) for cases E1 and E3, respectively. These times coincide with the point at which $v'_{rms}$ starts responding to the flow acceleration, as shown in Figures 5-13 (a) and 5-14(a) for E1 ($t^* = 29$) and E3 ($t^* = 122$), respectively. For calculations that require the onset of transition in this thesis, the critical time obtained from skin friction coefficient of ($C_f$) is used.

Finally, in slow accelerating flow, it is interesting to note that the onset of transition increases as the acceleration period increases from 2.73s (E1) to 4.73s (E3), using the time at which both wall-normal fluctuating velocity ($v'_{rms}$) and Reynolds shear stress ($\overline{u'v'}$) start responding to the flow acceleration. Though in E cases the final Reynolds number and acceleration period varied, in D cases only the acceleration period varied with a constant final Reynolds number. Moreover, the transition procedure for the two-group cases (E & D) are similar and the time of the onset of transition increases as the acceleration period increases.

#### *5.4.3.2 Time development of spatial distribution of mean velocity and turbulence statistics*

The development of the wall normal profiles of the streamwise mean velocity ($U$), streamwise fluctuating velocity ($u'_{rms}$), wall-normal fluctuating velocity ($v'_{rms}$) and Reynolds shear stress ($\overline{u'v'}$) is investigated at different times for cases D1, D4, D6, E1 and E3. Figures 5-15, 5-16, and 5-17 show time development for cases D1, D4, and D6, respectively. The time development for cases E1 and E3 is shown in Figures 5-18 and 5-19. The procedure of transition to turbulence earlier described is also revealed during the time development of mean and turbulence statistics as discussed below.

Immediately after the commencement of the slow acceleration, streamwise mean velocity starts responding and increases uniformly at all the times selected for each case. The streamwise mean velocity increases and becomes flatter during the transitional period and overlaps when the flow has become fully developed turbulent flow. This is more clearly evident in the faster transient in D1 than in the slower transient in D6, as shown in Figures 5-15a, 5-16a and 5-17a. Related trends are obtained during the experimental investigation of transition to turbulence carried out by Greenblatt and Moss (2004). The streamwise fluctuating velocity ($u'_{rms}$) starts increasing near the wall during the transitional time frame, as previously elucidated in §5.4.3.1. Figures 5-15b, 5-16b and 5-17b show such progressive increment of $u'_{rms}$ near the wall for cases D1, D4, and D6. The increment of $u'_{rms}$ continues throughout the pre-transitional phace; that is during time frame $t^* < 38$ , $t^* < 68$ and $t^* < 90$ for D1, D4 and D6, respectively. It is known that the stretching, enhancement and elongation of the pre-streaky structures in the initial flow before the commencement of the transient flow are responsible for the progressive increase of the $u'_{rms}$ observed here and the procedure is equivalent to the development of energy of the perturbations in the buffeted laminar layer of the flat plate boundary layer flow (Jacobs & Durbin, 2001; Nagarajan et al., 2007). Both wall-normal fluctuating velocity ($v'_{rms}$) and Reynolds shear stress ($\overline{u'v'}$) remain unchanged during the pre-transitional time frame, as shown in Figures 5-15 (c,d), 5-16 (c,d) and 5-17 (c,d).

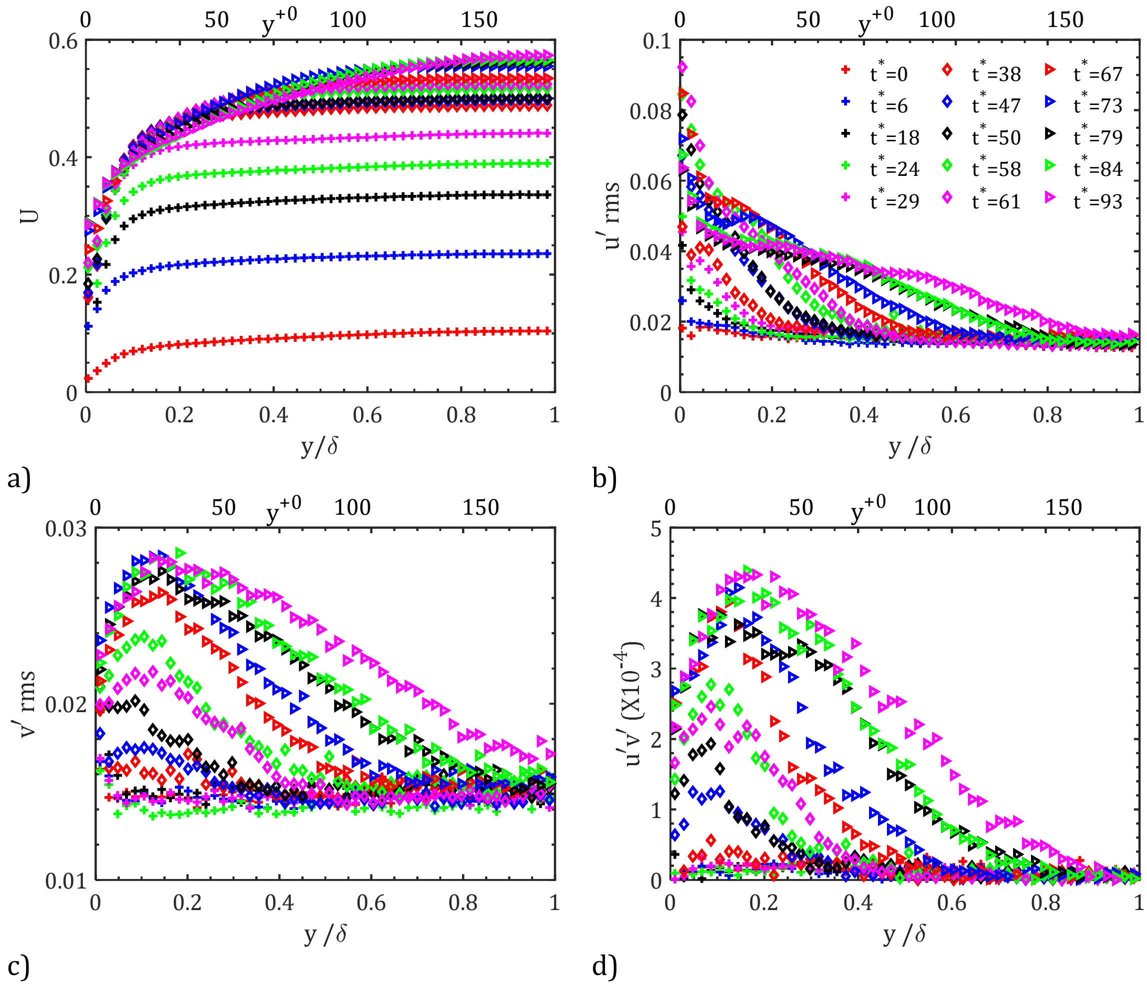

***Figure 5-15: Time development of streamwise mean velocity ($U$), streamwise fluctuating velocity ($u'_{rms}$), wall-normal fluctuating velocity ($v'_{rms}$), and Reynolds shear stress ($\overline{u'v'}$) for case D1 ($Re_b = 2799 - 15601$) with acceleration period of 1.87s. Legend is the same for the four subplots. The unit of subplots (a)-(c) is m/s and that of subplot (d) is m²/s².***

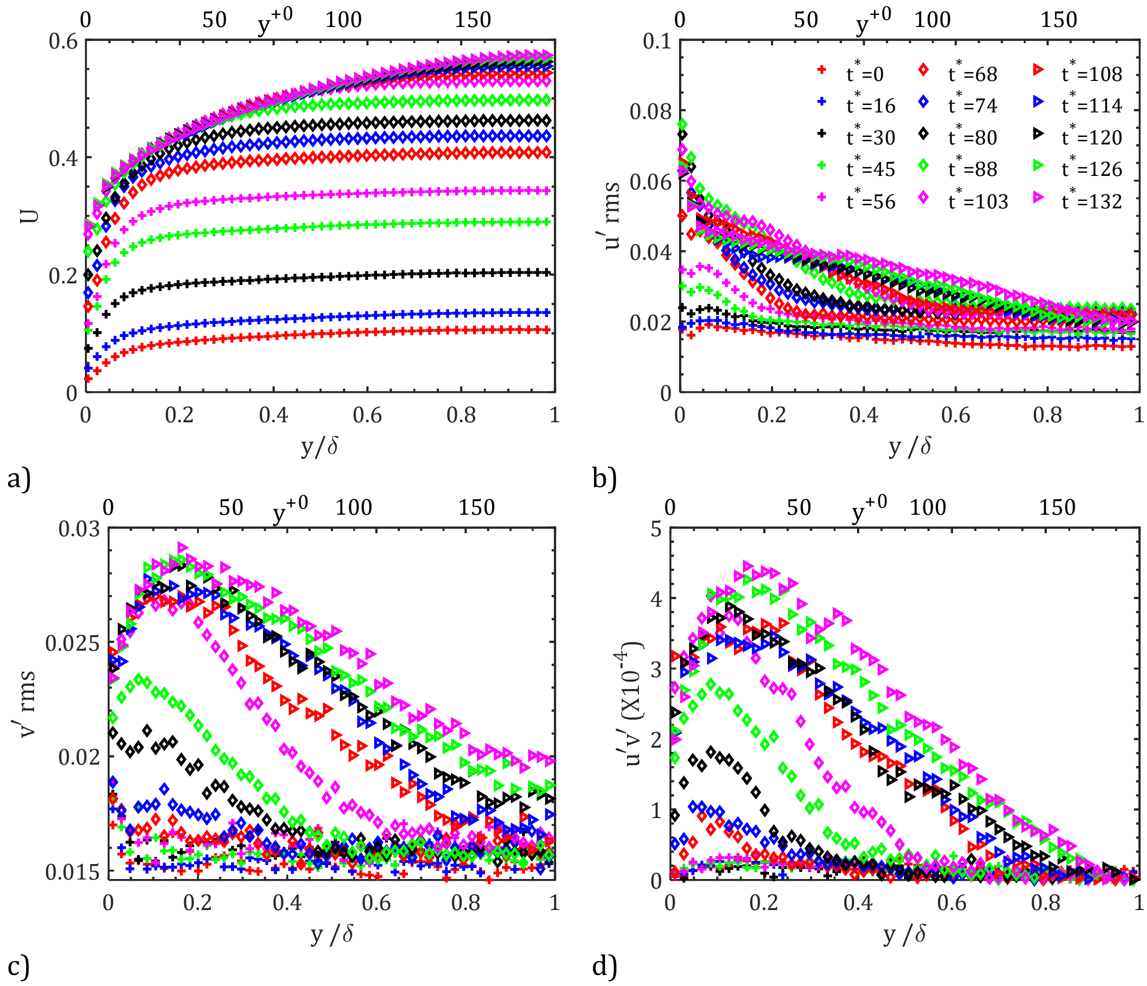

***Figure 5-16: Time development of streamwise mean velocity ($U$), streamwise fluctuating velocity ($u'_{rms}$), wall-normal fluctuating velocity ($v'_{rms}$), and Reynolds shear stress ($\overline{u'v'}$) for case D4 ($Re_b = 2813 - 15319$) with acceleration period of 4.26s. Legend is the same for the four subplots. The unit of subplots (a)-(c) is m/s and that of subplot (d) is m²/s².***

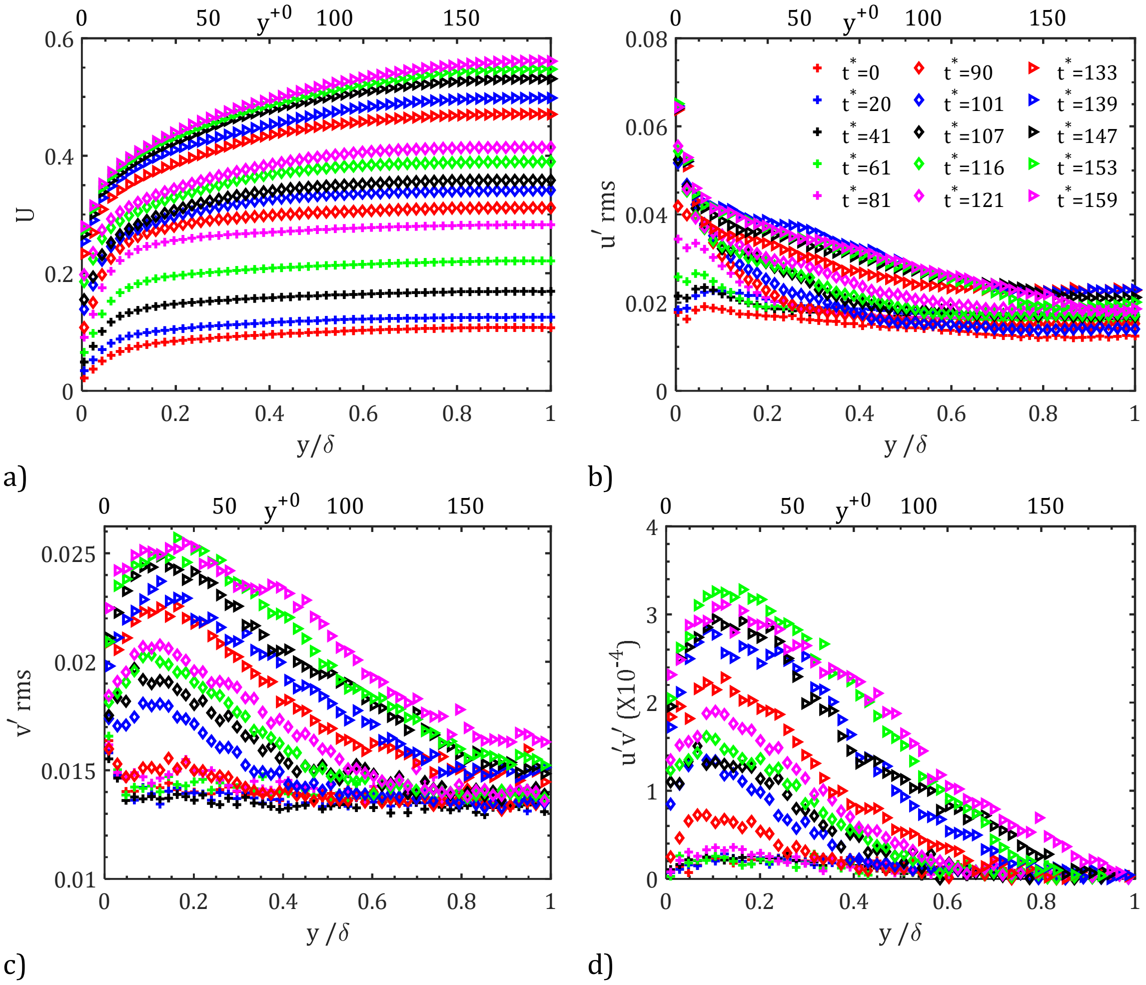

***Figure 5-17: Time development of streamwise mean velocity ($U$), streamwise fluctuating velocity ($u'_{rms}$), wall-normal fluctuating velocity ($v'_{rms}$), and Reynolds shear stress ($\overline{u'v'}$) for case D6 ($Re_b = 2865 - 15584$) with acceleration period of 6.94s. Legend is the same for the four subplots. The unit of subplots (a)-(c) is m/s and that of subplot (d) is m²/s².***

During the transitional time frame (approximately $38 < t^* < 61$, $68 < t^* < 103$ and $90 < t^* < 121$ for cases D1, D4 and D6, respectively), $u'_{rms}$ increases further to its peak near the wall. At the onset of transition (approximately $t^* = 38$, $t^* = 68$ and $t^* = 90$ for D1, D4 and D6, respectively), both the wall-normal fluctuating velocity ($v'_{rms}$) and Reynolds shear stress ($\overline{u'v'}$), which remain unchanged to the flow acceleration during the pre-transitional time frame, start responding monotonically and increase to their peak, as shown in Figures 5-15 (c,d), 5-16 (c,d) and 5-17 (c,d) for cases D1, D4 and D6, respectively. The time equivalent to when $v'_{rms}$ starts responding during the transitional time frame can be used to determine the onset of transition. The time of onset of transition is obtained using skin friction coefficient of ($C_f$) for cases D1, D4 and D6 are $t^* = 61$, $t^* = 102$ and $t^* = 121$ for D1, D4 and D6, respectively, as shown in Table 5-2. These times are equivalent to those obtained using $v'_{rms}$ (approximately $t^* = 61$, $t^* = 103$ and $t^* = 121$) for D1, D4 and D6, respectively.

Furthermore, at the end of transition (approximately $t^* > 68$ , $t^* > 103$ and $t^* > 121$) for D1, D4 and D6, respectively, streamwise mean velocity ($U$) profiles overlaps each other, and $u'_{rms}$ decreases slightly, overlapping each other near the wall. Though the turbulence in the centre of the flow is low at this time, it gradually increases with time from the wall to the core of the flow.

The flow parameters of E cases are similar to that of D cases but the final Reynolds numbers varied in addition to the variation of the acceleration periods, as previously elucidated in §5.4.2 and presented in Table 5.1. Figures 5-18 and 15-19 show the time development for E cases investigated. As with D cases, the streamwise mean velocity increases immediately after the commencement of the flow acceleration and overlaps when the flow has become turbulent, as shown in Figures 5-18a and 5-19a for E1 and E2 cases, respectively. During this pre-transitional time frame (approximately $\mathrm{t}^* < 29$ and $\mathrm{t}^* < 122$, for cases E1 and E2) $u'_{rms}$ increases progressively and continues to the onset of transition. The wall-normal fluctuating velocity ($v'_{rms}$) and Reynolds shear stress ($\overline{u'v'}$) during the pre-transitional stage do not change, as shown in Figures 5-18(c,d) and 5-19(c,d) for E1 and E2, respectively. During the transitional time frame (approximately $29 < t^* < 50$ and $122 < t^* < 137$ for cases E1 and E3), $u'_{rms}$ increases slightly near the wall then both $v'_{rms}$ and $u'v'$ start to increase at the onset of transition at approximately $t^* = 29$ and $t^* = 122$ for E1 and E2, respectively. In comparison to the onset of transition of $C_f$ previously presented in Table 5-2 ($t^* = 29$ and $t^* = 125$ for E1 and E3, respectively), the onset of transition of E1 is the same, and E3 very close. The same response can be seen in D cases: on the completion of the transition, streamwise mean velocity overlaps each other and the $u'_{rms}$ decreass slightly and approaching the statistically steady value of the flow.

The results of the slow acceleration of D and E cases reveal for the first time that the time of onset of transition increases as the acceleration period increases. The time of onset of transition increases from $t^* = 38 - 90$ as acceleration period increases from 1.87s to 6.94s for cases D1-D6. Moreover, it increases from $t^* = 29 - 122$ for cases E1-E3 as the acceleration period increases from 2.73s-4.73s, though the final Reynolds number has also been increased in this case.

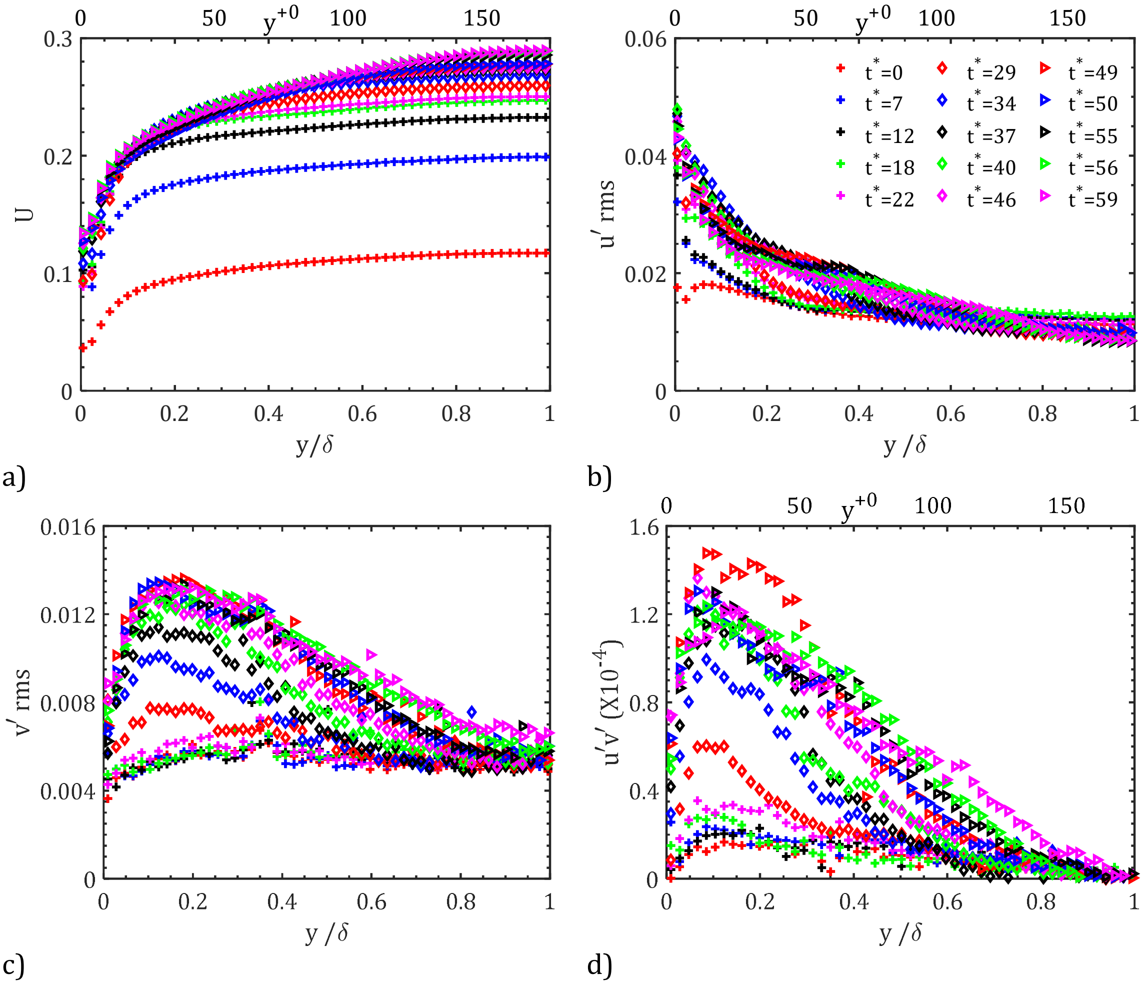

***Figure 5-18: Time development of streamwise mean velocity $(U)$, streamwise fluctuating velocity $(u'_{rms})$, wall-normal fluctuating velocity $(v'_{rms})$, and Reynolds shear stress $(\overline{u'v'})$ for case E1 $(Re_b = 2755 - 7440)$ with acceleration period of 1.87s. Legend is the same for the four subplots. The unit of subplots (a)-(c) is m/s and that of subplot (d) is m²/s².***

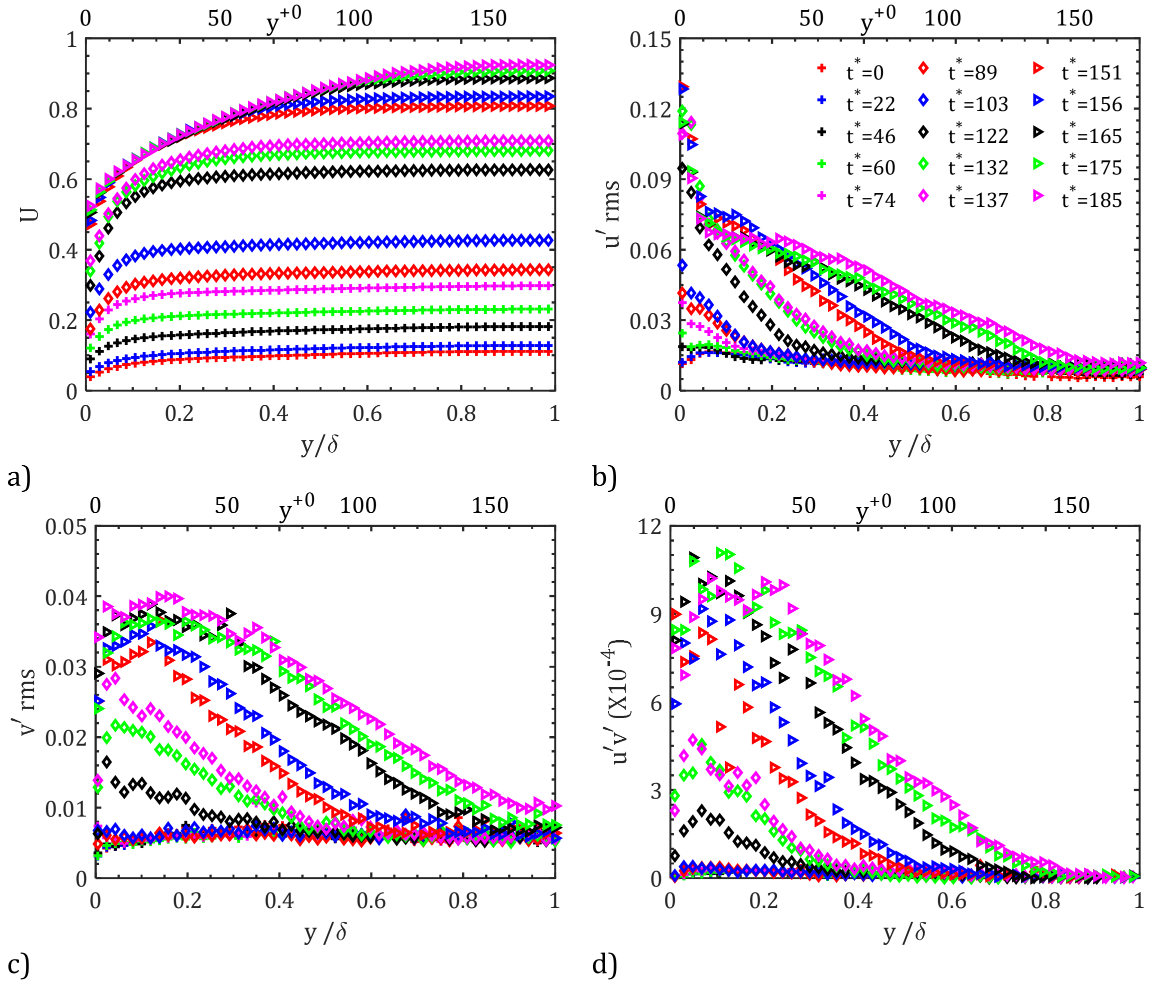

***Figure 5-19: Time development of streamwise mean velocity $(U)$, streamwise fluctuating velocity $(u'_{rms})$, wall-normal fluctuating velocity $(v'_{rms})$, and Reynolds shear stress $(\overline{u'v'})$ for case E3 ($Re_b = 2769 - 240100$) with acceleration period of 4.26s. Legend is the same for the four subplots. The unit of subplots (a)-(c) is m/s and that of subplot (d) is $m^2/s^2$.***

## 5.4.4 Temporal development of boundary layer

In this section, the temporal development of the boundary layer in the step increase of flow rate reported by He and Seddighi (2013; 2015) has been confirmed through the experiments presented, although here, the temporal development occurs at a slow rate as the acceleration period increases. It has been shown that a thin boundary layer of high shear is formed on the wall immediately following the commencement of transient flow and the thin boundary layer expands to the centre of the flow with time. This temporally developing boundary layer closely resembles that of the spatially developing boundary layer of external flow on a flat plate, in which the boundary layer grows as the distance from the leading-edge increases. In step increase of flow rate, the acceleration completes rapidly and the transition occurs in a short time whereas the transition is delayed in a slow accelerating flow presented in this section. The investigations of temporally developing boundary layer using perturbation velocity profiles at different times are carried out by He and Seddighi (2013; 2015). The authors introduced a perturbation velocity in order to describe the temporal development of boundary layer in a channel flow. Perturbation velocity equation was introduced in Chapter Four as Eq. (4.5) and the same equation is adopted in this slow accelerating flow as:

$$\bar{U}^{\wedge}\left({}^{y}/_{h}, t\right) = \frac{\bar{U}\left({}^{y}/_{h}, t\right) - \bar{U}\left({}^{y}/_{h}, 0\right)}{\bar{U}_c(t) - \bar{U}_c(0)} \tag{5.2}$$

where $\bar{U}\left({}^{y}/_{h}, t\right)$ is the ensemble-averaged streamwise mean velocity at a distance ${}^{y}/_{h}$ from the wall, at time $t$, and $\bar{U}_c(t)$ is the centreline velocity at time $t$. This equation is adopted to describe the temporal development boundary layer for the cases with different acceleration periods of this section. The development of the perturbation velocity can be represented by the growth of the laminar boundary layer in transient flow cases. Stokes' first problem is concerned mainly with a quick movement of a solid boundary at a constant velocity and simplifies the representation of the change in step increase of the flow (Schlichting, 2000). In the experiments described in this section, the development of the boundary layer occurs at a slow rate as the acceleration period increases. It has been reported from the DNS studies of a slow linearly accelerating flow of Seddighi et al. (2014) that temporally developing boundary layer can be viewed as a result of continuous changes of velocity gradient near the wall that then spreads to the flow. The temporal development of boundary layer of the slow accelerating flow can be represented in a better way by the extension of the Stokes' solution to perturbation velocity. If the temporally varying velocity is considered as a multi-step function with small steps, the whole solution comprises superposition of elementary solutions for all velocity steps. For the slow accelerating flow cases of this section, the time-varying velocity is represented as shown in Eq. (5.3). The same equation was utilised in Chapter Four to calculate velocity at wall distance, $y$ and time , $t$.

$$U(y,t) = \int_0^t \frac{dU_b}{dt} erfc\left(\frac{y}{2\sqrt{v(t-\tau)}}\right) d\tau \tag{5.3}$$

where $v$ is the kinematic viscosity, $y$ is the wall distance, $t$ is the actual time, $\tau$ is the small time step, $erfc$ is the complementary error function, and $U_b(t)$ is the temporally varying velocity function with small steps $dU_b$ in a range of small time step $d\tau$. For the determination of the temporal development of the laminar boundary layer in these present slow accelerating flow cases, Eq. (5.3) is used to provide the small finite steps of the flow. The cases investigated are divided into two groups, as previously discussed. For brevity, three cases each are presented from the D and E cases. Figures 5-20a, 5-20b and 5-20c show the profiles of the temporally developing perturbation velocity in comparison with corresponding extended laminar solutions for cases D1, D4 and D6, respectively. The profiles of the temporally developing perturbation velocity of the three E cases are compared with the extended Stokes laminar solution, as shown in Figures 5-21a, 5-21b & 5-21c. It is revealed from the figures of the two groups that the data of the various cases collapses with the result of the corresponding extended Stokes laminar solution in the pre-transitional stage of each case reported. From the onset of transition, the data is observed to deviate from the profile of the extended Stokes laminar solution. As shown in Figure 5-20a, for case D1,the data starts to deviate at roughly $t = 1.90$ ($t^{+0} = 79$). It deviated at roughly $t = 3.30$ ($t^{+0} = 143$) for case D4. The times at which cases D1 and D4 start to diverge from the profile of the laminar solution are almost the same as the onset of transition previously reported using the skin friction coefficient ($C_f$) as $t = 1.91$ ($t^{+0} = 79$) for case D1 and $t = 3.35$ ($t^{+0} = 146$) for case D2. It is observed that the time at which the data of case D6 starts to deviate from the extended Stokes laminar solution occurs earlier than that reported using $C_f$. The data is seen to diverge from the profile of the laminar solution roughly at $t = 4.15$ ($t^{+0} = 181$) and the time of the onset of transition obtained using $C_f$, $t = 4.45$ ($t^{+0} = 198$), as shown in Table 5-2. The close agreement of the temporally developing perturbation velocity profiles of the D cases reported in the pre-transitional stage and the extended Stokes laminar solution reveals that the transient turbulent flow during the pre-transitional stage closely resembles the laminar boundary layer flow.

For the three E cases presented, the profiles of the temporally developing perturbation velocity collapse with that of the laminar solution in the pre-transitional stage of the slow acceleration. As shown in Figure 5-21a, 5-21b and 5-21c, the profiles of the temporally developing perturbation velocity for the three cases start to deviate from the laminar solution before the onset transition that was previously reported in Table 5-2 using $C_f$. The divergence of the present data and the laminar solution is observed at roughly $t = 2.71$ ($t^{+0} = 116$) for case E1, at $t = 2.71$ ($t^{+0} = 116$) for case E2, and at $t = 3.57$ ($t^{+0} = 157$) for case E3. In addition, there is close agreement between the profiles of the temporally developing perturbation velocity of the three E cases reported with the extended Stokes laminar solution in the pre-transitional stage before the divergence. The close agreement again reveals that the transient turbulent flow resembles the laminar boundary layer flow in the pre-transitional stage of the flow. The divergence from the extended Stokes laminar solution is observed to delay as the acceleration period increases for the D and E cases presented. The results obtained from the present cases are similar with the previous experimental and numerical investigations on transient turbulent flow of He and Seddighi (2015), Gorji (2015) and Mathur et al. (2018).

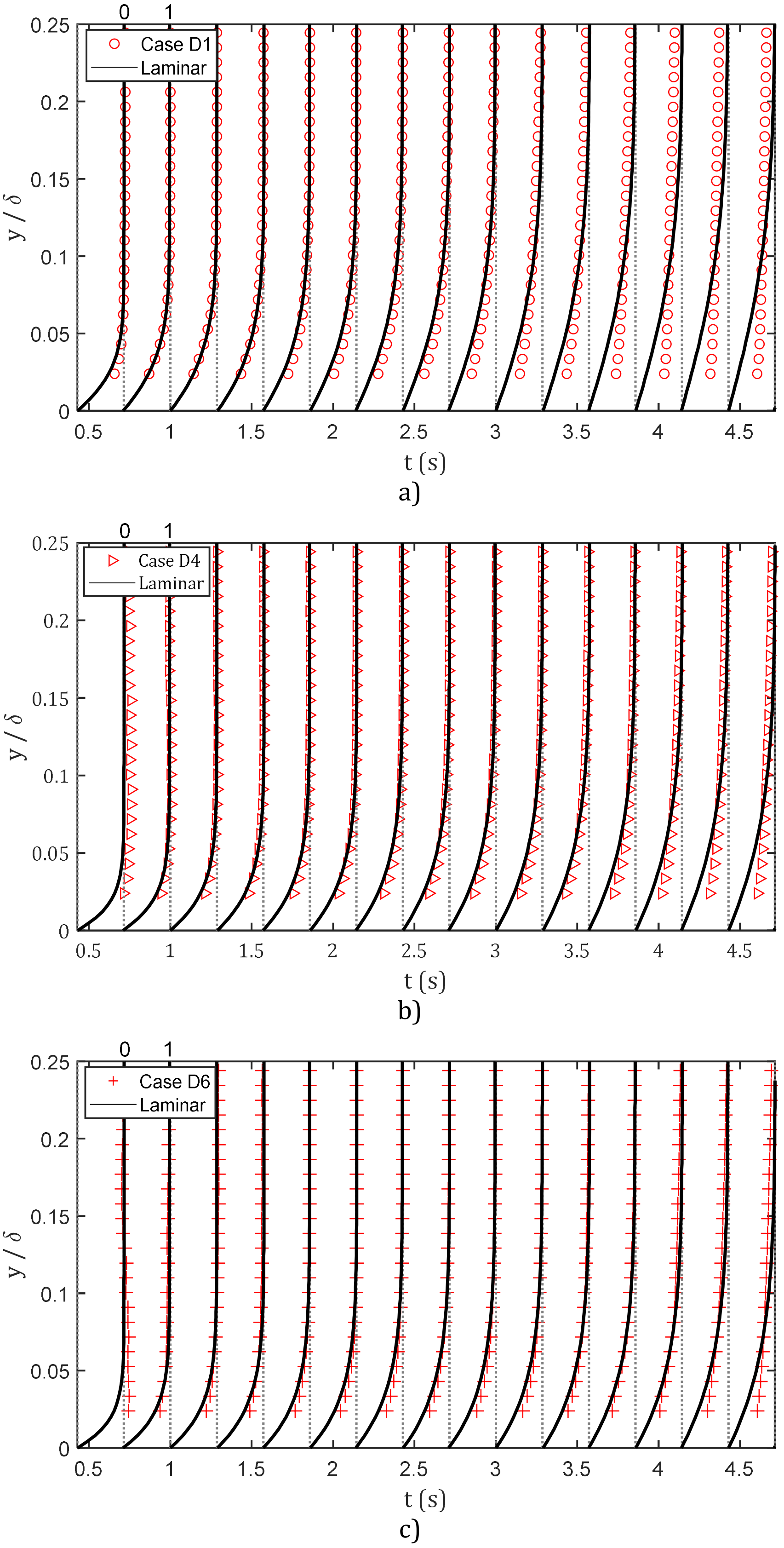

***Figure 5-20: The development of the perturbation velocity profiles in comparison with the extended Stokes laminar solution for cases D1 (a), D4 (b) and D6 (c).***

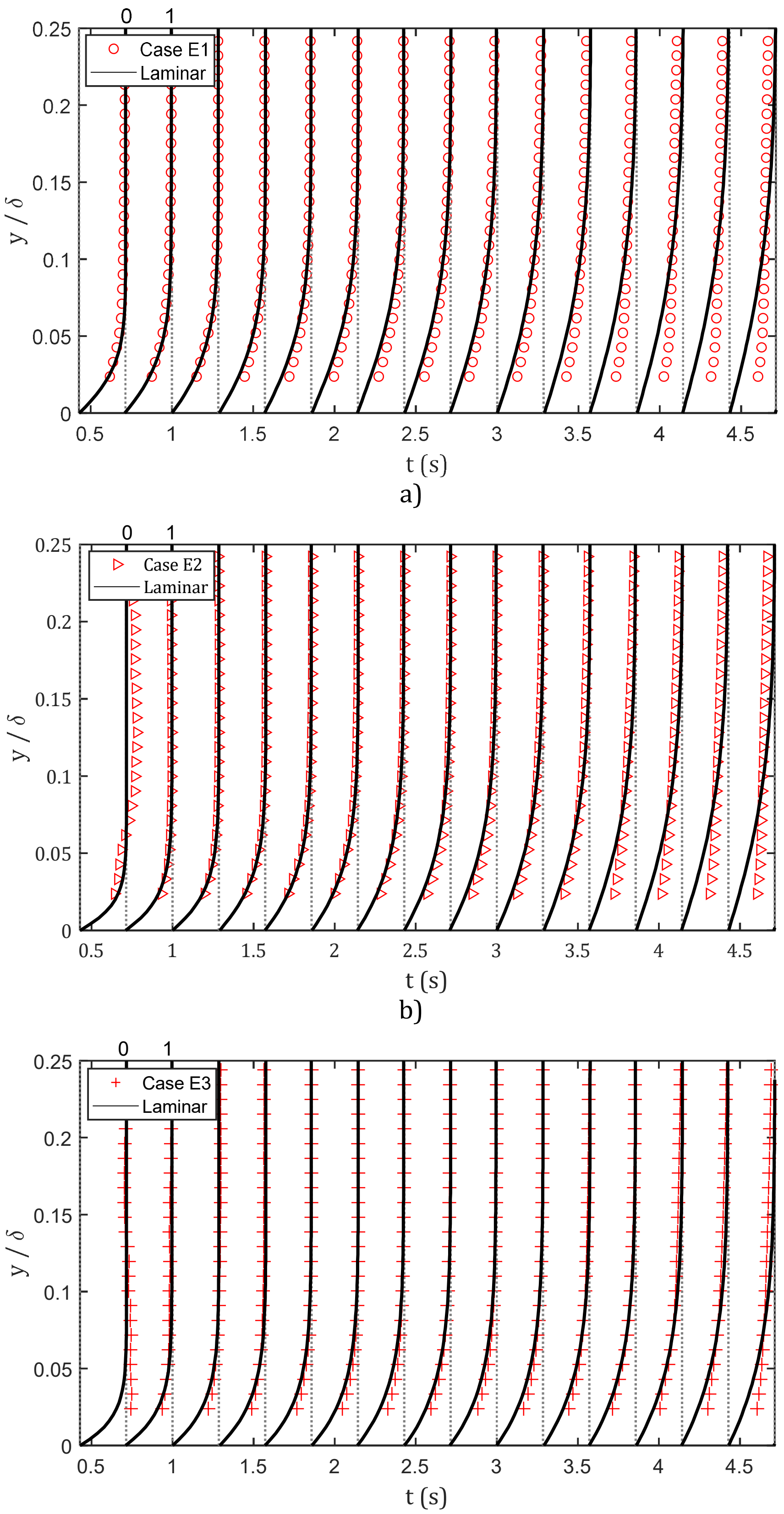

a)

b)

c)

***Figure 5-21: The development of the perturbation velocity profiles in comparison with the extended Stokes laminar solution for cases E1 (a), E2 (b) and E3 (c).***

For a better description of the temporally developing boundary layer of transient turbulent flow, He and Seddighi (2015) proposed an equation of a skin friction coefficient based on perturbation flow as the following equation (as used in § 4.4):

$$C_{f,du} = \frac{2 * \tau_{w,du}}{\rho(U_{b1} - U_{b0})^2} \tag{5.4}$$

where $\tau_{w,du} = \mu[\partial\{\bar{u}\left({}^{y}/_{h}, t\right) - \bar{u}({}^{y}/_{h}, 0)\}/\partial y]_{y=0} = \tau_w - \tau_{w,0}$ is the wall shear stress of perturbation flow, $\tau_w$ is the wall shear stress of the flow at time, $t$, $\tau_{w,0}$ is the wall shear stress of the flow at time, and $t = 0$. As the time-varying velocity profiles and extended Stokes' solution overlap each other during pre-transitional period, the modified skin friction coefficient as below also overlap each other.

$$C'_{f,du} = C_{f,du}\frac{(U_{b1} - U_{b0})}{u_{\tau 0}} = \frac{2 * \tau_{w,du}}{\rho(U_{b1} - U_{b0})u_{\tau 0}} \tag{5.5}$$

In the accelerating flow cases of He and Seddighi (2015), the modified $C_f$ is slightly elevated and is corrected. Also, in step-like accelerating flow, the initial bulk velocity ($U_{b0}$) increases and reaches the final bulk velocity ($U_{b1}$) immediately after the commencement of the transient flow. The response of the flow in these current slow accelerating cases is different as the evolution of the initial flow changes continuously to the final stage of the flow at a slow rate. In Eq. (5.5), the final bulk velocity ($U_{b1}$) is replaced with the temporally varying velocity $U_b(t)$ in current slow accelerating flow cases. However, Eq. (5.5) presents the modified skin friction coefficient as follows:

$$C''_{f,du} = \frac{2 * \tau_{w,du}}{\rho\{U_b(t) - U_{b0}\}u_{\tau 0}} \tag{5.6}$$

The laminar wall shear stress based on temporally varying perturbation is obtained following the differentiation of Eq. (5.3) of the extended Stokes' solution and is given as:

$$\tau_{w,lam} = \rho \int_0^t \frac{dU_b}{d\tau} \sqrt{\frac{v}{\pi(t-\tau)}}\, d\tau \tag{5.7}$$

As will be seen below, the data of the present cases is seen to follow the trend of the extended Stokes laminar solution $C''_{f,du}$ Eq.(5.6) except for case E3 during the pre-transitional period. The following equation provides an improvement to Eq. (5.6):

$$C''_{f,du\,(corrected)} = C''_{f,du}\,(t^{+0})^{0.03} \tag{5.8}$$

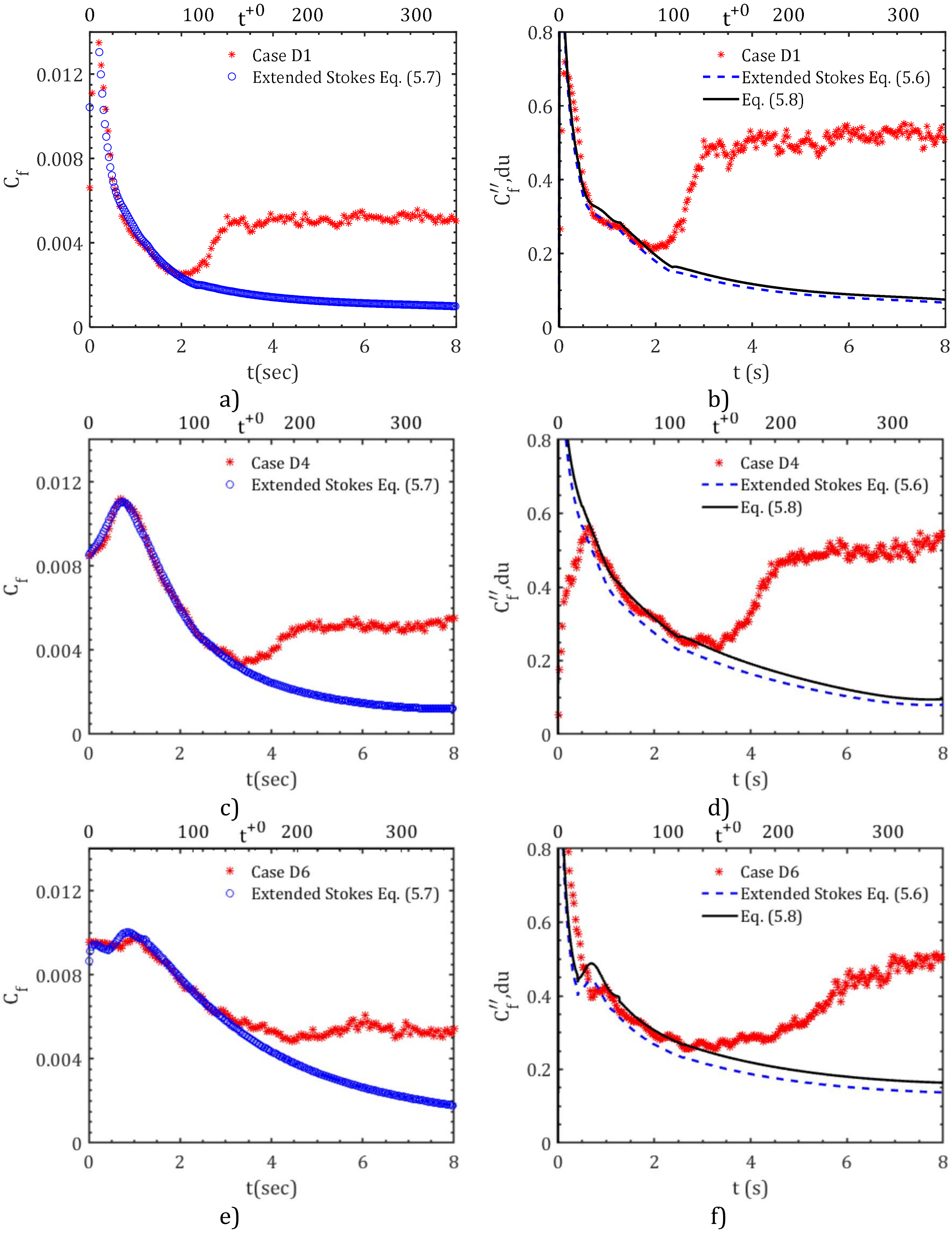

***Figure 5-22: Development of the skin friction coefficient $C_f$ Eq. (5.1) for cases D1 (a), D4 (c) and D6 (e) and the development of the modified skin friction coefficient $C''_{f,du}$ Eq.(5.6) for cases D1 (b), D4 (d) and D6 (f).***

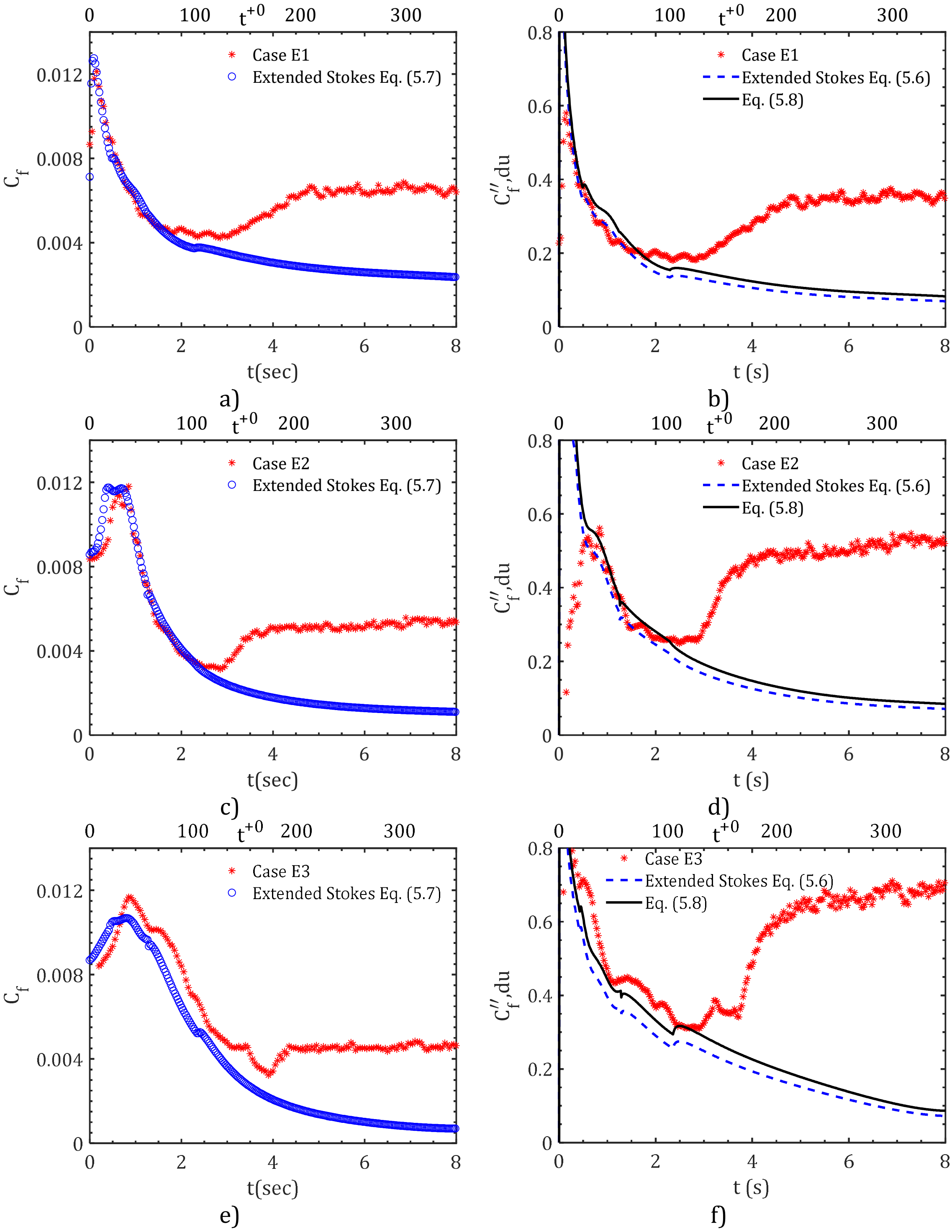

***Figure 5-23: Development of the skin friction coefficient $C_f$ Eq. (5.1) for cases E1 (a), E2 (c) and E3 (e) and the development of the modified skin friction coefficient $C''_{f,du}$ Eq.(5.6) for cases E1 (b), E2 (d) and E3 (f)***

Figure 5-22 (a, c & e) presents the comparison between the measured $C_f$ using equation Eq. (5.1) for D1, D4 and D6 with the extended Stokes laminar solution obtained from Eq. (5.7). The comparison for cases E1-E3 is shown in Figure 5-23 (a, c & e). The development of the modified skin friction coefficient $C''_{f,du}$ Eq.(5.6) for cases D1, D4 and D6 in comparison with the extended Stokes laminar solution and the slight correction from Eq. (5.8) is shown in Figure 5-22 (b, d & f) while that of cases E1-E3 is shown in Figure 5-23 (b, d & f). During the pre-transitional period, it can be seen from Figure 5-22 (a, c & e) and Figure 5-23 (a, c & e) that the data in terms of $C_f$ for cases D1, D4, D6, E1 and E2 collapses with the extended Stokes laminar solution but that of case E3 slightly deviates. The cause of the slight deviation is likely to be the higher acceleration period and final Reynolds number of the case. Moreover, it can be seen from Figure 5-22 (b, d & f) that the data of D1, D4 and D6 in terms of modified skin friction coefficient follows that of the extended Stokes laminar solution while the correction from Eq. (4.13) provides an improvement to slight deviation. As shown from Figure 5-23 (b, d & f) that the data of cases E1 & E2 follows the extended Stokes laminar solution during the pre-transitional period but the data of case E3 slightly overshoots the laminar solution and the Eq. (4.13) provides correction to the deviation. This is likely due to the fact that both acceleration period and final Reynolds number are higher. The above results show that as with the step increase of flow rate and that of the cases reported in Chapter Four of this thesis, the temporally developing boundary layer of the present slow accelerating flow cases during the pre-transitional time frame is represented by an extended solution to Stokes' first problem. Equations (5.6), (5.7) and (5.8) can be used to determine the early response of skin friction coefficient in transient flow.

For the determination of the displacement thickness $(\delta_{du})$, the shape factor $(H)$ and momentum thickness $(\theta_{du})$ in the present slow accelerating flow cases, the re-defined equations of He and Seddighi (2013) utilised in § 4.4.4 are adopted as follows:

$$\theta_{du}(t) = \int_0^1 \bar{U}^{\wedge}({}^{y}/_{\delta}, t)(1 - \bar{U}^{\wedge}({}^{y}/_{\delta}, t))d({}^{y}/_{\delta}) \tag{5.9}$$

$$\delta_{du}(t) = \int_0^1 (1 - \bar{U}^{\wedge}({}^{y}/_{\delta}, t))d({}^{y}/_{\delta}) \tag{5.10}$$

$$H(t) = \frac{\delta_{du}(t)}{\theta_{du}(t)} \tag{5.11}$$

The momentum-thickness Reynolds number ($Re_\theta$) is determined using $Re_\theta = \theta\bar{U}_c/v$ where $\bar{U}_c$ is the centreline velocity and $v$ is the kinematic viscosity. In order to compare the spatially developing boundary layer with the temporally developing boundary layer, a relationship has to be established. The Reynolds number of boundary layer flow on flat plate can obtained as $Re_x = {}^{xU_\infty}/_{v}$, where $x$ is the distance of the leading edge of the plate and $U_\infty$ is the free-stream velocity. Moreover, He and Seddighi (2013) re-defined the distance from the leading edge as $x = t * U_{conv}$ , where $U_{conv}$ is convective velocity. The $U_{conv}$ was determined by the authors to be equal to $0.74U_{b1}$ from the best curve-fitting of the transient turbulent flow with the Blasius solution in the early stage of the transient.

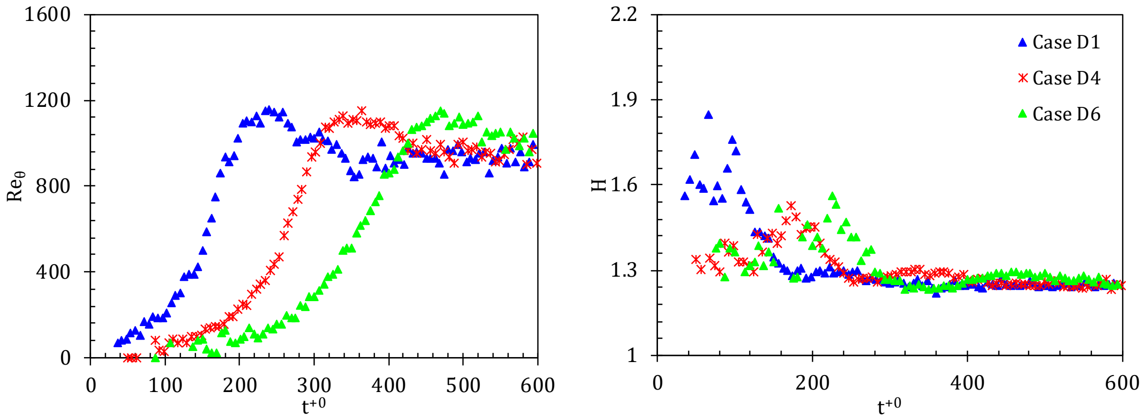

a) b)

*Figure 5-24: Development of momentum-thickness Reynolds number ($Re_\theta$) and shape factor (H) for cases D1, D4 and D6: a) momentum-thickness Reynolds number ($Re_\theta$), b) shape factor (H).*

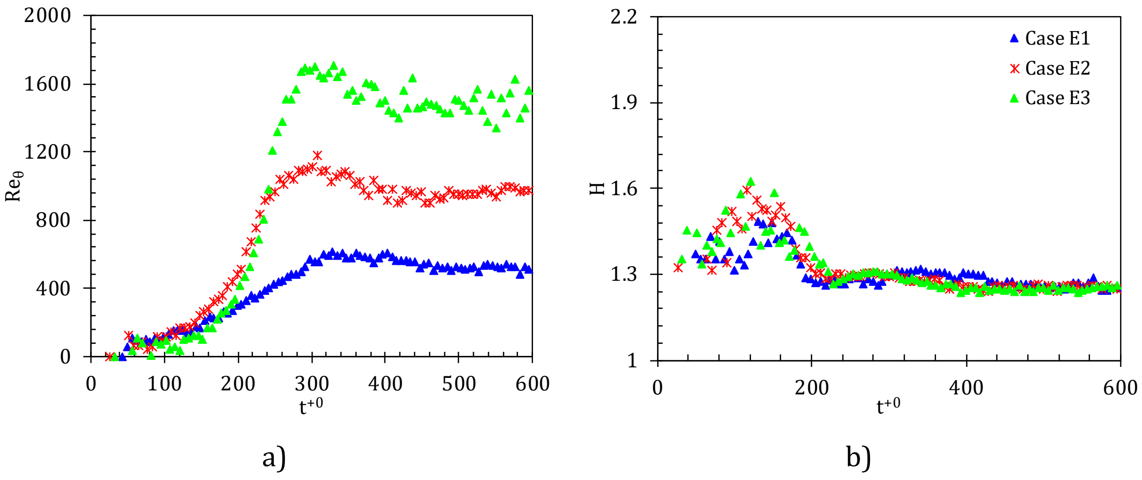

***Figure 5-25: Development of momentum-thickness Reynolds number ($Re_\theta$) and shape factor (H) for casesE1-E3: a) momentum-thickness Reynolds number ($Re_\theta$), b) shape factor (H).***

The development of the momentum-thickness Reynolds number and the shape factor for cases D1, D4 and D6 is shown in the Figures 5-24 (a & b). Figure 5-25 (a & b) presents the development of momentum-thickness Reynolds number and the shape factor for cases E1-E3. It can been that the $Re_\theta$ of case D1 develops more rapidly than that of the other two cases. This is likely due to the high acceleration rate in case D1. The development of $Re_\theta$ delays as the acceleration period increases. The trends of $Re_\theta$ for the three E cases are seen to collapse during the initial increase due to the same initial Reynolds number and increase to different final momentum-thickness Reynolds number. For cases D1, D4 and D6, the onset of transition and momentum-thickness Reynolds number occur at $t^{+0}$~78 and $Re_\theta$~159 for case D1, $t^{+0}$~148 and $Re_\theta$~107 for case D4 and $t^{+0}$~200 and $Re_\theta$~90 for case D6. In other words, the critical momentum-thickness Reynolds number decreases as the acceleration period increases. The onset of transition and momentum-thickness Reynolds number occur at $t^{+0}$~118 and $Re_\theta$~151, $t^{+0}$~128 and $Re_\theta$~163 and $t^{+0}$~165 and $Re_\theta$~169 for cases E1, E2 and E3, respectively. It is shown from the results that the critical momentum-thickness Reynolds number increases for E cases as both acceleration period and the final Reynolds number increase. He and Seddighi (2013) reported onset of transition at $t^{+0}$~90 and $Re_\theta$~250 and the difference in the values is due to the flow acceleration; the flow acceleration of the present cases increase slowly while that of He and Seddighi (2013) increases rapidly. Overall, the development of the momentum-thickness Reynolds number is similar to that of momentum-thickness Reynolds number of He and Seddighi (2013) and Mathur (2016).

He and Seddighi (2013) obtained the value of shape factor ($H$) as 2.4 in the initial stage of transient flow at $t^{+0}\sim 10$, which indicated a laminarising effect of the accelerating flow. For all the case presented, the values of shape factor corresponding to the points of transition are also reported. The values of shape factor for case D1, D4 and D6 are 1.59 (at $t^{+0}\sim 78$), 1.43 (at $t^{+0}\sim 148$) and 1.39 (at $t^{+0}\sim 200$), respectively. It is revealed that the value of $H$ decreases as the acceleration period increases while the acceleration rate decreases. For the three E cases, the values of shape factor are 1.37 (at $t^{+0}\sim 118$), 1.56 (at $t^{+0}\sim 128$) and 1.42 (at $t^{+0}\sim 165$), respectively. In these present slow accelerating flow cases, the transition is delayed in comparison with the step increase of flow rate of He and Seddighi (2013) and the cases reported in Chapter Four. As can be seen, the values of shape factor ($H$) in statistically steady turbulent flow for both D and E cases are less than 1.4 in comparison with that of step increase of flow rate of He and Seddighi (2013) due to the experimental errors during the experiments.

### 5.4.5 Correlations of transition to turbulence in transient channel flow

As with spatially developing boundary layer, the critical Reynolds number of the transition of the transient flow is correlated with the $FST$. Indeed, He and Seddighi (2015) have revealed that the onset of transition to turbulence in step increase of flow rate can be correlated with the initial turbulence intensity ($Tu_0$). The authors proposed Eq. (4.20) which is presented in Chapter Four, and it was modified to Eq. (4.22) due to slow acceleration in the experimental cases in comparison with the step increase of flow rate of He and Seddighi (2015). In this chapter, Eq. (5.12) is presented and used to determine the initial turbulence intensity ($Tu_0$) for all the slow acceleration cases investigated.

$$Tu_0 = \frac{(u'_{rms,0})max}{U_b(t_{cr})} = \left(\frac{U_{b0}}{U_b(t_{cr})}\right)\frac{(u'_{rms,0})max}{U_{b0}} \tag{5.12}$$

It has been revealed by He and Seddighi (2015) that the importance of the equivalent Reynolds number ($Re_t$) in the transition to turbulence of unsteady flow is the same as that of $Re_x$ in spatially developing boundary layer flow. Due to the delay in the flow acceleration of the present cases from the initial flow condition to the final flow condition in comparison with the step increase of flow rate, the equivalent length-scale (x) is modified. Moreover, the bulk velocity ($U_b(t_{cr})$) at the onset of transition to turbulence is used as the characteristic convective velocity instead the of the final bulk velocity ($U_{b1}$). The initial turbulence intensity ($Tu_0$) is described as the ratio of the maximum value of the streamwise fluctuating velocity at the commencement of the transient flow to the bulk velocity that is equivalent to the onset of transition, as presented in Eq.(5.12).

In Chapter Four, the critical equivalent Reynolds number and the transitional period Reynolds number are calculated as $Re_{t,cr} = U_b(t_{cr})/v \int_0^{t_{cr}} U_b(t)dt$ and $\Delta Re_{t,cr} = U_b(t_{turb})/v \int_{t_{cr}}^{t_{turb}} U_b(t)dt$, respectively. The same equations are utilised in this section that comprise much slow accelerating flow cases to determine both the critical equivalent Reynolds number and the transitional period Reynolds number. As with that of Chapter Four, the critical time of onset of transition ($t_{cr}$) and the time of end of transition ($t_{turb}$) are obtained using the skin friction coefficient ($C_f$).

Figure 5-26 shows the relationship between the critical equivalent Reynolds number ($Re_{t,cr}$) and the initial turbulence intensity ($Tu_0$) for all the cases investigated. The relation between $Re_{t,cr}$ and $Tu_0$ for cases investigated in both Chapter Four and this chapter are presented in Figure 5-28. As shown in Figure 5-26, the data of the experimental cases (D & E) follow the general trends of the data of He and Seddighi (2015) and Mathur (2016) although there are some detailed differences. The flow rate of the present cases increases slowly while that of He and Seddighi (2015) exhibits a step change behaviour. In the present cases, the initial Reynolds number, final Reynolds number and acceleration period are different from that of Mathur

(2016). For these slow accelerating flow cases presented, a power curve fit of $Re_{t,cr} = 1700Tu_0^{-1.64}$ is obtained from the data of D and E cases. He and Seddighi (2015), Mathur (2016) and Mathur et al. (2018) obtained relations as $Re_{t,cr} = 1340Tu_0^{-1.71}$ , $Re_{t,cr} = 1910Tu_0^{-1.62}$ and $Re_{t,cr} = 2575Tu_0^{-1.52}$, respectively. The variation in term of constants with that of Mathur (2016) and Mathur et al. (2018) is due to the difference in the initial flow condition, final flow condition and acceleration period. Moreover, the variation in the constants of the present experimental data with that of He and Seddighi (2015) is due to the different flow acceleration. The increment of flow rate for the D and E cases is slow in comparison with that of He and Seddighi (2015), in which the flow accelerates rapidly.

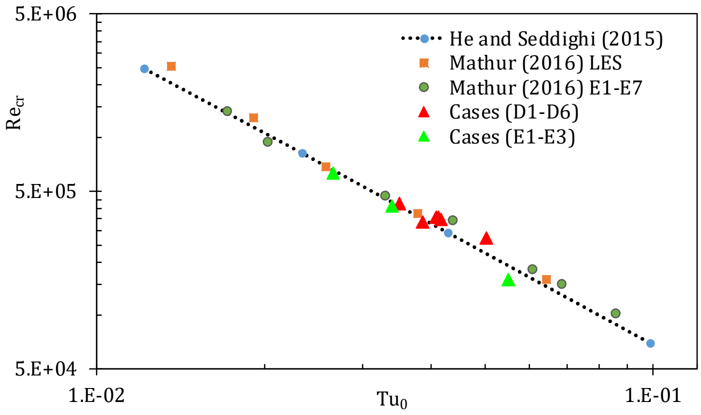

***Figure 5-26: Critical equivalent Reynolds number ($Re_{t,cr}$) as a function of initial turbulence intensity ($Tu_0$) for D cases and E cases in comparison with the data of He and Seddighi (2015) and Mathur (2016). Initial turbulence intensity ($Tu_0$) obtained using $U_{tcr}$ as a characteristic convective velocity.***

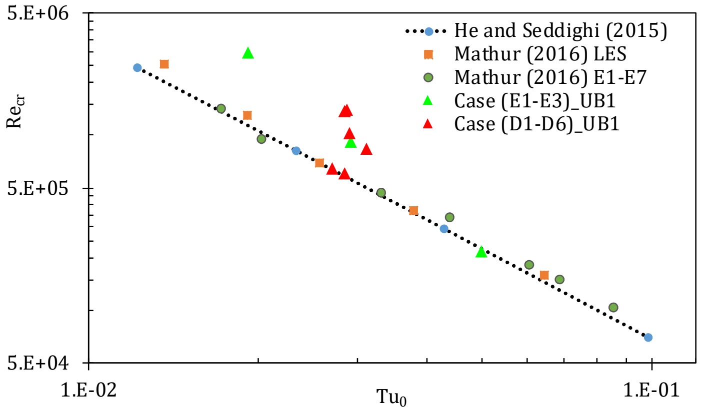

***Figure 5-27: Critical equivalent Reynolds number ($Re_{t,cr}$) as a function of initial turbulence intensity ($Tu_0$) for D cases and E cases in comparison with the data of He and Seddighi (2015) and Mathur (2016). Initial turbulence intensity ($Tu_0$) obtained using $U_{b1}$ as a characteristic convective velocity.***

Figure 5-27 shows the critical equivalent Reynolds number, $Re_{t,cr}$ plotted against the initial turbulence intensity, $Tu_0$ for cases D and E where the final bulk velocity, $U_{b1}$ is used as a characteristic convective velocity instead of the bulk velocity at the onset of transition $U_b(t_{cr})$ . As shown from the figure, three cases follow the trends of He and Seddighi (2015) and Mathur (2016) closely while other cases are seen to significantly overshoot the trends. This confirms that using bulk velocity at the onset of transition $U_b(t_{cr})$ as a characteristic convective velocity instead of the bulk velocity of the final stage of the flow is appropriate when slow accelerating flow cases are also included.

Figure 5-28 presents $Re_{t,cr}$ plotted against $Tu_0$ for the cases in Chapter Four and that of this chapter. As shown from the figure, the data follows the trends of He and Seddighi (2015) and Mathur (2016) but the constants of the power law are different. The results of the present experimental cases show the dependence of critical equivalent Reynolds number on the initial turbulence intensity. The data of the cases in Figure 5-28 can be represented as $Re_{t,cr} = 1409Tu_0^{-1.70}$and also similar to that of He and Seddighi (2015) and Mathur (2016) but their constants are not the same due to different rates of increasing flow.

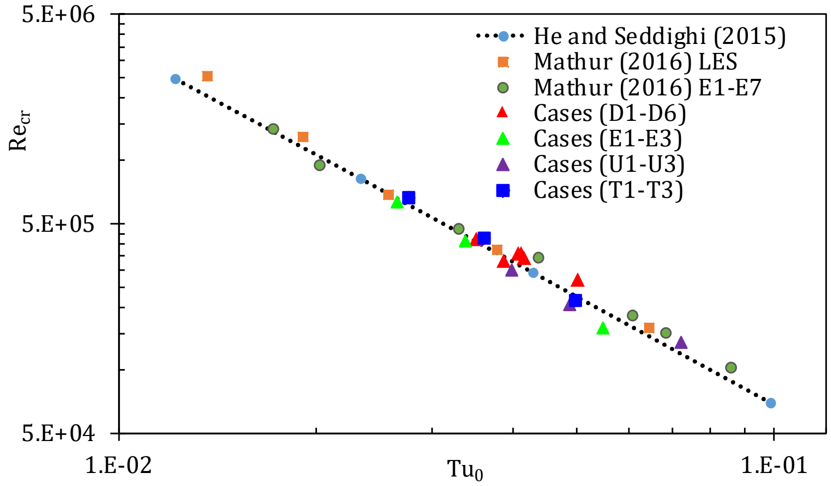

***Figure 5-28: Critical equivalent Reynolds number ($Re_{t,cr}$) as function of initial turbulence intensity ($Tu_0$) for D, E T and U cases in comparison with the data of He and Seddighi (2015) and Mathur (2016).***

All the data for the cases investigated in Chapter Four and in this section are seen again to follow the general trends of He and Seddighi (2015) and Mathur (2016). In these present slow accelerating flow cases, the modified equations of $Re_{t,cr} = U_b(t_{cr})/v \int_0^{t_{cr}} U_b(t)dt$ and that of Eq. (5.12) are used to obtain an estimation of onset of transition to turbulence.

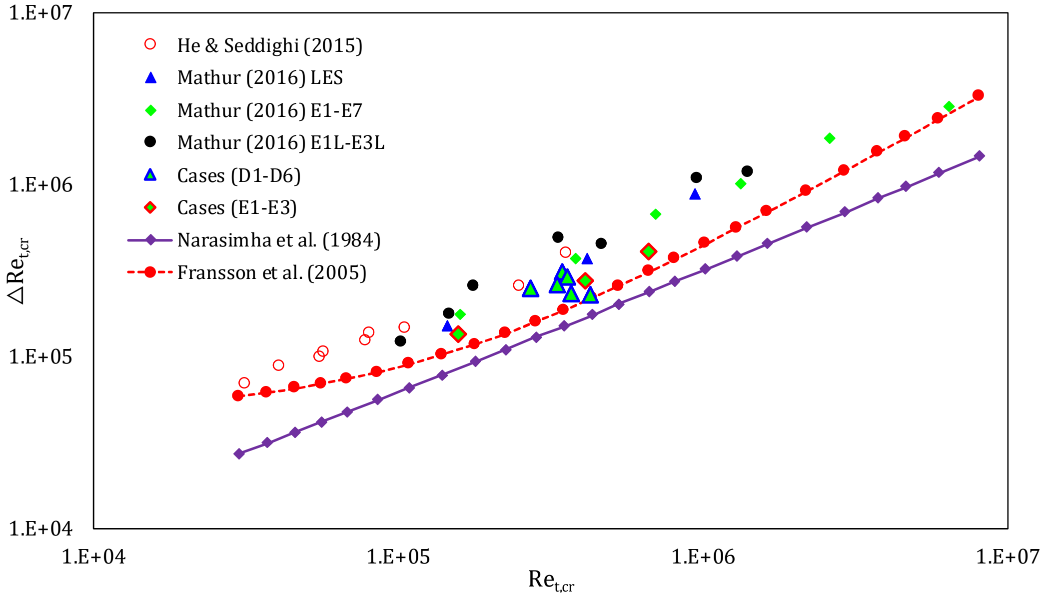

***Figure 5-29: Transitional period Reynolds number ($\Delta Re_{t,cr}$) as a function of the critical Reynolds number ($Re_{t,cr}$) of the present .slow accelerating flow cases (D & E).***

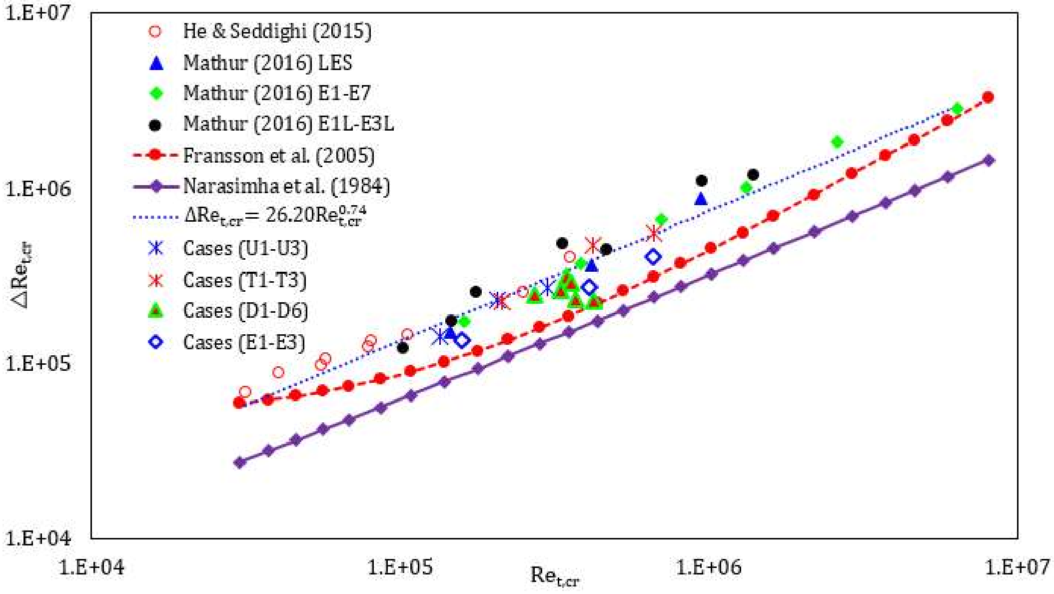

***Figure 5-30: Transitional period Reynolds number ($\Delta Re_{t,cr}$) as a function of the critical Reynolds number ($Re_{t,cr}$) for all cases (D, E, T & U) investigated in comparison with the data of He and Seddighi (2015) and Mathur (2016).***

The relationship between transitional period Reynolds number and the critical Reynolds number for D and E cases in comparison with the data of He and Seddighi (2015) and Mathur (2016) is shown in Figure 5-29. The data of the spatially developing boundary layer flow which is predicted from the unsteady flow data is also plotted in the figure when $Re_{x,\gamma=0.5}$ in Narasimha et al. (1984) and is replaced by $Re_{x,cr} + 0.5\Delta Re_{x,cr}$. It is revealed, as with the investigation of He and Seddighi (2015), that the current data is well predicted by the spatially developing boundary layer correlation if the present $\Delta Re_{t,cr}$ uses a factor of 0.5. The data of the current experimental cases follow the general trends of He and Seddighi (2015) and Mathur (2016). Moreover, a best power law relation of $\Delta Re_{t,cr} = 44.27 Re_{t,cr}^{0.68}$ is obtained from the data of cases D and E presented in Figure 5-29. It is interesting to note that the relation is similar to that of Narasimha et al. (1984) though the constants are different. Figure 5-30 presents data of all cases (D, E, T and U) investigated in comparison with the data of He and Seddighi (2015) and Mathur (2016) and a power law relation of $\Delta Re_{t,cr} = 26.20 Re_{t,cr}^{0.74}$ has been obtained which is again similar to that of flat plate boundary layer flow of Narasimha et al. (1984) with variations in constants because the present cases are temporally developing boundary layer flows.

## 5.5 Summary

The effects of varying acceleration periods on the flow response have been investigated using Particle Image Velocimetry (PIV) and Constant Temperature Anemometry (CTA) with hot-film sensors. Two groups are investigated; the first group (D) involved the variation of acceleration periods while both initial and final Reynolds numbers are fixed. In the second group (E), the initial Reynolds number is fixed while both acceleration periods and the final Reynolds numbers varied. It has been revealed that the fundamental nature of transition to turbulence of the slow accelerating flow cases investigated is the same as that of turbulent to turbulent flow cases presented in Chapter Four of this thesis and the step increase of flow rate, but at a much slow rate.

For all the D cases and E cases investigated, the time equivalent to the minimum skin friction coefficient ($C_f$) that determines the onset of transition increases as the acceleration period increases. The $C_f$ three-stage development corresponding to the three-stage development of the flow, that is, pre-transition, transition and fully turbulence. In the first stage, the pre-streaky structures in the flow are stretched and elongated which results in an increment of fluctuating velocity ($u'_{rms}$) in the streamwise direction of the flow while both wall normal fluctuating velocity ($v'_{rms}$) and the Reynolds shear stress ($\overline{u'v'}$) do not change. During the transitional stage, the formation of turbulence spots is first seen at the onset of transition to turbulence that marks the start of the transitional stage. The generated turbulence spots are seen to spread and merge together during this stage. Also, during this stage, both the $v'_{rms}$ and $\overline{u'v'}$ increase and attain their statistically steady values when the transition has been completed. The time equivalent to when $v'_{rms}$ and $\overline{u'v'}$ start to increase marks the onset of transition to turbulence.The turbulence spots are seen to cover the entire flow region when the flow has become fully developed turbulent flow. Due to the slow rate of flow development in all the cases reported, the time of transition to turbulence is delayed in comparison with the cases reported in Chapter Four and the step increase of flow rate reported. The three stages are similar to the step increase of flow rate reported by He and Seddighi (2013), the slow acceleration reported by Seddighi et al. (2014) and resemble that of bypass transition in flat plate boundary layer flow.

The development of the boundary layer in these present slow accelerating flow cases is caused as a result of continuous change in velocity gradient near the wall and then expands into the flow with time unlike the step change in flow rate reported by He and Seddighi (2013), which is characterised by a rapid growth of time-developing boundary layer. As reported previously, the temporal development of mean flow of step increase of flow rate resembles the laminar boundary layer using Stokes' first problem. In these present slow accelerating flow cases, the Stokes' solution is adjusted to enable multi-step increase of bulk velocity ($U_b$). For the D and E cases presented, it is seen that perturbation velocity, perturbation skin friction coefficient and the modified skin friction coefficient followed the extended Stokes laminar solution during the pre-transitional stage of the flow except for case E3.

The time elapsed from the start of the transient flow and the bulk velocity are used to define the equivalent Reynolds number ($Re_t$) for channel transient flow. The Reynolds number at which transition to turbulence takes place is important when studying transition procedure in unsteady flows. In flat plate boundary layer flow, it has been revealed that the critical Reynolds number depends on free-stream turbulence (Andersson et al., 1999; Fransson et al., 2005). Moreover, it has been shown from previous investigations carried out by He and Seddighi (2013; 2015) that for transition in a transient flow the transitional Reynolds number ($\Delta Re_{t,cr}$) is related with the initial turbulence intensity ($Tu_0$). In these present cases that involve time-varying bulk velocity, both the critical equivalent Reynolds number ($Re_{t,cr}$) and initial turbulence intensity ($Tu_0$) are modified and the power law relationships between the two parameters are obtained for all the cases investigated. In addition, the transitional period Reynolds number ($\Delta Re_{t,cr}$) is also modified for these much slow accelerating flow cases. A power curve relation of $Re_{t,cr} = 1700 Tu_0^{-1.64}$ is obtained between $Re_{t,cr}$ and $Tu_0$ from cases (D and E) while a power law fit of $\Delta Re_{t,cr} = 44.27 Re_{t,cr}^{0.68}$ is obtained between $\Delta Re_{t,cr}$ and $Re_{t,cr}$. In comparison with the power law relations ($Re_{t,cr} = 1340 Tu_0^{-1.71}$) of He and Seddighi (2015) and ($Re_{t,cr} = 1910 Tu_0^{-1.62}$) of Mathur (2016), the differences in constants are due to different flow accelerations. Moreover, the combined data of the cases in Chapter Four and in this chapter are represented as $\mathrm{Re_{t,cr}} = 1409 \mathrm{Tu_0^{-1.70}}$. A relation of $\Delta Re_{t,cr} = 44.27 Re_{t,cr}^{0.68}$ is obtained when the transitional period Reynolds number ($\Delta Re_{t,cr}$) and critical equivalent Reynolds number ($Re_{t,cr}$) is correlated and a power law relation of $\Delta Re_{t,cr} = 26.20 Re_{t,cr}^{0.74}$ is obtained for the data of this chapter and that of Chapter Four. Finally, the difference in the constants of the power relation between the transition period Reynolds number and the critical equivalent Reynolds with that of Narasimha et al. (1984) is because the present cases are temporally developing boundary layer flows while those of Narasimha et al. (1984) is spatially developing boundary layer flows.

There are detailed differences in the flows studied herein and those reported earlier. The enhancement and elongation of the pre-streaky structures in the flow are not strong in comparison with that of step increase of flow rate. During the slow acceleration, a boundary layer is generated continuously with time and then spreads to the flow. In a step increase of flow rate; however, an increase in flow rate occurs rapidly and then a thin boundary layer of high velocity gradient and high strain is generated near the wall and then spreads to the flow with time.

The correlation obtained from the plots of critical equivalent Reynolds number ($Re_{t,cr}$) against the initial turbulence intensity ($Tu_0$) has shown the dependence of $Re_{t,cr}$ on $Tu_0$ in the same way as that of the spatially developing boundary layer flow of Andersson et al. (1999) and Fransson et al. (2005). However, the present accelerating flow is different from the spatially developing boundary layer flow because the wall shear turbulence in transient flow, which serves as the free-stream turbulence decays very slowly in the region outside the boundary layer. This is in contrast to the spatially developing boundary layer where the turbulence is homogenous and it decays rapidly with the distance from the leading edge. In comparison with the step increase of flow rate of He and Seddighi (2015), the variation of the free-stream velocity of the present cases results in a complex boundary layer that comprises a summation of many small step changes in flow rate with differing starting times while the formation of the boundary layer in a step-change case occurs at once.

# Chapter 6

# Conclusions and Recommendations for Future Work

## 6.1 Conclusions

This current study has focused on the expansion of a novel perspective reported by He and Seddighi (2013), Seddighi et al. (2014) and He and Seddighi (2015) that the transient turbulent flow following a rapid increase in flow rate is effectively a laminar-turbulent transition and that it consists of three stages (pre-transition, transition and fully turbulence) despite the initial flow condition being turbulent. The three stages resemble that of bypass transition induced by free-stream turbulence that is buffeted laminar flow, intermittent flow and fully developed turbulent flow. The expansion of the novel perspective is done by increasing the initial and final Reynolds numbers far above the previous studies of Seddighi et al. (2014), He and Seddighi (2015) and Mathur (2018) while studying the turbulence structures in the transient turbulent flow. The ramp rate, and the period of acceleration are varied to study their effects during the flow acceleration. Experimental investigations of transition to turbulence of transient turbulent flows are carried out on a channel flow facility of length, width, and height of 8000 $mm$, 350 $mm$ and 50 $mm$, respectively. The studies are conducted on a smooth channel bed, and measurements are obtained through two laser-camera orientations (vertical-PIV and horizontal-PIV). Particle Image Velocimetry (PIV) is used to measure the mean and turbulence statistics of steady and unsteady flows. Constant Temperature Anemometry (CTA) with hot-film sensors is used to measure the wall shear stress during the transient flows. The statistically steady data obtained using PIV is compared with the recent DNS data of Lee and Moser (2015), and the results show close agreement. For all the transient flows investigated, the opening of pneumatic control valve is controlled in order to produce flow unsteadiness.

In this current study, two investigations have been conducted: (a) the effects of varying the initial Reynolds number and final Reynolds number on the transition to turbulence under transient conditions and; (b) the impact of the different acceleration periods on the transition to turbulence of the transient flows whereby both the initial and final Reynolds numbers are fixed and when the initial Reynolds number is fixed and the final Reynolds number is varied.

Chapter four reports results for the variation of the initial and final Reynolds numbers which produce different Reynolds number ratios. Skin friction coefficient ($C_f$) is used to obtain the onset of transition and the completion of it. The time equivalent to the minimum $C_f$ is used in this study to refer to the onset of transition while the time that is equivalent to the first peak of $C_f$ after its discovery denotes the end of transition. Results of cases (P,T and U) investigated have revealed that as the initial Reynolds number increases while the final Reynolds number remains fixed, the onset of transition reduces. As the initial Reynolds number remains fixed while the final Reynolds number increases, it has been shown that the onset of transition to turbulence reduces. Moreover, the effect of Reynolds number ratio is also determined on transient flow using the equivalent Reynolds number ($Re_t$). It has been shown that as the Reynolds number ratio decreases the critical Reynolds number ($Re_{t,cr}$) decreases and vice versa, conforming with the findings of He and Seddighi (2015).

During the pre-transitional time frame, when the transient flow has started, pre-streaky structures in the initial statistically steady turbulent flow are stretched and elongated. It has been shown during the transitional time frame, generation of "new" turbulence spots is recorded, and turbulence spots are seen growing with time and merging with each other. Following this, these turbulence spots fill the entire wall bounded surface when the flow has become fully developed turbulent flow. The results show for all the cases investigated that the streamwise mean velocity responds like a plug flow in all the wall locations immediately following the commencement of transient flows except near the wall while the streamwise fluctuating velocity ($u'_{rms}$) only responds at the locations close to the wall. The response of $u'_{rms}$ during the pre-transitional stage is due to the enhancement and elongation of the pre-streaky structures in the flow. However, both wall-normal fluctuating velocity ($v'_{rms}$) and the Reynolds shear stress ($\overline{u'v'}$) do not respond. The time equivalent to when both $v'_{rms}$ and $\overline{u'v'}$ start to respond to the flow marks the onset of transition to turbulence. The time at which the wall-normal fluctuating velocity ($v'_{rms}$) first respond in the flow is compared with that of the $C_f$ showing a very similar result. The slight variation found is due to the low frequency ($7Hz$) of the current PIV system utilised.

In contrast to the step increase of flow rate reported by He and Seddighi (2013), which is characterised by a rapid growth of the time-developing boundary layer, the temporally developing boundary layer of the cases reported occurs due to the continuous change in velocity gradient near the wall. It has been shown that the perturbation velocity profiles ($\bar{u}^{\wedge}$) from the different transient flow cases (T and U) investigated collapses with that of the extended Stokes' solution during the pre-transitional stage. Similarly, during the pre-transitional stage, the data of the modified skin friction coefficient of all cases investigated is slightly elevated the extended laminar solution but follows the trend of the correction made to the extended laminar solution.

Modifications are made to the equivalent Reynolds number ($Re_t$) and the initial turbulence intensity ($Tu_0$) proposed by He and Seddighi (2015) in order to account for the accelerating flows and continuous change of the bulk velocities of the cases investigated. After the modifications, the data of the current cases is seen to follow the correlation reported by He and Seddighi (2015). The authors obtained a power-law relation of $Re_{t,cr} = 1340Tu_0^{-1.71}$ when the critical equivalent Reynolds number ($Re_{t,cr}$) is plotted against the initial turbulence intensity ($Tu_0$), and a power-law relation of $Re_{t,cr} = 1319Tu_0^{-1.71}$ is obtained from the present T and U cases reported in Chapter Four. The slight differences in constants of the present cases with the step increase of flow rate reported by He and Seddighi (2015) is due to different accelerations. In comparison cases (T and U) with the step increase of flow rate, the increase of flow rate is slow. The transitional period Reynolds number and critical equivalent Reynolds number of the present data are correlated and a power-law relation of $\Delta Re_{t,cr} = 5.48Re_{t,cr}^{0.87}$ is obtained and is similar to that of Narasimha et al. (1984) of spatially developing boundary layer flows.

In chapter five, the variation of acceleration periods on slow accelerating flows is investigated. It can be seen that acceleration is slower and the onset of transition is delayed in this chapter in comparison with the cases reported in Chapter Four. It has been shown that the three-stage development of skin friction coefficient ($C_f$) of the slow accelerating cases is similar to that of Chapter Four of this thesis but at a much slower rate. It has also been shown from the cases (D and E) investigated that the onset of transition to turbulence increases as the acceleration period increases and it becomes shorter as the acceleration period reduces. Immediately following the commencement of the slow acceleration, the $C_f$ increases and reaches the maximum peak due to the formation of thin boundary layer near the wall. The $C_f$ reduces to its minimum value as the temporally developing boundary layer grows into the flow and causing the velocity gradient to reduce. It increases again due to the formation of ''new'' turbulence structures at the beginning of transition and approaches the final statistically steady flow when the transition has completed. In D cases, the $C_f$ increases and attains the highest peak for case D1 and the peak starts to reduce from case D2 and becomes unclear in case D6. The trends of the $C_f$ for D1 is similar to that of step increase of flow rate reported by He and Seddighi (2013) and the experimental studies of Mathur et al. (2018). As the acceleration period increases, the minimum $C_f$ increases from a large undershooting to a very small undershooting in D6. The transitional period reduces starting from case D2, as the acceleration period increases becoming subtle in case D6 similar to the results reported by Seddighi et al. (2014) and Jung and Kim (2017b). Though the final flow of E1 is the smallest among the E cases investigated, E1 has the highest initial increase of $C_f$. This is likely due to the fact that the initial acceleration is higher in E1 than other two E cases. The transitional period is longer in case E1 and reduces as the acceleration period and final Reynolds number increase. The final $C_f$ and the undershooting of the minimum $C_f$ reduce as both acceleration period and final stage of the flow increase.

The wall shear stress ($\tau_w$) appears to show four stages of development in the faster cases that is, D1, D2, D3,and E1. A sharp increase of wall shear stress ($\tau_w$) can be attributed to the high acceleration rate during the initial flow acceleration in stage 1 with the formation of a thin boundary layer of high velocity gradient near the wall. In stage 2, as the thin boundary layer transports into the flow, the wall shear stress ($\tau_w$) reduces. During this period, the mean acceleration continues, and an additional boundary layer also continues to form and transports into the flow, which causes the $\tau_w$ to increase gradually until the onset of transition signalling the start of stage 3. The length of stage 2 reduces as the acceleration period increases and vanishes completely in case D6. The transition of a temporally developing boundary layer occurs at stage 3, leading to further increase of the $\tau_w$, leading to stage 4 when the transition is complete. As the flow acceleration continues and an additional boundary layer is generated, $\tau_w$ increases also in stage 4 but at a very slow pace and attains the statistically steady flow eventually.

It has been revealed that the streamwise mean velocity ($U$) increases at the same rate across the flow and its profile becomes flatter during the transitional stage and overlaps with itself when the flow becomes fully developed turbulent flow. The procedure is more noticeable in case D1 than D6 and in case E1 than E3. The trends of the streamwise mean velocity ($U$) can be related to those of Greenblatt and Moss (2004). The enhancement and elongation of the pre-streaky structures causes the streamwise fluctuating velocity ($u'_{rms}$) to increase near the wall during the pre-transitional stage. During this pre-transitional stage, both wall-normal fluctuating velocity ($v'_{rms}$) and Reynolds shear stress ($\overline{u'v'}$) do not change. This indicates the absence of turbulence in the flow. Starting from the beginning of transitional stage, the $v'_{rms}$ and $\overline{u'v'}$ are observed to respond and increase to their statistically steady values, and the time equivalent to the first response of $v'_{rms}$ and $\overline{u'v'}$ marks the onset of transition. Moreover, during the transitional stage, $u'_{rms}$ continues to increase near the wall and starts to reduce when the flow has become turbulent.

The equivalent Reynolds number ($Re_t$) and the initial turbulence intensity ($Tu_0$) proposed by He and Seddighi (2015) are modified and a power law relation of $Re_{t,cr} = 1700 Tu_0^{-1.64}$ is obtained between $Re_{t,cr}$ and $Tu_0$ from cases (D&E) investigated. In comparison with the relation ($Re_{t,cr} = 1319 Tu_0^{-1.71}$) obtained in Chapter Four, it can be seen that the constants are different due to the fact that acceleration of these present cases is much slower. The relation is similar to $Re_{t,cr} = 1340Tu_0^{-1.71}$) of He and Seddighi (2015) and ($Re_{t,cr} = 1910Tu_0^{-1.62}$) of Mathur (2016) but the constants are different. The difference in the constants is due to the slow response of the flow cases investigated. The transitional period Reynolds number ($\Delta Re_{t,cr}$) and the critical equivalent Reynolds number ($Re_{t,cr}$) are also correlated and a power relation of $\Delta Re_{t,cr} = 44.27Re_{t,cr}^{0.68}$ is obtained. The power relation is similar to that of Narasimha et al. (1984) of spatially developing boundary layer but the constants are different because the present accelerating cases are temporally developing boundary layer flows.

The critical equivalent Reynolds number ($Re_{t,cr}$) and initial turbulence intensity ($Tu_0$) have been shown to correlate well and similar to that of the spatially developing boundary layer flow e.g., Andersson et al. (1999) and Fransson et al. (2005) and the step increase of flow rate of He and Seddighi (2015). There are however differences in the present flow cases, the wall shear turbulence in transient flow, which can be viewed as the free-stream turbulence, decays very slowly in the region outside the boundary layer which causes it to be different from the spatially developing boundary layer flow. In spatially developing boundary layer flow, the turbulence is homogeneous, and it decays rapidly with the distance from the leading edge. Furthermore, the variation of the free-stream velocity of the present slow accelerating flow cases (D and E) results in a complex boundary layer that comprises of the summation of small-step changes in flow rate with a slow development than in the step increase of flow rate of He and Seddighi (2015) in which the creation of a boundary layer happen very rapidly.

## 6.2 Recommendations for future work

The investigation of turbulence in unsteady flow is ongoing and suggestions for future work are necessary for the field to continue progressing. A number of key recommendations that will contribute to the success of future work of transient channel flow are outlined below:

- The experimental flow facility was moved from the old location (Mappin Building) to the present location (George Porter Building) due to the construction of Engineering Heartspace at the Mapping Building. At its current location, the pipeline system comprises many bends that lead to high friction loss and reduces the flow rate. When the flow facility is to be relocated permanently back to the Mappin Building, the pipeline system should consist of minimal bends. The height between the free surface of the overhead tank and the bottom tanks is currently 5.31 $m$. Reduction of the friction loss and an increment of the height from 5.31 $m$ will enable high bulk Reynold number ($Re_b$) during the experiments. This will enable experiments of higher Reynolds number ratios with higher final Reynolds numbers to be investigated.
- A Slight delay is experienced immediately following the opening of the pneumatic control valve in some of the experiments. In order to ensure repeatability of the pneumatic control valve in future and to obtain quality of measurements, the responsiveness of the valve needs to be improved.
- Though the impellers of both centrifugal pump and pneumatic control valve are made of stainless steel, their bodies are made of cast iron that can easily rust. The pump bodies rust easily and thus changes the colour of the water, contaminating the hot-film sensors. To provide better visualisation of the response of transient flow near the wall in the future, the cause of rusting inside the centrifugal pump and bottom pump of the control valve must be eradicated. The two pumps should be changed to stainless steel pumps in order to avoid water contamination that may reduce the efficiency of the hot-film sensors.
- Stokes solution is concerned with the early flow acceleration and the measurement through the particle image velocimetry (PIV) is sparse in this study because of the low pulsation frequency ($7Hz$) of the current laser. In order to improve data points and capture the early stage of the flow in the future, the current pulsation frequency will need to be increased.

- At a higher final Reynolds number above, $Re_b = 25000$, the vibration of the experimental rig becomes a problem. In the future, in order to avoid the transition to turbulence through external factors when high Reynolds number cases are being conducted, the stand of the pneumatic control valve needs to be supported to ensure its stability.
- Studies on the effects of external factors on the process of transition to turbulence should be carried out.
- For complete eradication of wiggles in the plots, the number of repeated experimental runs needs to be increased far above the present 80 repeated experimental runs.
- The regime of the experimental data in Figure 4-33 can be extended further by increasing the final Reynolds number of each case in order to study the procedure of transition of a transient turbulent flow in a channel.

# References

Abe, H., Kawamura, H., & Matsuo, Y. (2001). Direct numerical simulation of a fully developed turbulent channel flow with respect to the Reynolds number dependence. *Journal of Fluids Engineering (Transactions of the ASME)*, *123*(2), 382–393. https://doi.org/10.1115/1.1366680

Adrian, R J, Jerry, W. (2011). *Particle Image Velocimetry*. (J. Westerweel, J. Westerweel, J. (Jerry) Westerweel, & J. Westerweel, Eds.). Cambridge: Cambridge.

Ainola, L., Koppel. T., Lamb, J. & Liiv, U. (1983). The skin friction coefficient during accelerated flows in pipes. In *In Proceedings XX IAHR Congress, Moscow, USSR, vol. 6,* (pp. 453–460.).

Andersson, P, Brandt, L., Bottaro, A., & Henningson, D. S. (2001). On the breakdown of boundary layers streaks. *J. Fluid Mech.*, *428*, 29–60.

Andersson, Paul, Berggren, M., & Henningson, D. S. (1999). Optimal disturbances and bypass transition in boundary layers. *Physics of Fluids*, *11*(1), 134–150. https://doi.org/10.1063/1.869908

Annus, I., & Koppel, T. (2011). Transition to Turbulence in Accelerating Pipe Flow. *Journal of Fluids Engineering*, *133*(7), 071202. https://doi.org/10.1115/1.4004365

Annus, I., & Koppel, T. (2015). Development of radial velocity component in accelerating start-up pipe flow. *European Journal of Mechanics / B Fluids*, *53*, 48–54. https://doi.org/10.1016/j.euromechflu.2015.04.001

Ariyaratne, C., He, S., & Vardy, A. E. (2010). Wall friction and turbulence dynamics in decelerating pipe flows. *Journal of Hydraulic Research*, *48*(6), 810–821. https://doi.org/10.1080/00221686.2010.525372

Arnal D. Juillen, J. C. and Michel, R. (1978). Experimental analysis and computation of the onset and development of the boundary layer transition. *NASA Technical Memorandum*.

Bellhouse, B. J., & Schultz, D. L. (1966). Determination of mean and dynamic skin friction, separation and transition in low-speed flow with a thin-film heated element. *J. Fluid Mech.*, *24*(2), 379–400. https://doi.org/10.1017/S0022112066000715

Bhushan, S., Walters, D., Muthu, S., & Pasiliao, C. (2018). Identification of Bypass Transition Onset Markers Using Direct Numerical Simulation. *J. Fluids Eng.-Trans. ASME*, *140*(11). https://doi.org/10.1115/1.4040299

BLUMER, C. B., & VAN DRIEST, E. R. (1963). Boundary Layer Transition- Freestream Turbulence and Pressure Gradient Effects. *AIAA Journal*, *1*(6), 1303–1306. https://doi.org/10.2514/3.1784

Boiko, A., Westin, K., Klingmann, B., Kozlov, V., & Alfredsson, P. (1994). EXPERIMENTS IN A BOUNDARY-LAYER SUBJECTED TO FREE-STREAM TURBULENCE .2. THE ROLE OF TS WAVES IN THE TRANSITION PROCESS. *J. Fluid Mech.*, *281*, 219–245.

Brandt, L., Cossu, C., Chomaz, J.-M., Huerre, P., & Henningson, D. S. (2003). On the convectively unstable nature of optimal streaks in boundary layers. *J. Fluid Mech.*, *485*(25), 221–242. https://doi.org/10.1017/S0022112003004427

Brandt, L., Schlatter, P., & Henningson, D. S. (2004). Transition in boundary layers subject to free-stream turbulence. *Journal of Fluid Mechanics*, *517*, 167–198. https://doi.org/10.1017/S0022112004000941

Bruun, H. H. (Hans H. . (1995). *Hot-wire anemometry : principles and signal analysis*. Oxford: Oxford : Oxford University Press, 1995.

Burgers, J. M. (1924). The motion of a fluid in the boundary layer along a plain smooth surface. In *Proceedings of the First International Congress for Applied Mechanics, Delft* (pp. 113–128).

Carstens, M. R. (1956). Transition from Laminar to Turbulent Flow during Unsteady Flow in a Smooth Pipe. In *Proc., Int. Congress of Applied Mechanics.* (Vol. 3, pp. 370-377.).

Chung, Y. M. (2005). Unsteady turbulent flow with sudden pressure gradient changes. *International Journal for Numerical Methods in Fluids*, *47*(8–9), 925–930. https://doi.org/10.1002/fld.917

Coleman, G. N., Kim, J., & Spalart, P. R. (2003). Direct numerical simulation of a decelerated wall-bounded turbulent shear flow. *J. Fluid Mech.*, *495*(495), 1–18. https://doi.org/10.1017/S0022112003005883

Daily, J. W., Hankey, W. L, Olive, R. W. & Jordaan, J. M. (1955). *Resistance coefficients for accelerated and decelerated flows through smooth tubes and orifices. DTIC Document*.

Darbyshire, A. G., & Mullin, T. (1995). TRANSITION TO TURBULENCE IN CONSTANT-MASS-FLUX PIPE-FLOW. *J. Fluid Mech.*, *289*, 83–114.

Davidson, P. A. (2015). *Turbulence : An introduction for scientists and engineers* (Second edi). Oxford, UK: Oxford, UK.

Dean, R. B. (1978). Reynolds Number Dependence of Skin Friction and Other Bulk Flow Variables in Two-Dimensional Rectangular Duct Flow. *Journal of Fluids Engineering*, *100*(2), 215–223. Retrieved from http://dx.doi.org/10.1115/1.3448633

Dryden, H. L. (1938). Turbulence investigations at the National Bureau of Standards. In *Proc. Fifth Intern. Congress of Appl. Mechanics* (p. 362).

Durst, F., Kikura, H., Lekakis, I., Jovanović, J., & Ye, Q. (1996). Wall shear stress determination from near-wall mean velocity data in turbulent pipe and channel flows. *Experimental Methods and Their Applications to Fluid Flow*, *20*(6), 417–428. https://doi.org/10.1007/BF00189380

Fage, A., & Falkner. V. M. (1931). On the relation between heat transfer and surface friction for laminar flow. ARC R&M No 1408.

Finnicum, D. S. & Hanratty, T. J. (1998). Influence of imposed flow oscillations on turbulence. *Physio-Chem. Hydrodyn.*, *10*, 585–598.

Fornarelli, F., & Vittori, G. (2009). Oscillatory boundary layer close to a rough wall. *European Journal of Mechanics / B Fluids*, *28*(2), 283–295. https://doi.org/10.1016/j.euromechflu.2008.06.002

Fransson, J. H. M., Matsubara, M., & Alfredsson, P. H. (2005). Transition induced by free-stream turbulence. *Journal of Fluid Mechanics*, *527*, 1–25. https://doi.org/10.1017/S0022112004002770

Gasser, D., Thomann, H., & Dengel, P. (1993). Comparison of four methods to measure wall shear stress in a turbulent boundary layer with separation. *Experimental Methods and Their Applications to Fluid Flow*, *15*(1), 27–32. https://doi.org/10.1007/BF00195592

Gerrard, J. H. (1971). An experimental investigation of pulsating turbulent water flow in a tube. *J. Fluid Mech.*, *46*(1), 43–64. https://doi.org/10.1017/S0022112071000399

Goldstein, M. E., & Wundrow, D. W. (1998). On the Environmental Realizability of Algebraically Growing Disturbances and Their Relation to Klebanoff Modes. *Theoretical and Computational Fluid Dynamics*, *10*(1), 171–186. https://doi.org/10.1007/s001620050057

Goldstein, R. J. (1996). *Fluid Mechanics Measurements* (Second Edi). Bristol: Taylor & Francis.

Gorji, S. (2015). A study of turbulence in transient channel flows. University of Sheffield.

Greenblatt, D., & Moss, E. (2003). Rapid transition to turbulence in pipe flows accelerated from rest. *Journal of Fluids Engineering (Transactions of the ASME)*, *125*(6), 1072–1075. https://doi.org/10.1115/1.1624423

Greenblatt, D., & Moss, E. A. (2004). Rapid temporal acceleration of a turbulent pipe flow. *J. Fluid Mech.*, *514*, 65–75. https://doi.org/10.1017/S0022112004000114

Hanjalić, K., & Launder, B. E. (1972). Fully developed asymmetric flow in a plane channel. *Journal of Fluid Mechanics*, *51*(2), 301–335. https://doi.org/10.1017/S0022112072001211

Haywood, L. (1996). Airline Turbulence: Staying Safe in the Air. In *dspace.mit.edu.*

He, K., Seddighi, M., & He, S. (2016). DNS study of a pipe flow following a step increase in flow rate. *International Journal of Heat and Fluid Flow*, *57*(C), 130–141. https://doi.org/10.1016/j.ijheatfluidflow.2015.09.004

He, S., Ariyaratne, C., & Vardy, A. E. (2008). A computational study of wall friction and turbulence dynamics in accelerating pipe flows. *Computers and Fluids*, *37*(6), 674–689. https://doi.org/10.1016/j.compfluid.2007.09.001

He, S., Ariyaratne, C., & Vardy, A. E. (2011). Wall shear stress in accelerating turbulent pipe flow. *Journal of Fluid Mechanics*, *685*, 440–460. https://doi.org/10.1017/jfm.2011.328

He, S., & Jackson, J. D. (2000). A study of turbulence under conditions of transient flow in a pipe. *Journal of Fluid Mechanics*, *408*, 1–38. https://doi.org/10.1017/S0022112099007016

He, S., & Jackson, J. D. (2009). An experimental study of pulsating turbulent flow in a pipe. *European Journal of Mechanics, B/Fluids*, *28*(2), 309–320. https://doi.org/10.1016/j.euromechflu.2008.05.004

He, S., & Seddighi, M. (2013). Turbulence in transient channel flow. *Journal of Fluid Mechanics*, *715*, 60–102. https://doi.org/10.1017/jfm.2012.498

He, S., & Seddighi, M. (2015). Transition of transient channel flow after a change in Reynolds number. *Journal of Fluid Mechanics*, *764*, 395–427. https://doi.org/10.1017/jfm.2014.698

He, S, & Ariyaratne, C. (2011). Erratum for "Wall Shear Stress in the Early Stage of Unsteady Turbulent Pipe Flow" by S. He and C. Ariyaratne. *Journal of Hydraulic Engineering*, *137*(10), 1309. https://doi.org/10.1061/(ASCE)HY.1943-7900.0000448

He, S, & Seddighi, M. (2013). a Dns Study of Effects of Reynolds Number on Unsteady Channel Flow, 1–6.

He, Shuisheng, Seddighi, M., Gorji, S., & Mathur, A. (2015). *Transition of Transient Turbulent Channel Flow*. *Procedia Engineering* (Vol. 126). Elsevier B.V. https://doi.org/10.1016/j.proeng.2015.11.173

Hong, J., Katz, J., & Schultz, M. P. (2011). Near-wall turbulence statistics and flow structures over three-dimensional roughness in a turbulent channel flow. *J. Fluid Mech.*, *667*, 1–37. https://doi.org/10.1017/S0022112010003988

Incorporated, T. S. I. (2012). Turbulence Intensity Measurements. Retrieved from http://www.tsi.com/uploadedFiles/_Site_Root/Products/Literature/Application_Notes/TSI-141-A4.pdf

Jacobs, R. G., & Durbin, P. A. (2001). Simulations of bypass transition. *Journal of Fluid Mechanics*, *428*, 185–212. https://doi.org/10.1017/S0022112000002469

Jimenez, J., Martinez-Val, R., & Rebollo, M. (1981). Hot-film sensors calibration drift in water. *Journal of Physics E: Scientific Instruments*, *14*(5), 569–572. https://doi.org/10.1088/0022-3735/14/5/010

Jung, S. Y. & Kim, K. (2016). Effects of the Temporal Increase Rate of Reynolds Number on Turbulent Channel Flows. *Trans. Korean Soc. Mech. Eng*, *40*(7), 435–440.

Jung, S. Y., & Chung, Y. M. (2012). Large-eddy simulation of accelerated turbulent flow in a circular pipe. *International Journal of Heat and Fluid Flow*, *33*(1), 1–8. https://doi.org/10.1016/j.ijheatfluidflow.2011.11.005

Jung, S. Y., & Kim, K. (2017a). Responses of turbulent channel flows to temporal acceleration. *10th International Symposium on Turbulence and Shear Flow Phenomena, TSFP 2017*, *1*(1975).

Jung, S. Y., & Kim, K. (2017b). Transient behaviors of wall turbulence in temporally accelerating channel flows. *International Journal of Heat and Fluid Flow*, *67*(PA), 13–26. https://doi.org/10.1016/j.ijheatfluidflow.2017.06.012

Kachanov, Y. S. (1994). Physical Mechanisms of Laminar-Boundary-Layer Transition. *Annual Review of Fluid Mechanics*, *26*(1), 411–482. https://doi.org/10.1146/annurev.fl.26.010194.002211

Kataoka, K., Kawabata, T., & Miki, K. (1975). The start-up response of pipe flow to a step change in flow rate. *Journal of Chemical Engineering of Japan*. Tokyo. https://doi.org/10.1252/jcej.8.266

Keane, R., & Adrian, R. (1991). Optimization of particle veIocimeters: II. Multiple pulsed systems, *2*, 963–974. Retrieved from papers2://publication/uuid/8CE38F43-1071-491E-946D-4D67657C2F83

Keane, R. D., & Adrian, R. J. (1990). Optimization of particle image velocimeters. I. Double pulsed systems Optimization of particle image ve I oci m e te rs. Part I: Double pulsed systems. *Meas. Sci. Technol. Meas. Sci. Technol*, *1*(1), 1202–1215. Retrieved from http://iopscience.iop.org/0957-0233/1/11/013

Keane, R. D., & Adrian, R. J. (1992). Theory of cross-correlation analysis of PIV images RICHARD D. KEANE & RONALD J. ADRIAN. *Applied Scientific Research*, *49*, 191–215.

Kendall, J. M. (1985). Experimental study of disturbances produced in a pre-transitional laminar boundary layer by weak freestream turbulence. In *AIAA Paper*.

Kenneth, B., Takeo, K. (1993). Bypass transition in two- and three-dimensional boundary layers. In *23rd Fluid Dynamics, Plasmadynamics, and Lasers Conference. Fluid Dynamics and Colocated Conferences. American Institute of Aeronautics and Astronautics (1993)*.

Klebanoff, P. S., Tidstrom, K. D., & Sargent, L. M. (1962). The three-dimensional nature of boundary-layer instability. *J. Fluid Mech.*, *12*(1), 1–34. https://doi.org/10.1017/S0022112062000014

Kleiser, L., & Zang, T. A. (1991). Numerical Simulation of Transition in Wall-Bounded Shear Flows. *Annu. Rev. Fluid. Mech.*, *23*(1), 495–537. https://doi.org/10.1146/annurev.fl.23.010191.002431

Knisely, C., Nishihara, K., & Iguchi, M. (2010). Critical Reynolds Number in Constant-Acceleration Pipe Flow From an Initial Steady Laminar State. *Journal of Fluids Engineering (Transactions of the ASME)*, *132*(9), 091202 (4 )-091202 (4 ). https://doi.org/10.1115/1.4002358YouarenotloggedintotheASMEDigitalLibrary.

Koppel', T., & Liiv, U. (1977). Experimental investigation of the development of motion of liquid in conduits. *Fluid Dynamics*, *12*(6), 881–887. https://doi.org/10.1007/BF01090323

Kurokawa, J. and Morikawa, M. (1986). Accelerated and decelerated flows in a circular pipe. *Bulletin of JSME*, *29*, 758–765.

Lee, M., & Moser, R. D. (2015). Direct numerical simulation of turbulent channel flow up to. *Journal of Fluid Mechanics*, *774*, 395–415. https://doi.org/10.1017/jfm.2015.268

Lefebvre, P. J., & White, F. M. (1989). Experiments on transition to turbulence in a constant-acceleration pipe flow. *Journal of Fluids Engineering, Transactions of the ASME*, *111*(4), 428–432. https://doi.org/10.1115/1.3243663

Lefebvre, P. J., & White, F. M. (1991). Further experiments on transition to turbulence in constant-acceleration pipe flow. *Journal of Fluids Engineering, Transactions of the ASME*, *113*(2), 223–227. https://doi.org/10.1115/1.2909484

Leib, S. J., Wundrow, D., & Goldstein, M. E. (1999). Effect of free-stream turbulence and other vortical disturbances on a laminar boundary layer. *J. Fluid Mech.*, *380*, 169–203.

Leipmann, H. W., & Skinner, G. T. (1954). *Shearing-stress measurements of use of a heated element*.

Leutheusser, H. J., and Lam, K. W. (1977). Flow Instability in Accelerated Fluid Motion. In *Sixth Can. Congr. App. Mech.,* (pp. 679–680).

Lodahl, C. R., Sumer, B. M., & Fredsoe, J. (1998). Turbulent combined oscillatory flow and current in a pipe. *J. Fluid Mech.*, *373*, 313–348.

Lomas, C. G. (1986). *Fundamentals of hot wire anemometry*. Cambridge: Cambridge : Cambridge University Press, 1986.

Luchini, P. (2000). Reynolds-number-independent instability of the boundary layer over a flat surface: optimal perturbations. *J. Fluid Mech.*, *404*, 289–309.

Ludweig, H. (1950). *Instrument for measuring the wall shearing stress of turbulent boundary layers*.

Mandal, A. C., Venkatakrishnan, L., & Dey, J. (2010). A study on boundary-layer transition induced by free-stream turbulence. *Journal of Fluid Mechanics*, *660*, 114–146. https://doi.org/10.1017/S0022112010002600

Mankbadi, R. R., & Liu, J. T. C. (1992). Near-wall response in turbulent shear flows subjected to imposed unsteadiness. *Journal of Fluid Mechanics*, *238*(55), 55–71. https://doi.org/10.1017/S0022112092001630

Manna, M, Vacca, A., & Verzicco, R. (2012). Pulsating pipe flow with large-amplitude oscillations in the very high frequency regime. Part 1. Time-averaged analysis. *J. Fluid Mech.*, *700*, 246–282. https://doi.org/10.1017/jfm.2012.129

Manna, Marcello, & Vacca, A. (2008). Spectral dynamic of pulsating turbulent pipe flow. *Computers and Fluids*, *37*(7), 825–835. https://doi.org/10.1016/j.compfluid.2007.02.014

Mao, Z.-X., & Hanratty, T. J. (1986). Studies of the wall shear stress in a turbulent pulsating pipe flow. *Journal of Fluid Mechanics*, *170*, 545–564. https://doi.org/DOI: 10.1017/S0022112086001015

Maruyama, T., Kato, Y., & Mizushina, T. (1978). TRANSITION TO TURBULENCE IN STARTING PIPE FLOWS. *Journal of Chemical Engineering of Japan*, *11*(5), 346. https://doi.org/10.1252/jcej.11.346

Maruyama, T., Kuribayashi, T., & Mizushina, T. (1976). THE STRUCTURE OF THE TURBULENCE IN TRANSIENT PIPE FLOWS. *Journal of Chemical Engineering of Japan*, *9*(6), 431. https://doi.org/10.1252/jcej.9.431

Mathur, A., Gorji, S., He, S., Seddighi, M., Vardy, A. E., O'Donoghue, T., & Pokrajac, D. (2018). Temporal acceleration of a turbulent channel flow. *Journal of Fluid Mechanics*, *835*, 471–490. https://doi.org/10.1017/jfm.2017.753

Mathur, A, Gorji, S., He, S., Seddighi, M., Vardy, A. E., O'Donoghue, T., & Pokrajac, D. (2018). Temporal acceleration of a turbulent channel flow. *Journal of Fluid Mechanics*, *835*, 471–490. https://doi.org/DOI: 10.1017/jfm.2017.753

Mathur, Akshat. (2016). Study of accelerating and decelerating turbulent flows in a channel. University of Sheffield.

Mathur, Akshat, Seddighi, M., & He, S. (2018). Transition of Transient Channel Flow with High Reynolds Number Ratios. *Entropy*. Basel. https://doi.org/10.3390/e20050375

Menendez, A., & Ramaprian, B. (1985). The use of flush-mounted hot-film gauges to measure skin friction in unsteady boundary layers. *Journal of Fluid Mechanics*, *161*, 139–160.

Meseguer, Á., & Trefethen, L. N. (2003). Linearized pipe flow to Reynolds number 10 7. *Journal of Computational Physics*, *186*(1), 178–197. https://doi.org/10.1016/S0021-9991(03)00029-9

Mizushina, T, Maruyama, T., & Shiozaki, Y. (1974). Pulsating turbulent flow in a tube. *JOURNAL OF CHEMICAL ENGINEERING OF JAPAN*, *6*(6), 487–494. https://doi.org/10.1252/jcej.6.487

Mizushina, Tokuro, Maruyama, T., & Hirasawa, H. (1975). STRUCTURE OF THE TURBULENCE IN PULSATING PIPE FLOWS. *Journal of Chemical Engineering of Japan*. Tokyo. https://doi.org/10.1252/jcej.8.210

Monty, J. (2005). *Developments in smooth wall turbulent duct flows*. University of Melbourne.

Morkovin, M. V. (1984). Bypass transition to turbulence and research desiderata. In Transition in Turbines. *NASA Conf Publ.*, *2386*, pp.161-204.

Morkovin, Mark V. (1969). On the Many Faces of Transition BT - Viscous Drag Reduction. In C. S. Wells (Ed.) (pp. 1–31). Boston, MA: Springer US.

Moser, R. D., Kim, J., & Mansour, N. N. (1999). Direct numerical simulation of turbulent channel flow up to Re τ =590. *Physics of Fluids*, *11*(4), 943–945. https://doi.org/10.1063/1.869966

Musker, A. J. (1979). Explicit Expression for the Smooth Wall Velocity Distribution in a Turbulent Boundary Layer. *AIAA Journal*, *17*(6), 655–657. https://doi.org/10.2514/3.61193

Nagano, Y., Tsuji, T., & Houra, T. (1998). Structure of turbulent boundary layer subjected to adverse pressure gradient. *Int. J. Heat Fluid Fl.*, *19*, 563–572. https://doi.org/10.1016/S0142-727X(98)10013-9

Nagarajan, S., Lele, S. K., & Ferziger, J. H. (2007). *Leading-edge effects in bypass transition*. *Journal of Fluid Mechanics* (Vol. 572). University of Sheffield Library. https://doi.org/10.1017/S0022112006001893

Nakahata, Y., Knisely, C. W., Nishihara, K. Sasaki, Y., Iguchi, M. (2007). Critical Reynolds number in constant-accelerated pipe flow. *J. of the Japanese Society for Experimental Mechanics.*, *7*(2), 142–147.

Narasimha, R., Narayanan, M. A. B., & Subramanian, C. (1984). Turbulent spot growth in favorable pressure gradients. *AIAA Journal*, *22*(6), 837–839. https://doi.org/10.2514/3.8689

Ohmi, M., Kyomen, S.,Usui, T. (1978). No TitleAnalysis of velocity distribution in pulsating turbulent pipe flow with time-dependent friction velocity. In *Bulletin of JSME* (Vol. 21, pp. 1137–1143).

Orr, W. M. (1907). The Stability or Instability of the Steady Motions of a Perfect Liquid and of a Viscous Liquid. Part I: A Perfect Liquid. *Proceedings of the Royal Irish Academy. Section A: Mathematical and Physical Sciences*, *27*, 9–68.

Orszag, S. A. (1971). Accurate solution of the Orr–Sommerfeld stability equation. *Journal of Fluid Mechanics*, *50*(4), 689–703. https://doi.org/10.1017/S0022112071002842

Ovchinnikov, V., Choudhari, M. M., & Piomelli, U. (2008). Numerical simulations of boundary-layer bypass transition due to high-amplitude free-stream turbulence. *Journal of Fluid Mechanics*, *613*, 135–169. https://doi.org/10.1017/S0022112008003017

Pfenniger, W. (1961). *Transition in the inlet length of tubes at high Reynolds numbers. In Boundary Layer and Flow Control*. (G. V. Lanchman, Ed.). Pergamon.

Pope, S. B. (2000). *Turbulent Flows*. Cambridge University Press.

Raffel, M., Willert, C., Wereley, S., & Kompenhans, J. (2007). *Particle Image Velocimetry: A Practical Guide*. (M. Raffel, Ed.).

Ramaprian, B. R., & Tu, S.-W. (1980). An experimental study of oscillatory pipe flow at transitional Reynolds numbers. *J. Fluid Mech.*, *100*(3), 513–544. https://doi.org/10.1017/S0022112080001267

Ramaprian, B. R., & Tu, S. W. (1983). Fully developed periodic turbulent pipe flow. Part 2. The detailed structure of the flow. *J. Fluid Mech.*, *137*, 59–81. https://doi.org/10.1017/S0022112083002293

Reynolds, O. (1883). An Experimental Investigation of the Circumstances Which Determine Whether the Motion of Water Shall Be Direct or Sinuous, and of the Law of Resistance in Parallel Channels. *Philosophical Transactions of the Royal Society of London*, *174*(0), 935–982. https://doi.org/10.1098/rstl.1883.0029

Reynolds, Osborne. (1895). On the Dynamical Theory of Incompressible Viscous Fluids and the Determination of the Criterion. *Philosophical Transactions of the Royal Society of London. A*, *186*, 123–164.

Roach, P. E. and Brierley, D. H. (1992). The influence of a turbulent free-stream on zero pressure gradient transitional boundary layer development part I: test cases T3A and T3B. *Numerical Simulation of Unsteady Flows and Transition to Turbulence,* 319–347.

Rotta, J. (1956). An Experimental Contribution to the Transition from Laminar to Turbulent flow in a Pipe. In *Proc., Int. Congress of Applied Mechanics.* (Vol. 3, pp. 350-359.).

Saric, W. S., Reed, H. L., & Kerschen, E. J. (2002). BOUNDARY-LAYER RECEPTIVITY TO FREESTREAM DISTURBANCES. *Annu. Rev. Fluid Mech.*, *34*(1), 291–319. https://doi.org/10.1146/annurev.fluid.34.082701.161921

Schlichting, H. (2000). *Boundary-layer theory*. (K. Gersten, Ed.) (8th rev. a). Berlin : Berlin .

Schmid, P. J. (2001). *Stability and transition in shear flows*. (D. S. Henningson, Ed.). New York : New York .

Schubauer,. G. B. & Skramstad, H. K. (1948). Laminar boundary layer oscillations and transition on a flat plate. *NACA Rep. 909.*

Scotti, A., & Piomelli, U. (2001). Numerical simulation of pulsating turbulent channel flow. *Physics of Fluids*, *13*(5), 1367–1384. https://doi.org/10.1063/1.1359766

Sedat Tardu, F., & Maestri, R. (2010). Wall shear stress modulation in a turbulent flow subjected to imposed unsteadiness with adverse pressure gradient. *Fluid Dynamics Research*, *42*(3). https://doi.org/10.1088/0169-5983/42/3/035510

Seddighi, M., He, S., Vardy, A. E., & Orlandi, P. (2014). Direct numerical simulation of an accelerating channel flow. *Flow, Turbulence and Combustion*, *92*(1–2), 473–502. https://doi.org/10.1007/s10494-013-9519-z

Seddighi, M, He, S., Pokrajac, D., O'Donoghue, T., & Vardy, A. E. (2015). Turbulence in a transient channel flow with a wall of pyramid roughness. *Journal of Fluid Mechanics*, *781*, 226–260. https://doi.org/10.1017/jfm.2015.488

Seddighi, Mehdi, He, S., Orlandi, P., & Vardy, A. E. (2011). A comparative study of turbulence in ramp-up and ramp-down unsteady flows. *Flow, Turbulence and Combustion*, *86*(3–4), 439–454. https://doi.org/10.1007/s10494-011-9341-4

Shuy, E. B. (1996). Wall shear stress in accelerating and decelerating turbulent pipe flows. *Journal of Hydraulic Research*, *34*(2), 173–183. https://doi.org/10.1080/00221689609498495

Spalding, D. B. (1961). A Single Formula for the "Law of the Wall." *Journal of Applied Mechanics*, *28*(3), 455. https://doi.org/10.1115/1.3641728

Sundstrom, L.R. Joel and Cervantes, M. J. (2017). The response of the wall shear stress in uniformly and nonuniformly accelerating pipe flows. In *10th International Symposium on Turbulence and Shear Flow Phenomena (TSFP10), Chicago, USA*.

Sundstrom, L. R. J., & Cervantes, M. J. (2018a). Laminar similarities between accelerating and decelerating turbulent flows. *International Journal of Heat and Fluid Flow*. https://doi.org/10.1016/j.ijheatfluidflow.2018.03.005

Sundstrom, L. R. J., & Cervantes, M. J. (2018b). On the Similarity of Pulsating and Accelerating Turbulent Pipe Flows. *Flow, Turbulence and Combustion*, *100*(2), 417–436. https://doi.org/10.1007/s10494-017-9855-5

Sundstrom, L. R. J., & Cervantes, M. J. (2018c). The self-similarity of wall-bounded temporally accelerating turbulent flows. *Journal of Turbulence*, *19*(1), 49–60. https://doi.org/10.1080/14685248.2017.1390239

Sundstrom, L. R. J., Mulu, B. G., & Cervantes, M. J. (2016). Wall friction and velocity measurements in a double-frequency pulsating turbulent flow, 521–548. https://doi.org/10.1017/jfm.2015.722

Talha, T., & Chung, Y. M. (2015). Large-eddy simulations of temporally accelerating turbulent channel flow. *Journal of Turbulence*, *16*(11), 1091–1113. https://doi.org/10.1080/14685248.2015.1052464

Tardu, F. S., & Binder, G. (1993). Wall shear stress modulation in unsteady turbulent channel flow with high imposed frequencies. *Physics of Fluids A: Fluid Dynamics*, *5*(8), 2028–2037. https://doi.org/10.1063/1.858538

Tardu, F. S., & Vezin, P. (2004). Response of the streaks, the active and passive eddies in an unsteady channel flow. *International Journal of Heat and Fluid Flow*, *25*(6), 915–932. https://doi.org/10.1016/j.ijheatfluidflow.2004.02.026

Tardu, S. F. (2007). Spectral Characteristics of the Near-Wall Turbulence in an Unsteady Channel Flow. *Journal of Applied Mechanics*, *74*(1), 172. https://doi.org/10.1115/1.2166650

Tardu, S. F., Binder, G., & Blackwelder, R. F. (1994). Turbulent channel flow with large-amplitude velocity oscillations. *Journal of Fluid Mechanics*, *267*, 109–151. https://doi.org/DOI: 10.1017/S0022112094001138

Tennekes (Hendrik), H., & Tennekes, H. (Hendrik). (1972). *A first course in turbulence*. (J. L. (John L. Lumley, Ed.). Cambridge, Massachusetts: Cambridge, Massachusetts : MIT Press, 1972.

Tollmien, W. (1929). *Uber die entstehung der turbulenz. Nachr. Ges. Wiss. G¨ottingen 21-24 (English version: Tollmien, W.: The production of turbulence. NACA-TM-609-translated by D. M. Miner, Washington,D. C. 1931) translation*.

Tu, S. W., & Ramaprian, B. R. (1983). Fully developed periodic turbulent pipe flow. Part 1. Main experimental results and comparison with predictions. *J. Fluid Mech.*, *137*, 31–58. https://doi.org/10.1017/S0022112083002281

van der A, D. A., O'Donoghue, T., Davies, A. G., & Ribberink, J. S. (2011). Experimental study of the turbulent boundary layer in acceleration-skewed oscillatory flow. *J. Fluid Mech.*, *684*, 251–283. https://doi.org/10.1017/jfm.2011.300

Van der Sande, E. (1980). Velocity Profiles in Accelerating Pipe Flows Starting from Rest. In *Proc. 3rd Int. Conf. on Pressure Surges* (p. pp 1-14). Canterburry, England.

Vaughan, N. J., & Zaki, T. A. (2011). Stability of zero-pressure-gradient boundary layer distorted by unsteady Klebanoff streaks. *Journal of Fluid Mechanics*, *681*, 116–153. https://doi.org/10.1017/jfm.2011.177

von Kármán, T. (1930). Mechanische ahnlichkeit und turbulenz. In *In Third International Congress of Apllied Mechanics, Stockholm* (pp. 85–105).

Watmuff, J. H. (2004). Evolution of a Turbulent Wedge from a Streamwise Streak. In *15th Australasian Fluid Mechanics Conference* (pp. 13–17).

Weske, J. R. (1943). *A hot-wire circuit with very small time lag. NACA Technical Note No. 881*.

Westin, K., Boiko, A., Klingmann, B., Kozlov, V., & Alfredsson, P. (1994). Experiments in a boundary-layer subjected to free-stream turbulence.1. Boundary-layer structure and receptivity. *J. Fluid Mech.*, *281*, 193–218.

White, F. M. (1974). *Viscous Fluid Flow*. McGraw-Hill, New York.

Winter, K. (1977). An outline of the techniques available for the measurement of skin friction in turbulent boundary layers. *Progress in Aerospace Sciences*, *18*(1), 1–57.

Wygnanski, I., Sokolov, M., & Friedman, D. (1975). On transition in a pipe. Part 2. The equilibrium puff. *J. Fluid Mech.*, *69*(2), 283–304. https://doi.org/10.1017/S0022112075001449

Zaki, T. A. (2013). From Streaks to Spots and on to Turbulence : Exploring the Dynamics of Boundary Layer Transition, *91*(3), 451–473. https://doi.org/10.1007/s10494-013-9502-8

Zaki, T. A., & Saha, S. (2009). On shear sheltering and the structure of vortical modes in single- and two-fluid boundary layers. *Journal of Fluid Mechanics*, *626*, 111–147. https://doi.org/10.1017/S0022112008005648

# List of publications

Oluwadare, B. O., Mathur, A., & He, S. (2017). Study of Turbulence in Unsteady Flows using Particle Image Velocimetry (PIV) and Constant Temperature Anemometry (CTA). *Bulletin of the American Physical Society (APS), USA.* (Vol. 62).

Oluwadare, B. S., & He, S., (2018). Study Response of Turbulence in Transition of Unsteady Channel Flows. In *Proc. of the 5th International Conference of Fluid Flow, Heat and Mass Transfer, Niagara Falls, Canada*. Paper No 132.

Oluwadare, B. S., & He, S. (2018). Effect of Varying Reynolds Number Ratio on Transition to Turbulence in Unsteady Flows. In *Proc. of the* 48th AIAA Fluid Dynamics Conference, Atlanta, Georgia, USA.

# List of scholarships and awards

The following scholarships and awards have contributed substantially to the success of this research degree programme at the University of Sheffield:

1. IMechE Student Scholarship, London. 2019
2. Student Scholarship, Department of Mechanical Engineering, the University of Sheffield, United Kingdom. 2018
3. IMechE Student Scholarship, London. 2018
4. IMechE Award, London. 2018
5. Learned Societies Award, the University of Sheffield. 2018
6. ASME IGTI Student Scholarship, USA. 2017
7. Learned Societies Award, the University of Sheffield. 2017
8. PhD Scholarship by Petroleum Technology Development Fund (PTDF). 2015

# Appendix A

This section is incorporated to show the response of streamwise mean velocity and turbulence statistics during the acceleration from laminar flow to turbulent flow. The development of bulk velocity, skin friction coefficient, wall shear stress, streamwise mean velocity and turbulence statistics for the accelerating channel flow starting from laminar and ramping up to turbulent flow is presented. The procedure of transition to turbulence is similar to that of the transition of transient turbulent flows reported in Chapter Four and Chapter Five.

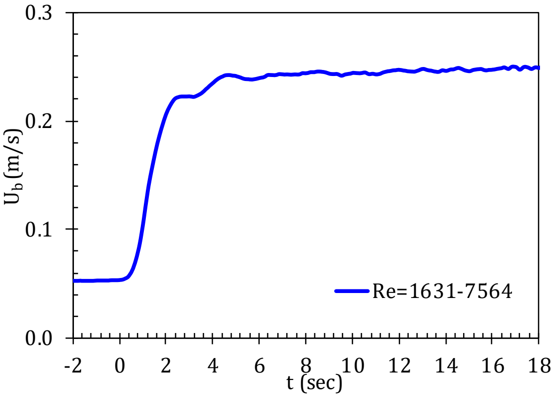

a)

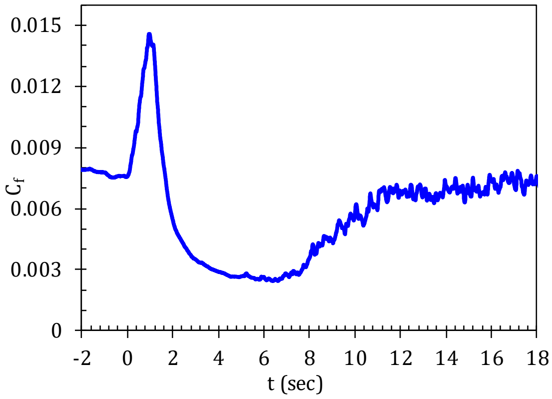

b)

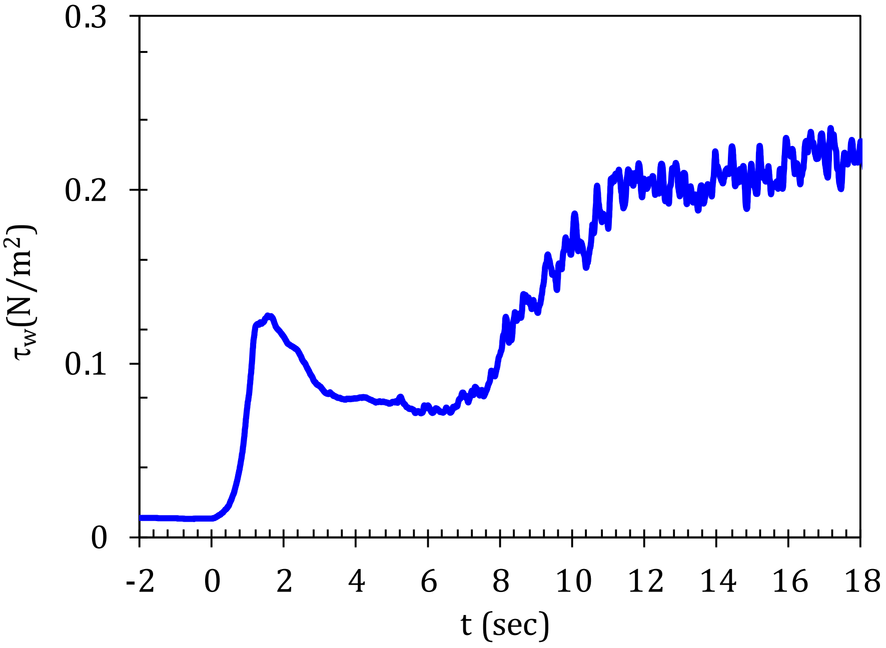

c)

***Figure A-1:Development of a) bulk velocity ($U_b$), b) skin friction coefficient ($C_f$) and c) wall shear stress ($\tau_w$) for laminar case ($Re_b = 1631 - 7564$).***

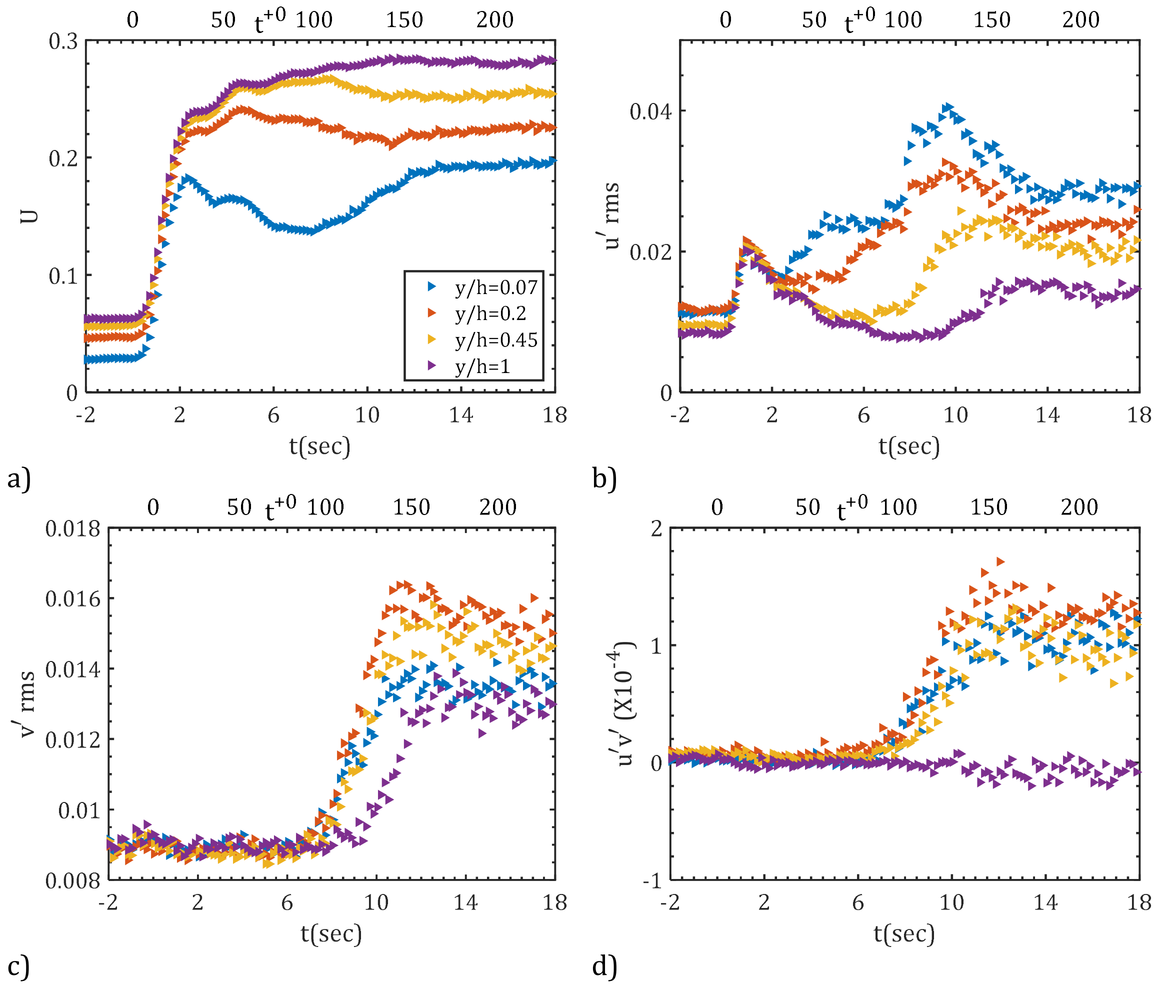

***Figure A-2:Development of streamwise mean velocity ($U$), streamwise fluctuating velocity ($u'_{rms}$), wall-normal fluctuating velocity ($v'_{rms}$) and Reynolds shear stress ($\overline{u'v'}$) for laminar case ($Re_b = 1631 - 7564$). Legend is the same for the four subplots and all quantities are not normalised. The unit of subplots (a)-(c) is m/s and that of subplot (d) is m²/s². Channel half-height δ=h.***

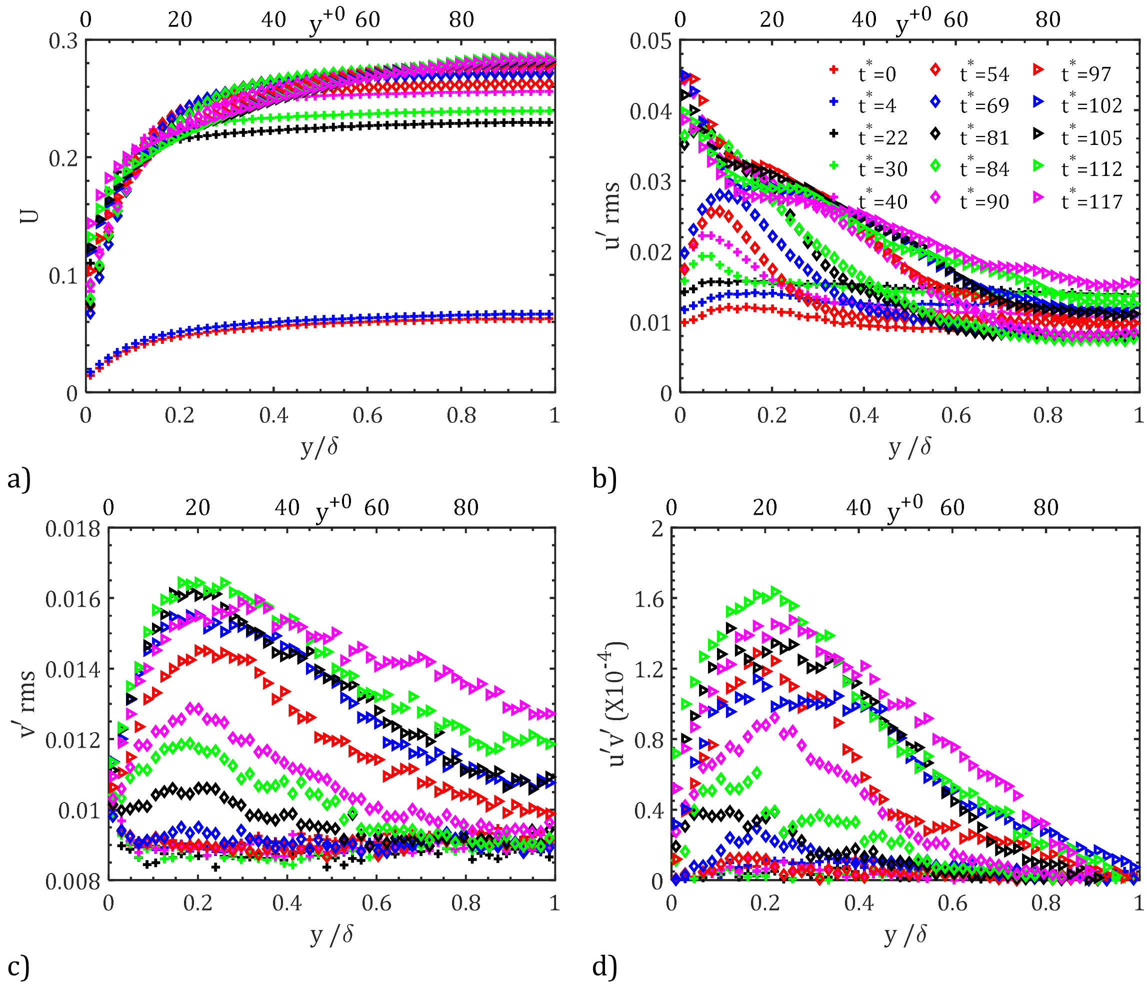

***Figure A-3: Temporal growth of streamwise mean velocity $(U)$, streamwise fluctuating velocity $(u'_{rms})$, wall-normal fluctuating velocity $(v'_{rms})$ and Reynolds shear stress $(\overline{u'v'})$ for laminar case $(Re_b = 1631 - 7564)$. Legend is the same for the four subplots. The unit of subplots (a)-(c) is m/s and that of subplot (d) is m²/s².***

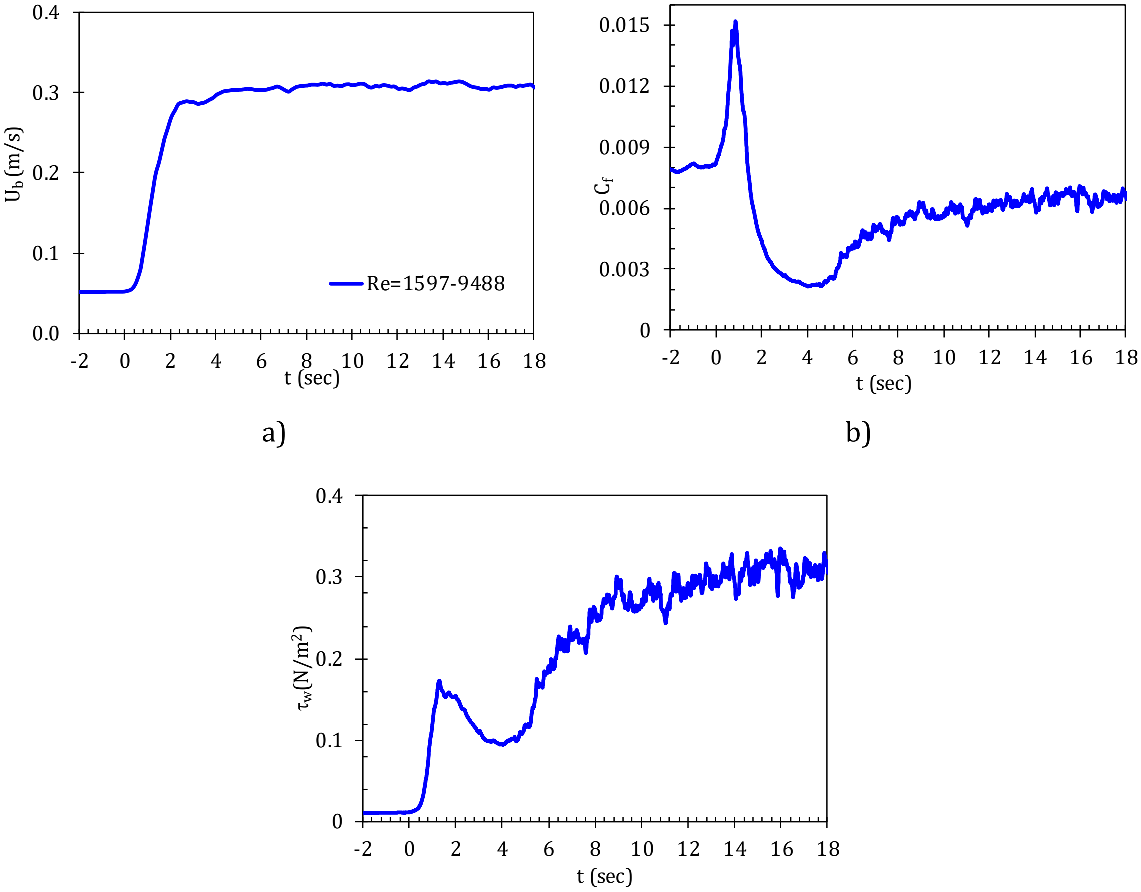

a)

b)

c)

***Figure A-4: Development of a) bulk velocity ($U_b$), b) skin friction coefficient ($C_f$) and c) wall shear stress ($\tau_w$) for laminar case ($Re_b = 1597 - 9488$).***

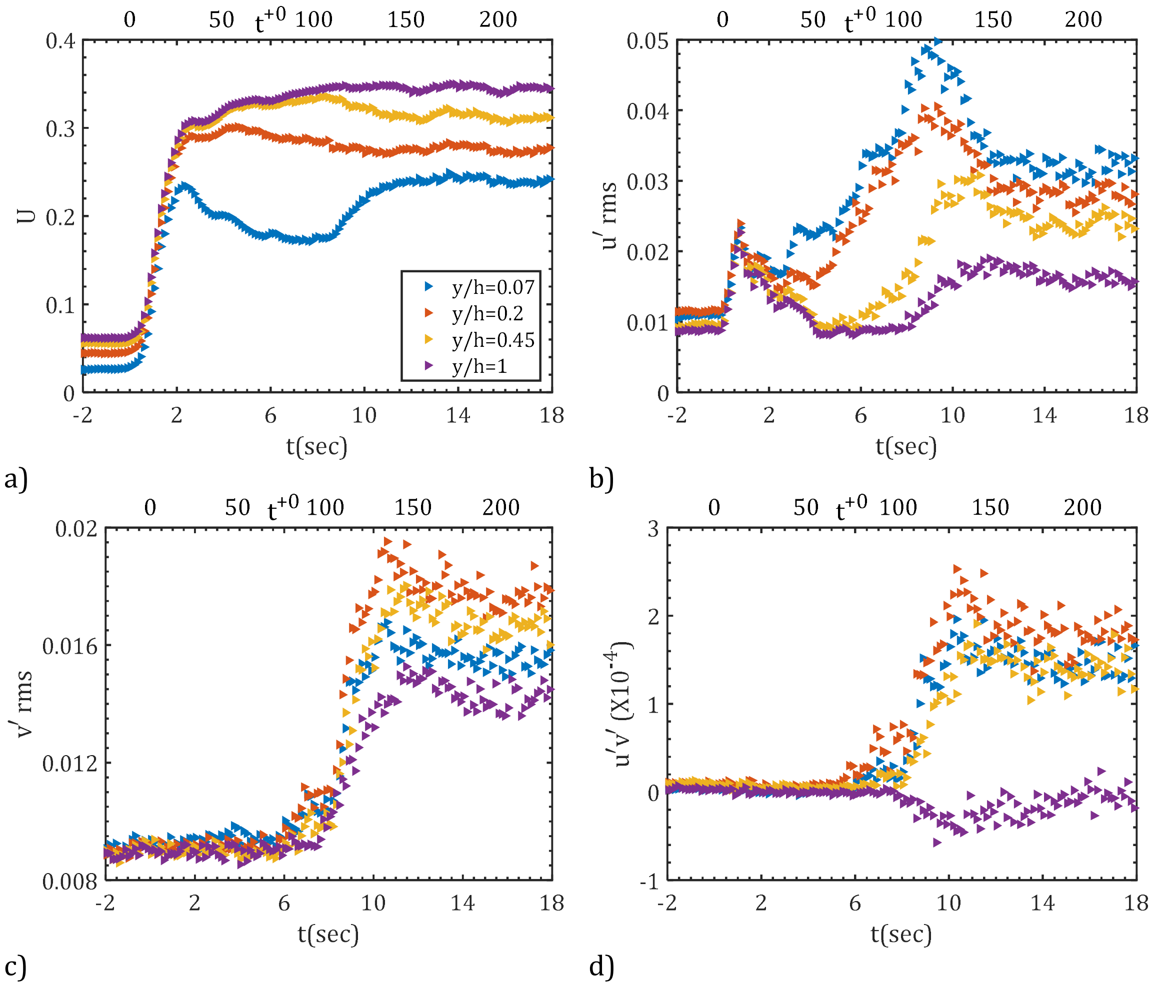

***Figure A-5:Development of streamwise mean velocity*** $(U)$***, streamwise fluctuating velocity (***$u'_{rms}$***), wall-normal fluctuating velocity (***$v'_{rms}$***) and Reynolds shear stress (***$\overline{u'v'}$***) for laminar case (***$Re_b = 1597 - 9488$***). Legend is the same for the four subplots and all quantities are not normalised. The unit of subplots (a)-(c) is m/s and that of subplot (d) is m²/s². Channel half-height δ=h.***

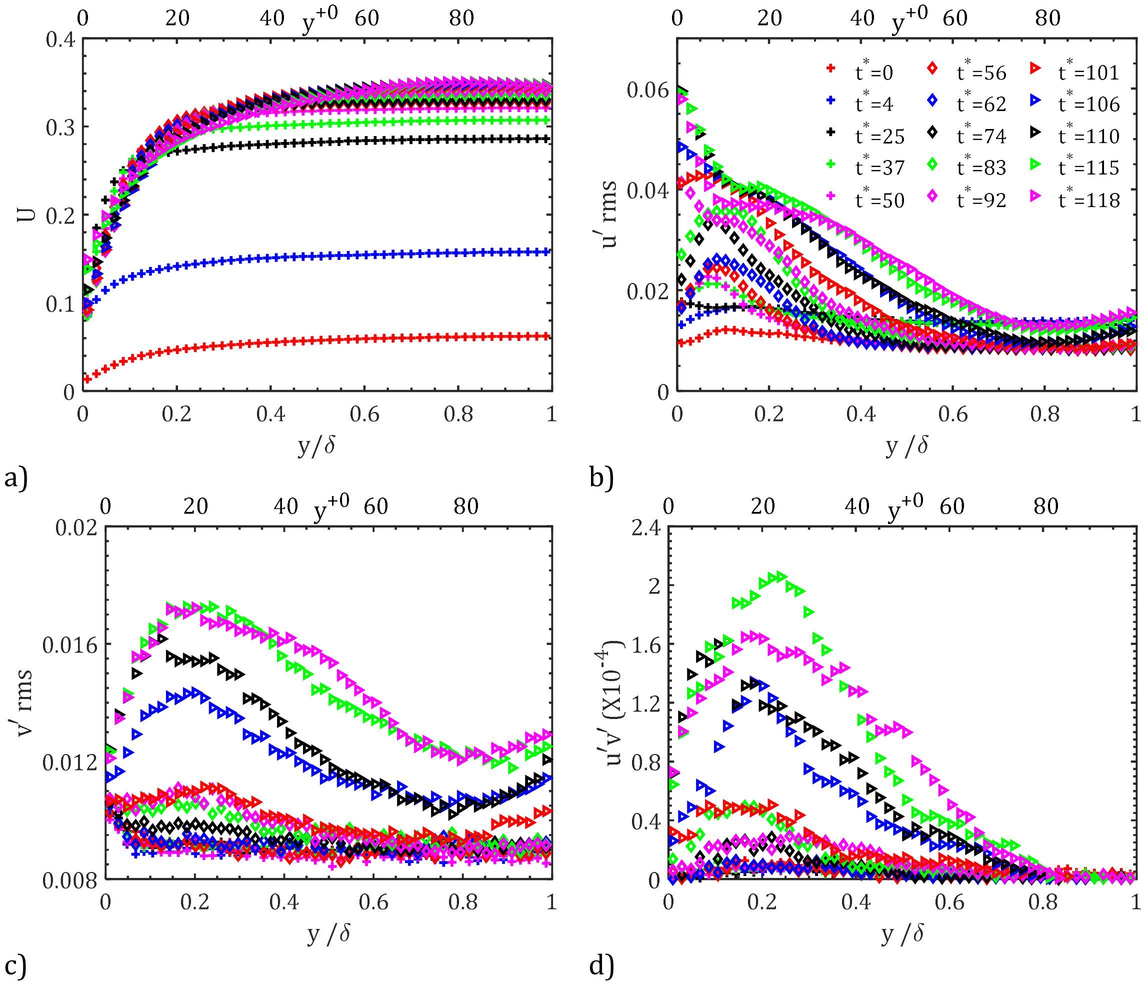

***Figure A-6: Temporal growth of streamwise mean velocity ($U$), streamwise fluctuating velocity ($u'_{rms}$), wall-normal fluctuating velocity ($v'_{rms}$) and Reynolds shear stress ($\overline{u'v'}$) for laminar case ($Re_b = 1597 - 9488$). Legend is the same for the four subplots. The unit of subplots (a)-(c) is m/s and that of subplot (d) is m²/s².***

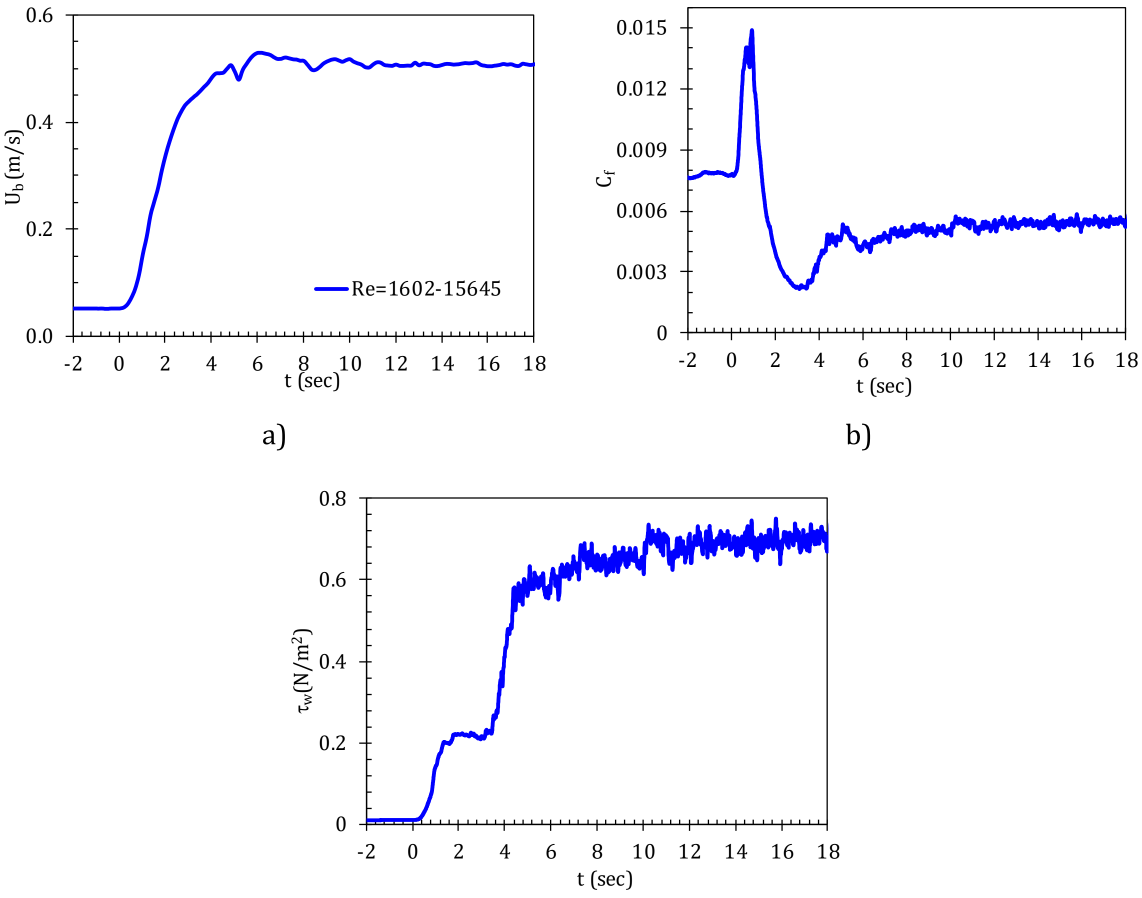

a)

b)

c)

***Figure A-7: Development of a) bulk velocity ($U_b$), b) skin friction coefficient ($C_f$) and c) wall shear stress ($\tau_w$) for laminar case ($Re_b = 1602 - 15645$).***

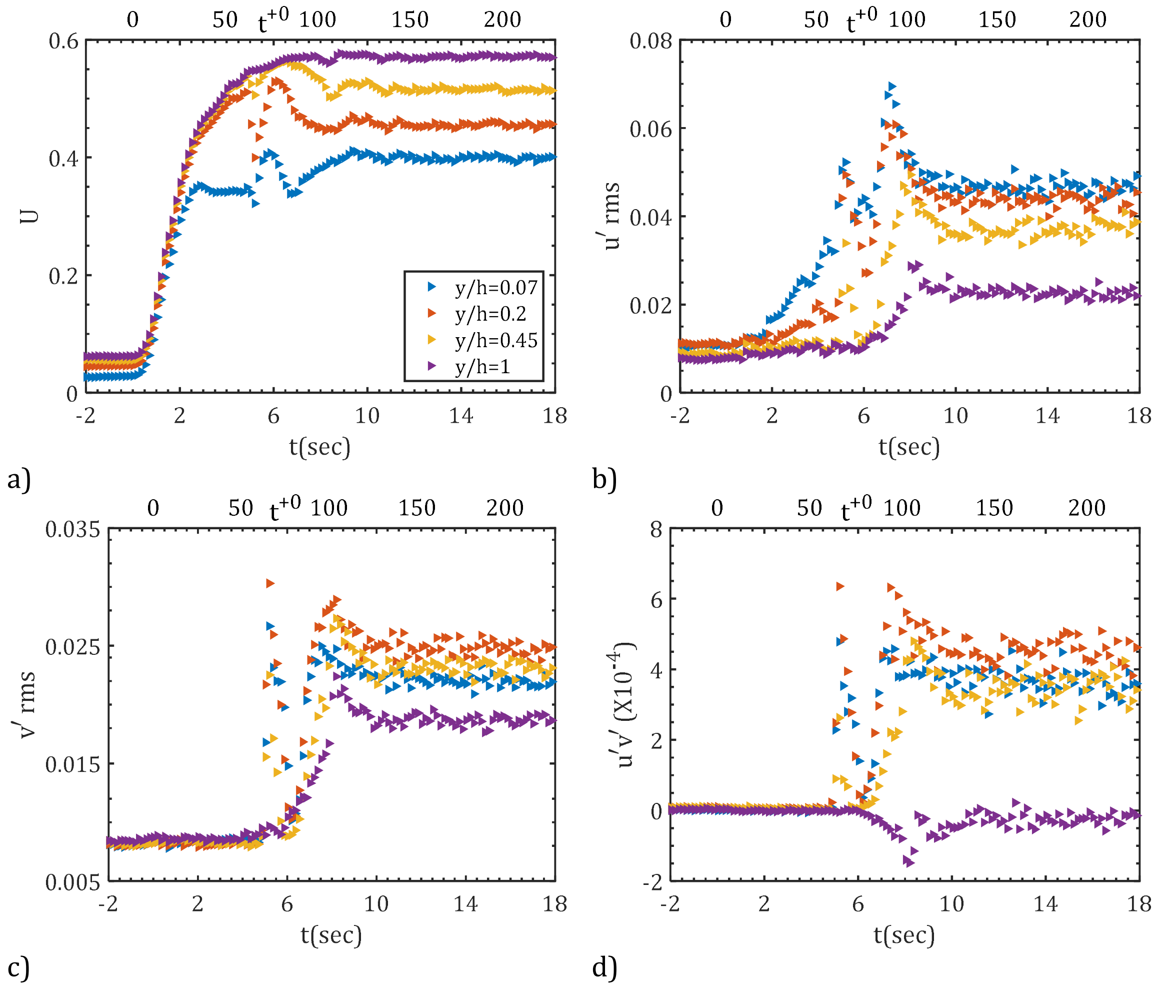

a) b) c) d)

*Figure A-8:Development of streamwise mean velocity $(U)$, streamwise fluctuating velocity $(u'_{rms})$, wall-normal fluctuating velocity $(v'_{rms})$ and Reynolds shear stress $(\overline{u'v'})$ for laminar case $(Re_b = 1602 - 15645)$. Legend is the same for the four subplots and all quantities are not normalised. The unit of subplots (a)-(c) is m/s and that of subplot (d) is m²/s². Channel half-height δ=h.*

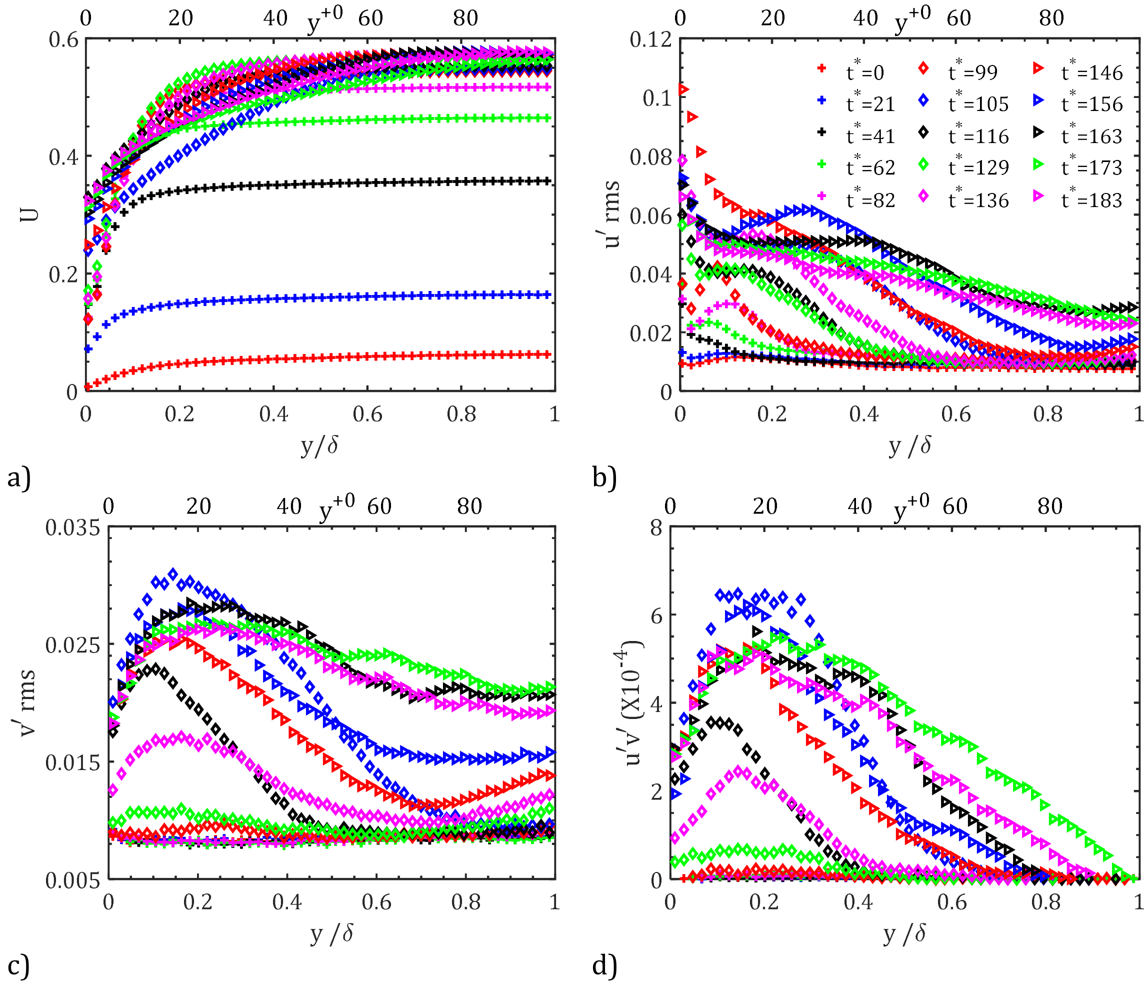

***Figure A-9: Temporal growth of streamwise mean velocity $(U)$, streamwise fluctuating velocity $(u'_{rms})$, wall-normal fluctuating velocity $(v'_{rms})$ and Reynolds shear stress $(\overline{u'v'})$ for laminar case $(1602-15645)$. Legend is the same for the four subplots. The unit of subplots (a)-(c) is m/s and that of subplot (d) is m²/s².***

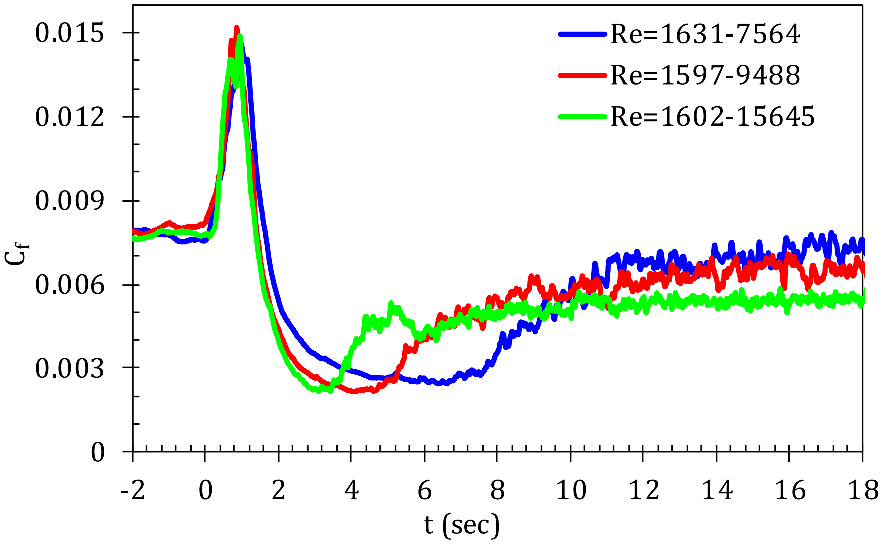

***Figure A-10: Time development of skin friction coefficient ($C_f$) for the three laminar cases ($Re_b = 1631 - 7564, Re_b = 1597 - 9488$ and $Re_b = 1602 - 15645$).***